Aqueous Solution Chemistry of Ruthenium Arene Anticancer Complexes

A Thesis Submitted for the Degree of

Doctor of Philosophy

by

Julie Ann Lough, *B.Sc.*

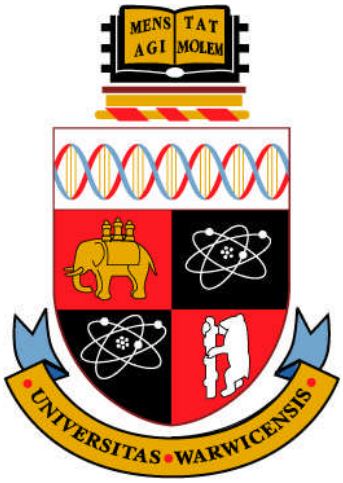

University of Warwick, Department of Chemistry

September 2010

To my family, Mam, Dad, Ian,
Viv and Mark, and my friends
Rod, Lou and Ciara, the best
friends a girl could ask for.

Contents

Chapter 3

Table of Figures

Table of Tables

Table of Schemes

Acknowledgements

Where does one start when it comes to thanking all of those people who have accompanied me on this long journey!

I suppose most importantly is the boss, Prof. Peter J. Sadler FRS. His help and guidance, not to mention patience every step of the way in this journey, has made the long journey, one of discovery and constant learning and enlightenment. His support has been invaluable and it has been a true honour to work for a man of such brilliance, not to mention one who gets my twisted humour!

A huge thank you must go to Dr Abraha Habtemariam, the daddy of the group, whose advice is invaluable and priceless! The mania of moving 5 labs over 300 miles, working and writing was made an awful lot easier by his presence. His ability to make me smile when I want to scream was much appreciated and he has certainly brought a light into my life.

To the other "early arrivers" from Edinburgh, Juanita (Dr Ana Pizarro) and little Sarah (Dr Sarah Farley) who are like sisters to me, I will miss you both so much. I know I don't often say it enough, but I love you guys!

A special mention to PJS people must also go to the following, Dr Sarah Dougan, a huge source of knowledge, chumming me to the shops and my Pepsi Max drinking buddy! Drs. Allison Ross and Stefan Weidt for their support, assistance and encouragement over the years!

To all the Warwick Pepes, Sole, Claire, Evyenia and Khatija, thanks for the laughs, hugs, food, support and so many happy memories Pasta le Pasta!!! Oh and Sabine – "Don't stop believing!" To my "little brother" Yao and everyone else in the PJS group (both from Edinburgh and Warwick), thanks a million!

Huge thanks must go to Ms Barbara Malinen of the student counselling service in the University of Edinburgh, who through her patience (over a very, very long time) and support gave me the strength to get through the dark days and see that life is worth living and I don't need to be superwoman all the time! Dr Christmas and Dr Kean, of the Royal Edinburgh Psychiatric Hospital , who may never read this but to whom I will always be grateful for the fact that they saved my life on a very dark August day in 2006. Without their help, guidance, strong medical intervention and support I have no doubt this thesis would never have been started, let alone finished.

A special thanks to Rod Walshe, a constant presence in my life without whom, I fear what remains of my sanity would have disappeared long ago! I've lost count of the number of rants, cries and laughs we have shared in long phonecalls over the Irish Sea over the last few years. You're a girl's best friend! He also thinks my posters are pretty because they have shiny colours and even read this thesis!!

Louise, Ciara, Susanne and all the ambulance folk back home, thanks for the support and gossip from home!

To all the crazy folk involved in RaW1251am, wow! What can I say, the distraction of radio has probably delayed my PhD mors than anything, but my, how it has changed my life and potential career path! Special thanks to James, Tash, Chris and Jon! You guys are amazing!

To everyone else I met along the way, Laura, Hannah, Damien, Aimee, just to name a few… some I still see some I don't but you all made the journey amazing! I know I have left people out, but if I write anymore this will be the longest part of my thesis!

A "thanks a million" and a "love ya" to Juraj Bella (Edinburgh NMR Guru), Dr Ivan Prokes and Lijiang Song in Warwick for their help with NMR and mass spectrometry respectively.

Also a thanks to my collaborators, not everything worked but it was great trying; Dr Steven Magennis and Anita Toulmin, (University of Manchester), Dr Jon Williams (Warwick and Now Waters), Prof. Stephen Neidle and Dr Nancy Campbell – a truly talented scientist and an amazing laugh!, Dr. HongKe Liu (Nanjing Normal University, China) and those who have been intellectual sounding boards for me over the course of my PhD, Dr. Neil Robertson (Edinburgh), Drs David Fox and Stefan Bon (Warwick).

Finally, to Mam, Dad, Vivien and Ian...I'm finished....slightly later than expected; I hope you are all proud. I can now begin to pay back those debts!

"Let it always be known that I was who I am"

It's been long, but amazing….this crazy Irish girl is outta here!
LY (NLT)
J. Lo

Declaration

I hereby declare that, except where specific reference is made to other sources, the work contained in this thesis is the original work of the author. It has been composed by myself and has not been submitted, in whole or in part, for any other degree, diploma, or other qualification.

Some of the Work included in this thesis has been previously to the following journal.

"Use of ion mobility mass spectrometry and a collision cross-section algorithm to study an organometallic ruthenium anticancer complex and its adducts with a DNA oligonucleotide" Williams, J. P.; Lough, J. A.; Campuzano, I.; Richardson, K.; Sadler, P. J. *Rapid Commun. Mass Spectrom.* 2009, *23* (22), 3563-3569.

_____

Julie Ann Lough

September 2010

Abstract

Metal complexes currently are currently of much interest in the field of anticancer drug development. Platinum complexes such as cisplatin, are now widely used in the clinic and have led to a focus on the synthesis of new classes of other metal-based complexes, such as ruthenium anticancer drugs. In order to understand the mechanism of action of these complexes and to improve structure-activity relationships thereof, a comprehensive study of the solution chemistry is important.

In this thesis the mechanism and kinetic detail of the exchange of amino protons on one such class of complex, [(η^6-biphenyl)Ru(*N*,*N*'-ethylenediamine)Cl]$^+$ was investigated in detail. Stereospecific assignment of NH protons was carried out by NOESY NMR on a pyridine adduct [(η^6-biphenyl)Ru(*N*,*N*'-ethylendiamine)(*N*-pyridine)]2+. Using ^{1}H and ^{2}H NMR spectroscopy, rates of exchange were observed at different pH values, temperatures and ionic strengths a series of N-H/^{2}H exchange reactions were studied and the data collected. The data are consistent with an exchange mechanism involving proton abstraction from the amine, followed by favourable reprotonation on the lowerface (relative to the overhanging arene) of the Ru(*N*,*N*'-ethylendiamine) five membered ring. In chlorido complexes this leads to the exchange of lower proton at a rate of three times that of those on the upperface at 298 K. To investigate the effects of electron density on the ruthenium on the exchange rates a series of π-donor pyridine ligands (pyridine, 4-methylpyridine, 4-tert-butylpyridine, and 4-methoxypyridine) in the place of the chloride were studied. The exchange rates were also investigated and showed a correlation between the basicity of the pyridine derivative and the favourability of exchange

on the lower face, increasing this bias upto 11 fold. Density functional theory calculations suggests that there is an overlap between the p-orbital of the (ethylenediamine) nitrogen and the π*-antibonding orbital on the Ru-N(Pyridine) bond and σ*- antibonding orbital on the Ru-Cl bond, in their respective complexes. This overlap is proposed as a stabilising force on the deprotonated nitrogen allowing for a negative charge to be more stabile in one lobe of the p-orbital preferential to another. Following abstraction of the proton, the lone pair on the nitrogen is stabilised by an antibonding orbital, the top face less is susceptible to proton addition.

Since DNA is a potential target for these complexes, the changes in shape induced by metal binding were investigated using Ion-Mobility Mass Spectrometry for the first time. Also in this work, the first ion-mobility mass spectrometry studies of the collisional cross sections (CCSs) of small complexes (<100 $Å^2$) is also presented. This was developed using a new glycine based calibrant. Following binding of [(η^6-biphenyl)Ru(*N*,*N*'- ethylenediamine)Cl]$^+$ to the DNA hexamer d(CACGTG) changes in CCS values between ruthenated and non-ruthenated hexamers were studied. The change in CCS between these was not additive and suggestive of some folding or intercalation occurring upon ruthenium binding.

Finally, attempts were madeto investigate shape change induced in DNA by binding to cisplatin using Förster Resonance Energy Transfer Methods are described. To date these results are inconclusive but work in this field is ongoing.

Abbreviations

9-EtG	9-Ethylguanine
acac	acetylacetate
ATDs	Arrival Time Distributions
BBO	Broadband Observe
ben	benzene
bip	biphenyl
bipy	2,2'-bipyridine
c.f.	Cross reference
CCS	Collision Cross-Sections
CD	Circular Dichroism
CHN	Carbon Hydrogen Nitrogen (elemental analysis)
CID	Collision induced decay
COSY	COrrellation SpectroscopY
DFT	Density Functional Theory
DHA	Dihydroanthracene
DNA	Deoxyribose Nucleic Acid
DOSY	Diffusion Ordered Spectroscopy
EHSS	Exact Hard Sphere scattering
en	ethylenediamine
ESI-MS	Electrospray Ionisation Mass Spectrometry
Et-en	N-Ethylethylenediamine
FID	Free Induction Decay
FRET	Forster Resonance Energy Transfer
h	hour

Hb	Haemoglobin
HDMS	High Definition Mass Spectrometer
HIV	Human Immunodeficency Virus
HMG	High Mobility Group protein
HOMO	Highest Occupied Molecular Orbital
HPLC	High Performance Liquid Chromatograhy
Hz	Hertz
IC_{50}	Concentration required to inhibit 50% growth
ICP-MS	Inductively Coupled Plasma-Mass Spectrometry
IM-MS	Ion-Mobility Mass Spectrometry
IR	Infrared
K	Kelvin
k	rate constant
kHz	Kilohertz
kJ	kilo-Joules
kV	kilo-Volts
lpe^-	Lone Pair of electrons
LUMO	Lowest Unoccupied Molecular Orbital
m/z	Mass to charge ratio
MHz	Mega-Hertz
MRI	Magnetic Resonance Imaging
ms	milliseconds
NMR	Nuclear Magnetic Resonance
NOE	Nuclear Overhauser Effect
PA	Projection Approximation

p-cym	para-cymene
ppb	parts per billion
ppm	parts per million
ppt	parts per trillion
pyr	pyridine
RP-HPLC	Reverse Phase High Performance Chromatography
$t_{½}$	Halftime
THA	Tetrahydroanthracene
ToF	Time of Flight
T-Wave	Travelling Wave
UHQ	Ultra High Quality
UV	Ultraviolet Light
Vis	Visible Light

Chapter 1

Introduction

Chapter 1
Introduction

This thesis is principally concerned with the mechanism of exchange of amino protons on the ethylenediamine ligand on [(η^6-biphenyl)Ru^{II}(ethylenediamine)Cl]$^+$ ([(η^6-bip)Ru(en)Cl]$^+$) and *o*-pyridine derivates ([(η^6-bip)Ru(en)(*p*-R-pyridine)]$^{2+}$) complexes in solution. The effects of exchanging the chlorido ligand for a pyridine derivative on the exchange rates were also investigated. In addition, studies into shape modifications by metallodrugs on short strands of DNA oligonucleotides were also carried out. This chapter is an introduction into the rationale behind the development of metal based anticancer complexes and structure activity relationships that can be used to increase their cytotoxicity.

1.1 Metals in Medicine

Traditionally, designed compounds for medicinal purposes have been organic molecules, with relatively very few inorganic compounds in use.[1] Perhaps this is because it has long been viewed that inorganic complexes and biology were mutually exclusive. In part, this was blamed on the tendency for many inorganic complexes to be air and moisture sensitive, two materials which are ubiquitous in biology. Other drawbacks with inorganic medicinal chemistry are issues with speciation (for example; in solution is the metal complex a chlorido, hydroxido or aqua adduct or a mixture of these?). So, for most of the last century the majority of designed synthetic medicinal compounds were organic based.

A further obstacle was the belief that the words "heavy metal" and "body", immediately meant death! Opinions of this nature have not been helped by such quotes as "Heavy metals are among the most dangerous and least understood of all contaminants".[2] The commonly known fact about "mad hatters" and the residents of Minamata[3,4] (Hg poisoning), lead contamination in water and the questions about the murder of Napoleon (As)[5], have further heightened the general public's, and indeed some scientists', fears about the dangers of mixing metals and biology.

However, long before the deliberate study of metal based anticancer drugs, there existed plenty of cases in nature where metals and biology quite happily interacted. Gold false teeth were regularly used by the ancient Egyptians and Chinese, mercury was also used by the ancient Greeks and in the middle ages as a cure for lice and scabies. Before the early 20th century the use of mercury in the treatment of syphilis was a wide spread practise, cinnabar (HgS) was painted onto lesions caused by syphilis to cure the illness unfortunately this lead to mercury poisoning in many cases. In fact, it is with interest to note that the first metallodrug which was discovered through systematic screening was also for the treatment of syphilis, this was Paul Ehrlich's discovery of Salvarsan in 1909[6] while much debate over exact structure of Salvarsan existed for some time, in 2005[7] it was confirmed to be the following;

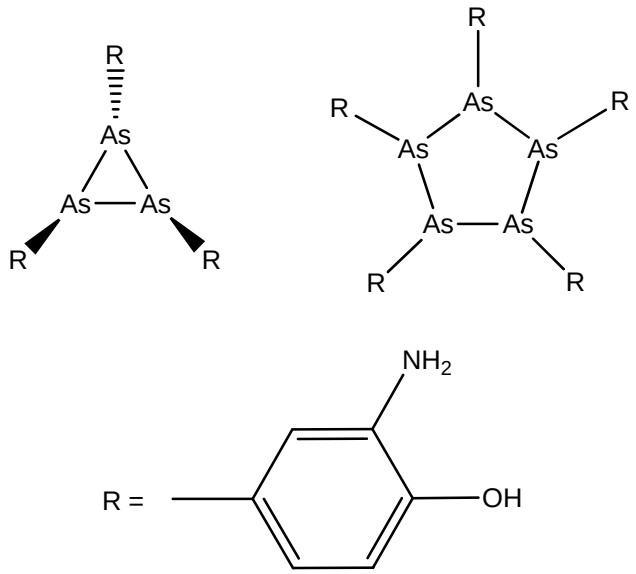

Figure 1.1: The structure of Salvarsan as determined by Lloyd *et al*.[7]

Not only have metals been used in medicine in the past, both through serendipity and systematic discovery but metals play a vital role in many biological systems. Nature uses metals in many ways, and many are vital to life, for example many other enzymes contain metal centres, including; haemoglobin (Fe), carbonic anhydrase (Zn and Ni), vitamin-B_{12} (Co), superoxide dismutase (Cu, Fe, Mn, Ni or Zn) to name just a few. In these cases the metal is the catalytic centre of these enzymes and therefore deficiency in these elements can lead to serious health complications even death!

The toxicity of a metal is rarely a hard and fast rule. It is all about the packaging (complexation). Thought must be given to the nature and number of the ligands, the oxidation state as well as the dose of any compound[8]. A classic example of this would be iron, of which we have about 4 g in our body[9]. We need Fe^{II} in haemoglobin in order to transport oxygen around the body; we get our iron as Fe^{II} (ferrous iron) from our food (meat, green root vegetables etc). However not every iron containing complex is beneficial for health, complexes such as

ironpentacarbonyl are toxic due to the ability to deliver carbon monoxide to the body. Perhaps it is best summarised in the words of Paracelsus (1493 – 1541) of the University of Basel. "Alle Ding sind Gift und nichts ohn Gift; alein die Dosis macht das ein Ding von Gift ist" [All these things are poison and not without poison, it is only the doses that makes a thing not a poison][10]. With iron, if there is too little in the body, a person can suffer from anaemia, too much can lead to haemochromatosis (an accumulation of iron in the organs) and long term accumulation of iron has been linked to Alzheimer's disease[11,12].

The usefulness of metals in the body is due to their ability to take up a number of different physical and chemical characteristics.

1 One of the key chemical properties with metals is they can undergo changes in oxidation states, since there are many different reducing and oxidising agents in cells and in blood.

2 Metals can also undergo ligand exchange and bind to different ligands other than those they entered the body with. In fact, metals cannot only bind to many different electron donating ligands, the coordination number of these ligands can change depending on the oxidation state of the metal and on steric and electronic effects from the ligand. Further to this metals can bind through a number of modes to the ligands, i.e. π- bonding and σ-bonding.

These traits give metals the flexibility in their steric, electronic and bonding structure that is not available to organic molecules. Therefore the

potential for application is wider in comparison with most organic compounds, which do not have such chemical dexterity.

In recent years the study and progression of metal-based pharmaceutical agents has increased and has lead to a more varied approach to the use of metals in biological and medicinal systems being adopted.[13-18] Some metal-based complexes in clinical use utilise the features discussed above to harness and increase their biological activity. These include; cisplatin[19] (*cis*-diamminedichloridoplatinium(II), $[Pt(NH_3)_2Cl_2]$), one of the world's leading anticancer drugs and radiopharmaceuticals containing technetium and rhenium[20] for imaging use in patients and gadolinium MRI contrast agents.[21-23] All of which have successfully overcome problems that organic chemistry alone could not have solved due to their ability to form dative bonds *via* the metal's d-orbitals, undergo radioactive decay or ligand exchange and therefore induce magnetic relaxation in water molecules in close proximity.

1.2 Platinum anticancer drugs

After the discovery of cisplatin's anticancer properties[19,24] in the 1960s and its subsequent success in treating many forms of cancer, a huge amount of research into the mechanism of cell uptake, activation and lethal lesion formation on DNA strands have been carried out, with over 7,000 reviews alone written on the subject to date (almost 70,000 papers). It has opened up a whole field of study into metal based anticancer drugs.

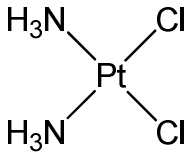

Figure 1.2 Chemical Structure of cisplatin

With over forty years having past since the initial discovery and thirty since the use of cisplatin (**1**) in clinical trials was licensed to Bristol-Myers Squibb in 1972, a complete mechanism of action has yet to be fully confirmed, but in brief it is believed to be as follows.[25]

Firstly, in aqueous solutions cisplatin undergoes hydrolysis[26], producing the active species *cis*-$[Pt(NH_3)_2(OH_2)_2]^{2+}$ and $[Pt(NH_3)_2(OH_2)Cl]^{+}$ where one or more chlorido ligands undergo substitution by a water molecule. These mono- and di- aqua complexes can then bind to the N7 of guanine residues of DNA strands[27] (Figure 1.3), forming 1,2-G,G and 1,3-G,G intrastrand crosslinks on DNA causing distortion in the shape of the strand and the duplex.[28]

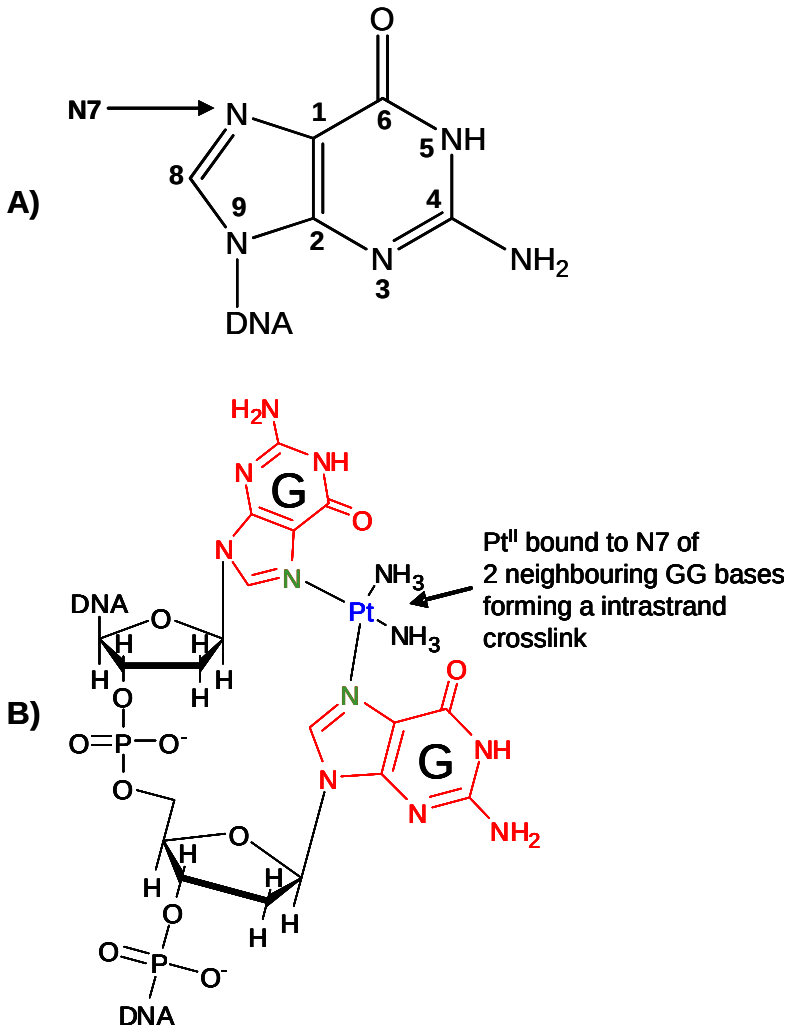

Figure 1.3. A) Guanine residues of DNA strands with N7 highlighted. **B)** A representation of the structure of binding of cisplatin via the N7 site on guanine bases, where the N7, the most electron rich regions on DNA are highlighted.

This kinking of the DNA as a consequence of metal binding leads to recognition by High Mobility Group (HMG) proteins (Figure 1.4). This recognition by the HMG proteins protects the DNA from the nucleotide excision/repair mechanism this in turn leads to cell death *via* apoptotic pathways. Cisplatin, however has many side effects[29], including loss of high frequency

hearing and nephrotoxicity and cells can develop resistance and can also be intrinsically resistant (unresponsive) to treatment. To add to this the presence of sulfur containing biomolecules such as glutathione which can bind to the platinum centre and block the active sites and cells also have an efflux mechanism[30] which can remove cisplatin from cells and reduce its cytotoxicity.

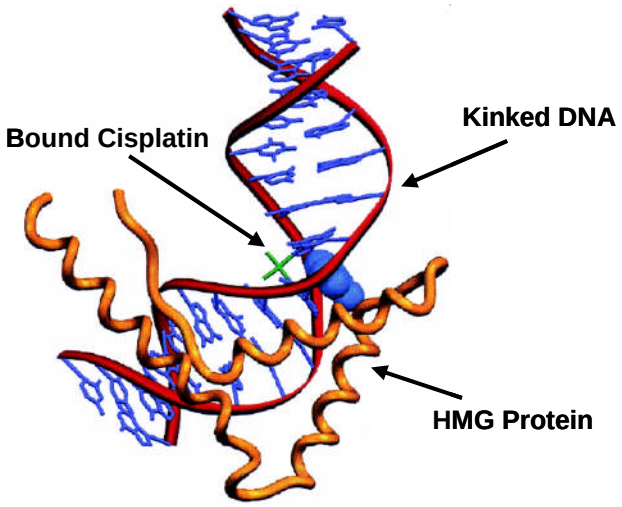

Figure 1.4 DNA kinked after binding to cisplatin and recognition by HMG protein. Image is modified from that by Lippard et al.[31]

It was these problems with side effects, resistance within cancer cells and the limitation on the number of cancer types that can be treated with cisplatin has led to the search for other metal-based complexes that may show anticancer activity. Part of this research has led to the discovery of ruthenium-based drugs.

1.3 Ruthenium anticancer drugs

In an effort to overcome the toxicity issues with platinum complexes, other metal complexes were studied to see if similar activity with fewer side effects could be observed. Given the fact that the rates of ligand exchange play a crucial

role in the activation of cisplatin (i.e.: it is in the "goldilocks" region where hydrolysis of the chlorido ligands occurs at just the right rate) metals with similar rates of ligand exchange were investigated. Ruthenium undergoes ligand exchange at a similar order of magnitude to rate platinum making it an ideal candidate for further study.[15]

One of the first references to ruthenium anticancer drugs in the literature is in 1975[32] when the activity of cisplatin, was compared to that of [$RuCl_2DMSO_4$] (Fig. 1.5). The study showed that they both had comparable activity in causing filamentous growth in *E. coli.*, implying that the ruthenium complexes can also have an effect on the replication activity in cells.

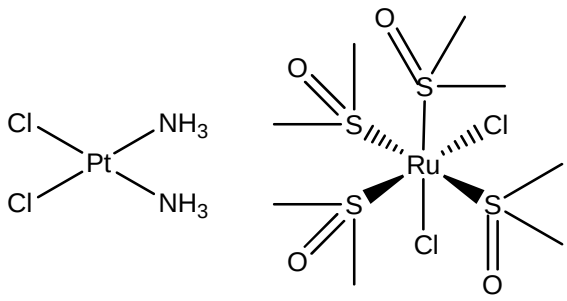

Figure 1.4. The chemical structure of cisplatin and *cis*-[$RuCl_2$(*S*-DMSO)$_4$]

These discoveries about the effects of ruthenium complexes on cellular processes have triggered much research into alternatives to cisplatin. Efforts have been made to "tune" the anti-cancer activity of ruthenium complexes and understand its mechanism of action[33]. This has lead to the development of Ru(III) anti-metastatic agents NAMI-A[34] and the anticancer agent KP1019[35] (Fig. 1.6).

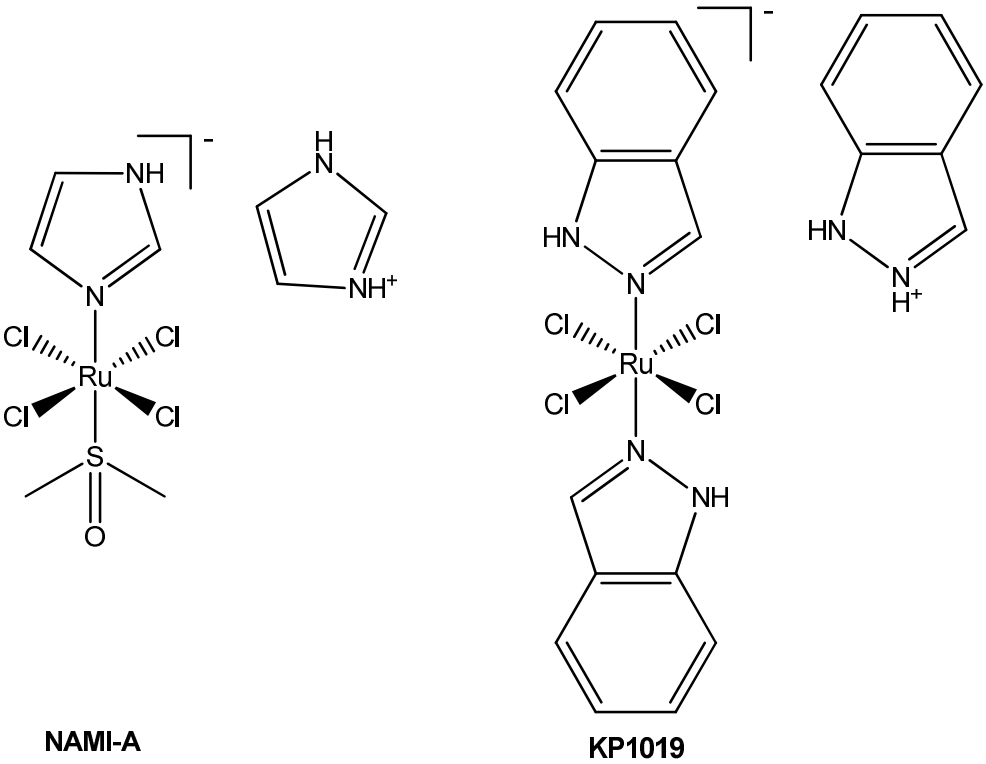

Figure 1.6. Chemical structure of NAMI-A and KP1019

NAMI-A has been shown to have antimetastatic properties, and while it does not inhibit the growth of primary cancer cells, it does however prevent the spread of cancer cells around the body to form secondary tumours. KP1019 on the other hand has shown cytotoxic activity in colorectal cancer cells[36] and both these complexes are currently undergoing clinical trials[37].

These complexes are believed to enter cells *via* binding to transferrin and serum albumin[38-40]. Cancer cells are fast growing and so require more iron and other biomolecules; this is why targeting of transferrin or using biomolecules (or derivatives close to biologically relevant molecules) as ligands, is an increasing approach for metal-based anticancer therapies.[18,41-43] Evidence has shown that *in vivo* Ru(III) complexes are reduced to Ru(II) by reducing agents which would be available in the cell,[44] such as glutathione. Given there are many reducing agents

in cells, the possibility of a mechanism *in vivo* involving reduction of Ru(III) to Ru(II) is highly probable. This field of study has recently taken an exciting new development with the relatively recent completion of Phase I clinical trials of KP1019[18,37,45,46]. These trials observed patients capable of taking a high dose of ruthenium complexes and a stabilising effect on the size of solid tumours, with complete remission in approximately a third of all observed tumours[37]. This has highlighted the potential for patient tolerance of ruthenium drugs and the feasibility of using such complexes in the clinic.

Looking at NAMI-A on the otherhand, a different mechanism of action appears to be at work. Some schools of thought have suggested that the mechanism for the antimetastatic activity of NAMI-A is more based on the interaction with extracellular components such as actin,[47] chorio allantoic membrane,[48] and intercornial matrigel sponge, which has been observed in rabbit studies.[49] It is this adhesion as opposed to invasive action upon the cell that in believed to explain why NAMI-A is a metastatic agent as opposed to an antitumour one[50]. This is itself is another area of interest for metallopharmaceutical agents but will not be discussed further in this thesis.

Given the fact that *in vivo* reduction of Ru(III) → Ru(II) occurs, it appears that in fact the Ru(II) species is the form of ruthenium with anticancer activity (in the case of KP1019), with this in mind and the previous observations of potential drugs from Ru(II) complexes[51-53], much work in the area of Ru(II) anticancer agents has been undertaken in recent years[14,15]. Of particular interest to this work are ruthenium(II) η^6-arene anticancer complexes.

1.4 Ruthenium(II) η^6-arene anticancer drugs

Ruthenium(II) aminophosphines[54] were synthesised and had shown some cytotoxicity, however it was noted that there were issues with solubility and stability of these complexes. To overcome these hurdles, η^6-arene ligands were introduced to these complexes as they can stabilise Ru(II) to prevent oxidation to Ru(III) species[55] and the formation of Ru(II) complexes with a positive charge allows for an increased solubility in water. This led to the synthesis of Ru(II) η^6-arene complexes with 3 other ligands attached in a "Piano-Stool" formation. (Figure 1.7).

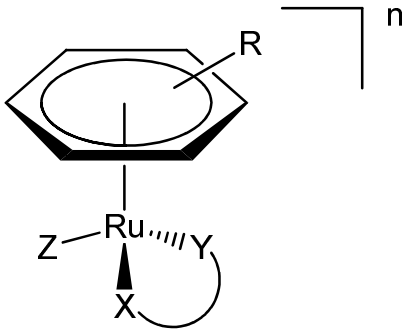

Figure 1.7. A typical structure of a $[Ru(II)(\eta^6\text{-arene})(XY)Z]^n$ complex, where XY = bidentate ligand, Z is a leaving group and n is the charge which can be 0, +1 or +2 in most cases.

The first complexes of this type to show cytotoxicity comparable to that of cisplatin[56] were $[Ru(\eta^6\text{-}p\text{-cym})(en)Cl]PF_6$ (**1**), $[Ru(\eta^6\text{-bip})(en)Cl]PF_6$ (**2**) and $[Ru(\eta^6\text{-tha})(en)Cl]PF_6$ (**3**) (Figure 1.8), where bip = biphenyl; p-cym = para-cymene; tha = tetrahydroanthracene and en = ethylenediamine. In experiments to investigate their IC_{50} values, (minimum concentration of complex required to inhibit cell growth of 50% of the cells compared to control), in a variety of human cancer cell lines, the complexes where found to all have IC_{50} values close to those

of cisplatin, the leading anticancer metallodrug in use in the clinic. The first reported IC_{50} values for this class of compounds are shown below and showed some interesting trends.

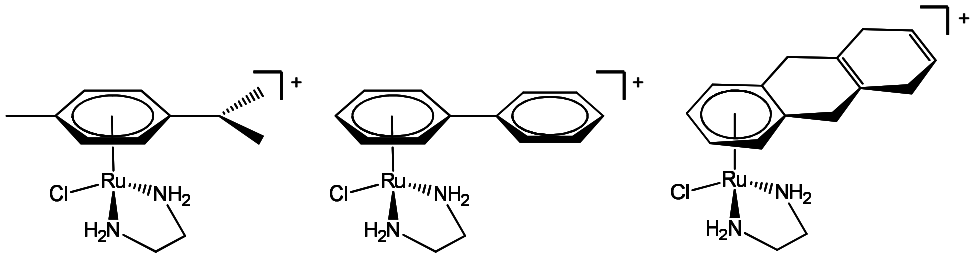

Complex	1	2	3
IC_{50} (μM)	10	5	0.5

Figure 1.8. The structures of **1**, **2** and **3** and their IC_{50} values (μM) in A2780, a human ovarian cancer cell line after 24 h exposure to the drug followed by 72 h for cell recovery in an assay where the IC_{50} value for cisplatin is 0.6 μM[57].

It is immediately obvious that as the size of the arene increases, so does the cytotoxicity (i.e.: IC_{50} values decrease) this is one of the first structure-activity relationships to be observed and it unveils the rich structural versatility of this class of complexes; the ability to systematically change all the ligands on the molecule to allow for complete "tuning" of the activity of each complex. While these complexes have IC_{50} values comparable to those of cisplatin[57], they only have one coordination site or labile ligand for coordination to biomolecules (compared to the 2 of cisplatin), this, along with activity of these complexes in cicplatin resistant cell lines implies that the ruthenium complexes must cause cell death by a different pathway to that induced by cisplatin.

Ruthenium(II) complexes have a number of different ways in which they can be tuned. The four main ways the complexes can be modified are; the arene

can be varied in size and electronic character, the XY bidentate ligand can be varied by changing the size and electronic properties of the ligand, the leaving group (Z) can also be changed to be more or less labile to substitution, and finally the overall charge of the species can also be varied.

Increasing the arene size results in increased cytotoxcity, as mentioned above, and will be discussed more in detail later on. Changes in the bidentate ligand have a large effect on the cytotoxicity; complexes which have three monodentate ligands showed no cytotoxicity compared to those with bidentate ligands[56,58]. Likewise changes in the leaving group, X, can also affect cytotoxcicity by having an effect on the rate and equilibrium constant of the aqua species formation[59]. Recently, efforts have been made to develop osmium analogues and these too can also be "tuned" by varying the building blocks around the metal centre. Similar to the ruthenium complexes, it has been observed that changes to the overall charge of the complex can also affect the activity of the osmium analogues of these complexes[60].

Over the past ten years, much work has been carried out investigating the mechanism of action of these complexes and further refining of the complex to increase the cytotoxicity has occurred. Studies have shown that many of these complexes are active against cisplatin-resistant cell lines[57,61] further supporting a different mechanism of action than that of cisplatin must be occurring.

As previously mentioned, the size of the arene has an effect on the cytotoxicity of these complexes; this is believed to be due to two major factors. Firstly, the arenes can provide a hydrophobic face to facilitate entry through the cell membrane. This has been seen in studies which have shown that when A2780 cancer cells are exposed to 2.7 μM of $[Ru(\eta^6\text{-bip})(en)Cl]PF_6$ and $[Ru(\eta^6\text{-}$

tha)(en)Cl]PF_6 for 24 h, the more hydrophobic tetrahydroanthracene ruthenium complex is found to be taken up over 7 times more readily than the biphenyl analogue into the cells, with 37 pmol/10^6 cells compared to 5 pmol/10^6 cells respetively[62]. Other work[63] which investigated both polar and non-polar substituents on the arene found that polar substituents had a negative effect on the cytotoxicity of the complexes, adding further weight to the argument that the hydrophobic nature of the arene is essential for the activity of these complexes. The original paper reporting the anticancer activity of the ruthenium(II) η^6-arene complexes[56] showed that the complexes can bind to DNA, similarly to cisplatin, *via* the guanine residues. While platinum has two coordination sites, the ruthenium only has one so will not cause the same kinking of DNA. This links to the other possible role the extended arene system plays in the mechanism of action, that is the importance of π-π stacking of the intercalating arene and the purine rings of the nucleobases[64] (Figure 1.9).

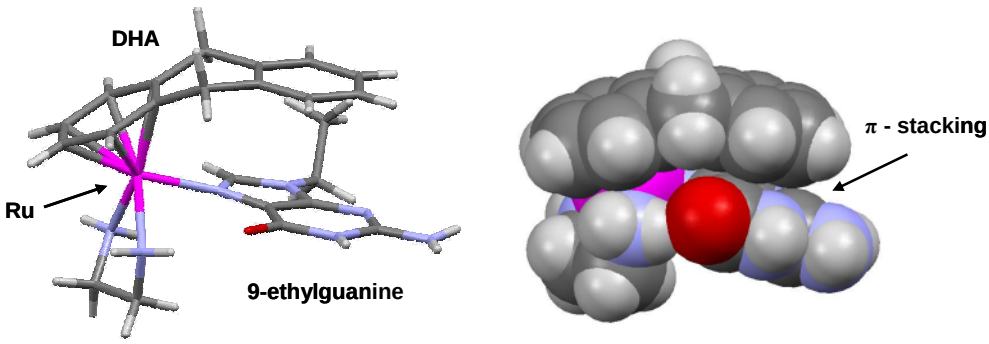

Figure 1.9. A crystal structure of [Ru(η^6-DHA)(en)(9-EtG-*N7*)]$^{2+}$. The space filling model shows the arene-guanine base π-π stacking. (DHA = dihydroanthracene)[64]

Interaction studies of this class of complexes with Calf Thymus DNA have shown that complexes with larger arenes are harder to remove by excision repair processes[65] and in further studies those complexes with extended arene systems cause increased unwinding of plasmid DNA[66]. The same studies show that in ethidium bromide competition experiments (EtBr is a known DNA intercalator, it is 20 times more fluorescent when bound to DNA and when displaced by other intercalators, the fluorescence is quenched[67]) the fluorescence is quenched in the presence of complexes with extended arenes, such as biphenyl, dihydroanthracene and tetrahydroanthracene, but with complexes containing para-cymene and benzene as the η^6-arene, no change in fluorescence is observed.

In Figure 1.9, above, and in other crystal structures of similar 9-Ethylguanine (9-EtG) adducts of $[Ru(\eta^6\text{-arene})en]^{2+}$ complexes, the close proximity of protons on the ethylenediamine nitrogens and the exocyclic oxygen atoms on C6 of the guanine is notable (Figure 1.10). The distance between these nitrogen and oxygen is ca. 2.8 Å and so appears to provide evidence for hydrogen bonding. Further studies[68] found this hydrogen bonding was part of the binding and recognition mechanism. When the ethylenediamine group is replaced by an acetylacetone group ($acac^-$, $CH_3C(O^-)CHC(O)CH_3$) ligand), hydrogen bonding is no longer able to occur and complexes then preferentially bind to adenine bases on DNA strands[59,68].

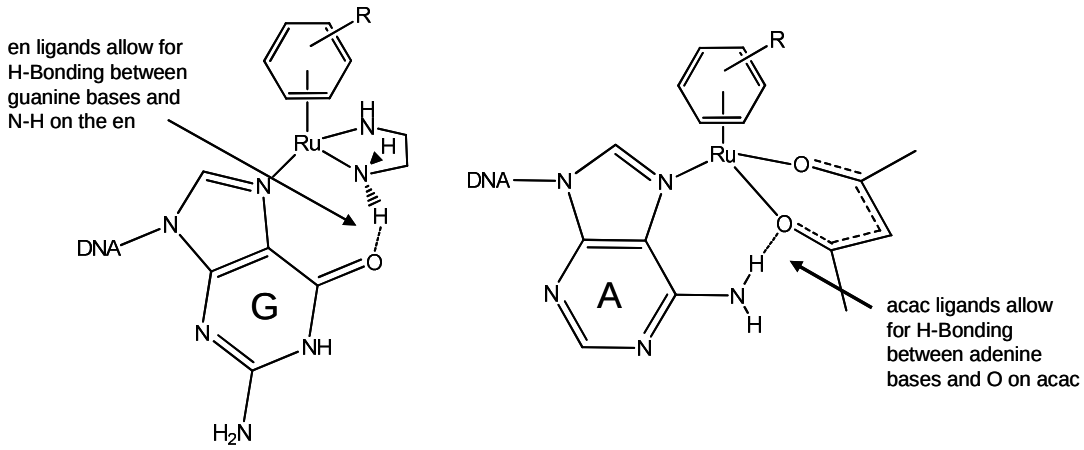

Guanine Residue Adenine Residue

Figure 1.10. The bidentate ligand on the ruthenium can ensure the selectivity of nucleobase binding on DNA, depending on whether the ligand is an H-bond donor (en) or an acceptor (acac) it will bind to a nucleobase which can form the other side of the H-bond. Charges are excluded for clarity.

The importance of this hydrogen bonding cannot be under-estimated, when protons are removed from the nitrogens on ethylenediamine, as with tetramethylethylenediamine (Me_4-en), the cytotoxicity drops dramatically[63]. In some studies where the ruthenium complexes are bearing ligands which can be reduced to products which contain NH_2 containing ligands[69], this could provide a mechanism of action which is "switched on" in the cell by reducing agents (Figure 1.11). Computational studies have suggested the activity of the complex with a reduced ligand is linked to the ability of the new complex to H-bond to the oxygen on guanine residues along with the expected N7-Ru bond. This shows potentials for prodrugs, *i.e.* non toxic complexes delivered to the body which can be activated *in vivo* by intracellular reductants.

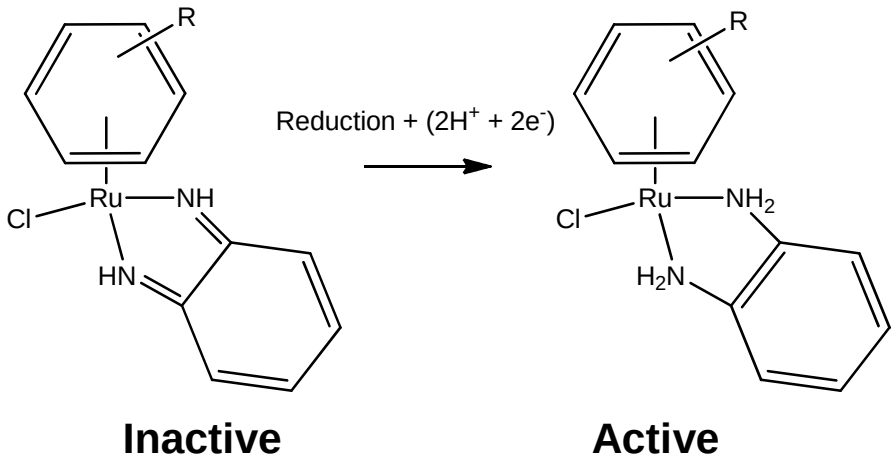

Figure 1.11. Complexes studied which showed activity increasing upon ligand based reduction reduction[69].

Some complexes with one substituent on a nitrogen of the ethylenediamine ligand have shown excellent cytotoxicity, one such complex is the diruthenium complex in which two of the initial complexes (in this example **2**) are connected by a long aliphatic chain[70] to produce complex **4**. Studies of supercoiled plasmid DNA with **4** have shown significant unwinding of the plasmid compared to mononuclear complexes.

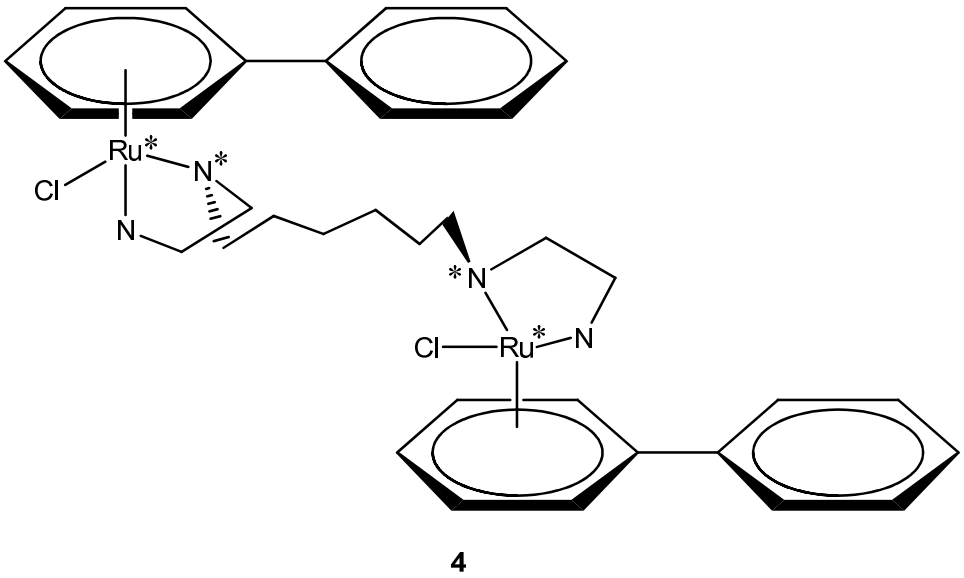

4

Figure 1.12. The chemical structure of the dinuclear complex **4**[70]. There are four chiral centres (*) and so 16 possible isomers.

In order to further understand the mechanism of action of this dinuclear complex, smaller model, **5**, was synthesised. Due to the two chiral centres 4 different isomers exist in solution as **5A** and **5B** (and their respective diastereoisomers) (Figure 1.13) with **5A** being the more preferred isomer. When these isomers are separated they will return to an equilibrium racemic mix over time. Of key interest is the observation that these molecules have been shown to undergo stereochemical inversion in order to selectively bind with guanine residues (Figure 1.13). More detail on this will be discussed in the next chapter as the mechanism of inversion is one of the main points of interest to this thesis.

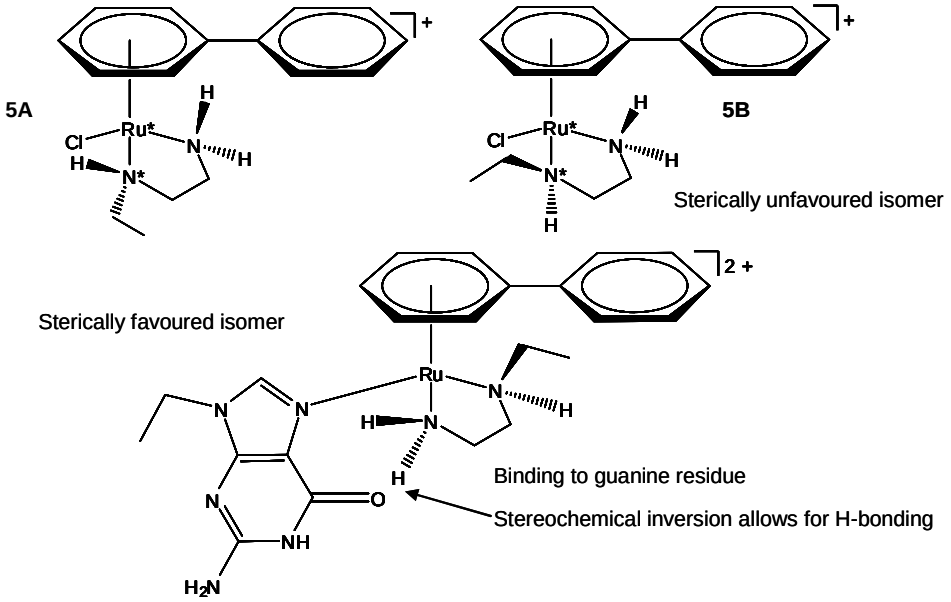

Figure 1.13. Ru(II) complexes with chiral amines (**5A** and **5B**) can invert their stereochemistry to allow for optimum H-bonding with guanine residues. (In this example, taken from work by Chen et al.[70] the guanine residue is 9-ethylguanine). The * symbolises chiral centres.

This inversion of stereochemistry to allow for a sterically hindered product to form, provides evidence for the importance of the hydrogen bonding between the hydrogens on the ethylenediamine ligands and the exocyclic oxygen on the guanine residues.

The final part of the complex that is tuneable is the Z ligand. This usually needs to be a leaving group for the complex to show cytotoxicity. Hydrolysis of the leaving group prior to DNA binding has been observed to play a pivitol role in the cytotoxic behaviour of this class of complexes. Studies have shown that a relationship between hydrolysis rates (and the extent of hydrolysis) and cytotoxicity exists[71]. Complexes which do not readily hydrolyse have shown low cytotoxicity. In fact this behaviour is employed in the development of

photoactivated complexes[72] in which non-hydrolysing complexes can be activated by light breaking the Ru-Z bond to allow for hydrolysis to occur, or in tethered complexes which are pH activated by breaking a single bond between the tether and the ruthenium to allow binding of the complex to DNA[73]. While there are some Ru(II) η^6-arene complexes that are active despite the lack of hydrolysis, however these complexes are believed to have a completely different mechanism of action, involving the potential generation of reactive oxygen species (ROS) in cells[74]. Hydrolysis has been found to occur in an associative manner[75]. Understanding the rate and extent of hydrolysis and the pK_a of the aqua adduct is important, since the chloride complex is itself inactive but undergoes hydrolysis to form the active species upon entry into the cell (where the chloride concentration is too low to suppress hydrolysis). If the pK_a of the aqua complex (Ru-OH_2) is too low, inactive hydroxyl complexes (Ru-OH) can be formed as is the case with some Osmium complexes where the formation of Os-OH-Os bridged dimers have been observed[76].

1.5 Interaction of Ruthenium anticancer drugs with DNA and other biomolecules

Now that there is an understanding of the three key features that are required to make Ru(II) complexes of this class with good cytotoxicity, they can be summarised as follows

1. Extended arenes lead to better cell up take due to their hydrophobicity and the extended arene can intercalate into duplex DNA

2. Bidentate chelating ligands (XY), provide stability to the complex and increase the cytotoxic behaviour. The ligand also plays a role in selective binding to adenine or guanine base pairs on DNA.
3. A good leaving group (Z) is essential for the complex to undergo hydrolysis, and a pK_a value above 7 of the resulting aqua complex is also essential to prevent deprotonation at physiological pH values which would result in deactivation by forming hydroxido complexes.

As with cisplatin, the main target for Ru(II) η^6-arene complexes is believed to be DNA, particularly guanine residues.[77] Other studies have shown that binding can also occur with enzymes[78] via ruthenation of the imidazole ring of histidine residues. Binding via the sulfur of cysteine and methionine amino acids has also been observed.[79] With this in mind, and the knowledge that cisplatin can be deactivated by binding to glutathione, competition studies were carried out between glutathione (GSH) and guanine in biologically relevant conditions[80]. Interestingly it was found that even in large excesses of glutathione binding to guanine was still favoured. Further work[81] showed that the glutathione did initially bind to the $[Ru(\eta^6\text{-arene})(en)]^{2+}$ moiety via an Ru-S bond, to form a Ru-S-G structure. This ligand is then oxidised in solution resulting in a much more labile GS(O)H adduct which is then substituted by guanine residues. This interesting result shows the potential for this class of compound to be successful against cisplatin resistant as they will not be inhibited by sulfur binding, removing one possibly pathway of deactivation.

DNA binding studies have shown that some distortions to the shape of the DNA strands upon binding of Ru(II) complexes occurs, both computationally[82] and experimentally[83,84]. There appears to be at least two modes of binding to the DNA strands, the extended arene can either intercalate or occupy a non-intercalating position in which a neighbouring thymine base can be twisted out of the duplex, distorting the shape of the DNA strand (Figure. 1.14).

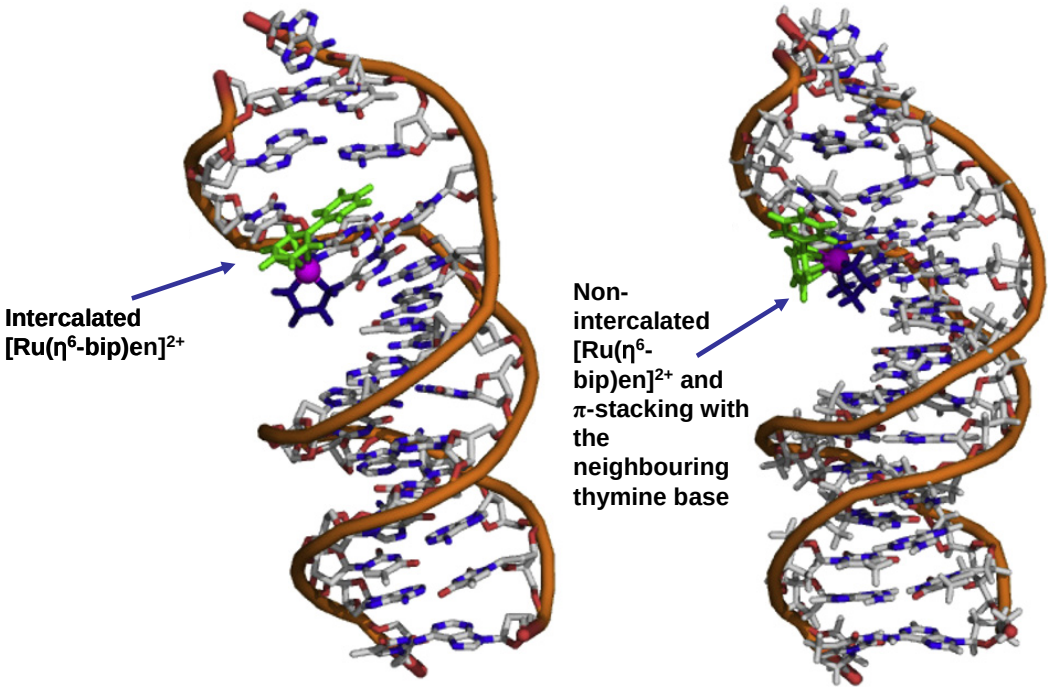

Figure 1.14. Images produced from both computational and experimental NMR data showing the two ways in which $[Ru(\eta^6\text{-bip})(en)]^{2+}$ can bind to 14-mer DNA strands. Image adapted from Liu *et al*. based on experimental data[83].

The only similarities between the mechanism of action of this class of complex and cisplatin appears to be the activation pathway (hydrolysis) and binding to guanine. These ruthenium complexes only bind mono-functionally to DNA strands and so do not cause the same amount of binding and kinking of the strand. Evidence has also shown that the intercalation of the extended arene

system plays a role in the unwinding of the DNA duplex and that the complexes are not inhibited by the presence of sulfur containing biomolecules in the cell. While these differences have all been observed the exact process of apoptosis which is induced within the cell has yet to be determined.

1.6 Other potential uses of ruthenium in biology

Apart from the uses of ruthenium complexes anticancer and antimetastatic agents, other uses for ruthenium complexes in biology have been observed. One such use is as a nitric oxide scavenger. Work by Fricker *et al*[85] has shown that the ruthenium(III) complex JM1226 (Figure 1.15) can be used to control the levels of nitric oxide in the blood which can bind to the iron in haemoglobin. Nitric oxide binding to iron in haemoglobin is believed to contribute to health problems such as septic shock, diabetes, arthritis, inflammation and epilepsy.[86,87]

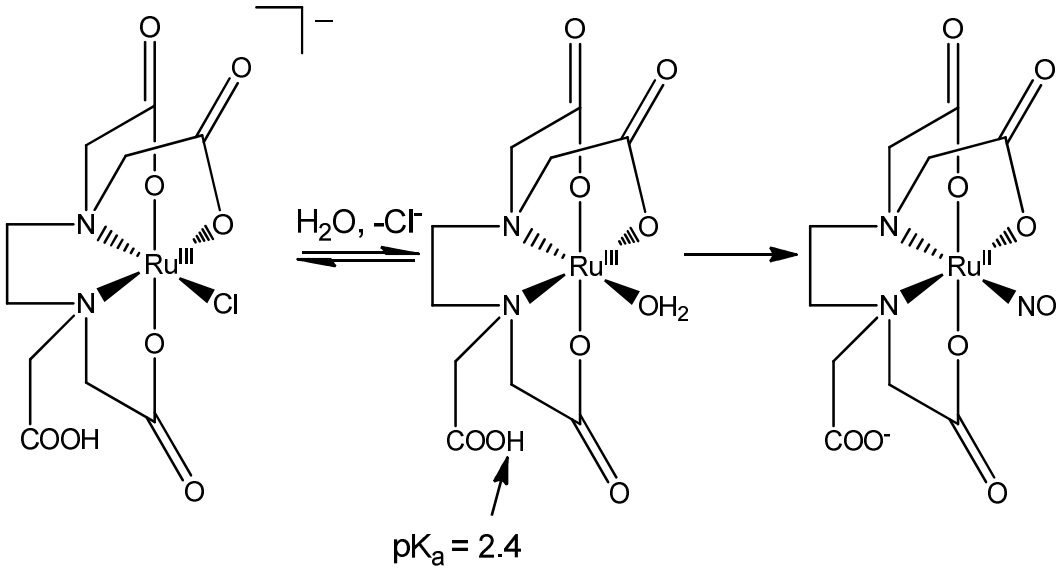

Figure 1.15. The process through which JM1226 undergoes hydrolysis and then reduction of Ru(III) to Ru(II) by binding to nitric oxide.

JM1226 binding to the nitric oxide is fast ($k > 10^8\ M^{-1}\ s^{-1}$) and strong ($K_{binding} > 10^8\ M^{-1}$) and forms a linear nitrosonium Ru^{II}-NO adduct. JM1226 has also shown excellent activity in cell studies.[86] Other studies,[88] have confirmed that scavenging of NO is indeed the mechanism of action as opposed to interference with the NO production pathways. The NO scavenging ability of the cytotoxic complex NAMI-A[49] may play some role in the mechanism of anti-metastatic action of this class of Ru(III) complexes.

Another compound, Ruthenium Red (Figure 1.16) has been used for over a century as a cytological staining agent for tumour due to its affinity to mucopolysaccarides.[40] Tests on Ruthenium Red and the commonly found impurity Ru360 (Figure 1.16) have shown binding to a number of calcium (Ca^{2+}) binding proteins and has inhibited mitochondrial uptake of calcium ions. Independently, Ru360 has been used as a probe to isolate and investigate Ca^{2+} uniporters in cell mitochondria.[89] The mechanism of action is believed to be high affinity binding of the Ru complexes to the highly anionic phospholipid membrane region near the calcium channels in the mitochondria.

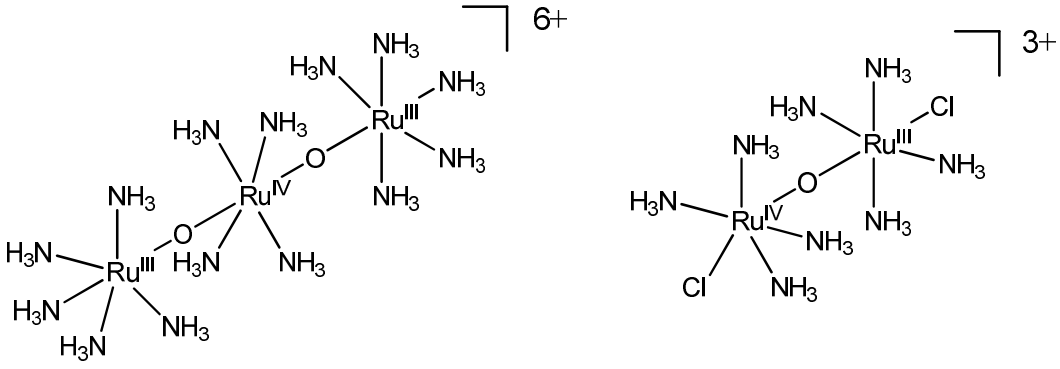

Ruthenium Red Ru360

Figure 1.16. The chemical structure of ruthenium red and its major impurity Ru360.

Further to the potential use of Ru-Red and Ru-360 in blocking Ca^{2+} channels in mitochondria, their potential use as immunosuppressant was also investigated.[90] The activity was found to be similar to that a drug already in the clinic, cyclosporin A. Cyclosporin A functions by interfering with the calcium dependent steps in immune response[40]. The similar activity provides insight into the potential for ruthenium complexes to interfere calcium dependent steps in immune response processes.

Further studies[91-93] have shown that by using Ru^{2+}/Ru^{3+} complexes with nitrogen based ligands that are substitution inert (NH_3, pyridine or imidazole derivatives) could inhibit antigen-stimulated T lymphocyte proliferation, but with a lot less side effects.[40] The mechanism of these complexes appears to be different from organic molecules in the clinic. This may be due to an electron-transfer process as the potential required for such a reaction is easily accessible within the redox window of cell.[94]

1.7 Closing comments on the biological application of ruthenium complexes

Ruthenium (II) η^6-arene complexes have been shown to possess cytotoxic activity in a range of cancer cell lines comparable to those seen in cisplatin, which is in widespread clinical use. Activity in cisplatin resistant cell lines has also been observed, indicating that a different mechanism of action is responsible for cell death for ruthenium complexes. By altering the ligands around the central ruthenium metal the activity of the complex can be tuned and activity increased.

One potential target for these complexes is DNA and much work has shown the ability of this class of compounds to bind to DNA bases. Other

studies[95] have shown that ruthenium complexes can catalytically induce reduction of NAD^+ (nicotineamide adenine dinucleotide) to NADH which can affect various steps in the metabolic pathway.

The activity of ruthenium(III) complexes has not only shown anticancer activity in reducing the size of tumour grafts on mice,[96] but also antimethesatic activity in preventing the spread of the cancer around the body.[34] Excitingly, some Ru(III) complexes now in clinical trials.[45,46] Part of the activity of NAMI-A and KP1019 has been attributed to the reduction of the Ru(III) to Ru(II) in the cell. The ability of ruthenium(III) complexes to undergo reduction at potentials easily accessible in the cell has been observed several times and may be a possible pathway for cytotoxic activity. The nitric oxide scavenging and immunosuppressant activity possessed by many of the complexes discussed above may also be as a result of reduction of Ru(III) to Ru(II). This provides another tool in the potential different mechanisms available to ruthenium to enhance its use in biological systems.

1.8 Overview of the contents of this thesis

The presence of the N-H protons on the ethylenediamine ligand has been shown to be essential for the anticancer activity of ruthenium-arene anticancer complexes.[68] Their role is to stabilise, by H-bonding, the binding of nucleobases to ruthenium as is shown in Figure 1.10. Similar observations have been made with cisplatin derivatives, in these studies removal of am(m)ino protons reduces their cytotoxic activity.[97] The importance of H-bonding between the exocyclic oxygen on guanine bases and the amino protons of the ethylenediamine is highlighted in Figure 1.13. Complexes **5A** and **5B** have been shown to

interconvert in order to bind to guanine bases.[70] The mechanism for this interconversion is unknown and to date there have been no investigations into mechanisms for interconversion of chiral amine ligands on metal centres. Chapter 3 of this thesis investigates the amino proton exchange rates of **1** ([Ru(η^6-bip)(Et-en)Cl]$^+$) in aqueous solutions. The data are then used to infer the possible mechanism for the interconversion of the stereocentres. The author believes this is the first such in-depth study into a widely observed phenomenon in six co-ordinate metal complexes. Further analysis in Chapter 4 investigates the effects of electron donation to the metal from other ligands on the exchange rates of the amino protons. Together both studies show evidence for a complicated interconversion mechanism. It is believed that the determination of this mechanism will allow for further understanding of ligand choice in the design of ruthenium(II) anticancer complexes. Further to this, suggestions are made as to how to control this interconversion and highlight the difficulties involved in attempting to separate stereoisomers of this type are discussed. The discovery of the influence of other ligands on the mechanism will provide a greater understanding of the exchange pathway and will have implications not only in drug discovery but also in the development of asymmetric-catalysts.

Chapter 5 investigates the shape changes that can occur for short strands of oligonucleotides (DNA). Previous work has shown that ruthenium(II) arene complexes can cause unwinding of supercoiled plasmid DNA.[98,99] Unlike cisplatin, there is currently no crystal structure of ruthenium bound DNA.[100] As a result any kinking, stretching or bending of the DNA by ruthenation has not been characterised by x-ray crystallography and so other methods must be employed. The author investigated the use of Ion-mobility Mass spectrometry (IM-MS) and

Förster Resonance Energy Transfer spectroscopy (FRET) for determining shape changes to DNA strands as a result of ruthenation. Understanding DNA shape changes will provide a greater insight into the mechanism of action for this class of compounds. Such knowledge might allow new complexes to be developed which will selectively change the shape of DNA to give rise to the most cytotoxic lesion on DNA, and hence the greatest anticancer activity.

1.9 Aims

The aims of the work described in this thesis are listed below.

1) To investigate the mechanism of stereochemical inversion between (R^*,S^*) and (S^*,S^*) isomers of [Ru(η^6-bip)(Et-en)Cl]$^+$ (*c.f.*: Fig. 1.13). The question as to whether inversions occur on the chiral nitrogen or the chiral ruthenium or both in the complex in aqueous solutions is studied by observing the exchange rate of amino protons in [Ru(η^6-bip)(en)Cl]$^+$ at various pH values, temperatures and ionic strengths using nuclear magnetic resonance spectroscopy (NMR). Knowledge of this mechanism of exchange is important since the use of racemic mixtures is usually avoided in pharmaceuticals. The ability to control this exchange may allow the formation of a racemic mixture to be avoided.

2) To investigate the effects of nitrogen based π-acceptor ligands (pyridine derivatives) in the Z position of [Ru(η^6-bip)(en)Z]$^{n+}$ on the rate and mechanism of exchange using NMR and computational methods. A comparison of the exchange rates using a Hammett plot provided an understanding of the electronic effects of the monodentate ligand on the exchange rates. A combination of the data in Chapters 3 and 4 will provide a greater understanding of the effects of ligands on the ability of a complex to undergo inversion. The data will also assist the design of improved anticancer complexes and reduce the complications arising from stereoisomers interconverting in aqueous solutions.

3) To use Ion-Mobility Mass Spectrometry (IM-MS) to investigate changes in the 3D conformation of the short DNA strand, d(CACGTG), as a result of interaction with $\{Ru(\eta^6\text{-bip})(en)\}^{2+}$. This should provide an understanding of the conformational changes to DNA molecules induced by binding to ruthenium-arene complexes. This appears to be the first IM-MS study of ruthenated DNA.

4) To use IM-MS to determine the collision cross sections of ruthenium-arene complexes. This appears to be the first usage of IM-MS to determine the collision cross section of a small molecule (< 100 $Å^2$). To facilitate this a new calibration process was developed. Previously this technique had only been suitable to larger molecules.

5) To investigate the potential of Förster Resonance Energy Transfer (FRET) to determine shape changes to 30mer oligonucleotides induced by binding to metal-based anticancer drugs. It was hoped that these results would allow analysis bending, kinking or any other shape changes on longer strands of DNA. Initial studies were carried using cisplatin with the intention of developing the technique for use with ruthenium-arene anticancer complexes.

1.10 References

(1) Clarke, M. J.; Zhu, F.; Frasca, D. R. *Chem. Rev.* **1999**, *99*, 2511.

(2) Tucker, A. in *The Toxic Metals*, Earth Island Ltd. London, 1972.

(3) Tsubaki, T.; Irukayama, K.; Editors in *Minamata Disease: Methylmercury Poisoning in Minamata and Niigata, Japan*, Elsevier, Tokyo, 1977.

(4) Eto, K.; Tokunaga, H.; Nagashima, K.; Takeuchi, T. *Toxicol. Pathol.* **2002**, *30*, 714.

(5) Jones, D. E.; Ledingham, K. W. *Nature* **1982**, *299*, 626.

(6) Ehrlich, P.; Bertheim, A.; US patent no: 909380, 1909.

(7) Lloyd Nicholas, C.; Morgan Hugh, W.; Nicholson Brian, K.; Ronimus Ron, S. *Angew. Chem. Int. Ed.* **2005**, *44*, 941.

(8) Sadler, P. J.; Muncie, C.; Shipman, M. A. in *Biological and Inorganic Chemistry*; Bertini, I.; Gray, H. B.; Steifel, E. I and Valentine, J. S., Ed; Univeristy Science Books, California, 2009.

(9) Emsley, J. in *Nature's Building Blocks*; Oxford University Press: Oxford, 2003.

(10) Jaouen, G.; Top, S; Vessieres, A, in *Bioorganometallics: Biomolecules, Labeling, Medicine*; Jaouen G,, Ed.; Wiley-VCH: Germany. 2006

(11) Perez, L. R.; Franz, K. J. *Dalton Trans.* **2010**, *39*, 2177.

(12) Ghosh, S.; Mukherjee, A.; Sadler, P. J.; Verma, S. *Angew. Chem., Int. Ed.* **2008**, *47*, 2217.

(13) Kostova, I. in *Metal-Containing Drugs And Novel Coordination Complexes In Therapeutic Anticancer Applications - Part I. [In: Anti-Cancer Agents Med. Chem., 2010; 10(4)]*, 2010; p 81 pp.

(14) Sakurai, H. *Journal of Health Science* **2010**, *56*, 129.

(15) Suess-Fink, G. *Dalton Trans.* **2010**, *39*, 1673.

(16) van Rijt, S. H.; Sadler, P. J. *Drug Discovery Today* **2009**, *14*, 1089.

(17) Pizarro, A. M.; Sadler, P. J. *Biochimie* **2009**, *91*, 1198.

(18) Bruijnincx, P. C. A.; Sadler, P. J. *Curr. Opin. Chem. Biol.* **2008**, *12*, 197.

(19) Rosenberg, B.; VanCamp, L.; Trosko, J. E.; Mansour, V. H. *Nature* **1969**, *222*, 385.

(20) Santos, I.; Paulo, A.; Correia, J. D. G. *Top. Curr. Chem.* **2005**, *252*, 45.

(21) Vitha, T.; Kubicek, V.; Hermann, P.; Elst Luce, V.; Muller Robert, N.; Kolar Zvonimir, I.; Wolterbeek Hubert, T.; Breeman Wouter, A. P.; Lukes, I.; Peters Joop, A. *J. Med. Chem.* **2008**, *51*, 677.

(22) Thakral, C.; Alhariri, J.; Abraham, J. L. *Contrast Media & Molecular Imaging* **2007**, *2*, 199.

(23) Uppal, R.; Caravan, P. *Future Medicinal Chemistry* **2010**, *2*, 451.

(24) Rosenberg, B.; Van Camp, L.; Krigas, T. *Nature* **1965**, *205*, 698.

(25) Lippert, B.; in *Cisplatin: Chemistry and Biochemistry of a Leading Anticancer Drug*; Wiley-VCH: Zurich, 1999

(26) Lippard, S. J. *Science* **1982**, *218*, 1075.

(27) Sadler, P. J. *ChemBioChem* **2009**, *10*, 73.

(28) Jung, Y.; Lippard Stephen, J. *Chem. Rev.* **2007**, *107*, 1387.

(29) Zhang, C. X.; Lippard, S. J. *Curr. Opin. Chem. Biol.* **2003**, *7*, 481.

(30) Chau, Q.; Stewart, D. J. *Cancer Chemother. Pharmacol.* **1999**, *44*, 193.

(31) Dunham, S. U.; Lippard, S. J. *Biochemistry* **1997**, *36*, 11428.

(32) Monti-Bragadin, C.; Ramani, L.; Samer, L.; Mestroni, G.; Zassinovich, G. *Antimicrob. Agents Chemother.* **1975**, *7*, 825.

(33) Levina, A.; Mitra, A.; Lay, P. A. *Metallomics* **2009**, *1*, 458.

(34) Sava, G.; Capozzi, I.; Clerici, K.; Gagliardi, G.; Alessio, E.; Mestroni, G. *Clin. Exp. Metastasis* **1998**, *16*, 371.

(35) Galanski, M.; Arion, V. B.; Jakupec, M. A.; Keppler, B. K. *Curr. Pharm. Des.* **2003**, *9*, 2078.

(36) Kapitza, S.; Jakupec, M. A.; Uhl, M.; Keppler, B. K.; Marian, B. *Cancer Letters* **2005**, *226*, 115.

(37) Hartinger, C. G.; Jakupec, M. A.; Zorbas-Seifried, S.; Groessl, M.; Egger, A.; Berger, W.; Zorbas, H.; Dyson, P. J.; Keppler, B. K. *Chemistry & Biodiversity* **2008**, *5*, 2140.

(38) Liu, M.; Lim, Z. J.; Gwee, Y. Y.; Levina, A.; Lay, P. A. *Angew. Chem., Int.l Ed.***2010**, *49*, 1661.

(39) Piccioli, F.; Sabatini, S.; Messori, L.; Orioli, P.; Hartinger, C. G.; Keppler, B. K. *J. Inorg. Biochem.* **2004**, *98*, 1135.

(40) Clarke, M. J. *Coord. Chem. Rev.* **2003**, *236*, 209.

(41) Gray, J. C.; Habtemariam, A.; Winnig, M.; Meyerhof, W.; Sadler, P. J. *JBIC, J. Biol. Inorg. Chem.* **2008**, *13*, 1111.

(42) Ang, W. H.; Dyson, P. J. *Eur. J. Inorg. Chem.* **2006**, 4003.

(43) Hanif, M.; Nazarov, A. A.; Hartinger, C. G.; Kandioller, W.; Jakupec, M. A.; Arion, V. B.; Dyson, P. J.; Keppler, B. K. *Dalton Trans.* **2010**, *39*, 7345.

(44) Sava, G.; Bergamo, A.; Zorzet, S.; Gava, B.; Casarsa, C.; Cocchietto, M.; Furlani, A.; Scarcia, V.; Serli, B.; Iengo, E.; Alessio, E.; Mestroni, G. *Eur. J. Cancer* **2002**, *38*, 427.

(45) Hartinger, C. G.; Zorbas-Seifried, S.; Jakupec, M. A.; Kynast, B.; Zorbas, H.; Keppler, B. K. *J. Inorg. Biochem.* **2006**, *100*, 891.

(46) Rademaker-Lakhai, J. M.; Van Den Bongard, D.; Pluim, D.; Beijnen, J. H.; Schellens, J. H. M. *Clin. Cancer Res.* **2004**, *10*, 3717.

(47) Sava, G.; Frausin, F.; Cocchietto, M.; Vita, F.; Podda, E.; Spessotto, P.; Furlani, A.; Scarcia, V.; Zabucchi, G. *Eur. J. Cancer* **2004**, *40*, 1383.

(48) Vacca, A.; Bruno, M.; Boccarelli, A.; Coluccia, M.; Ribatti, D.; Bergamo, A.; Garbisa, S.; Sartor, L.; Sava, G. *Br. J. Cancer* **2002**, *86*, 993.

(49) Morbidelli, L.; Donnini, S.; Filippi, S.; Messori, L.; Piccioli, F.; Orioli, P.; Sava, G.; Ziche, M. *Br. J. Cancer* **2003**, *88*, 1484.

(50) Bergamo, A.; Sava, G. *Dalton Trans.* **2007**, 1267.

(51) Sava, G.; Zorzet, S.; Giraldi, T.; Mestroni, G.; Zassinovich, G. *Eur. J. Cancer Clin. Oncol.* **1984**, *20*, 841.

(52) Sava, G.; Pacor, S.; Zorzet, S.; Alessio, E.; Mestroni, G. *Pharmacol. Res.* **1989**, *21*, 617.

(53) Mestroni, G.; Alessio, E.; Calligaris, M.; Attia, W. M.; Quadrifoglio, F.; Cauci, S.; Sava, G.; Zorzet, S.; Pacor, S.; et al. *Progress in Clinical Biochemistry and Medicine* **1989**, *10*, 71.

(54) Guo, Z.; Habtemariam, A.; Sadler, P. J.; James, B. R. *Inorg. Chim. Acta* **1998**, *273*, 1.

(55) Bennett, M. A.; Byrnes, M. J.; Kovacik, I. *J. Organomet. Chem.* **2004**, *689*, 4463.

(56) Morris, R. E.; Aird, R. E.; Murdoch, P. d. S.; Chen, H.; Cummings, J.; Hughes, N. D.; Parsons, S.; Parkin, A.; Boyd, G.; Jodrell, D. I.; Sadler, P. J. *J. Med. Chem.* **2001**, *44*, 3616.

(57) Aird, R. E.; Cummings, J.; Ritchie, A. A.; Muir, M.; Morris, R. E.; Chen, H.; Sadler, P. J.; Jodrell, D. I. *Br. J. Cancer* **2002**, *86*, 1652.

(58) Vock, C. A.; Scolaro, C.; Phillips, A. D.; Scopelliti, R.; Sava, G.; Dyson, P. J. *J. Med. Chem.* **2006**, *49*, 5552.

(59) Fernandez, R.; Melchart, M.; Habtemariam, A.; Parsons, S.; Sadler, P. J. *Chem.--Eur. J.* **2004**, *10*, 5173.

(60) van Rijt, S. H.; Peacock, A. F. A.; Johnstone, R. D. L.; Parsons, S.; Sadler, P. J. *Inorg. Chem.* **2009**, *48*, 1753.

(61) Guichard, S. M.; Else, R.; Reid, E.; Zeitlin, B.; Aird, R.; Muir, M.; Dodds, M.; Fiebig, H.; Sadler, P. J.; Jodrell, D. I. *Biochem. Pharmacol.* **2006**, *71*, 408.

(62) Wang, F.; Guichard, R.; Aird, R. E.; Zeitlin, B.; L., E.; Habtemariam, A.; Haimei, C.; Jodrell, D. I.; Sadler Peter, J.; *unpublished data.*

(63) Habtemariam, A.; Melchart, M.; Fernandez, R.; Parsons, S.; Oswald, I. D. H.; Parkin, A.; Fabbiani, F. P. A.; Davidson, J. E.; Dawson, A.; Aird, R. E.; Jodrell, D. I.; Sadler, P. J. *J. Med. Chem.* **2006**, *49*, 6858.

(64) Chen, H.; Parkinson, J. A.; Parsons, S.; Coxall, R. A.; Gould, R. O.; Sadler, P. J. *J. Am. Chem. Soc.* **2002**, *124*, 3064.

(65) Novakova, O.; Kasparkova, J.; Bursova, V.; Hofr, C.; Vojtiskova, M.; Chen, H.; Sadler, P. J.; Brabec, V. *Chem. Biol.* **2005**, *12*, 121.

(66) Novakova, O.; Chen, H.; Vrana, O.; Rodger, A.; Sadler, P. J.; Brabec, V. *Biochemistry* **2003**, *42*, 11544.

(67) Jenkins, T. C. *Methods Mol. Biol.* **1997**, *90*, 195.

(68) Chen, H.; Parkinson, J. A.; Morris, R. E.; Sadler, P. J. *J. Am. Chem. Soc.* **2003**, *125*, 173.

(69) Bugarcic, T.; Habtemariam, A.; Deeth, R. J.; Fabbiani, F. P. A.; Parsons, S.; Sadler, P. J. *Inorg. Chem.* **2009**, *48*, 9444.

(70) Chen, H.; Parkinson, J. A.; Novakova, O.; Bella, J.; Wang, F.; Dawson, A.; Gould, R.; Parsons, S.; Brabec, V.; Sadler, P. J. *Proc. Natl. Acad. Sci. U. S. A.* **2003**, *100*, 14623.

(71) Wang, F.; Habtemariam, A.; van der Geer, E. P. L.; Fernandez, R.; Melchart, M.; Deeth, R. J.; Aird, R.; Guichard, S.; Fabbiani, F. P. A.; Lozano-Casal, P.; Oswald, I. D. H.; Jodrell, D. I.; Parsons, S.; Sadler, P. J. *Proc. Natl. Acad. Sci. U. S. A.* **2005**, *102*, 18269.

(72) Betanzos-Lara, S.; Salassa, L.; Habtemariam, A.; Sadler, P. J. *Chemical Communications (Cambridge, United Kingdom)* **2009**, 6622.

(73) Pizarro, A. M.; Melchart, M.; Habtemariam, A.; Salassa, L.; Fabbiani, F. P. A.; Parsons, S.; Sadler, P. J. *Inorg. Chem.* **2010**, *49*, 3310.

(74) Dougan S. J.; Habtemariam, A.; McHale S. E.; Parsons, S.; Sadler P. J. *Proc. Natl. Acad. Sci. U. S. A.* **2008**, *105*, 11628.

(75) F. Wang, H. C., S. Parsons, I. D. H. Oswald, J. E. Davidson and P. J. Sadler *Chem. Eur. J.* **2003**, *9*, 5810

(76) Peacock, A. F. A.; Habtemariam, A.; Fernandez, R.; Walland, V.; Fabbiani, F. P. A.; Parsons, S.; Aird, R. E.; Jodrell, D. I.; Sadler, P. J. *J. Am. Chem. Soc.* **2006**, *128*, 1739.

(77) Gkionis, K.; Platts, J. A.; Hill, J. G. *Inorg. Chem.* **2008**, *47*, 3893.

(78) McNae, I. W.; Fishburne, K.; Habtemariam, A.; Hunter, T. M.; Melchart, M.; Wang, F.; Walkinshaw, M. D.; Sadler, P. J. *Chem. Commun.* **2004**, 1786.

(79) Wang, F.; Chen, H.; Parkinson, J. A.; Murdoch, P. d. S.; Sadler, P. J. *Inorg. Chem.* **2002**, *41*, 4509.

(80) Wang, F.; Xu, J.; Habtemariam, A.; Bella, J.; Sadler, P. J. *J. Am. Chem. Soc.* **2005**, *127*, 17734.

(81) Wang, F.; Weidt, S.; Xu, J.; Mackay, C. L.; Langridge-Smith, P. R. R.; Sadler, P. J. *J. Am. Soc. Mass Spectrom.* **2008**, *19*, 544.

(82) Colombo, M. C.; Gossens, C.; Tavernelli, I.; Rothlisberger, U. *Modelling Molecular Structure and Reactivity in Biological Systems* **2006**, 85.

(83) Liu, H.-K.; Berners-Price, S. J.; Wang, F.; Parkinson, J. A.; Xu, J.; Bella, J.; Sadler, P. J. *Angew. Chem. Int. Ed.n* **2006**, *45*, 8153.

(84) Liu, H.-K.; Parkinson, J. A.; Bella, J.; Wang, F.; Sadler, P. J. *Chemical Science* **2010**, *1*, 258.

(85) Davies, N. A.; Wilson, M. T.; Slade, E.; Fricker, S. P.; Murrer, B. A.; Powell, N. A.; Henderson, G. R. *Chem. Commun.* **1997**, 47.

(86) Fricker, S. P.; Slade, E.; Powell, N. A.; Vaughan, O. J.; Henderson, G. R.; Murrer, B. A.; Megson, I. L.; Bisland, S. K.; Flitney, F. W. *Br. J. Pharmacol.* **1997**, *122*, 1441.

(87) Guo, Z.; Sadler, P. J. *Angew. Chem. Int. Ed.* **1999**, *38*, 1512.

(88) Mosi, R.; Seguin, B.; Cameron, B.; Amankwa, L.; Darkes, M. C.; Fricker, S. P. *Biochem. Biophys. Res. Commun.* **2002**, *292*, 519.

(89) Zazueta, C.; Zafra, G.; Vera, G.; Sanchez, C.; Chavez, E. *J. Bioenerg. Biomembr.* **1998**, *30*, 489.

(90) Dwyer, D. S.; Esenther, K.; (Procept, Inc., USA); US Patent 93-109232, **1996**.

(91) Ocain, T. D.; Bastos, C. M.; Gordon, K. A.; Granstein, R. D.; Jenson, J. C.; Jones, B.; McAuliffe, D. J.; Newcomb, J. R. *Transplant. Proc.* **1996**, *28*, 3032.

(92) Clarke, M. J.; Bailey, V.; Doan, P.; Hiller, C.; LaChance-Galang, K. J.; Daghlian, H.; Mandal, S.; Bastos, C. M.; Lang, D. *Inorg. Chem.* **1996**, *35*, 4896.

(93) Bastos, C. M.; Gordon, K. A.; Ocain, T. D. *Bioorg. Med. Chem. Lett.* **1998**, *8*, 147.

(94) Franolic, J. D.; Bastos, C. M.; Ocain, T. D.; Gordon, K. A. *Book of Abstracts, 212th ACS National Meeting, Orlando, FL, August 25-29* **1996**, INOR.

(95) Yan, Y. K.; Melchart, M.; Habtemariam, A.; Peacock, A. F. A.; Sadler, P. J. *JBIC, J. Biol.l Inorg. Chem.* **2006**, *11*, 483.

(96) Sava, G.; Pacor, S.; Mestroni, G.; Alessio, E. *Anticancer. Drugs* **1992**, *3*, 25.

(97) Cleare, M. J.; Hoeschele, J. D. *Platinum Metals Rev.* **1973**, *17*, 2.

(98) Novakova, O.; Chen, H.; Vrana, O.; Rodger, A.; Sadler Peter, J.; Brabec, V. *Biochemistry* **2003**, *42*, 11544.

(99) Bugarcic, T.; Novakova, O.; Halamikova, A.; Zerzankova, L.; Vrana, O.; Kasparkova, J.; Habtemariam, A.; Parsons, S.; Sadler Peter, J.; Brabec, V. *J. Med. Chem.* **2008**, *51*, 5310.

(100) Takahara, P. M.; Rosenzweig, A. C.; Frederick, C. A.; Lippard, S. J. *Nature* **1995**, *377*, 649.

Chapter 2

Experimental Methods

Chapter 2

Experimental Methods

This chapter contains details of general analytical methods which are used throughout this thesis. Some more specific methods will be discussed in the relevant chapters. The synthesis and characterisation of Ru(II) arene complexes used for investigations in later chapters is also discussed here.

2.1 Nuclear Magnetic Resonance Spectroscopy (NMR)[1,2]

Nuclear magnetic resonance spectroscopy is the most widely used analytical technique in this work. NMR is still one of the most powerful tools for elucidating the 2D and 3D structure of organic and inorganic molecules. New methods, probes and larger magnets are constantly in development making this technique more and more powerful. In this thesis the following nuclei are studied via NMR; ^{1}H, ^{2}H, ^{13}C, ^{15}N, ^{31}P and ^{99}Ru.

2.1.1 Experimental Overview

Nuclei are positively charged entities and when spinning they generate magnetic fields. When nuclei are subjected to an external magnetic field of strength B_0 their spins lose their degeneracy and nuclei will occupy one of two possible energy levels (α and β) (for nuclei with spin = ½. ^{2}H and ^{99}Ru, which have spins of 1 and 5/2 respectively[3,4], are quadrupolar nuclei and will be discussed in more detail later).

Nuclei in each of the α and β states will precess around the direction of B_0, with a frequency unique to that nucleus, known as the Larmor frequency. The precession has a directional vector aligned to (α) or opposing (β) the vector of the applied magnetic field. There is a small population difference between the α and β states, and so there is a net overall magnetisation of the sample. These population differences are small, eg: an additional 76 protons in the α state for every million protons in the β state in ^{1}H NMR at 298 K in a 500 MHz instrument. This population difference is crucial and is related to the susceptibility of a nuclei to NMR. The more susceptible a nucleus is the greater the population. In NMR a second magnetic field B_1 is applied in short bursts at the Larmor frequency of each nuclei. This in turn leads to a shift of the magnetisation vector away from the z-axis equilibrium position to the x-y plane. (Figure 2.1)

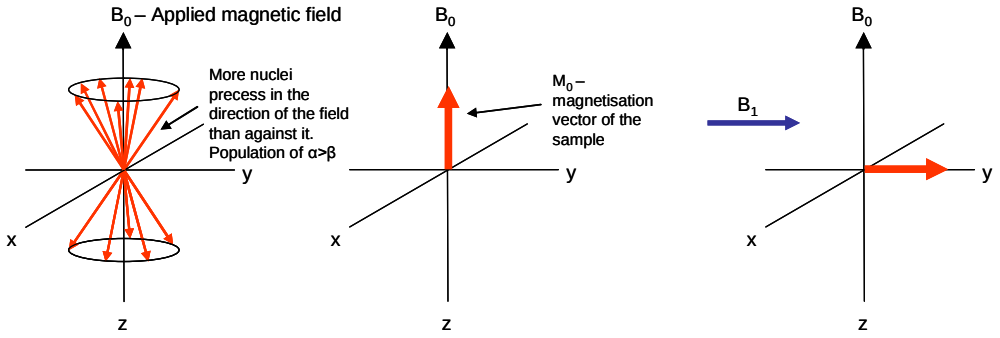

Figure 2.1. A schematic results of applying an external pulse of magnetic field B_1, onto the magnetisation vector of a sample in an external field B_0. (While here is shown a 90^o pulse, many standard pulse programmes use 30^o pulse, but the principle is the same, and M_0 is only flipped 30^o).

As the nuclei relax and return to equilibrium the magnetisation in the x and y axes decays with time and the resulting Free Induction Decay (FID) is observed. The FID is then Fourier transformed to produce an NMR spectrum. In an NMR spectrum the signals are plotted as a function of frequency difference compared to the Larmor frequency of a known standard. (Figure. 2.2)

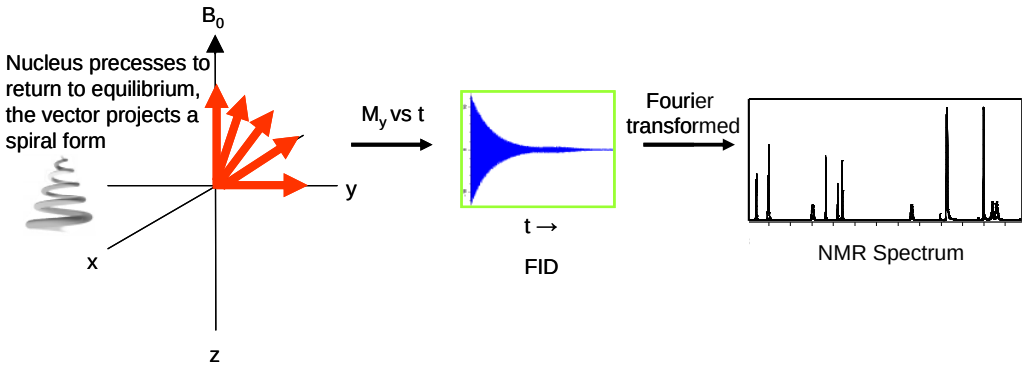

Figure 2.2. The magnetisation vector in the y-plane, M_y is plotted against time to provide an FID. This FID is then processed using a Fourier transform function and an NMR spectrum is generated.

In order to ensure accurate NMR spectra are produced, it is essential that the nuclei can fully relax (i.e.: M_0 being only in the z-axis, $M_y = 0$, $M_x = 0$). This process of relaxation has two components, T_1 is called the spin-lattice relaxation time and is a measure of how long magnetisation take to return to M_0 (magnetisation at equilibrium). The second relaxation parameter is T_2 (Spin-spin relaxation time) which characterises of time taken for M_y (and M_x) to go to zero. As a rule $T_1 \geq T_2$ and so when designing NMR experiments a delay of at least three times T_1 should be left between each pulse of B_1. The relaxation pathways for both these relaxations are very different. Spin-lattice relaxation occurs via interactions between different molecules within the lattice, molecules which are more mobile will, in general relax faster than those that are less mobile. However

fluids are highly mobile and this reduces their ability to restore energy to the lattice, it is for this reason that MRI contrast agents are use to promote relaxation and lead to sharper signals. For spin-spin relaxation, this is the process by which neighbouring nuclei relax through interactions with each other to return to their equilibrium. Nuclei without neighbouring nuclei will relax substantially slower than those with neighbouring nuclei. This is something that must be considered when assigning the relaxation time for an experiment, for example, CH_3 protons which are attached to a quaternary carbon will relax substantially slower than CH_3 protons in a saturated aliphatic chain.

NMR is the study of the resonance frequency required to "flip" the directional vector of the magnetisation on each nucleus. This chemical shift is dependent upon the local chemical environment of the nucleus. Information from the chemical shift of the nuclei within an NMR spectrum can provide much detail on the neighbouring atoms and the magnetic environment of each nuclide in a molecule. Table 2.1 lists some of the NMR properties of the nuclei which will be discussed in this thesis.

Table 2.1. NMR properties of all nuclei investigated in this thesis

Nucleus	Natural Abundance (%)	Sensitivity *(based on natural %)*	ν at 14.1 T *(MHz)*	Spin
^{1}H	99.98	1	600	½
^{2}H	0.015	1.45×10^{-6}	92.102	1
^{13}C	1.108	1.76×10^{-4}	150.864	½
^{15}N	0.37	3.85×10^{-6}	60.796	½
^{31}P	100	6.63×10^{-2}	242.884	½
^{99}Ru	12.72	2.48×10^{-5}	20.338	5/2

2.1.2 Instrumentation

NMR spectra were recorded on Bruker DMX 500 (^{1}H, 500.13 MHz, ^{13}C, 125.72 MHz; ^{15}N, 50.66 MHz; ^{99}Ru, 16.949 MHz), Bruker DRX 500 (^{1}H, 500.13 MHz; ^{2}H, 76.753 MHz; ^{13}C, 125.72 MHz; ^{15}N, 50.66 MHz;), Bruker AV III 600 (^{1}H, 600.16 MHz; ^{13}C, 150.86 MHz; ^{15}N, 60.79 MHz; ^{31}P, 242.884) or Bruker AV II 700 (^{1}H, 700.13 MHz; ^{13}C, 176.08 MHz; ^{15}N, 70.931 MHz) NMR spectrometers using either TBI [^{1}H, ^{13}C, X] or BBO [^{1}H, ^{13}C, ^{15}N] 5 mm probehead fitted with the appropriate signal filters for the nucleus being observed.

2.1.3 Preparation of Samples

Samples were prepared in deuterated solvents (DMSO-d_6, D_2O, MeOD-d_4) or H_2O/D_2O 90/10 mixtures or in the case of ^2H NMR, H_2O, in 5 mm high quality quartz NMR tubes (Wilmad UK) with a typical volume of 0.6 – 1 mL. In D_2O and H_2O/D_2O samples ^1H chemical shifts were internally referenced using a 1% 1,4 – dioxane solution in D_2O (δ = 3.763 ppm) for the $C_4\underline{H}_8O_2$ signal. In the case of MeOD and DMSO the protonated residual solvent was used as an internal calibrant, $C(D_2\underline{H})COD$ in MeOD-d_4 (δ = 3.31 ppm) and $(CD_2\underline{H})(CD_3)SO$ (δ = 2.50 ppm) in DMSO-d_6.[5] In the case of ^2H NMR samples were prepared in 100% H_2O and an internal reference of MeOD-d_4 was added (2 μL), all ^2H chemical shifts were calibrated to a chemical shift of $C\underline{D}_3OD$ at 3.34 ppm as per the chemical shift of $C\underline{H}_3OH$ in D_2O.

^{15}N chemical shifts were externally referenced to $^{15}\underline{N}H_4Cl$ (1 M) in HCl (1.5 M) (δ = 0 ppm). ^{31}P chemical shifts were externally referenced to $H_3\underline{P}O_4$ 85% solution in H_2O (δ = 0 ppm). ^{99}Ru signals were externally referenced to $K_4[\underline{Ru}(CN)_6]$ (1 M in D_2O) (δ = 0 ppm).

2.1.3.1 Acquisition and processing of data

Except where specified, all data was acquired at 298 K. Spectra were acquired using Bruker standard 90° and 30° degree pulse sequences. Standard pulse sequences were used in this work and any major modifications to pulse sequences are mentioned where relevant. Spectral data were acquired over 16 – 2 k scans, depending on the concentration and the nature of the experiment, with an average of 32K data points over 6000 Hz. Measurements of T_1 were carried out

using the standard inversion recovery pulse sequences, and lead to a typical relaxation delay of 2 seconds being used to allow full relaxation of all protons in ^{1}H NMR experiments.

All experiments were carried out in temperature controlled conditions, using the variable temperature and chiller unit attached to the relevant NMR spectrometer and monitored throughout.

Free Induction Decays (FID) were processed using an exponential decay based Fourier transformation. A line broadening value of 0.5 Hz to increase the signal to noise ratio was used as were phasing and standard baseline correction on all ^{1}H spectra. All data were processed using either XWIN-NMR (version 2 or 3.6, Bruker UK Ltd.) or Topspin (version 1.3 or 2.0 Bruker UK Ltd).

2.1.3.2 Assignment and identification of peaks

Identification of NMR peaks in this thesis has been confirmed using 2D NMR techniques, COrrelation SpectroscopY (COSY), Hetreonuclear Spin Quantum Spectroscopy (HSQC) (for both ^{13}C and ^{15}N), Total COrrelation SpectroscopY (TOCSY), to identify pairs of nuclei that are J coupled to one another and protons that are attached to heteroatoms.

2.1.4 Water suppression sequences[6,7]

In order to study small oligonucleotides by NMR, it is best to carry out these experiments in 90% H_2O/ 10% D_2O solutions. However, if no special pulse sequences were used, all ^{1}H signals would be eclipsed by the broad signal from the H_2O protons. In order to prevent this, pulse programs were used whereby the

^{1}H signal for the H_2O was suppressed. In this thesis the sequence used with most success was the WATERGATE (WATER suppression by GrAdient-Tailored Excitation) sequence developed by Sklenář and coworkers[6].

2.1.5 Nuclear Overhauser Effect Spectroscopy (NOESY)[8]

The Nuclear Overhauser Effect (NOE) is observed when two protons couple (*i.e.* affect each others local magnetic environment). This coupling is not scalar (through bonds) but is rather dipolar coupling (through space). NOESY is the technique used to study this coupling and is generally a homonuclear ^{1}H-^{1}H experiment in which direct dipolar couplings are observed by means of a cross peak in a 2D NMR spectrum (Figure. 2.3). The pulse sequence for NOESY involves 3 distinct 90^o pulses, the first pulse will move $M_0$1 (of the principal proton) into the y-axis. M_y1 then relaxes for a time t_1, (the same applies for M_x1, magnetisation in the x-axis) during which time there is some recovery of M_0 in the z-axis. After time (t_1) another 90^o pulse is applied and the M_y1 magnetisation vector returns to the z-axis (M_z1). It is at this point that magnetisation transfer to the secondary proton can occur. This happens during a mixing time τ_m which is defined by the user, the longer τ_m the further away from the principal proton the magnetisation can transfer, (a very useful tool in using NMR to determine the 3D structure in large biomolecules). After the magnetisation transfer the secondary proton now has an M_z2 magnetisation vector. This then experiences an applied a 90^o pulse to yield M_y2, this precesses and the frequency is detected and an FID collected yielding a 2D spectrum.

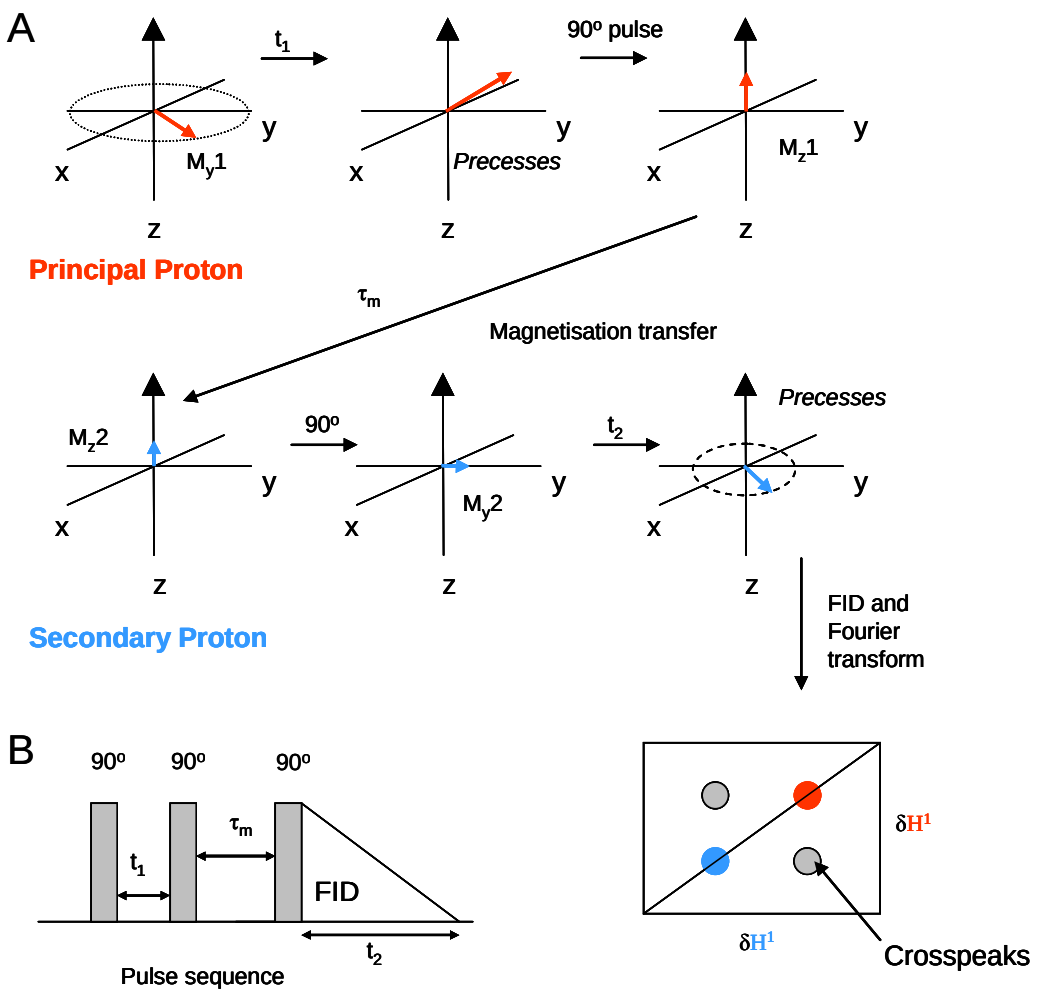

Figure 2.3. A schematic of the steps involved in a NOESY pulse sequence. A) The effects of each pulse on the magnetisation vector of each proton, resulting in a 2D spectrum with crosspeaks as shown. B) The pulse sequence used for all NOESY experiments discussed in this thesis.

2.1.5.1 Experimental detail

NOESY experiments were carried out on a DPX500 MHz NMR spectrometer at 298 K. Acquisition was over 64 scans with each scan contained 200 data points. The mixing time allowed for coupling was 600 ms.

2.1.6 ^{2}H NMR

Deuterium NMR (^{2}H NMR) was carried out using a BBO probe. The broadband channel was used to record the deuterium signal by fitting the ^{2}H filter which is normally used on the dedicated ^{2}H channel (used when locking to ^{2}H solvent signals). Samples were dissolved in H_2O and referenced to MeOD-d_4 at 3.34 ppm. As no ^{2}H signal was available for locking, samples were not locked. The D_2O/HOD peak from MeOD/H_2O solvent was used for shimming purposes. The probe-head was manually tuned to provide the best signal symmetry based on the D_2O peak using tuning and matching operations on the broadband channel. Since ^{2}H signals are broad (I = 1, quadrupole moment = 0.2886 10^{-30} m^2), shimming of the signal was essential to obtain as sharp a signal as possible. Due to sensitivity problems with ^{2}H (9.65 x 10^{-3} less receptive to NMR compared to ^{1}H) higher concentrations of samples were used in order to obtain spectra with reasonable signal:noise ratios to obtain data suitable for kinetic analysis. All ^{2}H spectra were acquired over 128 scans. Relaxation delays for ^{2}H experiments were 2 seconds to allow for full recovery of the MeOD-d_4 signal.

2.1.7 ^{99}Ru NMR

Ruthenium has two NMR active isotopes; ^{99}Ru and ^{101}Ru, which are both quadrupolar with a spin of 5/2.[9] ^{99}Ru is a considerably easier isotope to work with, as although it is less sensitive, it has a lower nuclear quadrupole moment, and therefore gives rise to sharper lines.

Table 2.2. Physical data for the magnetically-active isotopes of ruthenium[10].

Isotope	Mass	Abundance (%)	Relative sensitivity	Relative Magnetic moment (μ_N)	Nuclear Quadrupole Moment 10^{30} Q/m^2
^{99}Ru	98.9	12.76	0.0013	0.645	+ 7.9
^{101}Ru	100.9	17.06	0.00152	0.719	+ 45.7

The fact that ^{99}Ru is quadrupolar causes considerable complications in acquiring data. Signals are broad, with linewidths of up to 4.4 kHz being recorded.[11] The other problem is the low frequency of resonance; with a low frequency of resonance, the Boltzmann distribution of nuclei in different states results in smaller population differences between the higher and lower energy states. There is also the problem of acoustic ringing due to vibrations in the probe and the electronics of the system due to the lower frequency being applied to the sample (*vida infra*). Various procedures[12,13] have been used in attempts to overcome this; however it is still a problem.

^{99}Ru is a quadrupolar nucleus, as the number of unpaired nucleons is >1. This has the following effects on the nucleus; not only is there a magnetic moment, there is also an electric quadrupole moment. This electric quadrupole moment arises from the ellipsoidal shape of the positive charge distribution. Due to the laws of physics, positive charges are in excess at the poles of the ellipsoid and therefore the nucleus is similar to two back-to-back dipoles. In external electric fields which are uniform, there is no interaction between the nucleus and

the field. However in non-uniform external electric fields, there is an interaction between the external field and the electric quadrupole moment of the nucleus.

At the nucleus, the electric field gradients are a result of the ligands, which in turn affects the electron density around the nucleus. In a symmetrical environment, all electric fields cancel out and so no quadrupolar interactions are observed. In non-symmetrical environments, the electric field is non-uniform (i.e. there is an electric field gradient) and a higher electron density can be found at the points of the ellipsoid due to columbic interactions. The interaction between the external electric fields and the electric quadrupole moment results in fast relaxation times. The rapid relaxation leads to broad signals. Also due to rapid relaxation there are no multiplets arising from the different energy levels found due to the rapid interchange (Figure 2.4). All these issues lead to broadening of the NMR signal. Unfortunately in many cases this makes the signal unobservable. This is a regular problem with ^{99}Ru NMR, with less than 20 published papers containing experimentally derived data, although a number of computational studies have been reported. [9,11,14-29]

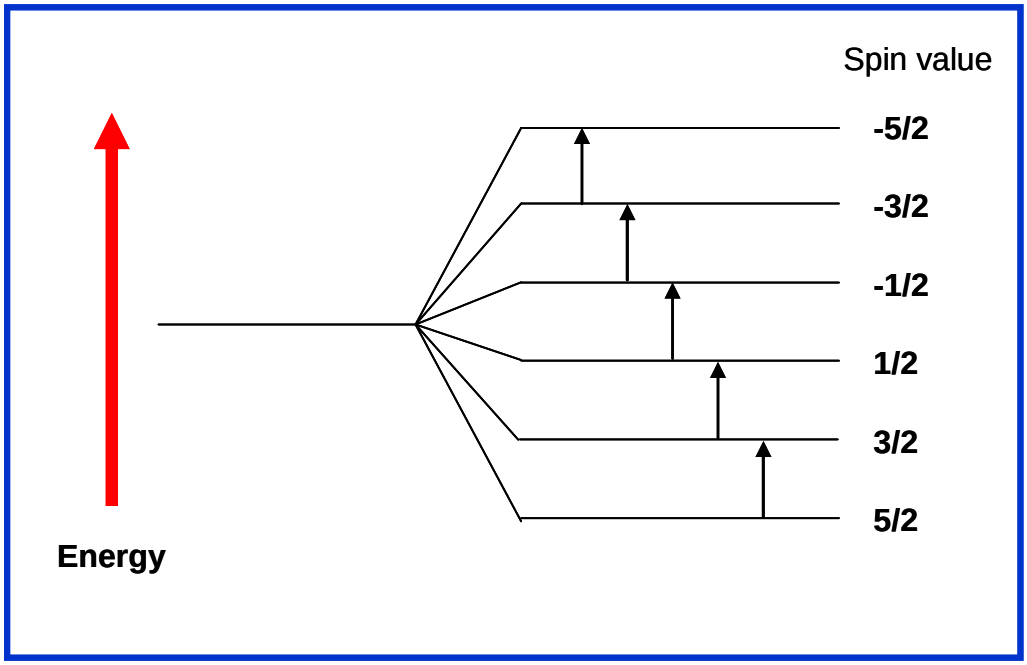

Figure 2.4. The energy levels and transitions available to the magnetic moment of the nucleus of ^{99}Ru.

The NMR standard for ruthenium NMR (0 ppm) is $K_4[Ru(CN)_6]$, which gives rise to a very sharp signal due to the high symmetry of the molecule. Very broad signals, which often occur for quadrupolar nuclei, can be easily lost if the signal-to-noise ratio is poor or the base line is curved due to acoustic ringing. This acoustic ringing occurs, when low frequency pulses cause vibrations in the metal components of the probe. These in turn generate a signal which is detected by the coil, leading to a large signal at the start of the FID (Figure 2.5). Upon Fourier transformation, a rolling baseline is observed. In order to reduce rolling of the base line and acoustic ringing further, sufficient time must be allowed to allow the system to relax between pulses. Therefore a short pulse time and a relatively long relaxation delay are often employed to reduce acoustic ringing.

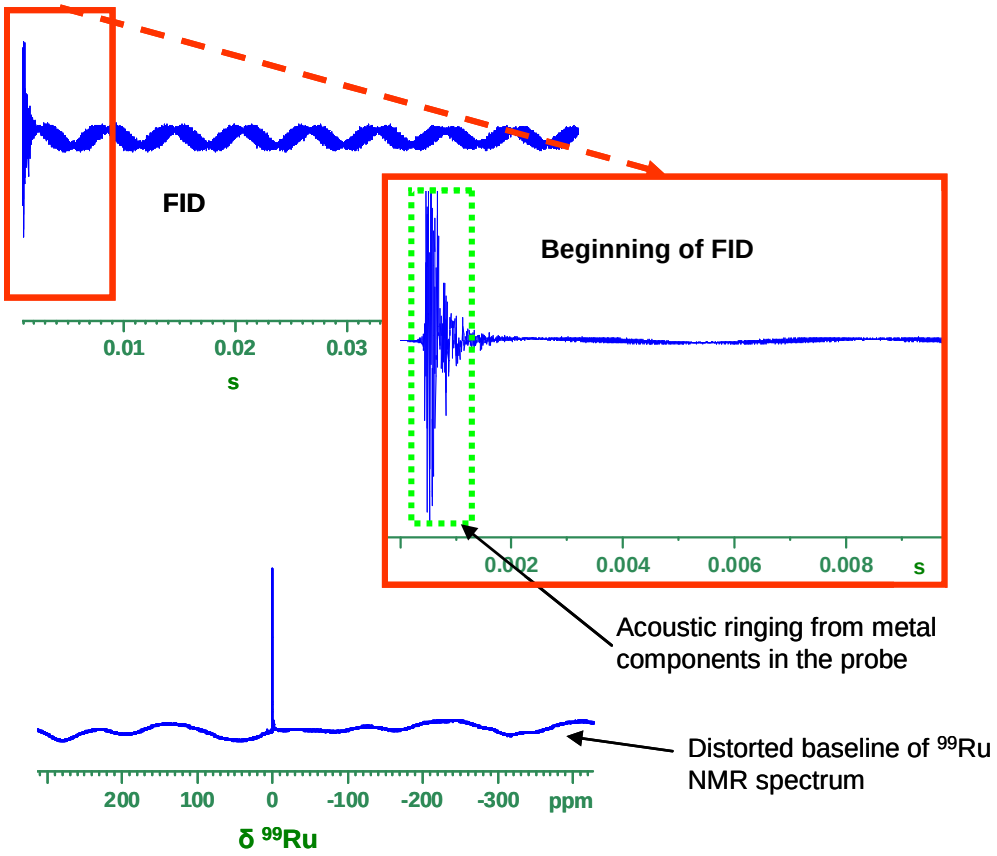

Figure 2.5. The FID and subsequent ^{99}Ru NMR spectrum of $K_4[Ru(CN)_6]$ in H_2O on a Bruker DMX500 NMR spectrometer. The beginning of the FID is highlighted to show the effect of acoustic ringing on the FID and the subsequent baseline rolling observed in the NMR.

The first reported ^{99}Ru NMR study was in 1981[16,26] and included the introduction of $K_4[Ru(CN)_6]$ as the chemical shift standard (0 ppm). In that work, signals between -112 ppm and +7680 ppm were recorded for various ruthenium(II) complexes. The effects of temperature and concentration on the chemical shift of the ruthenium signal were observed. Since then, much work has been done on the development of ^{99}Ru NMR as a valuable analytical tool as can

be seen in Figure 2.6, which has been compiled from previous studies[11,14,15,17,19,21,26,30].

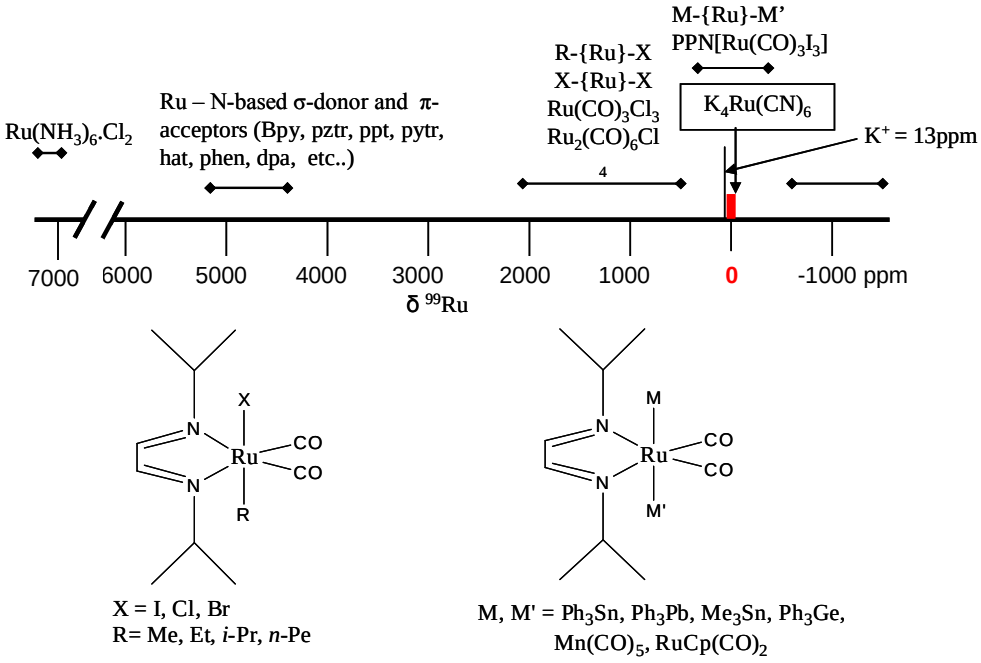

PPN = bis(triphenylphosphine)iminium cation

ppt = 3-(pyrazin-2-yl)-5-(pyridine-2-yl)-1,2,4-triazole

pztr = 3-(pyrazin-2-yl)-1,2,4-triazole

bpy = bipyridine (2, 2' dipyridyl)

pytr = 3-(pyridine-2-yl)-1,2,4-triazole

hat = 1,4,5,8,9,12 - hexaazatriphenylene

phen = 1, 10-phenanthroline

dpa = dipyridylamine

Figure. 2.6. The chemical shift range for ^{99}Ru in a variety of Ru(II) complexes. It should also be noted that the ^{39}K signal of K^+ appears at 13 ppm.[11,14-20]

Another significant use for ^{99}Ru NMR is in distinguishing between *fac* and *mer* isomers of ruthenium complexes which possess three identical ligands. The common thread being that *fac* isomers resonate at lower field that the *mer* isomer. Another interesting factor is that the concentration and counterion can also affect the chemical shift. Studies on *fac*-$[Ru(CO)_3I_3]^-$ have shown that the linewidth can

be significantly increased by increasing the concentration[9] and the counterion has effects on the chemical shift also.

From the data in Figure 2.6, the following trends have been noted. [11,14-20]

1. An inverse relationship between the crystal field splitting and the chemical shift.
2. Large $\delta(^{99}Ru)$ values are observed with increasing Ru – C bond lengths.
3. Where back-bonding occurs via π-systems, the chemical shift is large as less shielding of ^{99}Ru occurs.

It is interesting to note at this stage that no signal has been reported in the literature for Ru(II) arene systems. It was hoped to use ^{99}Ru NMR to monitor changes in the electronic effects around the ruthenium centre of various Ru (II) η^6-arene anticancer drugs.

In the course of this work, attempts were made to study $[Ru(\eta^6\text{-biphenyl})_2]^{2+}$ sandwich complexes with ^{99}Ru NMR. A signal for the $K_4[Ru(CN)_6]$ was obtained but unfortunately no signal was observed for the sandwich complex despite using a sweepwidth of over 200,000 ppm. The complex was also sent to Dr. Christian Brevard in Bruker's research facility in France for further analysis and still no signal was observed.

Given the difficulty in observing broad signals, and the constraints of using only symmetrical complexes it may be more practical to use osmium analogues. ^{187}Os is NMR active and with a nuclear spin of ½, however the natural abundance and susceptibility of this isotope of osmium is very low. This can be overcome to some extent by using polarization transfer methods and these have

previously been demonstrated[31]. The use of ^{187}Os will not only allow for an understanding of the nuclear environment of the Os and may assist with defining the characteristics of the ligands. Given the similarities in structures between Os and Ru complexes comparisons could be made based on ^{187}Os data.

2.1.8. Measurement of kinetics of H/D exchange in D_2O.

Exchange rates of the amine protons for deuterons were determined using NMR data. Samples were dissolved (t = 0) in D_2O (with dioxane as a chemical shift calibrant) and the pH meter reading recorded. Samples were then placed in the NMR spectrometer and FIDs collected at set time intervals over about 24 h. T_1 (spin lattice relaxation time) values were determined for all protons in the spectrum to ensure that the relaxation delay times were sufficient to allow full recovery of the magnetization to the z-axis after each pulse. FIDs were processed and the integral volume of each peak was determined (Figure 2.7), and plotted using Origin 8.1 (OriginLab Corporation, US). The rate constants were determined by fitting the data to the first-order (exponential) rate equation using Origin 8.1. First order equations provided the best fit to the data.

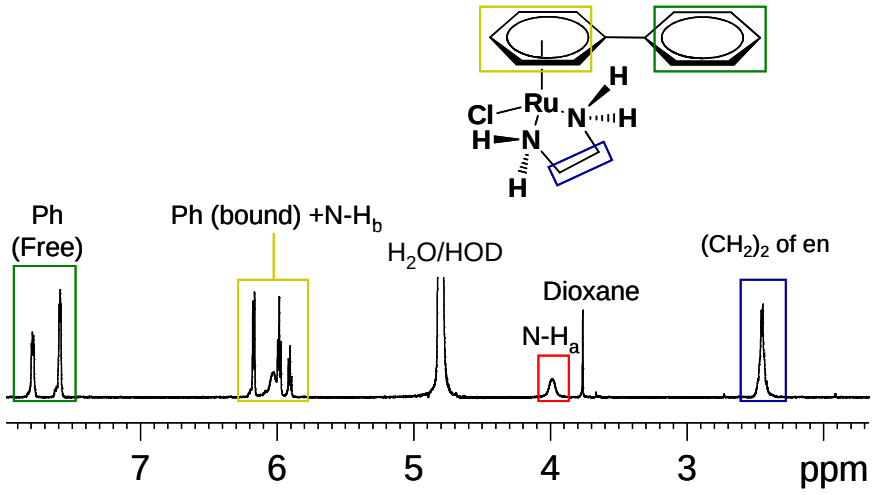

Figure 2.7. ^{1}H NMR spectrum of **[1-PF$_6$]** in D_2O showing the peaks that were integrated to study N-H/D exchange rates. Highlighted in green are the peaks for the uncoordinated phenyl ring. The value of this integral was set at 5 and used to normalise the integrals of the bound phenyl peaks with one N-H peak (yellow) and the other N-H peak at ca 4 ppm (red) and $(CH_2)_2$ peaks of the backbone of the ethylenediamine.

Given the overlap of the bound phenyl and N-H$_b$ a correction to the integral must be made. For this purpose the integral volume of the free phenyl peaks was subtracted from the combined bound phenyl and N-H$_b$ integral value to yield an accurate N-H$_b$ intergral. This was deemed as the best approach given that the free and bound phenyl protons would have similar relaxation times and should therefore have a similar volume. The data were collected and analysed in the following way; NH$_a$ and NH$_b$ integrals (normalised to the peak for the 5 unbound phenyl protons) were plotted against time, to provide decay curves. As a second means of normalising peaks, the integral of the two CH_2 peaks from the ethylenediamine was set to 4 and the integral of NH$_a$ and NH$_b$ peaks redetermined.

The overall error associated with peak integration is estimated to be 5 – 10 %. Broadened peaks are especially subject to larger integration errors.

2.2 pH measurements

All pH measurements were made using Corning 240 pH meter, a Fisher Brand Hydrus 500 pH meter, or a Martini Instruments MI150 pH Meter with glass electrodes filled with either a KCl (or a KNO_3 for chloride free work) solution supplies by Thermo Scientific. Electrodes were calibrated with standard buffer solutions from Sigma-Aldrich at pH 4, 7 and 10 pH units. For NMR samples, the pH values were recorded in D_2O in the NMR tube.

Of use also was a IQ Scientific IQ125 pH electrode with Silicon chip sensor, which is a hand held pH meter and requires 50 μL of sample. This was calibrated with IQ-supplied standard buffers at 4, 7 and 10 pH units. No corrections were made for the effects of deuterium (^2H) on the electrodes, therefore all pH values recorded in D_2O are termed as pH^* (the meter reading).

2.3 Electrospray Ionisation Mass Spectrometry (ESI-MS)

ESI-MS is a widely used and powerful technique for the determination of the masses of complexes. This solution-based analytical technique is very sensitive and concentrations of 10 – 50 μM are usually sufficient to acquire data with a good signal-to-noise ratio. ESI-MS can not only be used to determine the mass-to-charge ratio (*m/z*) of a complex, but can also induce fragmentation of a molecule to allow for analysis of binding sites on proteins and DNA etc.

2.3.1 Experimental detail

ESI-MS discussed in this thesis was obtained on the following instruments; a Bruker HCT-Ultra spectrometer, a Bruker MicroToF spectrometer and a Bruker MaXis spectrometer. Samples were injected in 50/50, MeOH/H_2O solutions and all data were processed and analysed using DataAnalysis 4.0, part of the Compass package from Bruker Daltronics.

2.4 Ion-Mobility Mass Spectrometry (IM-MS) [32-34]

Ion-mobility Mass Spectrometry (IM-MS) is the combination of two very powerful separation techniques. IM-MS can provide a wealth of information about small molecules and, as with all mass spectrometry, only a very small amount of sample is required. This technique can be used to measure the collision cross sections (CCS) of molecules.

2.4.1 Technical overview

Ion mass mobility Mass spectrometry (IM-MS) is fast becoming a widely used technique. Ion mobility has been widely used to separate gases for decades, since the pioneering work of E. W. Mc Daniel in the 1950s[32]. The principle being the separation of ions based on their size using a counterflow gas. (Figure 2.8)

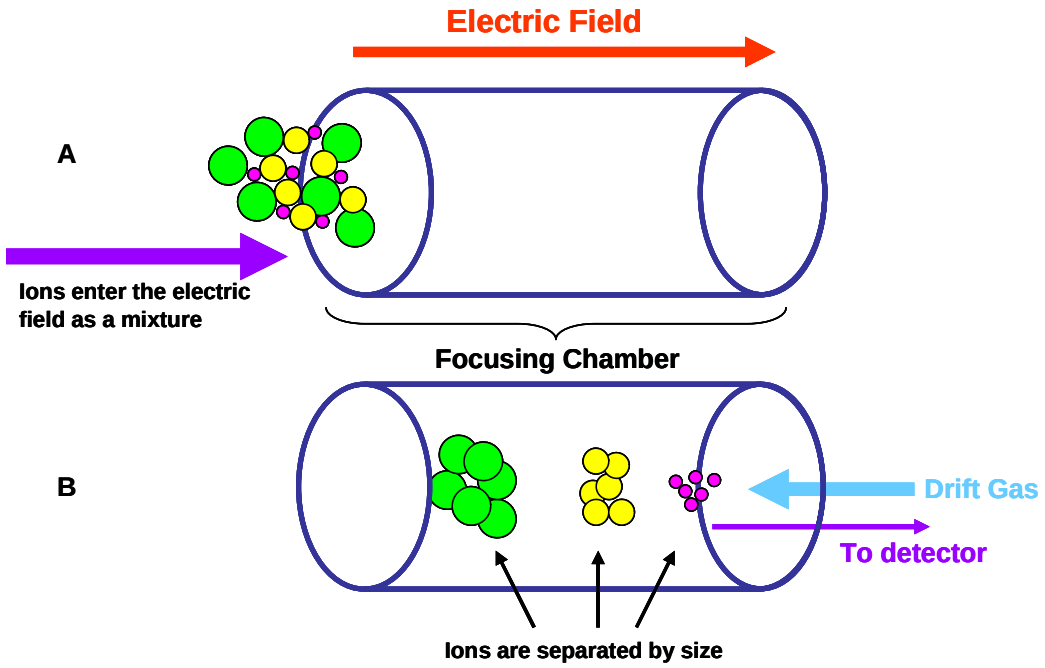

Figure 2.8. The principal workings of an ion-mobility spectrometer cell (IMS cell). **A)** The ions enter as a mixture into the focusing rings. **B)** The drift gas then separates ions based on their size and on to the detector.

The coupling of ion-mobility to mass spectrometry has allowed CCS values of ions with the same m/z value to be determined. The introduction of a quadrupole and an ion trap prior to the IMS cell allows for particular m/z values to be isolated and then separated using ion-mobility. The further addition of a Time-of-Flight (ToF) chamber after the IMS focusing chamber allows for increased sensitivity and resolution in the mass spectrometry data of the separated ions (Figure 2.9).[33]

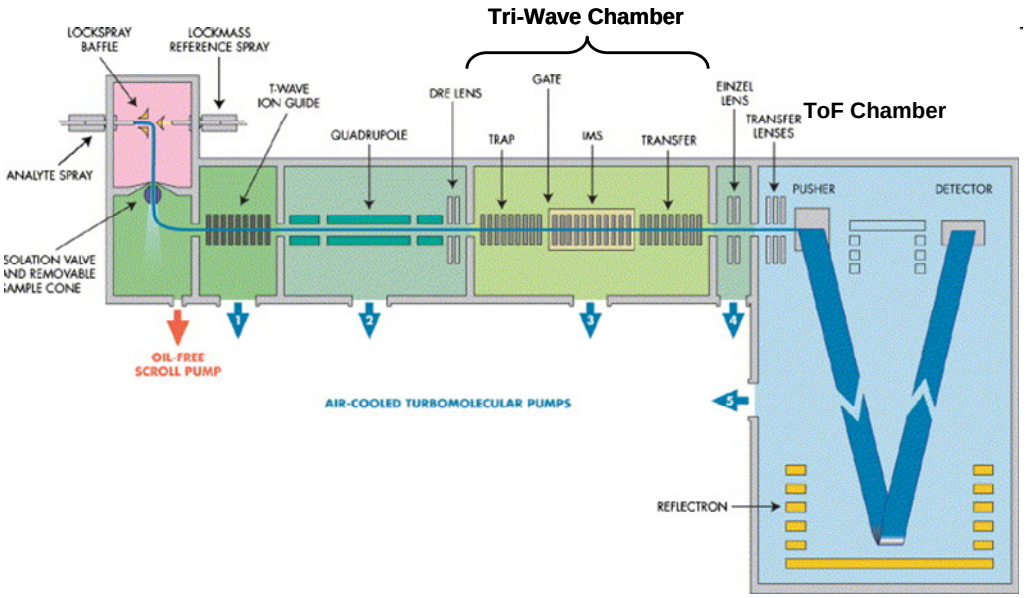

Figure 2.9. A schematic diagram of a Synapt HDMS (High Definition Mass Spectrometer), similar to the type used in this thesis.[33]

In the Waters Synapt device (Figure 2.9) the triwave chamber consists of; the ion trap; for isolating a particular m/z ion, the focussing rings (as outlines in Figure 2.7) and the transfer unit to transfer the ions to the ToF chamber. The IMS chamber in this instance utilises travelling wave (T-wave) technology to allow for better separation and resolution of samples. Unlike traditional IMS whereby ions are subjected to a uniform electric field, in T-wave IMS, an electric field sweeps through the cell one segment at a time forming in pulses. This forms an electrical field "wave" which the ions can "surf" and be separated by their size. This technique has very successfully used for the separation of isomers of small molecules with excellent resolution[35]. IM-MS can also be used to investigate peptide shape changes upon binding to medicinal agents[36] and as is shown later in

this thesis it can be used successfully to determine the collision cross section of ions < 100 Å^2.[37]

2.4.2 Experimental overview

The potential use of IM-MS to study the CCS of small molecules is investigated in this thesis. As part of this work, a new method for calibration was developed and this will be discussed in more detail in Chapter 5. Comparisons were also made between the current algorithm for determining CCS values and a new method developed by Water Corps.

All IM-MS experiments were preformed by Dr Jonathan Williams (University of Warwick) at Waters Corp., Manchester on a Waters Synapt HDMS instrument. Ions were released from the trap, through the mobility device and then through the transfer focussing coils onto the orthogonal accelerated time of flight (oa-ToF) analyser. The arrival time distributions (ATDs) are determined as the time taken for the sample to leave the ion trap and to pass through the rest of the Tri-wave chamber and on to the detector. The instrument was operated with a capillary voltage of 3.0 kV and the ion source block and nitrogen desolvation gas temperature were 80 and 100 ^{o}C respectively. This technique works best with a high vacuum atmosphere and so the ion trap and the transfer section of the tri-wave section were operated at 2 x 10^{-2} mbar of sulfur hexafluoride and the ion-mobility cell was at 3.0 mbar of helium gas. Within the mobility cell the T-wave was operated at a velocity of 250 m s^{-1} and with a pulse height optimised between 4.5 and 8.0 V. Data was acquired and processed using MassLynx (V4.1, Waters Corp.), analysis of the data was carried out by both Dr Williams and the author.

The conversion of arrival time distributions to collision cross section values is through a variety of calibration steps with compounds of known CCS values. This will be discussed in more detail in Chapter 5.

2.5. High-Performance Liquid Chromatography (HPLC)

High Performance Liquid Chromatography (HPLC) is a widely used technique for analysing the purity of products, the analysis of mixtures, and the subsequent separation of those mixtures. In this thesis HPLC was used for the separation and purification of biomolecules attached to ruthenium and platinum complexes for further analysis.

2.5.1Overview of Technique

The discovery and development of HPLC is viewed with such importance that it was the reason the Nobel Prize was awarded to Martin and Synge in 1952[38].

The principle behind HPLC is the separation of molecules based on their hydrophobicity and interactions with the stationary phase in the column. Since hydrophobicities are the main separating feature, it is important to have complexes that are as neutral as possible. It is for that reason that counter ion salts should be used when separating charged complexes.

2.5.2 Technical detail

The work in this thesis was primarily performed on C_8 and C_{18} reverse phase columns. These columns contain silica based polymers which work well for

separating long-chained DNA molecules. Their chemical formulae are shown in Figure 2.10.

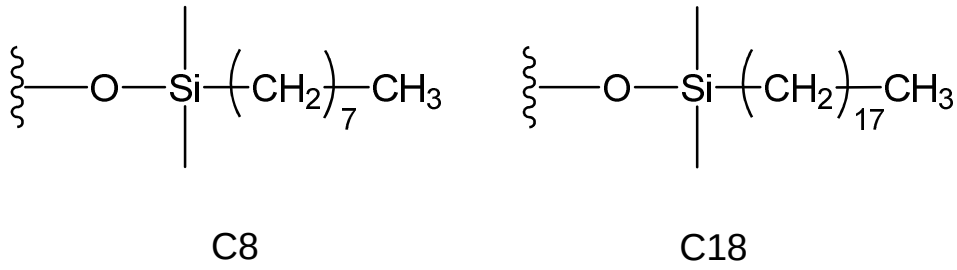

C8 C18

Figure 2.10. The chemical structure of the polymeric material in the C8 and C18 HPLC columns.

The difference in the length of the CH_2 chain has a crucial role in the different properties of both polymers. C18 columns tend to be more retentive for hydrophobic compounds, due to their more hydrophobic nature. The complexes separated in this thesis are all charged species, and so counterions of ammonium acetate (NH_4OAc) and triethylammonium acetate ($NHEt_3OAc$) were used as ion pairing agents to assist with their separation.

2.5.3 Experimental Detail

Reverse-Phase HPLC (RP-HPLC) was carried out on a HP 1100 Series HPLC system (Agilent Technologies) using one of the following columns; an analytical ACE-5-C8-300 (250 x 4.6 mm, ACE); an analytical Zorbax Eclipse Plus C18 (250 x 4.6 mm, 5 μm, Agilent Technologies) or a semi-preparative C18 PLRP-S (300 x 7.5 mm, 300 Å / 8 μm, Polymer Laboratories). The mobile phases were HPLC

grade solvents; water, methanol and acetonitrile purchased from Fischer Scientific. The gradients, flow rate, mobile phase and pairing agent used were unique to each experiment as specified in the individual chapters.

2.6 Ultra-Violet and Visible absorption spectroscopy

Ultra-violet/visible absorption spectroscopy (UV/Vis) is a widely used technique and has a number of functions. These functions vary from determining concentrations of samples to distinguishing between different excitation bands for photochemistry. In this work UV/Vis is used for determine the concentration of DNA samples using the Beer-Lambert Law (Eqn 2.1). As will be discussed later in this Chapter, UV-Vis spectroscopy is also useful for determining whether a DNA sample is a duplex or single stranded.

$$\mathbf{A = \varepsilon \cdot c \cdot \mathit{l}} \qquad \textbf{(Equation 2.1)}$$

The Beer-Lambert Equation, in which **A** is the absorbance, **ε** is the absorption (extinction) co-efficent and is unique to each molecule, **c** corresponds to the concentration of the sample in mol L^{-1} and ***l*** is the length of the light path through the sample in cm. Since absorbance has no units ε must have units of L mol^{-1} cm^{-1}.

2.6.1 Overview of Technique[39,40]

While the UV/Vis region of the electromagnetic spectrum ranges from <100 nm to 800nm, the majority of UV/Vis machines only focus on the region from 200 – 700 nm. This is principally due to the poor reliability of results below 200 nm without a vacuum. UV/Vis electromagnetic radiation produces photons of

energy between 170 – 600 kJ mol^{-1}. Transitions in UV/Vis spectroscopy are between electronic energy levels, so usually a lone pair and an unfilled non-bonding or antibonding orbital. Transistions can also occur between a HOMO (Highest Occupied Molecular Orbital) and the LUMO (Lowest Unoccupied Molecular Orbital), (Figure 2.11). These electronic transitions can present themselves in many different ways in molecules; they can be p-electrons moving to d-orbitals or sp-hybridised electrons, (those partaking in σ-bonding), being excited to p-orbitals, and forming π-orbitals. Commonly seen in organic compounds are electrons in π-orbitals of conjugated systems, those with a large numbers of double bounds, being excited to anti-bonding orbitals in $\pi \rightarrow \pi^*$ transitions.

In order for absorption to occur, the transition must be allowed by the selection rules. (i.e.: ground and excited state must have the same symmetry and multiplicity). However some "forbidden" transitions can occur, but when they do it is mainly as a result of molecular vibrations and will have low intensity due to low extinction coefficients.

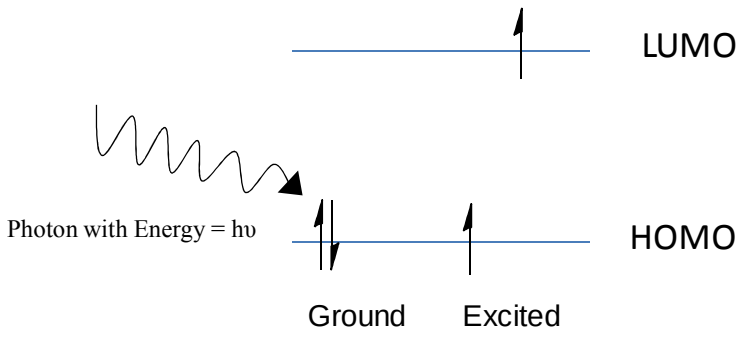

Figure 2.11. Electrons are excited by a photon from the HOMO to the LUMO, the excited state. The absorption of this photon can provide much insight into the electronic structure of the molecule.

DNA absorbs radiation typically in the 200 – 300 nm region via $\pi \rightarrow \pi^*$ transitions of the purine and pyrimidine bases. In DNA samples purines and pyrimidines absorb close to 260 nm and so can be used as a tool to determine the concentration of DNA solutions (Table 2.3). Interestingly, when DNA forms a duplex the extinction coefficient decreases when compared to single strands. This decrease in intensity is due to electrons being partially removed from the conjugated systems as they are involved in H-bonding. Therefore UV/Vis absorbance spectroscopy is a useful tool for investigating whether annealing has occurred, by heating the sample slowly and monitoring the absorbance at $\lambda = 260$ nm. If the sample is a duplex there will be a distinct melting curve, which has a sigmodial shape as the duplex dissociates to individual DNA single strands. The inflection point on the curve is the melting temperature, T_m, and is the temperature above which the duplex is no longer stable and will revert to its individual components (single strands).

Table 2.3. Values of ε and λ_{max} for all four nucleobases in DNA

Residue	(ε) L Mol^{-1} cm^{-1}	λ_{max}(nm)
Adenine	15200	259
Guanine	12010	253
Cytosine	7050	271
Thymine	8400	267

2.6.2 Experimental detail

All UV/Vis spectra in this thesis were measured on a Varian Cary 300 Scan spectrometer. Data were collected using Cary WinUV software by Varian Inc, © 2004. Samples were prepared in Ultra High Quality (UHQ) water and of volume 600 µL and run in quartz UV/Vis quality cuvettes of path length 1 cm. Spectral values were averaged over three scans and a background of UHQ water was subtracted to determine the spectra of the DNA.

2.7 CD Spectroscopy[41]

Circular dichroism is used to determine the extent of chirality of a molecule. In this thesis the effects of binding of complexes to strands of duplex DNA are investigated. Electromagnetic radiation consists of two elements, electric and magnetic components which co-exist and propagate in waves in perpendicular planes (Figure 2.12).

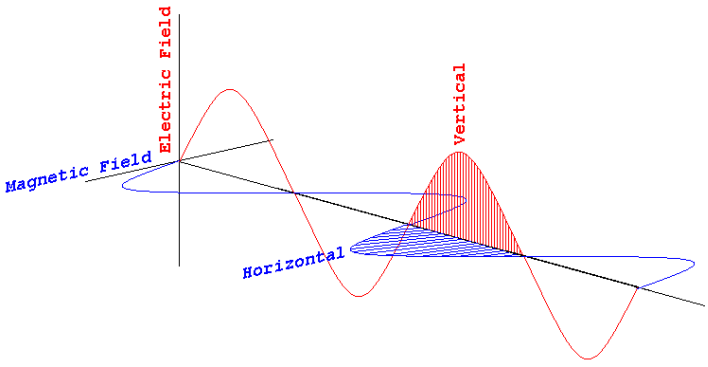

Figure 2.12. A representation of the two vectors that make up light. In the vertical plane is the electric field vector (red) and in the horizontal plan is the magnetic vector (blue).[42]

In non-polarised light the vector (sum of the electric and magnetic field vectors) is a sine function but it propagates in the 45^{o} plane between the vertical and horizontal axis. In circular dichroism the light is filtered to form a universally sized vector which propagates right- or left-handed helices (Figure 2.13) of electromagnetic radiation.

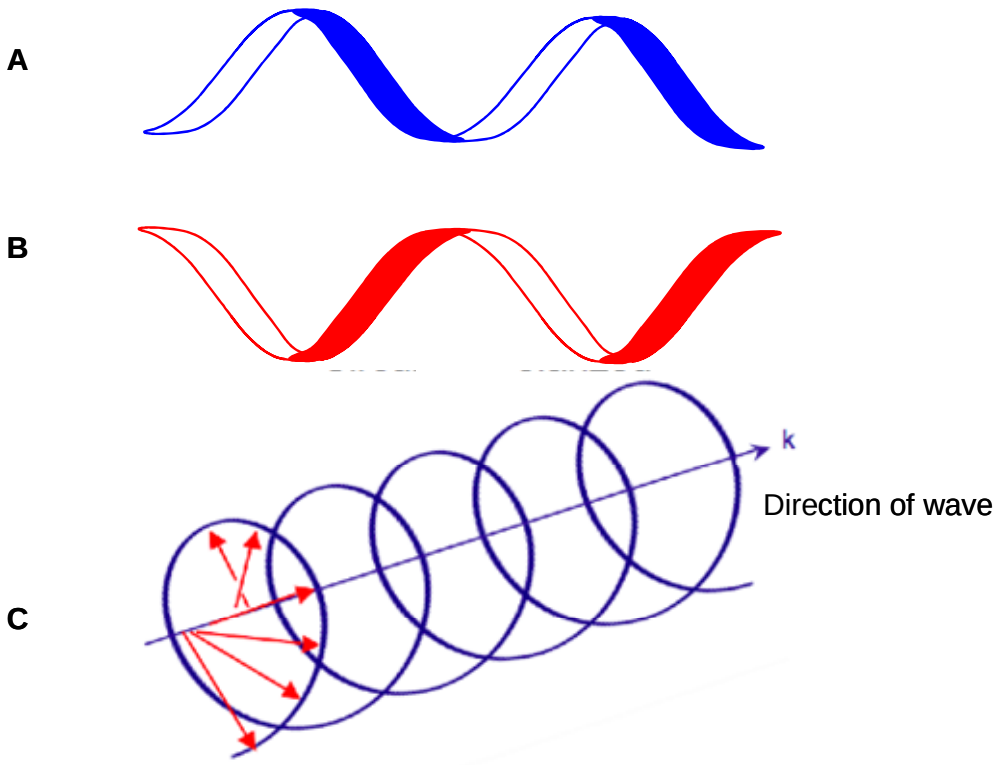

Figure 2.13. (A) A right and (B) left handed helix. (C) A representation[43] of left-handed circularly polarised light.

CD spectra arise form the differential absorption of left and right circularly polarized light. Chiral molecules absorb UV/Vis circularly-polarised light differently depending on the direction of polarity. So by recording the difference between absorbance of left and right handed light, chirality can be detected.

When DNA forms a helix, the helix itself is chiral, and has a unique CD spectrum. CD is a useful technique for looking at whether a helix has been formed or not, i.e. when annealing has taken place. Also upon binding metal complexes some unravelling of the duplex can occur. This too will have an effect on the chirality of the sample. Non-chiral or racemic mixes will not show any difference between the absorption of left- and right- circularly polarised light and will not give rise to CD spectra.

2.7.1 Experimental Detail

CD spectra were acquired on a JASCO J-815 CD Spectrometer and data processed with J815 Spectra Manager Version 2. 07.02 (Build 4) by JASCO Corporation. Samples of volume 180 μL were prepared using UHQ water and run in a CD cuvette of thickness 1 mm.

2.8 Inductively Coupled Plasma Mass Spectrometry (ICP-MS)

ICP-MS is a highly sensitive and reliable analytical technique for determining concentrations of elements in solution. There are more than 75 suitable elements which can have their solution concentrations determined by ICP-MS, many to concentration in parts per trillion (ppt) ranges.

2.8.1 Overview of Technique

First developed in 1980 by Gray[44,45] and co-workers, ICP-MS uses the main principles of breaking molecules down to their atoms, ionising the atoms and then focusing the ion path using a quadrupole onto a mass spectrometry detector.

Once the sample is injected as a liquid into the instrument, it undergoes nebulisation to ensure the liquid forms an aerosol. The aerosol is then desolvated into smaller particles and from there they are vaporised to individual molecules. These molecules are then broken to individual atoms, which are then ionised. Once produced, the ions are then focused using a quadrupole into a mass spectrometer and the output then analysed. A schematic of the internal parts of an ICP-MS instrument can be seen in Figure 2.14.

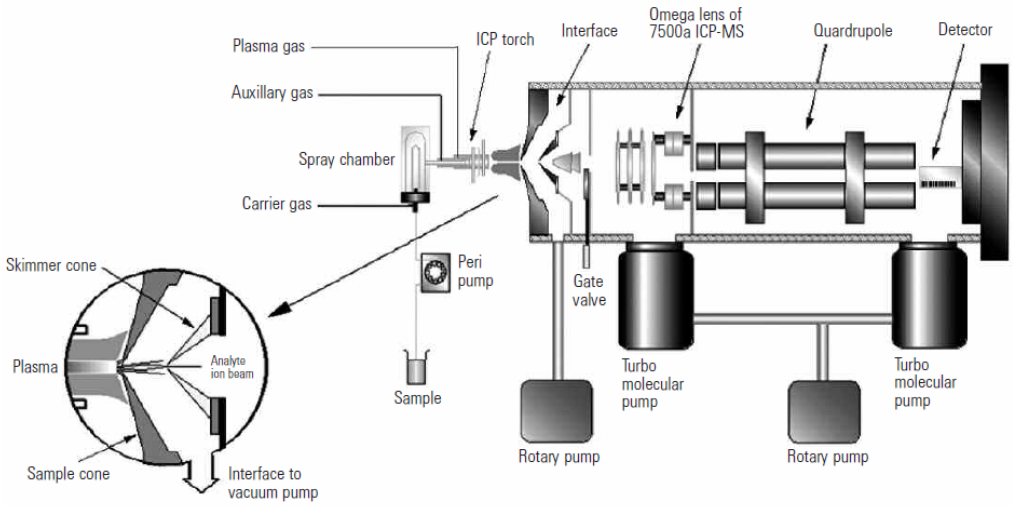

Figure 2.14. A schematic diagram of an ICP-MS Instrument[46] (Reproduced from Agilent Technologies users manual)

The sample is introduced via the peristaltic pump to join the carrier gas, in this case helium, where it enters the spray chamber. It is at this point that the

sample is nebulised to an aerosol, where heavier and larger droplets are removed to waste. Only the smaller droplets remain and the aerosol mixes with the auxiliary gas, argon, and enters the plasma torch (ICP torch). Here the mix is subjected to radiofrequency voltage, which causes the Ar ions and electrons to oscillate and causes temperatures to exceed 10,000 K. At this temperature the molecules form plasma as they lose some of their outer electrons.

From here the samples go through a sample and skimmer cone, the function of which is to focus the beam of ions onto the lens of the mass spectrometer. The quadrupole then separates out the ions by mass so that only the ions of interest are focused onto the mass detector. This increases the sensitivity of the signal, as it accumulates ions based on their mass, but also due to the high vacuum, there is no interference from ion collisions which would neutralise ions.

The final step is the detection of the concentration of the sample. This is done by recording the counts per second of the signal at the required mass. This is then converted into ppb (or ppt) by comparing it to calibrants measured immediately prior to measurements on the sample.

2.8.2 Experimental Details

Samples were prepared in UHQ water to an estimated concentration of 5 – 80 ppb of the metal to be investigated. Calibration was against freshly prepared solutions of fixed concentrations of 0.1, 1, 2, 5, 10, 20, 40, 50, 80, 100, 200, 400 and 500 ppb of metal prepared from a 1000 ppm ICP standard purchased from Alfa Aesar.

In this thesis, the primary role of ICP-MS was to determine the concentration of solutions of ruthenium and platinum anti-cancer drugs prior to

addition to DNA samples. All ICP-MS analyses were carried out on an Agilent Technologies 7500 series ICP-MS instrument. The settings of the instrument are as described in Table 2.4.

Table 2.4 Instrument settings for ICP-MS

Plasma conditions	
Plasma gas / $Lmin^{-1}$	15
Auxiliary gas / $Lmin^{-1}$	0.2
Forward power / W	1550
Reflected Power / W	1
RF Matching / V	1.8
Sample Depth / mm	9
Carrier Gas / $Lmin^{-1}$	0.9
Makeup Gas / $Lmin^{-1}$	0.2
Nebulizer Pump / rps	0.08
S/C Temp / degC	15
Analyser Pressur/ Pa	10^{-3}
FF/BK Pressure / Pa	343
Peristaltic pump/ rpm	0.08
Ion Lenses	
Extract 1 / V	0
Extract 2 / V	-130
Omega Bias-ce / V	-16
Omega Lens-ce / V	1.8
Cell Entrance / V	-20
QP Focus / V	5
Cell Exit / V	-20
Quadruple Parameters	
AMU Gain	127
AMU offset	128
Axis gain	0.9998
Axis Offset	0
QP Bias / V	-5
Octopole Parameters	
Octopole RF / V	180
Octopole Bias / V	-50
Detector Parameters	
Discriminator / mV	8
Analog HV / V	1730
Pulse HV / V	1070

2.9 X-Ray Crystallography

X-ray crystallography is an important tool for determining the 3D coordinates of all atoms in a molecule in the solid state. The technique involves bombarding a suitable crystal with x-rays and analysing the diffraction pattern.

2.9.1 Experimental Detail

X-ray crystallographic studies of suitable crystals of Ru(arene) complexes synthesised in this thesis were carried out at the University of Edinburgh by Professor Simon Parsons and colleagues, the EPSRC National Crystallography Service, the University of Southampton or at the University of Warwick by Dr Guy Clarkson. Details of the techniques and instrumentation used to obtain specific structures are discussed in the relevant chapters.

2.10 CHN Analysis

CHN elemental analysis is one of the most common forms of elemental analysis of compounds. The process of analysis is based on fully combusting samples in excess of oxygen, leading to the production of CO_2, H_2O and NO_2. The masses of the combusted products are then measured and from that the initial amounts of all carbon, hydrogen and nitrogen in the sample are then determined. This is then compared to the initial mass of the sample to provide the percentage of each element present and thus the molecular formula.

2.10.1 Experimental detail

CHN analysis was carried out, following submission of ca. 3 mg samples, at St Andrew's University, St Andrew's, Fife, Scotland on a Carlo Erba CHNS analyser or Warwick Analytical Services, using an Exeter Analytical Element Analyser (CE440).

2.11 Förster Resonance Energy Transfer (FRET)

Förster Resonance Energy Transfer (FRET), was discovered in 1948 by the German Scientist Theodar Förster.[47] FRET is used to describe the transfer of energy from a donor chromophore to an acceptor chromophore. Energy transfer occurs via nonradiative energy transfer from the excited state of the donor fluorescent molecule to the acceptor molecule *without emission* of an electron, but through photon transfer[48]. (Figure 2.15)

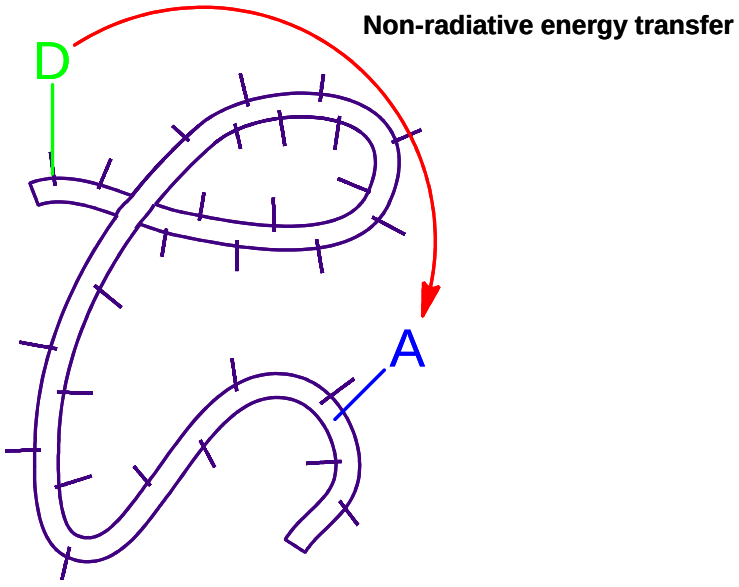

Figure 2.15. A schematic of how energy can transfer from the donor to the acceptor dyes on a macromolecule.

The efficiency of FRET is dependent on the distance, *R*, between the donor and acceptor chromophores and is a function of the distance to the 6th power. (Equation 2.2)

$$E = \frac{R_0^{\,6}}{R_0^{\,6} + R^6} \qquad \text{(Equation 2.2)}$$

where *E* is the efficiency of FRET (the quantum yield of the energy transfer) and R_0 is the Förster distance, a parameter which is dye-pair dependent[49].

The other requirement for FRET is that the emission spectrum of the donor must overlap with the absorbance spectrum of the acceptor. (Figure 2.16)

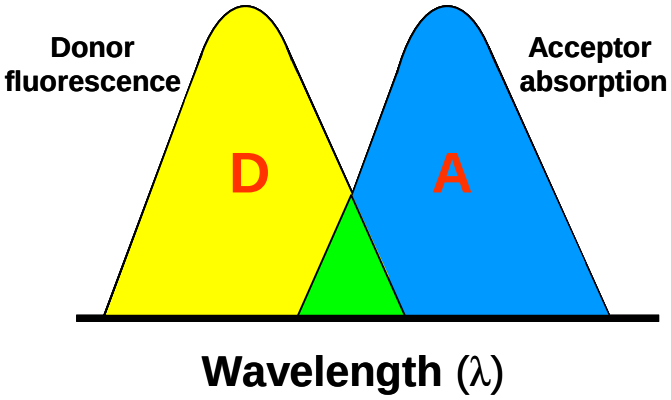

Figure 2.16 In order for FRET to occur there must be an overlap between the emission spectrum of the donor (D) and the absorption spectrum of the acceptor (A).

This technique is very useful for studying the distance between two sites on a macromolecule[50] and interaction distances between two large molecules[51]

(eg: binding of DNA to proteins). FRET can be used to determine the distance between the donor and acceptor dyes at distances up to 100 Å.[52]

In this thesis, attempts were made to study the shape change of 30-mer duplex strands of DNA following binding to cisplatin [cis-dichlorodiammineplatinum(II)]. Previous work[53-55] has shown that when DNA strands are platinated, kinking of the duplex strands occurs and this leads to programmed cell death. FRET has been used in the past to investigate a DNA duplex, which had been synthesised to be kinked.[56] Studies of DNA dissociating from nucleosomes[57] and investigations into HIV reverse transcriptase interactions with nucleic acids have also been carried out using FRET.[58] A previous study,[51] has looked at the effects of cisplatin binding to a 20-mer duplex and observed FRET indicating that the DNA was bent at an angle of 58^{o} when 1,2 GpG intrastrand platinum crosslinks are present.

The chromophores used in this study, along with the appropriate fluorescence data are shown in Figure 2.17.

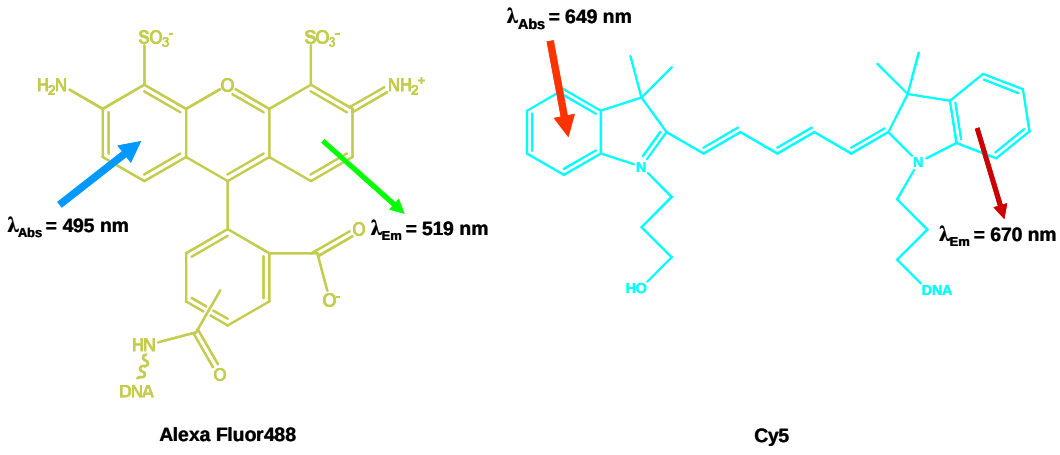

Figure 2.17. The chromophores used in this study. Alexa Fluor488 is the donor chromophore and Cy5 is the acceptor tag.

The overlap between the Alexa Fluor488 emission spectra and the Cy5 absorbance spectra can be seen in Figure 2.18 below.

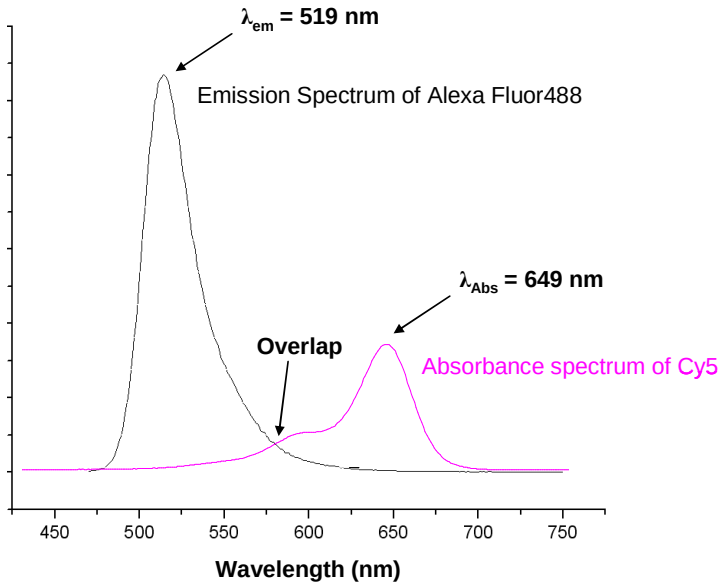

Figure 2.18. The emission spectrum of Alexa Fluor488 when excited at 488 nm; this is overlapped with an absorbance spectrum of Cy5 to show that there is an overlap, ensuring FRET can occur.

When making decisions on the sequences to be used, the ability of guanine residues and platinum to quench fluorescence must be considered. However, to stabilise the duplex formed, and to allow for platination, two adjacent guanine residues must be included in the sequence. It was for this reason that the tags were placed as far away as possible from the guanine bases.

2.11.1 FRET analysis

Single molecule experiments were carried out at the Photonics Institute at the University of Manchester by Ms. Anita Toulmin and Dr. Steven Magennis using a confocal microscope with multiple photon-counting detectors for simultaneous measuring of fluorescence colour, intensity, lifetime and polarisation.

2.12 Computational Studies

Computational studies were employed in this thesis to investigate the molecular orbitals on a variety of ruthenium-arene complexes. All calculations were performed using Gaussian 03[59] (G03) employing the DFT method.

2.12.1 Density Functional Theory[60]

Density Functional Theory (DFT) is a commonly used molecular modeling method to investigate the molecular orbitals on molecules. DFT is not based on wavefunctions, but rather on the Hohenberg-Kohn theorem. Hohenberg-Kohn theorem states that ground state properties can be determined purely from the electron density. DFT calculations optimize the electron density to determine the most stable ground state of a molecule.

2.12.2 Experimental detail

The correlation functional PBE1PBE[61,62] was tested using the LanL2DZ basis set[63] as the effective core potential for the ruthenium and 6-31G**+ basis set for

all other atoms. The coordinates for each molecule were taken directly from the X-ray structures (less the PF_6 counterions). Geometry optimization in the ground state was performed in the gas phase. The molecular orbitals were viewed in GaussView 03. These computations were carried out with the advice and assistance of Dr Luca Salassa.

2.13 Melting Points

All melting points were obtained using a Sanyo Gallenkamp melting point apparatus with a variable heater. A mercury thermometer was used to record the melting temperature.

2.14 Materials and Synthetic Methods

2.14.1 Chemicals

Most reagents were purchased from Sigma-Aldrich (Dorset, UK), with the exception of the following; sodium chloride (99%) was purchased from Acros (Geel, Belgium); dioxane from Rathburn (Walkerburn, Scotland, UK) and bench solvents (methanol, ethanol and diethylether) were purchased from Fischer Scientific (Loughborough, UK). Deuterated solvents were used as purchased from either Sigma-Aldrich (Dorset, UK) or Cambridge Isotopes Limited (Cambridge, UK). DNA samples were purchased from either Sigma-Aldrich, DNA Technology (Aarhus, Denmark), Purimex (Grebenstein, Germany) or Eurogentec (Southampton, UK) and used as the sodium salt. $RuCl_3.xH_2O$ was purchased from Precious Metals Online (Australia).

2.14.2 Specific Preparation Methods

2.14.2.1 Synthesis of the dimer and the main starting material

The initial dimer, $[(\eta^6\text{-biphenyl})RuCl_2]_2$ was prepared using the method described in previous work[64,65] and references therein. This was then used to prepare $[(\eta^6\text{-biphenyl})Ru(N,N' - 1,2\text{ -ethylenediamineCl}].PF_6$ (**1_PF$_6$**) using the previously published procedure[66], this was used to study exchange rates and as a starting material for most of the complexes synthesised in this thesis.

2.14.2.2 $[(\eta^6\text{-biphenyl})Ru(en)OH_2]^{2+}$ (1a)

This complex was prepared in solution. $[(\eta^6\text{-biphenyl})Ru(II)enCl].PF_6$ (**1**) (199 mg, 0.4 mmol) was dissolved in 250 mL of a 1:1 MeOH/H_2O v/v. To this, 67 mg (0.39 mmol) of $AgNO_3$ (99.99% purity) was added and the solution left to stir at 298 K overnight and then centrifuged, decanted and filtered through celite, microglass filter and a fritte to remove precipitated AgCl. This solution was used without further purification as starting material for the preparation of some of the compounds synthesised in this thesis.

2.14.2.3. $[(\eta^6\text{-biphenyl})Ru(N^2H_2,N'^2H_2\text{–1,2–ethylenediamine})Cl]PF_6$ (1D_PF$_6$)

$[(\eta^6\text{-bip})Ru(en)Cl]^+$ (**1**) (4 mg, 8 nmol) was dissolved in 4 mL 154 mM NaCl solution in D_2O. This solution was allowed to stand at 313 K for 6 hours and lyophilized. This resulted in a yellow solid which contained a mixture of **1D** and NaCl, suitable for monitoring $^2H - {}^1H$ exchange on the amine in H_2O.

2.14.2.4 $[(\eta^6\text{-biphenyl})Ru(en)(N\text{-pyridine})]2PF_6$ (6_2PF$_6$)

$[(\eta^6\text{-biphenyl})Ru(N,N' - 1,2 \text{ –ethylenediamine})H_2O].2PF_6$ (**1a_2PF$_6$**) (20.5 mg, 0.043 mmol) was dissolved in ca. 20 mL of 1:1 v/w methanol/water solution. To this pyridine (68 μL, 66.5 mg, 0.841 mmol) was added, the solution stirred for 72

h at room temperature. To this solution ammonium hexaflorophosphate (70.1 mg. 4.3 mmol) was added and volume reduced under vacuum and stored at 277 K for 24 h. A yellow/brown solid was filtered from the solution, washed in water, ethanol, methanol and diethylether and left to dry under vacuum, yielding a yellow microcrystalline solid (10 mg, 14.6 μmol, 34%) which was dried under vacuum. Crystals of **6_2PF$_6$**, suitable for X-ray diffraction, were obtained from a methanol solution at 277 K. m/z (ES+) in MeOH gave two major peaks, $[RuC_{19}H_{23}N_3]^{2+}$ = 197.98 amu (Calculated = 198.55 amu), $[RuC_{19}H_{23}N_3PF_6]^{+}$ = 540.38 amu (Calculated = 540.06).

^{1}H NMR (DMSO-d_6) δ_H: 8.54 ppm (d, 2H, J = 5.2 Hz o-*H*-pyr), 7.91 ppm (t, 1H, J = 8.75Hz, p-*H*-pyr), 7.53 ppm (d, 2H, J= 6.35, o-*H*-free phenyl), 7.43 ppm (m, 3H, m-*H*-pyr and p-*H*-free phenyl), 7.34 ppm (t, 2H, J = 7.9 Hz, m-*H*-free phenyl), 6.87 ppm (b, 2H, en-N$H_{2(up)}$), 6.33 ppm (d, 2H, J = 6.45Hz, o-*H*-bound phenyl), 6.25 ppm (t, 2H, J = 5.9, m-*H*-bound phenyl), 5.87 ppm (t, 1H, J = 5.53Hz, p-*H*-bound phenyl), 3.53 ppm (b, 2H, en-N$H_{2(down)}$), 2.36 (m, 2H, en-C$H_{2(up)}$), 1.87 ppm (m, 2H, en-C$H_{2(down)}$).

^{1}H NMR (90% H_2O/10% D_2O, pH 6.98) δ_H: 8.48 ppm (d, 2H, J = 5.0 Hz, o-*H*-pyr), 7.90 ppm (t, 1H, J = 7.73Hz, p-*H*-pyr), 7.55 ppm (d, 2H, J = 7.55Hz, o-*H*-free phenyl), 7.51 ppm (t, 1H, J= 7.45Hz, p-*H*-free phenyl), 7.41 ppm (m, 4H, m-*H*-pyr and m-*H*-free phenyl), 6.63 ppm (b, 2H, en-N$H_{2(up)}$), 6.36 ppm (d, 2H, J = 7.45, o-*H*-bound phenyl), 6.32 ppm (t, 2H, J = 6Hz, m-*H*-bound phenyl), 5.89 ppm (t, 1H, J = 5.58Hz, p-*H*-bound phenyl), 4.26 ppm (b, 2H, en-N$H_{2(down)}$), 2.57 ppm (m, 2H, en-C$H_{2(up)}$), 2.12 ppm (m, 2H, en-C$H_{2(down)}$). Elemental analysis; calcd (%) for $C_{19}H_{23}N_3P_2F_{12}$: C 33.34, H 3.39, N 6.14, found: C 33.00, H 3.19, N 6.05.

2.14.2.5. [(η^6-biphenyl)Ru(en)(*N*-4-methylpyridine)]2PF_6. (7_2PF_6)

An aliquot of 60 mL of **1a** (*c.f.: 2.14.2.2*) was taken from the 1.6 mM solution (ca 0.1 mmol). To this 4-picoline (4-methylpyridine) was added (1.948 mL, 1.826g, 20 mmol). The solution was stirred for 15 h at 298 K and filtered into a solution of ammonium hexafluorophosphate (326 mg, 2 mmol) in MeOH (5 mL). The volume of the solution was reduced under vacuum until the product began to precipitate. This precipitate was then redissolved in a small amount of acetone and the entire solution left at 277 K to allow the product to crystalise slowly. Yellow crystals suitable for X-ray diffraction studies formed in the mother liquor. After further cooling of the mother liquor yielded a golden yellow microcrystalline product (10 mg, 13.77% yield) was collected by filtration and washed with cold water, ethanol and diethyl ether and dried under vacuum.

Elemental analysis: calculated (%) for $C_{20}H_{25}N_3P_2F_{12}$: C 34.39, H 3.61, N 6.01, found: C 34.26, H 3.58, N 6.01.

^{1}H NMR (DMSO-d_6) δ_H: 8.36 ppm (d, 2H, J = 6.47 Hz, o-*H*-4-methylpyridine), 7.53 ppm (d, 2H, J = 7.35 Hz, o-*H*-free phenyl), 7.45 ppm (t, 1H, J = 7.35 Hz, p-*H*-free phenyl), 7.34 ppm (t, 2H, J = 7.65Hz, m-*H*-free phenyl), 7.286 ppm (d, 2H, J = 6.05 Hz, m-*H*-4-methylpyridine), 6.83 ppm (t, 2H, J = 5.1 Hz, en-N$H_{2(up)}$), 6.33 ppm (d, 2H, J = 6.2 Hz, o-*H*-bound phenyl), 6.20 ppm (t, 2H, J = 6.0 Hz, m-*H*-bound phenyl), 5.88 ppm (t, 1H, J = 5.6 Hz, p-*H*-bound phenyl), 4.49 ppm (t, 2H, J = 5.1 Hz, en-$NH_{2(down)}$), 2.35 ppm (s, 3H, pyr-CH_3), 2.34 ppm (m, 2H, en-CH_2), 1.85 (m, 2H, en-CH_2).

2.14.2.6 [(η^6-benzene)Ru(en)(*N*-pyridine)].2PF_6. [9_2PF_6]

[(η^6-Benzene)Ru(*en*)Cl].PF_6 (**8**, kindly donated by Dr. A. Habtemariam) (72.2 mg, 0.168 mmol) in 140 mL methanol/water (50/50, v/v) and silver nitrate (28 mg, 0.165 mmol, 99.99% purity) were stirred for 15 h at 298 K, and centrifuged, decanted and filtered through celite, microglass filter and a fritte to remove the AgCl precipitate. To the resulting clear yellow solution, pyridine (272 μL, 265 mg, 3.35 mmol) was added and stirred for a further 72 h, filtered and ammonium hexafluorophosphate (0.548 mg, 3.36 mmol) was added. The volume of the solution was reduced under vacuum until the product began to precipitate. This precipitate was then redissolved in a small amount of acetone and the entire solution left at 298 K to crystallise slowly. The product, long dark yellow needle-like crystals, which appeared (18mg, 17.2 %), this was collected by filtration and washed with cold water, ethanol and diethyl ether and dried under vacuum. Yellow crystals suitable for X-ray diffraction were produced by slow diffusion of acetone into a solution of the product in methanol.

^{1}H NMR (DMSO-d_6) δ_H : 8.74 ppm (d, 2H, J = 5.48 Hz, o-*H*-pyridine), 8.09 ppm (t, 1H, J = 7.47 Hz, p-*H*-pyridine), 7.63 ppm (t, 2H, J = 6.91 Hz, m-*H*-pyridine), 6.98 ppm (m, 2H, en-N$H_{2(up)}$), 5.85 ppm (s, 6H, bound phenyl), 4.48 ppm (m, 2H, en-N$H_{2(down)}$), 2.39 ppm (m, 2H, en-CH_2), 1.88 ppm (m, 2H, en-CH_2). ^{13}C NMR (DMSO-d_6) δ_C : 154.7 ppm (o-*C*H-pyr), 139.4 ppm (p-*C*H-pyr), 126.2 ppm (*C*H-m-pyr), 85.51 ppm (*C*H-bound phenyl), 45.1 ppm (*C*H_2-en). *(Insufficient sample for a CHN analysis).*

2.14.2.7 [(η^6-biphenyl)Ru(en)(*N*-4-tertbutylpyridine)].2PF_6. [10_2PF_6]

[(η^6-biphenyl)Ru(en)H_2O].2PF_6 (**1a_2PF_6**) (100 mg, 0.160 mmol) was dissolved in 150 mL MeOH/H_2O (50/50, v/v) and 4-t-butylpyridine (524 µL, 500 mg, 3.7 mmol). The solution was stirred for 24 h, filtered and the volume of solution was reduced and ammonium hexafluorophosphate (155 mg, 9.50 mmol) added. The filtrate was then cooled to 277 K and left to crystalise. Dark golden needle-like crystals precipitated (24 mg) which were collected by filtration and washed with cold H_2O, ethanol and diethylether and dried under vacuum. Crystals suitable for X-ray diffraction were obtained from a solution of the product in methanol after slow infusion of ethylacetate.

^{1}H NMR (DMSO-d_6) δ_H :8.39 ppm (d, 2H, J = 6.7 Hz, o-*H*-4-t-bu-pyr), 7.47 ppm (d, 2H, J = 7.5 Hz, o-*H*-free phenyl), 7.41 ppm (t, 1H, J = 7.5 Hz, p-*H*-free phenyl), 7.34 ppm (d, 2H, J = 6.7 Hz, m-*H*-4-t-bu-pyr), 7.29 ppm (t, 2H, J = 7.8 Hz, m-*H*-free phenyl), 6.85 ppm (b, 2H, en-N$H_{2(up)}$), 6.291 and 6.288 ppm (very close and distinguished from [^{1}H,^{13}C] HSQC data) (m, 4H, o-*H*-bound phenyl and m-*H*-bound phenyl), 5.76 ppm (m, 1H, p-*H*-bound phenyl), 4.53 ppm (b, 2H, en-$NH_{2(down)}$), 2.35 ppm (m, 2H, en-CH_2), 1.89 ppm (m, 2H, en-CH_2), 1.26 ppm (s, 9H, (CH_3)$_3$-C-pyridine). ^{13}C NMR (DMSO-d_6) δ_C : 153 ppm (o-*C*H-4-t-buty-pyr), 137 ppm (p-*C*H-pyr), 131.5 ppm (free phenyl-*C*-C-bound phenyl), 130.3 ppm (*C*H-p-free phenyl), 128.8 ppm (*C*H-m-free phenyl), 127.5 ppm (*C*H-o-free phenyl), 123 (*C*H-m-4-t-bu-pyr), 102.5 ppm (free phenyl-C-*C*-bound phenyl), 88.8 ppm and 79.8 ppm (o/m-*C*H-bound phenyl), 79.2 ppm (p-*C*H-bound phenyl), 45 (*C*H_2-en), 34.5 ppm ((CH_3)$_3$-*C*-pyr, 29.6 ppm ((*C*H_3)$_3$-t-bu-pyr).

2.14.2.8. [(η^6-biphenyl)Ru(en)(*N*-4-methoxypyridine)].2PF_6. [11_2PF_6]

[(η^6-biphenyl)Ru(*en*)H_2O].2PF_6 (100 mg, 0.160 mmol) was dissolved in 150 mL MeoH/H_2O (50/50, v/v) and 4-methoxypyridine (376 µL, 404 mg, 3.7 mmol) was added to the solution. The solution was stirred for 48 h, filtered, and the volume of solution was reduced and ammonium hexafluorophosphate (151 mg, 9.26 mmol) was added and the solution volume further reduced under vacuum. The filtrate was then cooled to 277 K and left to crystallise. Crystals suitable for x-ray diffraction were obtained from the mother liquor. On further cooling, a dark brown solid (15 mg) precipitated. This was collected by filtration and washed with cold H_2O, ethanol and diethylether and dried under vacuum.

^{1}H NMR (DMSO-d_6): δ 8.36 ppm (d, 2H, J = 6.1 Hz, o-*H*-4-methoxypyridine), 7.53 ppm (d, 2H, J = 7.8 Hz, o-*H*-free phenyl), 7.45 ppm (t, 1H, J = 7.8 Hz, p-*H*-free phenyl), 7.36 ppm (t, 2H, J = 6.1 Hz, m-*H*-free phenyl), 7.28 ppm (d, 2H, J = 7.8 Hz, m-*H*-4-methylpyridine), 6.86 ppm (b, 2H, en-N$H_{2(up)}$), 6.2 ppm (d, 2H, J = 6.3 Hz, o-*H*-bound phenyl), 6.21 ppm (t, 2H, J = 6 Hz, m-*H*-bound phenyl), 5.88 ppm (t, 1H, J = 5.4 Hz, p-*H*-bound phenyl), 4.5 ppm (b, 2H, en-$NH_{2(down)}$), 2.35 ppm (s, 3H, CH_3-O-pyridine), 2.34 ppm (m, 2H, en-CH_2), 1.85 ppm (m, 2H, en-CH_2). Elemental analysis; calcd (%) for $C_{20}H_{25}N_3OP_2F_{12}$: C 33.62, H 3.53, N 5.88, found: C 33.28, H 3.43, N 5.88.

2.15.2.9 Synthesis of [(η^6-biphenyl)Ru(^{15}*N*,^{15}*N*′-^{15}Nen)Cl].PF_6 (1-^{15}N.PF_6)

In 50mL H_2O, [(η^6-biphenyl)$RuCl_2$]$_2$ (171 mg, 0.262 mmol) was dissolved and refluxed for 4 h. To this solution, ^{15}N-ethylenediamine.2hydrochloride (71mg, 0.524 mmol, in 5 mL H_2O, pH ca 9 by addition of KOH, to activate the en) was

added and refluxed for a further hour. The solution was filtered hot and ammonium hexafluorophosphate (419 mg, 2.889 mmol) was added. The resulting yellow solution was then lyophilised and the yellow solid extracted and recrystalised from methanol. Solution was washed with cold H_2O, ethanol and diethylether and dried under vacuum yielding a golden semi-crystalline product (56.4mg, 21.6 %). ^{1}H NMR (DMSO-d_6): δ 7.755 ppm (2H, d, J = 7.85 Hz, o-*H*-free Phenyl), 7.52 – 7.42 ppm (3H, m and p-*H*-free phenyl), 6.52 ppm (2H, d, J = 74.5 Hz, en-^{15}N*H*$_{2(up)}$), 6.14 ppm (2H, d, J = 5.96 Hz, o-*H*-bound phenyl), 5.90 ppm (1H, t, J = 5.39 Hz, p-*H*-bound phenyl), 5.8 ppm (2H, t, J = 5.7 Hz, m-*H*-bound phenyl), 4.15 ppm (2H, dm, J = 74.5 Hz, en-^{15}N*H*$_{2(down)}$), 2.30 ppm (m, 2H, ^{15}N-en-C*H*$_2$), 2.20 ppm (m, 2H, ^{15}N-en-C*H*$_2$). [^{1}H-^{15}N] 2D HMBC NMR (DMSO-d_6): δ [6.52 , -24.3], en-^{15}*NH*$_{2(up)}$, [4.15 , -24.3], en-^{15}*NH*$_{2(down)}$.

2.15 References

(1) Keeler, J. in *Understanding NMR*; John Wiley & Sons: Chichester, 2007.

(2) Hore, P. J. in *Nuclear Magnetic Resonance*; Oxford University Press: Oxford, 1995.

(3) Harris, R. K.; Mann, B. E.; in *NMR and the Periodic Table,* Academic Press; London 1978.

(4) Mason, J.; *Multinuclear NMR*, Plenum Press: New York, 1987.

(5) Gottlieb, H. E.; Kotlyar, V.; Nudelman, A. *J. Org. Chem.* **1997**, *62*, 7512.

(6) Piotto, M.; Saudek, V.; Sklenar, V. *J. Biomol. NMR* **1992**, *2*, 661.

(7) Sklenar, V.; Piotto, M.; Leppik, R.; Saudek, V. *J. Mag. Res., Series A* **1993**, *102*, 241.

(8) Neuhaus, D.; Williamson, M. P. in *The Nuclear Overhauser Effect in Structural and Conformational Analysis*, VCH-Publishers: New York,1989.

(9) Dykstra, R. W.; Harrison, A. M. *J. Mag. Res.* **1982**, *46*, 338.

(10) *CRC Handbook of Chemistry and Physics*; 82nd ed.; CRC Press: London.

(11) Gaemers, S.; Van Slageren, J.; O'Connor, C. M.; Vos, J. G.; Hage, R.; Elsevier, C. J. *Organometallics* **1999**, *18*, 5238.

(12) Germann, M. W.; Aramini, J. M.; Vogel, H. J. *J. Am. Chem. Soc.* **1994**, *116*, 6971.

(13) Aramini, J. M.; Vogel, H. J. *J. Am. Chem. Soc.* **1994**, *116*, 1988.

(14) Xiaoming, X.; Matsumura-Inoue, T.; Mizutani, S. *Chem. Lett.* **1997**, 241.

(15) Predieri, G.; Vignali, C.; Denti, G.; Serroni, S. *Inorg. Chim. Acta* **1993**, *205*, 145.

(16) Brevard, C.; Granger, P. *J. Chem. Phys.* **1981**, *75*, 4175.

(17) Marzin, C.; Budde, F.; Steel, P. J.; Lerner, D. *New J. Chem.* **1987**, *11*, 33.

(18) Burgstaller, A.; Ebert, H.; Voitlaender, J. *Hyperfine Interact.* **1993**, *80*, 1015.

(19) Orellana, G.; Kirsch-De Mesmaeker, A.; Turro, N. J. *Inorg. Chem.* **1990**, *29*, 882.

(20) Emel'yanov, V. A.; Fedotov, M. A.; Belyaev, A. V. *Zh. Neorg. Khim.* **1993**, *38*, 1842.

(21) Braunstein, P.; Rose, J.; Granger, P.; Richert, T. *Magn. Reson. Chem.* **1991**, *29*, S31.

(22) Buhl, M.; Gaemers, S.; Elsevier, C. J. *Chem.--A Eur. J.* **2000**, *6*, 3272.

(23) Burgstaller, A.; Voitlaender, J.; Ebert, H. *J. Phys.: Condens. Matter* **1994**, *6*, 8335.

(24) Carter, J. C.; Good, M. L. *J. Mol. Struct.* **1980**, *58*, 415.

(25) De Marco, M.; Coffey, D.; Tallon, J.; Haka, M.; Toorongian, S.; Fridmann, J. *Physical Review B: Condensed Matter and Materials Physics* **2002**, *65*, 212506/1.

(26) Dykstra, R. W.; Harrison, A. M. *J. Mag. Res.* **1981**, *45*, 108.

(27) Han, Z. H.; Mohottala, H. E.; Budnick, J. I.; Hines, W. A.; Klamut, P. W.; Dabrowski, B.; Maxwell, M. *J. Phys.: Condens. Matter* **2006**, *18*, 2273.

(28) Ishida, K.; Kawasaki, Y.; Kitaoka, Y.; Asayama, K.; Nakamura, H.; Flouquet, J. *Physical Review B: Condensed Matter and Materials Physics* **1998**, *57*, R11054.

(29) Ooms, K. J.; Wasylishen, R. E. *J. Am. Chem. Soc.* **2004**, *126*, 10972.

(30) Brevard, C.; Granger, P. *Inorg. Chem.* **1983**, *22*, 532.

(31) Gray, J. C.; Pagelot, A.; Collins, A.; Fabbiani, F. P. A.; Parsons, S.; Sadler, P. J. *Eur. J. Inorg. Chem.* **2009**, 2673.

(32) Kanu, A. B.; Dwivedi, P.; Tam, M.; Matz, L.; Hill, H. H., Jr. *J. Mass Spectrom.* **2008**, *43*, 1.

(33) Pringle, S. D.; Giles, K.; Wildgoose, J. L.; Williams, J. P.; Slade, S. E.; Thalassinos, K.; Bateman, R. H.; Bowers, M. T.; Scrivens, J. H. *International Journal of Mass Spectrometry* **2007**, *261*, 1.

(34) Stach, J.; Baumbach, J. I. *Inter. J. Ion Mob. Spectro.* **2002**, *5*, 1.

(35) Williams, J. P.; Bugarcic, T.; Habtemariam, A.; Giles, K.; Campuzano, I.; Rodger, P. M.; Sadler, P. J. *J. Am. Soc. Mass Spectrom.* **2009**, *20*, 1119.

(36) Williams, J. P.; Phillips, H. I. A.; Campuzano, I.; Sadler, P. J. *J. Am. Soc. Mass Spectrom.* **2010**, *21*, 1097.

(37) Williams, J. P.; Lough, J. A.; Campuzano, I.; Richardson, K.; Sadler, P. J. *Rapid Commun. Mass Spectrom.* **2009**, *23*, 3563.

(38) Nobelprize.org 2010; accessed 30 March 2010.

(39) Williams, D. H.; Fleming, I. in *Spectoscopic Methods in Organic Chemistry*; Fifth ed.; McGraw-Hill Publishing Company: Glasgow, 1995.

(40) Harwood, L. M.; Moody, C. J.; Percy, J. M. in *Experimental Organic Chemistry*; Second ed.; Blackwell Science Ltd.: Oxford, 1999.

(41) Rodger, A.; Nordén, B. in *Circular Dichroism and Linear Dichroism*; Oxford University Press: Oxford, 1997.

(42) Image from: http://www.softwareforeducation.com/electronics/notes/A2/Antenna/polarisation.php

(43) Snyder, R. A. http://en.wikipedia.org/wiki/File:Circularly_pol.png accessed 26 March 2010.

(44) Houk, R. S.; Fassel, V. A.; Flesch, G. D.; Svec, H. J.; Gray, A. L.; Taylor, C. E. *Anal. Chem.* **1980**, *52*, 2283.

(45) Olivares, J. A.; Houk, R. S. *Anal. Chem.* **1985**, *57*, 2674.

(46) Agilent Technologies Inc, ICP-MS users manual, 2005.

(47) Förster, T. *Annalen der Physik* **1948**, *437*, 55.

(48) Stryer, L.; Haugland, R. P. *Proc. Natl. Acad. Sci. U. S. A.* **1967**, *58*, 719.

(49) Wu, P.; Brand, L. *Anal. Biochem.* **1994**, *218*, 1.

(50) Gryczynski, Z.; Gryczynski, I.; Lakowicz, J. R. In *Molecular Imaging*; Ammasi, P., Richard, N. D., Eds.; American Physiological Society: San Diego, 2005.

(51) Murata, S.; Mizumura, Y.; Hino, K.; Ueno, Y.; Ichikawa, S.; Matsuda, A. *J. Am. Chem. Soc.* **2007**, *129*, 10300.

(52) Hillisch, A.; Lorenz, M.; Diekmann, S. *Curr. Opin. Struct. Biol.* **2001**, *11*, 201.

(53) Takahara, P. M.; Rosenzweig, A. C.; Frederick, C. A.; Lippard, S. J. *Nature* **1995**, *377*, 649.

(54) Jamieson, E. R.; Jacobson, M. P.; Barnes, C. M.; Chow, C. S.; Lippard, S. J. *J. Biol. Chem.* **1999**, *274*, 12346.

(55) Todd, R. C.; Lippard, S. J. *J. Inorg. Biochem.* **2010**, *104*, 902.

(56) Wozniak, A. K.; Schroder, G. F.; Grubmueller, H.; Seidel, C. A. M.; Oesterhelt, F. *Proc. Natl. Acad. Sci. U. S. A.* **2008**, *105*, 18337.

(57) Wozniak Anna, K.; Schroder Gunnar, F.; Grubmuller, H.; Seidel Claus, A. M.; Oesterhelt, F. *Proc. Natl. Acad. Sci. U. S. A.* **2008**, *105*, 18337.

(58) Rothwell, P. J.; Berger, S.; Kensch, O.; Felekyan, S.; Antonik, M.; Wohrl, B. M.; Restle, T.; Goody, R. S.; Seidel, C. A. M. *Proc. Natl. Acad. Sci. U. S. A.* **2003**, *100*, 1655.

(59) M. J. Frisch, G. W. T., H. B. Schlegel, G. E. Scuseria, M. A. Robb, J. R. Cheeseman, J. A. Montgomery, Jr., T. Vreven, K. N. Kudin, J. C. Burant, J. M. Millam, S. S. Iyengar, J. Tomasi, V. Barone, B. Mennucci, M. Cossi, G. Scalmani, N. Rega, G. A. Petersson, H. Nakatsuji, M. Hada, M. Ehara, K. Toyota, R. Fukuda, J. Hasegawa, M. Ishida, T. Nakajima, Y. Honda, O. Kitao, H. Nakai, M. Klene, X. Li, J. E. Knox, H. P. Hratchian, J. B. Cross, C. Adamo, J. Jaramillo, R. Gomperts, R. E. Stratmann, O. Yazyev, A. J. Austin, R. Cammi, C. Pomelli, J. W. Ochterski, P. Y. Ayala, K. Morokuma, G. A. Voth, P. Salvador, J. J. Dannenberg, V. G. Zakrzewski, A. D. Daniels, O. Farkas, A. D. Rabuck, K. Raghavachari and J. V. Ortiz.; Guassiam 03w. Pittsburgh, GA, 2003.

(60) Vlcek, A.; Zalis, S. *Coord. Chem. Rev.* **2007**, *251*, 258.

(61) Ernzerhof, M.; Scuseria, G. E. *J. Chem. Phys.* **1999**, *110*, 5029.

(62) Ernzerhof, M.; Perdew, J. P.; Burke, K. *Int. J. Quantum Chem.* **1997**, *64*, 285.

(63) Hay, P. J.; Wadt, W. R. *J. Chem. Phys.* **1985**, *82*, 270.

(64) Zelonka, R. A.; Baird, M. C. *Can. J. Chem.* **1972**, *50*, 3063.

(65) Zelonka, R. A.; Baird, M. C. *J. Organomet. Chem.* **1972**, *35*, C43.

(66) Morris, R. E.; Aird, R. E.; Murdoch, P. d. S.; Chen, H.; Cummings, J.; Hughes, N. D.; Parsons, S.; Parkin, A.; Boyd, G.; Jodrell, D. I.; Sadler, P. J. *J. Med. Chem.* **2001**, *44*, 3616.

Chapter 3

Kinetics and Mechanism of N-H/D Exchange on

$[Ru(II)(\eta^6\text{-bip})(en)Cl]^+$

Chapter 3

Kinetics and mechanism of N-H/D exchange on $[Ru(II)(\eta^6\text{-bip})(en)Cl]^+$

3.1 Introduction

Ruthenium (η^6-arene) half-sandwich, piano-stool complexes (Figure 3.1) in which the arene, leaving group and bidentate ligand can be varied to tune the reactivity of the complex have shown good anti-cancer activity *in vitro* and *in vivo*[1]. Structure activity relationships between the cytotoxicity and the increasing size of the arene and the ability of the Z group to undergo hydrolysis have been reported[2].

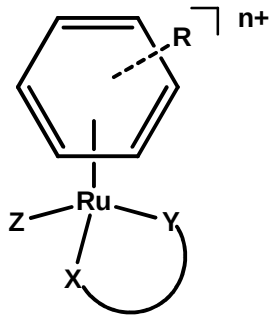

Figure 3.1. The basic "piano-stool" geometry of the Ru (II) η^6-arene complexes.

Work in this field has included extending the arene from para-cymene (p-cym), to biphenyl (bip), dihydroanthracene (DHA) and tetrahydroanthracene (THA). X,Y is a bidentate ligand such as ethylenediamine (en), 2,2'-bipyridine (bipy) or acetylacetonate (acac). Z is a monodentate ligand such as chloride, water or bromine.

The mechanism of cytotoxic action of $[Ru(\eta^6\text{-bip})enCl]^+$ (**1**) is believed to involve (i) binding of the ruthenium to N7 of guanine (the most nucleophilic site on DNA),[3] (ii) intercalation of the extended arene system into the base stacking of DNA[4] and (iii) hydrogen bonding that has been shown to occur between the exocyclic oxygen on C6 of the purine ring of guanine and protons from the amine of the ethylenediamine ligand (Figure 3.2)[5,6]

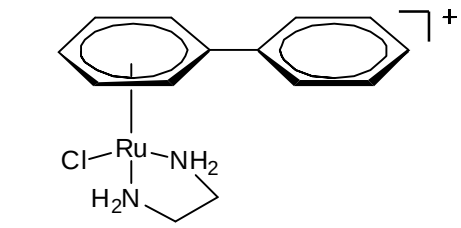

a

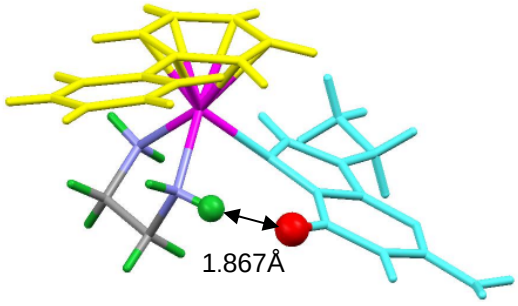

b

Figure 3.2. a) Structure of **1** $[Ru(\eta^6\text{-Bip})enCl]^-$ (the counterion PF_6^- is not shown here for clarity). b) X-ray crystal structure of 9-Et-guanine bound via N7 to $[(\eta^6\text{-bip})Ru(en)]^{2+}$ (the counter ions 2 PF_6^- and the solvent molecules CH_3OH are excluded for clarity). The 2 atoms involved in hydrogen bonding are shown as green and red balls here[6]. *Colour scheme: 9-ethylguanine: cyan, ruthenium: pink, biphenyl: yellow. Green: hydrogen from the ethylenediamine, purple: nitrogen of ethylenediamine, grey: carbon of ethylenediamine and red: oxygen of the carbonyl carbon 6 on the guanine residue.*

Changing the ethylenediamine ligand for an amine without any amino hydrogens (e.g.: *N,N'*-tetramethylethylenediamine) removed any cytotoxic properties[7]. This provides insight into the importance of the H-bonding between guanine's exocyclic oxygen and the hydrogens on the ethylenediamine ligand.

Further evidence of this is seen with the introduction of an ethyl group on the nitrogen, (i.e. *N*-Et-en)[8] to yield four diastereoisomers of the product $[(\eta^6\text{-bip})Ru^*(N^*\text{-Et-en})Cl]^+$ (where Ru and N are both chiral). When in aqueous solutions, the chlorido and aqua complexes favour the less sterically hindered stereoisomer, $(R^*_{Ru}R^*_N)$ **5A** over the more sterically hindered $(S^*_{Ru}R^*_N)$ **5B** (Figure 3.3a) by 73.7:26.3 and by 77:23 for the chlorido and aqua adducts, respectively. However, when aqueous solutions of enantiomerically pure complexes are prepared, racemisation to give the ratios above readily occurs in solution. The mechanism of interconversion between the stereoisomers has yet to be investigated.[8]

Interestingly, when the racemic mixture is reacted with 9-ethylguanine, conversion to the more sterically hindered $(S^*_{Ru}R^*_N)$ isomer **5B-9Et-Guanine** is observed in which 95% of the product is now in this form (Figure 3.3b). One of the driving forces behind this is the favourable H-bonding between the exocylic oxygen on the guanine and the amino protons on the ethylenediamine which this configuration allows.

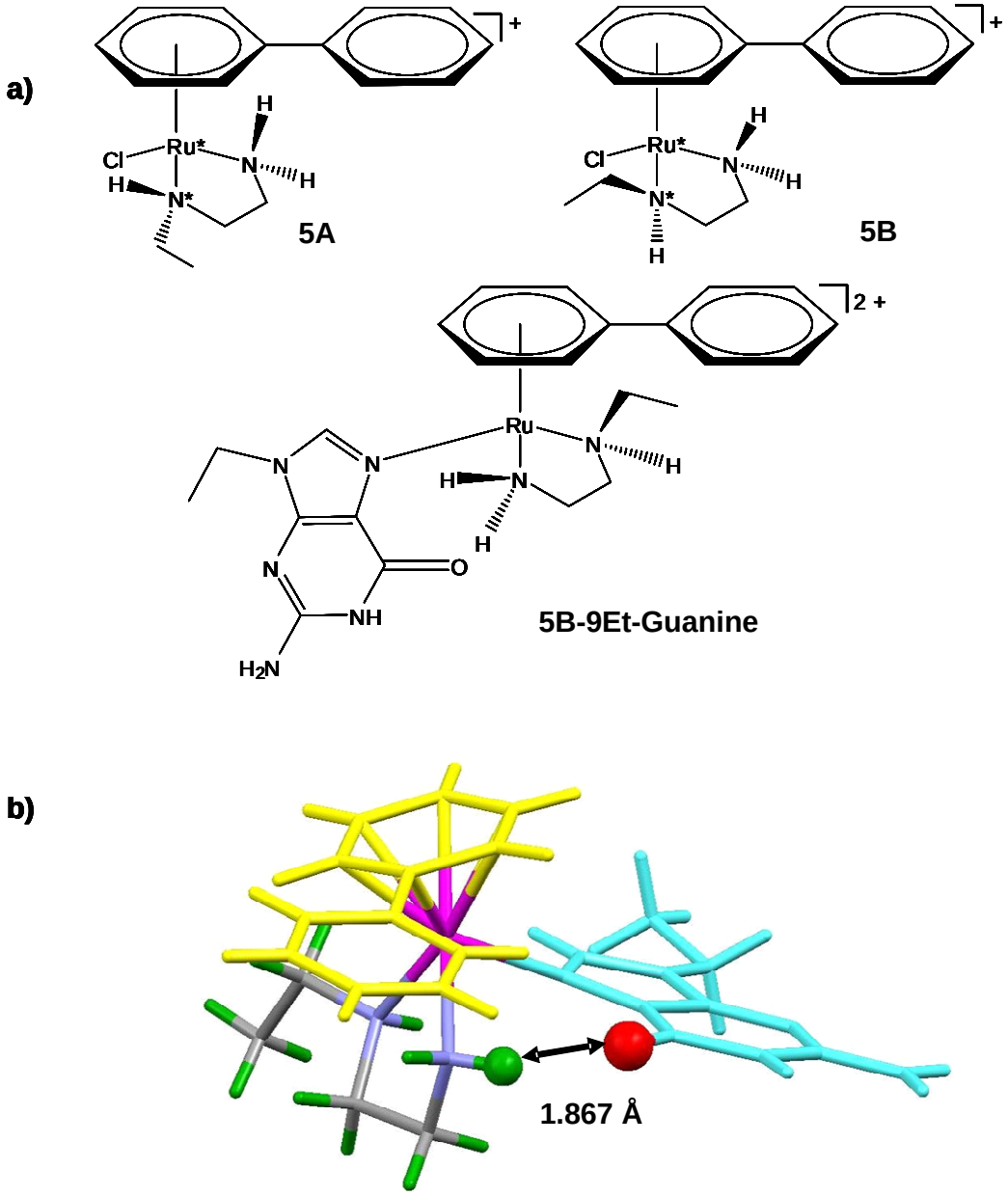

Figure 3.3. a) Structure of complex **5A** ($R^*_{Ru}R^*_N$ isomer), **5B** ($S^*_{Ru}R^*_N$) and **5B-9Et-Guanine** (S^*_{Ru},R^*_N)-[(η^6-bip)Ru(*N*7-9EtG)(Et-en)]$^{2+}$ counterions of PF_6^- have been excluded b) Stick model of the crystal structure of **5B-9Et-Guanine** showing the hydrogen bonding between the ethylenediamine and the exocyclic oxygen on the 9-ethylguanine residue.[8] (The counterions of 2.PF_6^- and the solvent molecule CH_3OH are omitted for clarity). *Colour scheme: 9-ethylguanine, cyan; ruthenium, pink; biphenyl, yellow. The 2 atoms involved in hydrogen bonding are shown as balls. Green, hydrogen; red, oxygen of the guanine residue. The distance between the two atoms is also highlighted.*

The aim of this Chapter is to investigate the mechanism of inversion of chiral molecules such as **5A** and **5B**, and the factors that allow for inversion of stereochemistry to take place. Are ruthenium-nitrogen and/or ruthenium chloride bond breaking, or other, processes occurring? Given that **5A** and **5B** rapidly interconvert, mechanistic studies would prove very difficult on these molecules. To overcome this, the exchange of the protons on the nitrogens of the ethylenediamine ligands of $[(\eta^6\text{-bip})Ru(en)Cl]^+$ (**1**) with deuterium was studied in D_2O solution by NMR.

To date, studies on hydrogen exchange rates on nitrogens have been largely carried out for proteins, using either mass spectrometry,[9,10] NMR[11,12] or IR[13]. For proteins, the rates of exchange in D_2O solutions have been used to study 3^o and 4^o structures as amide protons on the surface exchange much more rapidly than those in the centre of the protein[14]. For amides, there is a lone pair of electrons on the nitrogen atom of the amide which facilitates the exchange of protons for deuterons. This is not the case with the complexes investigated here as the lone pair on the nitrogen is involved in a dative bond to ruthenium(II).

Other N-H exchange mechanisms studied recently[15] include solution based "Nitrogen Inversion/Rotation" (NIR), where tertiary amines undergo stereo inversion via pyramidal inversion (umbrella type rotation) around the nitrogen via the lone pair on the nitrogen "moving" from one face to another (Figure 3.4).

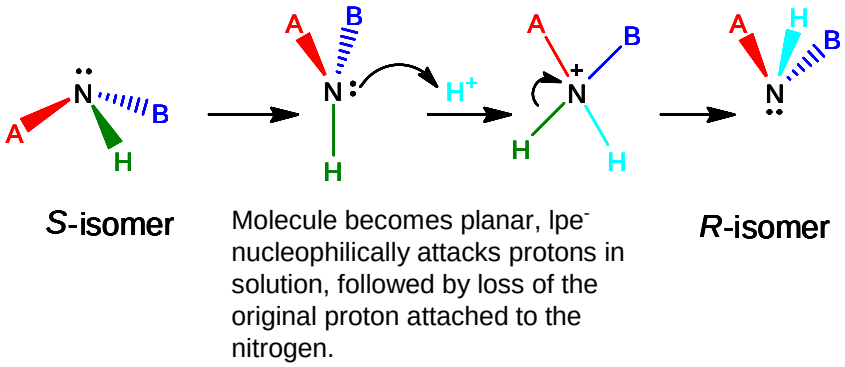

Figure 3.4. The mechanism of stereocentre inversion on nitrogens where lone pair electons (lpe$^-$) are available to assist inversion. This mechanism is often referred to as 'umbrella inversion' or 'nitrogen inversion rotation' (NIR) .

Research by Raymond *et al*[15] investigated the activation energy of this inversion using chiral trapping agents. The activation energy was found to be between 10 and 17 kcal mol^{-1} for the variety of amines investigated. While this provides some thermodynamic detail, it is only relevant for nitrogens where the lone-pair of electrons is available to accept protons in solution and participate in the mechanism of inversion.

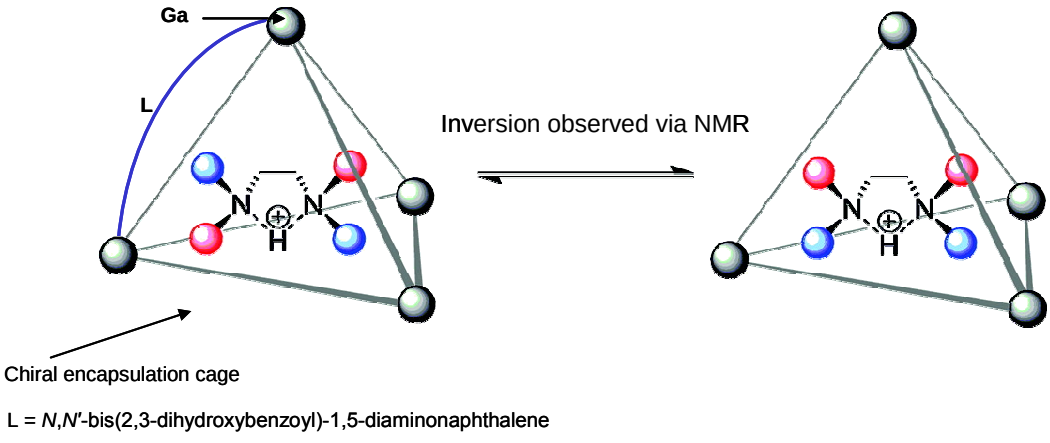

Figure 3.5. Monitoring the activation energy for NIR (pyramidal inversion of the tetrahedral shape of NR_3 molecules). *Adapted from work by K. N. Raymond*[15].

However, in the systems investigated in this thesis the amines are attached to metals as ligands. The lone pair of electrons on the nitrogen atoms is now involved in metal-ligand bond formation and therefore cannot partake in inversion processes. The lack of availability of the lone pair of electrons also has an affect in the chemistry of the ligand as will be discussed below.

3.1.1 pK_a changes

The pK_a values of free amines are well studied and many tables have been published.[16] However, when these are bound through the nitrogen to metal atoms, there is a noticeable effect on the pK_a values due to the change of electronic properties of the nitrogen. This leads to a more acidic pK_a value (when comparing N^+HR_3 to M-NHR_2). As the nitrogen donates more of its electronic density to the metal, the N-H bond is weakened and so the pK_a of $HR_2N \rightarrow R_2N^-$ is reduced (when viewing the properties of the ligand alone). This acidification is indicative of the strength of the Ru-N bond, in which the more acidic the complex (the lower the pK_a value) the weaker the N-H bond and the stronger the Ru-N bond. This increase in acidity of ligands upon coordination to metal centres is key to many chemical reactions (not all beneficial) including the formation of hydroxido form of cis-platin, [*Cis*-diamminodihydroxyplatinum(II)]. This is an inhibitory factor to the potency of the cisplatin; in this case the pK_a of the water molecule drops from 15.7 to 5.24 upon binding to the platinum and leading to the formation of the less cytotoxic hydroxido complex and the hydroxido bridged dimer at neutral pH.

To date, and after extensive literature searches, the only information available on NH/ND exchange rates and mechanisms for am(m)ino ligands on metal ions appears to be for Co(III) complexes. This thesis describes the first extensive investigation, as far as the author is aware, into the mechanism of inversion of stereochemistry, the effects of pH, ionic strength and temperature on the exchange rates. In the following paragraphs a brief survey of the literature currently available is described.

3.1.2 Catalysts

Xiao[17], Noyori[18,19], Wills[20,21] and co-workers have studied ruthenium catalytic asymmetric transfer hydrogenation reactions (Figure 3.6) in which a proton is transferred from the amine to a carbonyl group on a ketone asymmetrically to form a chiral alcohol.

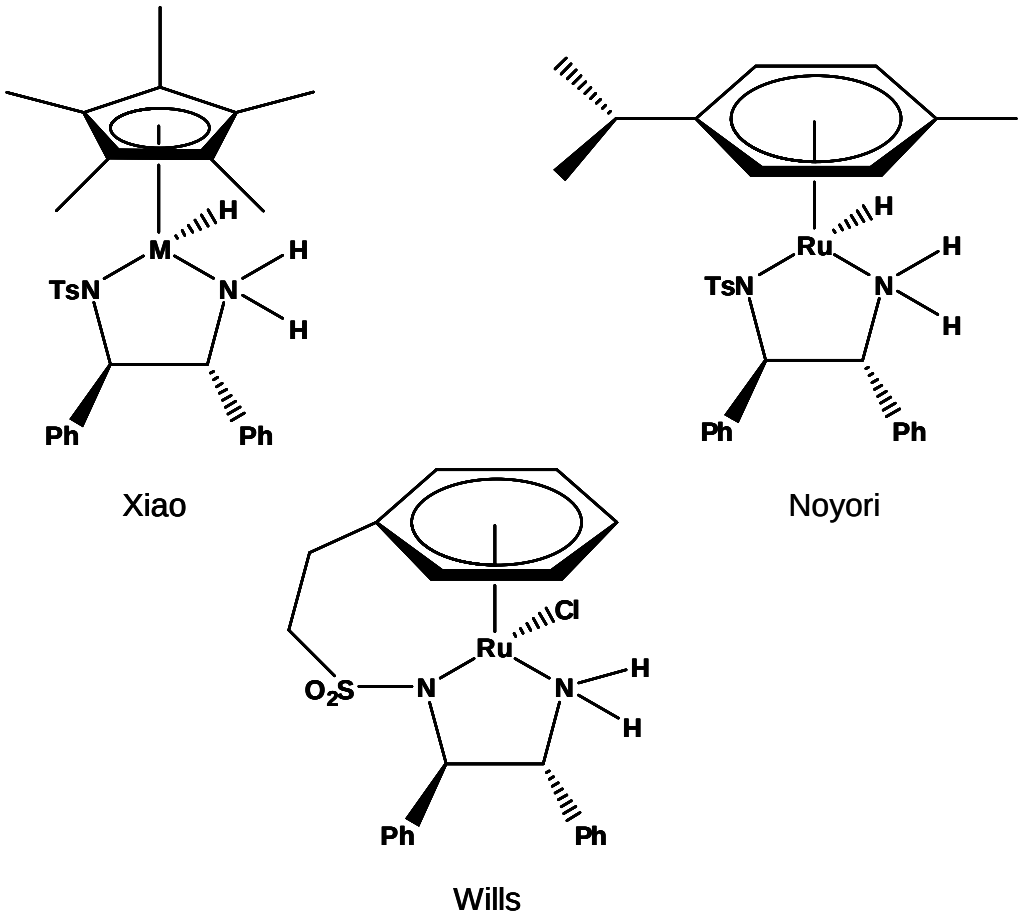

Figure 3.6. Examples of Ru(II) asymmetric hydrogenation catalysts from each of the groups mentioned.

The catalytic mechanism for all these complexes is similar to that shown in Scheme 3.1, where the intermediate product is a 16-electron species which has been isolated and crystallised.

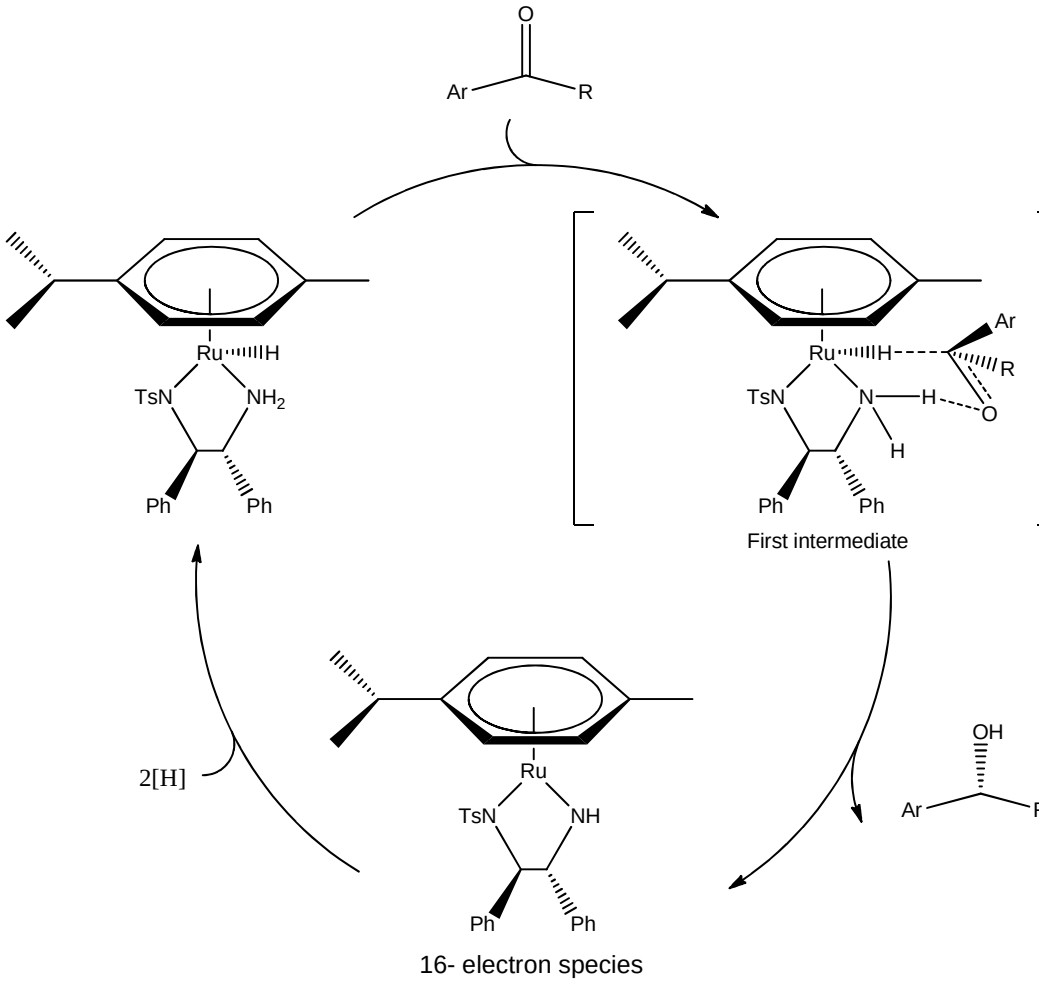

Scheme 3.1. A catalytic cycle for asymmetric hydrogenation by a Ru(II) η^6-arene complex, with the 16-electron species indicated.[22]

In this cycle, there is a concerted removal of hydrogen from both the amine and the hydride to hydrogenate the ketone. Of real interest here is the formation of a stabilised 16-electron species, which in the case of the complex [Ru(η^6-p-cym)((*S,S*)-*N*-*p*-toluenesulfonyl-1,2-diphenylethylenediamine)] has been characterised by X-ray crystallography[23]. This may provide insight into a possible mechanism for the stereo-centre inversions that are observed for complexes **5A** and **5B**.

In work of Fryzuk[24], the intramolecular transfer of protons through stereo-inversion of ruthenium (II) amidophosphine complexes as a proton exchanges intramolecularly between two amines has been discussed. However no suggestions were made as to a possible mechanism, or the effects of other ligands on the exchange rate.

Work by Morris *et al.*[25] has also involved investigation of intramolecular transfer of protons in organometallic complexes. Shipman and co-workers have described an example of organic synthesis using metals to control pyramidal inversion rates.[26,27] This is done by "locking" the lone pair of the nitrogen into the dative bond with the metal, thereby preventing nitrogen inversion occurring.

To date, no studies of N-H/D exchange for amino protons on ruthenium (II) ethylenediamine complexes have been reported. However, there is much published on cobalt(III) complexes (*vide infra*). Since both metals have d^6 low-spin electronic structures, some comparisons can be made. It was with this lack of previous studies in mind that the studies presented in this thesis were undertaken.

3.1.3 Cobalt(III) complexes

One of the earliest papers on Co(III) complexes was published by Yoneda *et al.* in 1981.[28] In this work, magnetic anisotropy among the amine protons on ethylenediamine ligands on cobalt(III) ions was reported. This effect was also observed for ammine groups on pentamminecobalt(III) complexes[29,30]. They noted a difference in the exchange rates of protons which are on the same nitrogen but pointing in different directions.

Work of Fujita et al[31] on the octahedral complex of $[Co(acac)_2(Ph\text{-}en)]^+$ (acac = 2,4 –pentanedionate ion, Ph-en = *N*-phenylethylenediamine) showed that inversion of chiral nitrogen centres and chiral cobalt centres occurred in basic solutions (Figure 3.7). Similar to the present study, they followed the proton exchange on the amines by NMR spectroscopy. They found that the inversion rates increased in basic conditions and were slower than the proton exchange rates on the free ligands. It was proposed that the N-phenylethylenediamine ligands on the Co(III) ion are stabilised by $(p\text{-}p)_\pi$ conjugation and this must lower the activation energy of epimerization (compared to Me-en complexes). Also they proposed that proton loss is essential in the activation process for stereochemical inversion of the nitrogen.

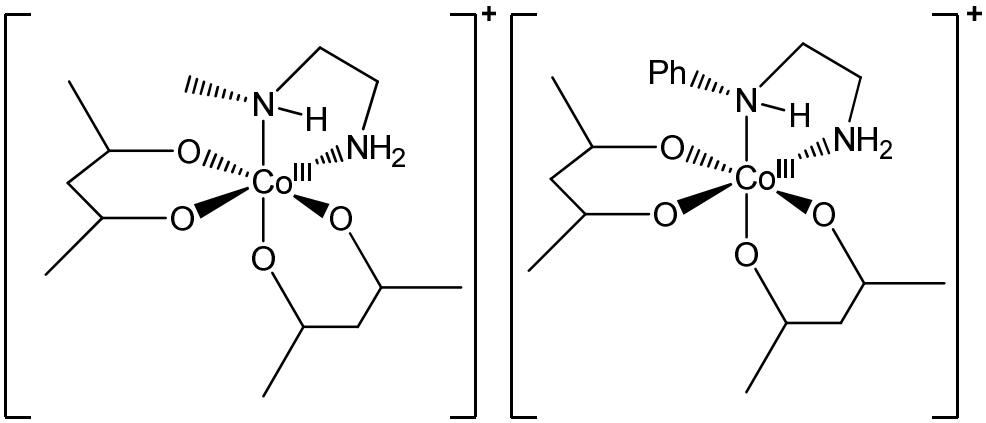

[Co(acac)$_2$(Me-en)]$^+$ **[Co(acac)$_2$(Ph-en)]$^+$**

Figure 3.7. The two complexes studied by Fujita[31]; these complexes not only undergo proton exchange but also racemisation in solution.

$[Co(ox)_2(Me_3\text{-}en)]^-$ undergoes proton exchange an order of magnitude faster than $[Co(acac)_2(Me_3\text{-}en)]^+$. This is believed to arise from the effect of the ligands on the metal, in this case because acac forms a chelate ring with delocalised π-electrons. The effects of the neighbouring ligands have been noted

in many other papers, especially work on $[Co(en)_2AB]^{n+}$ complexes. Work by Yoneda et al, has shown that AB ligands can induce a *trans*-effect on the exchange rates of amines[32]. In other work by the same authors,[33] a kinetic isotope effect on the exchange rates was observed, providing further evidence of proton loss being the rate limiting step on cobalt(III) complexes.

House[34] has reviewed many of the observations on the exchange of amine protons on cobalt. It was noted that the exchange rates were much slower than for free amines and therefore coordination often makes these exchanges observable. Further comments here[34] into the catalytic effects of hydroxide ions and observation of the kinetic isotope effect add weight to the theory that exchange was due to a mechanism of proton abstraction prior to inversion of the stereo centres on the nitrogen.

From the detailed discussion above, two potential mechanisms of exchange of protons on metal-(en) complexes emerge. The Ru(II) catalysts show inversion on the metal centre by loss of a leaving group from the metal, whereas the cobalt(III) exchange mechanism is believed to involve proton abstraction. This raises the question as to whether racemisation of $[(\eta^6\text{-bip})Ru(Et\text{-en})Cl]^+$ stereoisomers in solution is due to stereochemical inversion at the Ru centre via a 16-electron intermediate, or to inversion at the nitrogen centre in a similar manner to that seen for cobalt(III) complexes?

3.1.4 Aim

The aim of this Chapter is to investigate the exchange rates of protons for deuterons on the amines of the ethylenediamine ligand on $[(\eta^6\text{-bip})Ru(en)Cl]^+$ complexes in 154 mM NaCl solutions in D_2O, in order to elucidate the mechanism of proton exchange and infer the mechanism of stereocentre inversion. To determine this, measurements of proton/deuteron exchange rates were carried out at various temperatures, ionic strengths and pH values, using NMR spectroscopy to monitor decreases in N-H signals with time. To the author's knowledge, this is the first time a comprehensive analysis of proton exchange mechanisms on ruthenium-arene complexes has been reported. Understanding of this mechanism is crucial to control the synthesis of chiral metal molecules and of the epimerisation of complexes in soluition.

3.2 Results

3.2.1 Synthesis and Characterisation

This work was concerned with the studies of $[(\eta^6\text{-bip})Ru(en)Cl].PF_6$ **(1-PF_6)** its deuterated amine version $[(\eta^6\text{-bip})Ru(N,N'\text{-}N^2H_2CH_2CH_2N^2H_2)Cl].PF_6$ (**1D_PF_6**) and $[(\eta^6\text{-bip})Ru(en)(\underline{N}\text{-pyr})].2PF_6$ (**6_2PF_6**) (Figure 3.8). The latter was studied to provide insight into the assignment of the non-equivalent NH_a and NH_b peaks in the ^{1}H NMR spectrum of **1** using NOE peaks between these protons and pyridine protons.

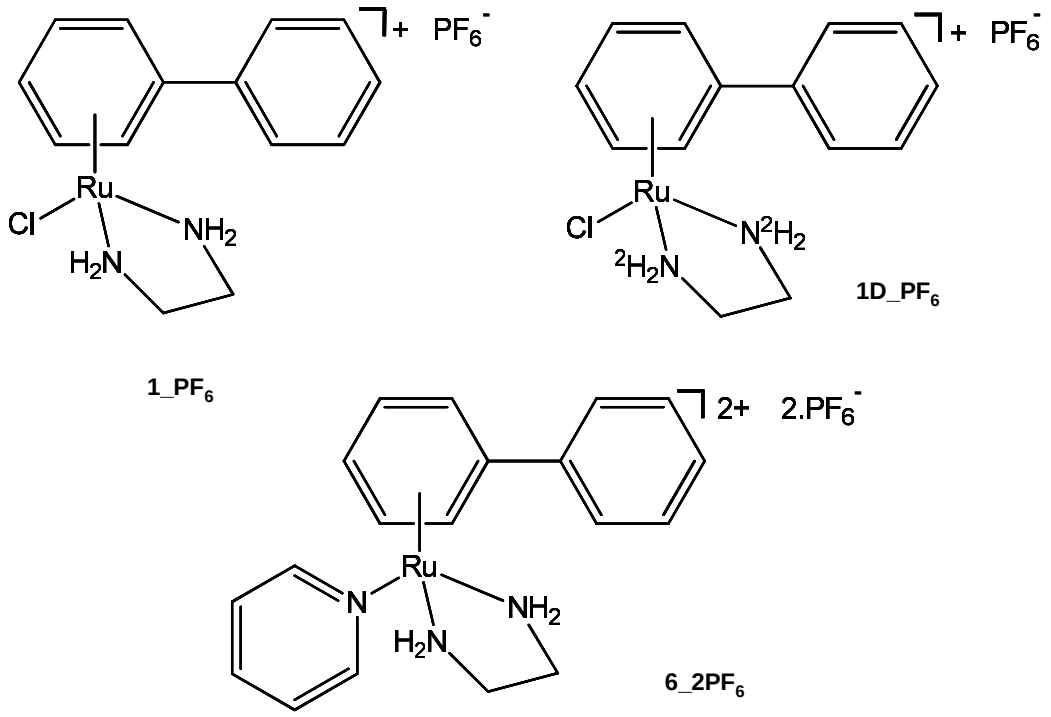

Figure 3.8. The complexes studied in this chapter.

3.2.2 NMR of $[(\eta^6\text{-bip})Ru(en)Cl]PF_6$ (1-PF_6)

NMR was carried out as described in Chapter 2, *c.f.* **§2.1**. The ^{1}H NMR spectrum of **1-PF_6** in DMSO-d_6, gives two distinct N-H peaks labelled N-H_a and N-H_b (Figure 3.9). This was also observed in D_2O and MeOD-d_4 and has been

previously observed in work by Yoneda[32] and others when investigating cobalt(III) complexes.

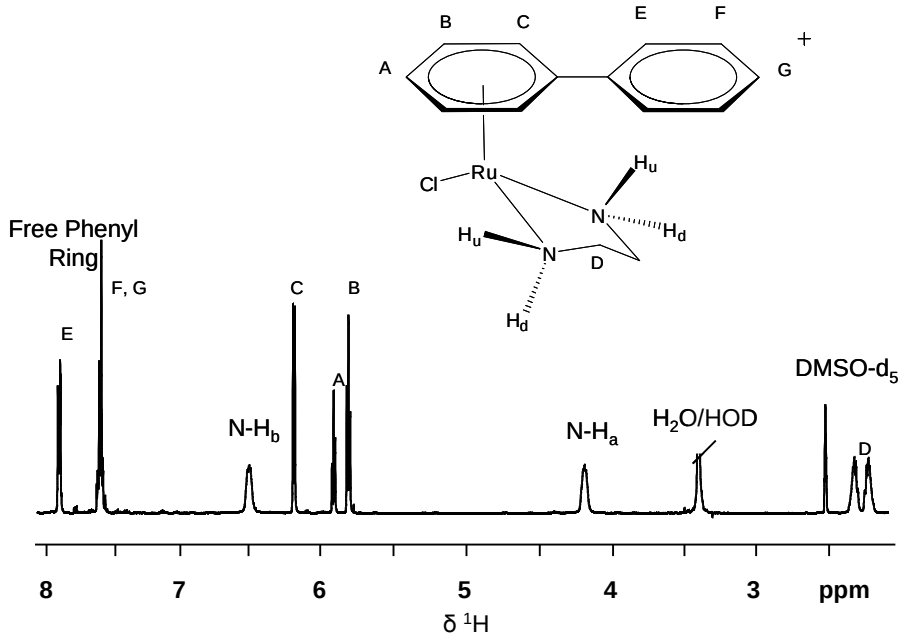

Figure 3.9. ^{1}H NMR of **1** in DMSO-d_6 at 298 K, with signals assigned. Two distinct N-H peaks are present labelled as N-H_a (4.17 ppm) and N-H_b (6.47 ppm) as the spatial arrangement of these protons was yet to be defined. This magnetic anisotropy is believed to be a result of the effects of the ring current from the biphenyl bound to the arene.

Of interest to note when looking at Figure 3.9, is the shift of the N-H_b peaks downfield of the normal region for the aromatic protons. This split in N-H peaks leads to a complex multipet for the C-*H* peaks on the ethylenediamine backbone, due to each proton on the carbon being non-equivalent and coupled with the different N-*H* protons also. To confirm these broad peaks are amino protons, 2D NMR was preformed and showed that H_a and H_b are bonded to the same nitrogen (Figure 3.10).

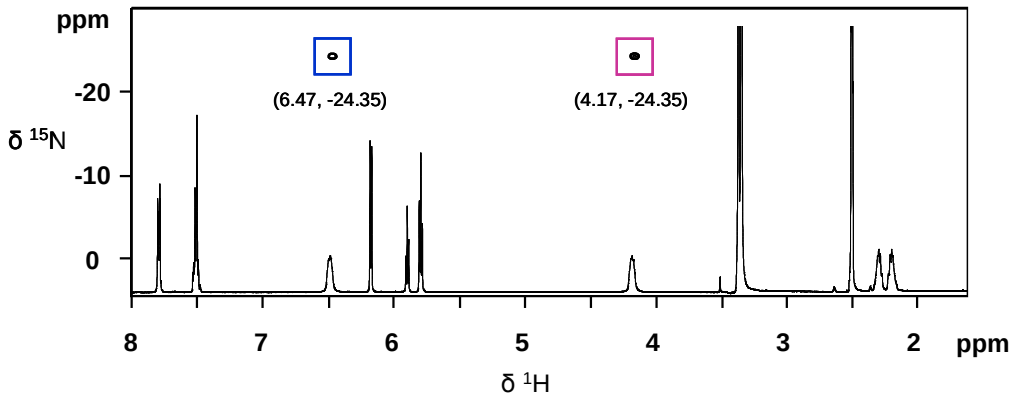

Figure 3.10. [^{1}H, ^{15}N] 500 MHz NMR of **1** in DMSO at 298K, confirming the presence of NH peaks at ca. 4 and 6 ppm and that these protons are on the same nitrogen. The difference in shifts is as a result of the ring current from the aromatic ring on the ruthenium.

To identify the location of each amino proton relative to the biphenyl ligand, the pyridine adduct [(η^6-bip)Ru(en)pyr]2PF$_6$ (**6_2PF$_6$**) was synthesised. This was to allow NOEs to be detected between the NH protons and the pyridine ring to provide specific NH$_a$ and NH$_b$ assignments.

3.2.3 Synthesis of [(η^6-bip)Ru(en)pyr]2PF$_6$ (6_2PF$_6$)

3.2.3.1 X-ray Crystal Structure

Yellow crystals of **2-2PF$_6$** were obtained. Diffraction data were collected by Prof. Simon Parsons (University of Edinburgh) using a Brüker Smart Apex CCD diffractometer equipped with an Oxford Cryosystems low-temperature device operating at 150 K. Absorption corrections for all data sets were preformed with the multiscan procedure SADABS.[35] The structure of **6_2PF$_6$** was solved by

using direct methods (DIRDIF-96)[36] and CRYSTALS used for refinement of the structure, based on data from 34269 reflections (Figure 3.11).

The x-ray crystallographic data of selected bond lengths and angles are listed in Tables 3.1 and 3.2) were obtained. Interestingly the crystal structure does not show any π-stacking between the pyridine ring and the unbound phenyl from biphenyl.

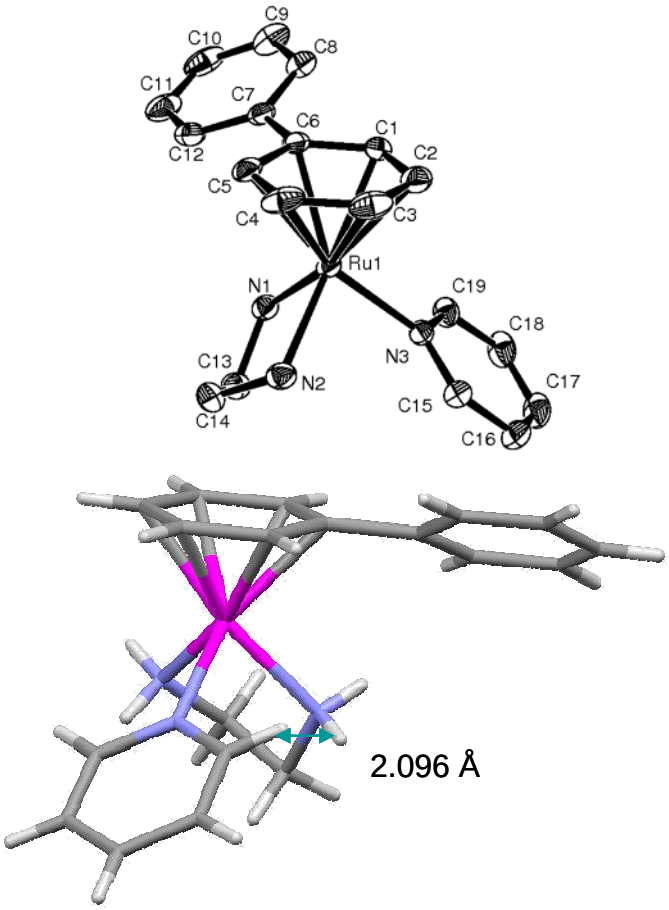

Figure 3.11. Complex **6** [(η^6-biphenyl)Ru(en)*N*-pyridine)]$^{2+}$. The crystal structure is shown here in ellipsoidal (50% probability) representation and the lower figure is a stick model. The distance between the downward pointing proton of the amine on the ethylene diamine and the ortho-proton on the pyridine ring is 2.096Å in the crystal structure. (PF_6^- counterions have been omitted for clarity)

Table 3.1. Crystallographic data and structure refinement details for **6_2PF$_6$.**

	6_2PF$_6$
Formula	$C_{19}H_{23}F_{12}N_3P_2Ru$
Molar mass	684.41
Crystal system	Triclinic
Crystal size /mm	0.61 × 0.36 × 0.20
Space group	P-1
Crystal	Yellow Tablet
a / Å	9.9090(3)
b / Å	10.2134(3)
c / Å	13.3074(4)
α / deg	93.232(2)
β / deg	102.160(2)
γ / deg	113.464(2)
T / K	150
Z	2
R [F > 4σ (F)][a]	0.0307
R_w [b]	0.0743
GOF[c]	1.0273
Δρ max and min, / eÅ^{-3}	0.84, -0.70

[a] $R = \sum||F_o| - |F_c||/\sum|F_o|$. [b] $R_w = [\sum w(F_o^2 - F_c^2)^2/\sum wF_o^2)]^{1/2}$. [c] $GOF = [\sum w(F_o^2 - F_c^2)^2/(n-p)]^{1/2}$, where n = number of reflections and p = number of parameters.

Table 3.2. Selected bond lengths (Å) and angles (º) for complex **6_2PF$_6$**

Bond/Angle	**2-2PF$_6$**
Ru-N1	2.1399(18)
Ru-N2	2.1253(17)
Ru-N3	2.1315(16)
Ru-C1	2.2152(19)
Ru-C2	2.184(2)
Ru-C3	2.209(2)
Ru-C4	2.180(0)
Ru-C5	2.1948(19)
Ru-C6	2.2430(19)
N2-Ru-N1	79.09(7)
N1-Ru-N3	85.04(6)
N2-Ru-N2	88.12(7)

Comparisons between the pyridine and chlorido complex were made (Table 3.3) and as expected, the Ru-Cl bond is longer than that of Ru-(*N*-Pyr); this is due to a number of features. Firstly the chlorine is large atom compared to the nitrogen and secondly pyridine is a σ-donor and a π-acceptor so it can form shorter bonds with the Ru(II), compared to an NH_3 ligand for example.[37]

Table 3.3. Selected bond lengths and a comparison between **1-PF$_6$** and **2-2PF$_6$**

Bond	[(η^6-bip)Ru(en)Cl]$^+$ (**1**)[2]	[(η^6-bip)Ru(en)Pyridine]$^{2+}$ (**6**)
Ru – Cl/N(py) (Å)	2.408(15)	2.1315(16)
Ru – coordinated phenyl carbons (Å)	2.138(5) - 2.244(6)	2.180(2) - 2.2430(19)
Ru – Centroid (Co-ord-ring) (Å)	1.663(3)	1.69

3.2.4 Assignment of N-H peaks

[(η^6-Bip)Ru(en)(*N*-pyr)]2PF$_6$ (**6_2PF$_6$**) was characterised by NMR and like **1**, two distinct peaks for the N-Hs in the NMR spectrum were observed, (Figure 3.12). 2D [^{1}H, ^{1}H] NOESY spectra in acidic D_2O showed coupling between only one N-H resonance and the resonance of the ortho-hydrogen on the pyridine ring.

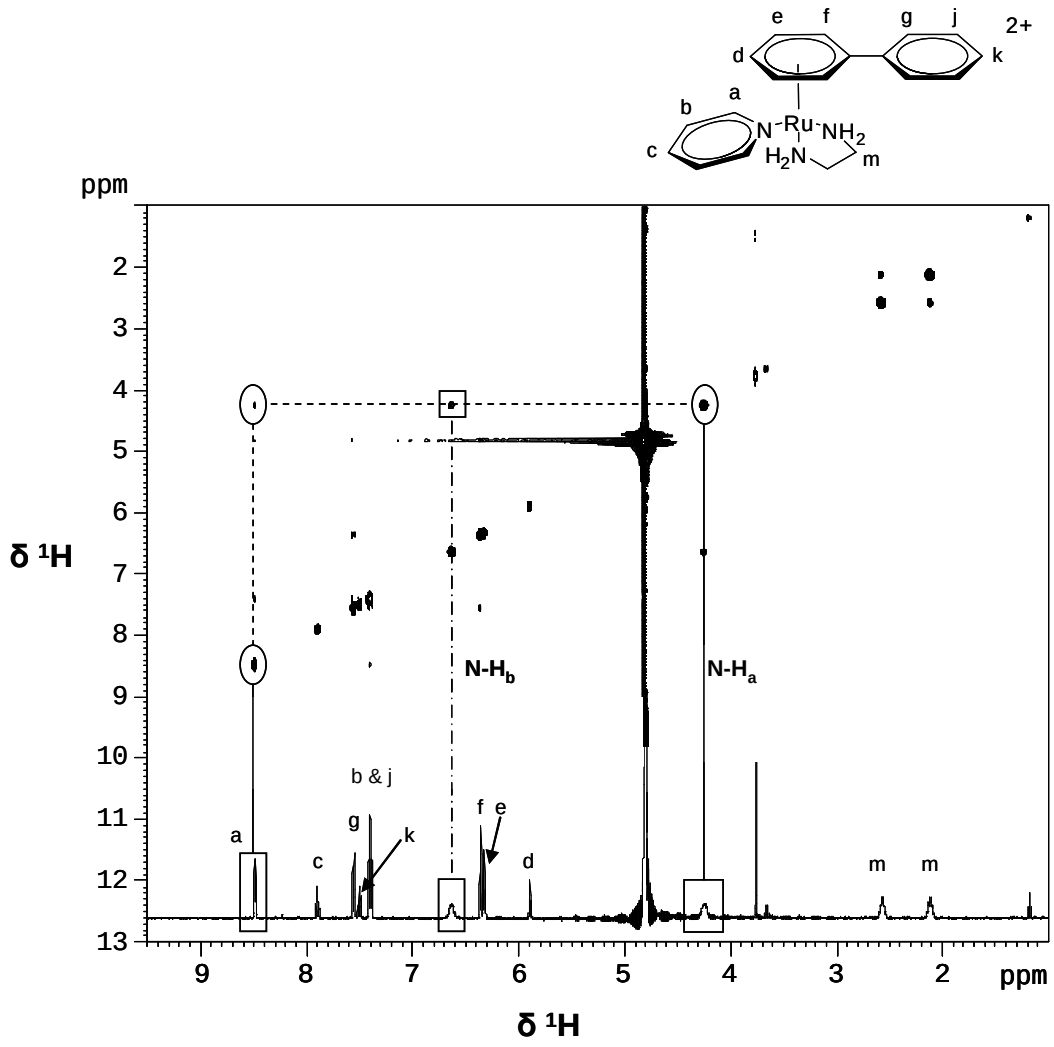

Figure 3.12. ^{1}H and [^{1}H-^{1}H] 2D NOESY spectrum of **6_2PF$_6$** in acidic D_2O. A clear NOE crosspeak between one N-H peak (NH_a) and the ortho-proton (a) on the pyridine ligand is highlighted. The NOE crosspeak between the N-H protons is also highlighted. It is noticeable that the N-Hs which resonate at 6.6 ppm do not exhibit NOEs to the ortho-protons of the pyridine.

There is an inversely-proportional relationship between the intensity of an NOE cross-peak and the distance between the two atoms concerned. The relationship is shown in Equation 3.1.

$$Crosspeak\ Volume = k\ {}^{1}\!/_{r^6} \qquad \textbf{(Equation 3.1)}$$

Where, r is the distance between the two atoms through space and k is the proportionality constant. In order to determine the proportionality constant for this experiment, a comparison must be made between crosspeaks for known distances. For this, comparisons between the NOE for C-$H_{m(pyr)}$ and C-$H_{p(pyr)}$ (the ortho and meta protons on the pyridine ligand) was examined. The average crosspeak volume was 86600 (arbitrary units) and from the crystal structure these protons are a fixed distance of 2.347 Å from each other. Given the volume of the cross peak had an intensity = k/(2.347Å)^6, k is determined as 14474262 Å^{-6}. Applying the proportionality constant, k to the crosspeak for (N-*H*)-(o-*H*) with an average intensity of 82698 a distance of 2.365 Å was determined. This is comparable to the average distance observed in the crystal structure (2.287 Å).

From the identification of the peaks for the up and down protons in **6**, an assumption that the effect on the protons in the chlorido complex (**1**) from the overhanging biphenyl system would be the same can be made. Figure 3.13 explains the meaning of up and down protons. From this point forward, upward pointing protons will be labelled NH_u and downward pointing amino protons will be NH_d.

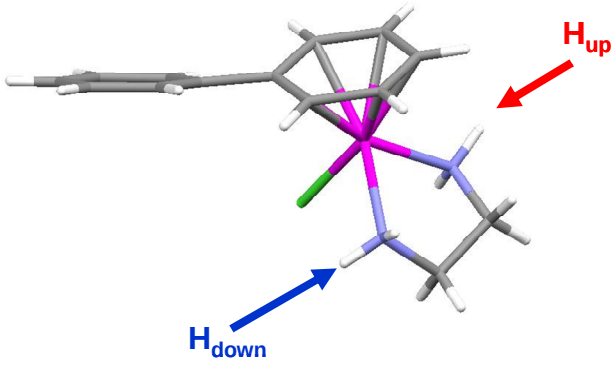

Figure 3.13. Crystal structure of **1** used to explain the meaning of H_u and H_d.

3.2.5 Exchange of Hydrogen for Deuterium

Initial deuterium exchange studies were carried out on **1** following dissolution in 154 mM NaCl in D_2O at 298 K (*c.f.* **§2.3**). The presence of NaCl ensured that the predominant species was the chlorido complex rather than the aqua adduct, where the chlorido ligand is replaced by an aqua ligand. These initial NMR studies showed that one of the protons (NH_d) exchanges more rapidly than the other (NH_u), Figure 3.14.

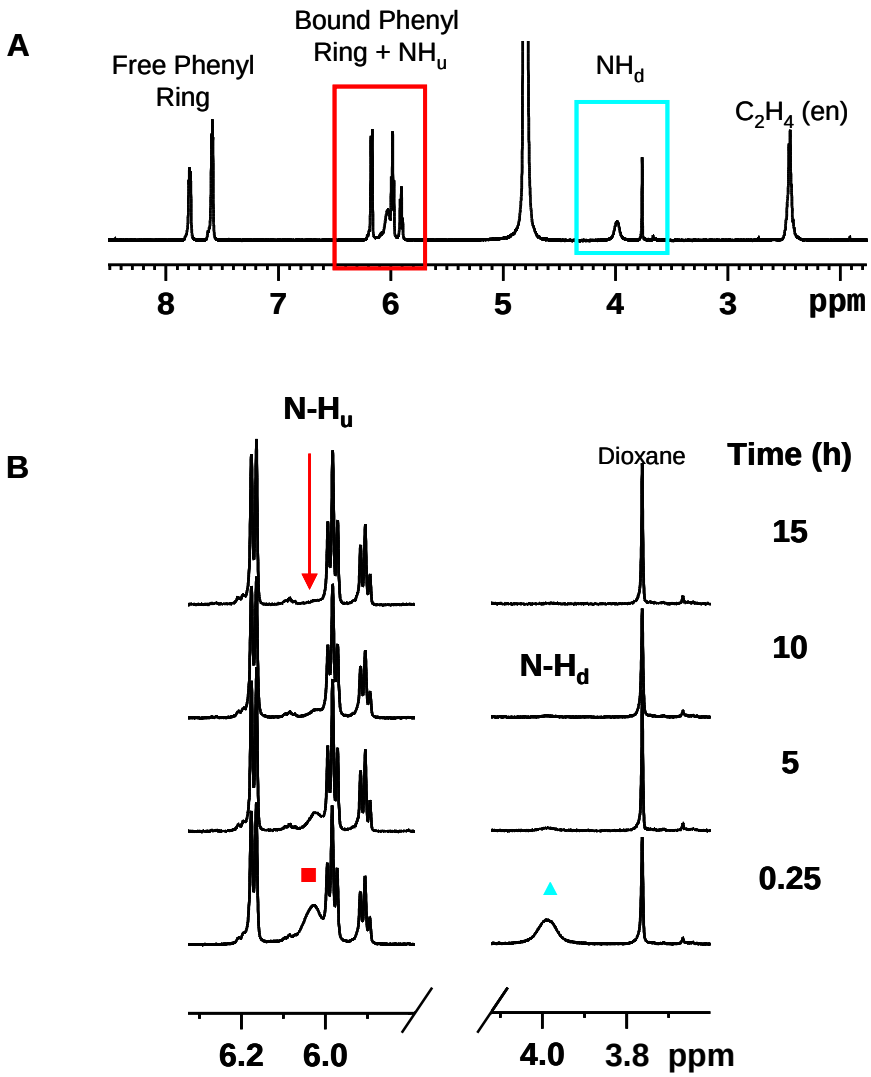

Figure 3.14. A) 500 MHz ^{1}H NMR spectrum of **1** in 154 mM NaCl/D_2O solution at 298 K; highlighted in red and blue are the regions of interest expanded. B) Time dependent ^{1}H NMR signals showing the decay of the N-H_u (■) and N-H_d (▲) signals as a function of time. (pH*= 7.37; temperature controlled at 298K)

Plots of the intensity (peak volume) of the NH_u and NH_d peaks against time show exponential decay curves (Figure 3.15).

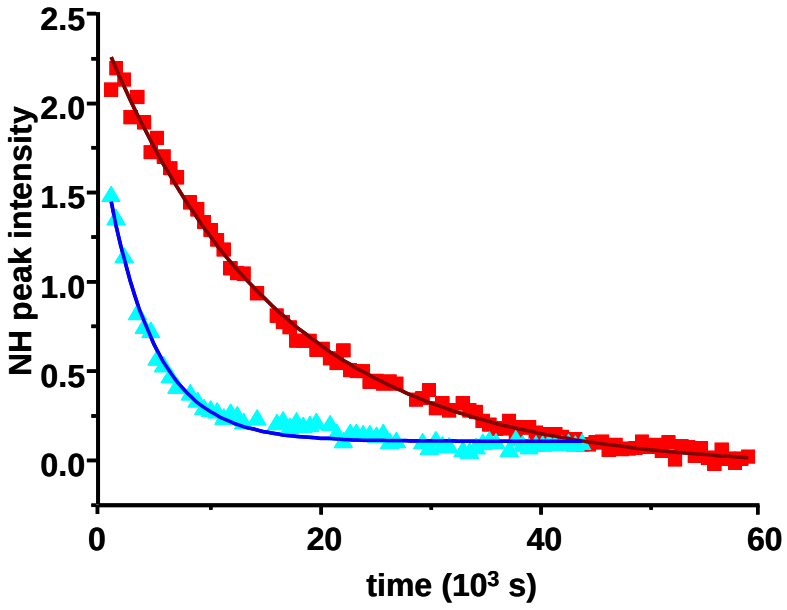

Figure 3.15. Time dependent plot of the decay for N-H_u (■) and N-H_d (▲) NMR peaks over time. The solid lines correspond to the best fit of the data and follow first order exponential decay.

The reaction shows itself to be first-order, in that the best fit for the data is an exponential decay curve. First-order reactions follow the rate equation; rate = k[reactants], where k = the rate constant, and are described by the equation $[A]_t = [A]_0.e^{-kt}$, where $[A]_t$ is the concentration of A at time t, $[A]_0$ is the concentration of A at time = 0 s, and k is the rate constant. However, given that the solvent is a reactant in this case but is in large excess, the reaction is pseudo first-order.

From the best fit decay curves observed in Figure 3.15 it can be seen that NH_d protons exchange with ^2H approximately three times more rapidly than NH_u. Details of the average half lives, determined from 4 rate constants from the best fits of the intensity of the peak normalised to the free phenyl ring or the $(C\underline{H_2})_2$ of the ethylenediamine backbone and comparing the best fit of the

intensity vs time exponential decay curve and the linear plot of ln(intensity) vs time, are listed in Table 3.4.

Table 3.4. The average rate constants and half-lives of the N-H/D exchange reaction at $pH^* = 7.36$, 298K.

Proton	Rate Constant (s^{-1})	Half life (min)
$N\text{-}H_u$	$6.55 (\pm 0.23) \times 10^{-5}$	176.3
$N\text{-}H_d$	$2.24 (\pm 0.25) \times 10^{-4}$	51.5

3.2.6 Effect of temperature

For temperature-dependent NMR, the temperature was varied from 283 K to 298 K and 313 K using the variable temperature and chiller unit attached to the DMX500 MHz (TBI probe). Experiments at 288 K were carried out using the AV600 MHz NMR spectrometer and a BBO Probe.

Exchange studies of **1** were carried out in 154 mM NaCl in D_2O solutions at 283 K, 288 K, 298 K and 313 K. Due to the use of sodium chloride to suppress hydrolysis, problems with a very broad residual H_2O peak led to difficulty in observing the NH_u peak intensity at 283 K. Water suppression would have affected the reliability of the experiment as the suppression sequence would pulse in a close to the resonance frequency of the NH_d protons and could have affected the intensity of the signal. As expected, rates increase with temperature, yet an observable difference between the decay of the $N\text{-}H_u$ and $N\text{-}H_d$ peak was still observed. The data were then used to calculate the activation parameters of the transition states, in an attempt to further elucidate the mechanism.

The data were gathered in the same way as for 298 K and all showed the same underlying feature of NH_d undergoing deuterium exchange substantially faster than NH_u. The time-dependent decay plots of the NH peak intensities are shown in Figures 3.16 and 3.17. Figure 3.18 shows a comparison between exchange rates at a variety of temperatures.

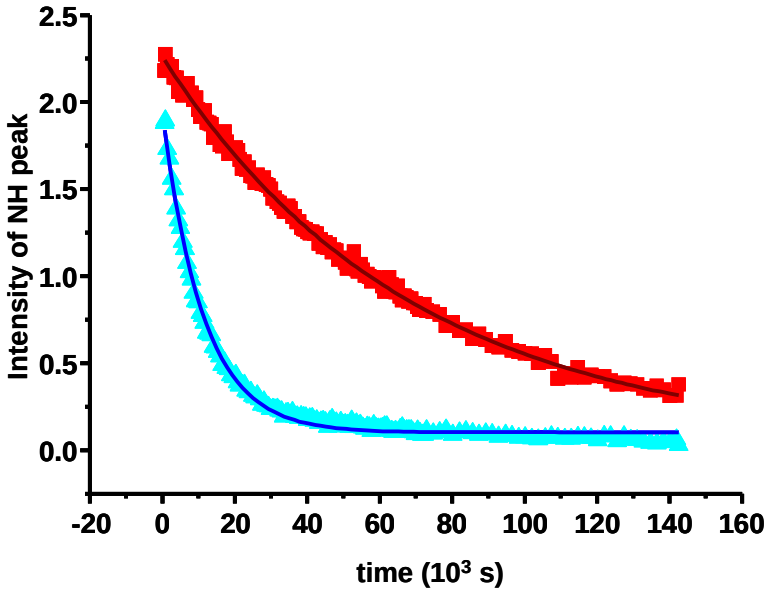

Figure 3.16. Time-dependent plot for the decay for N-H_u (■) and N-H_d (▲) NMR peaks over time at 288 K. The solid lines correspond to the best fits of the data to first order exponential decays. Of note is the difference between the exchange rates for NH_u and NH_d with exchange of NH_d being faster.

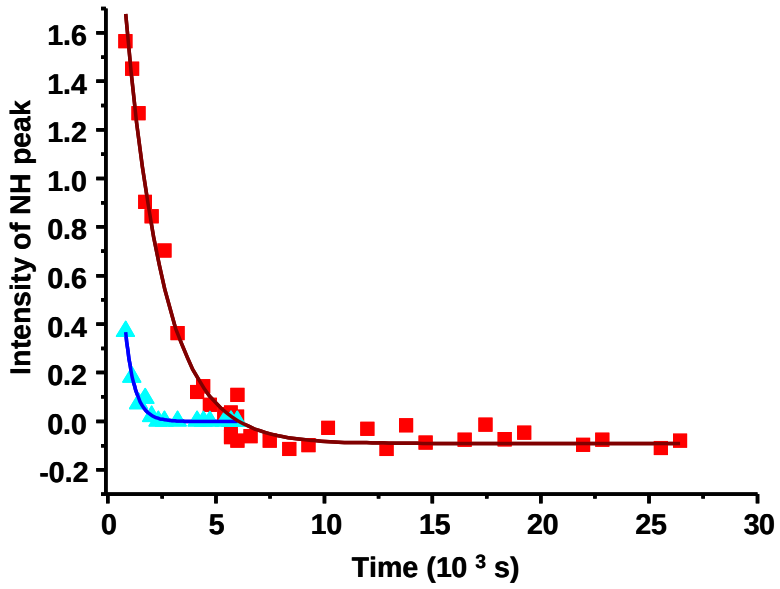

Figure 3.17. Time dependent plot of the decay for N-H_u (■) and N-H_d (▲) NMR peaks over time at 313 K. The solid lines correspond to the best fits of the data to first order exponential decays. Of interest is the fact that the N-H_d peak has almost completely disappeared after 30 minutes.

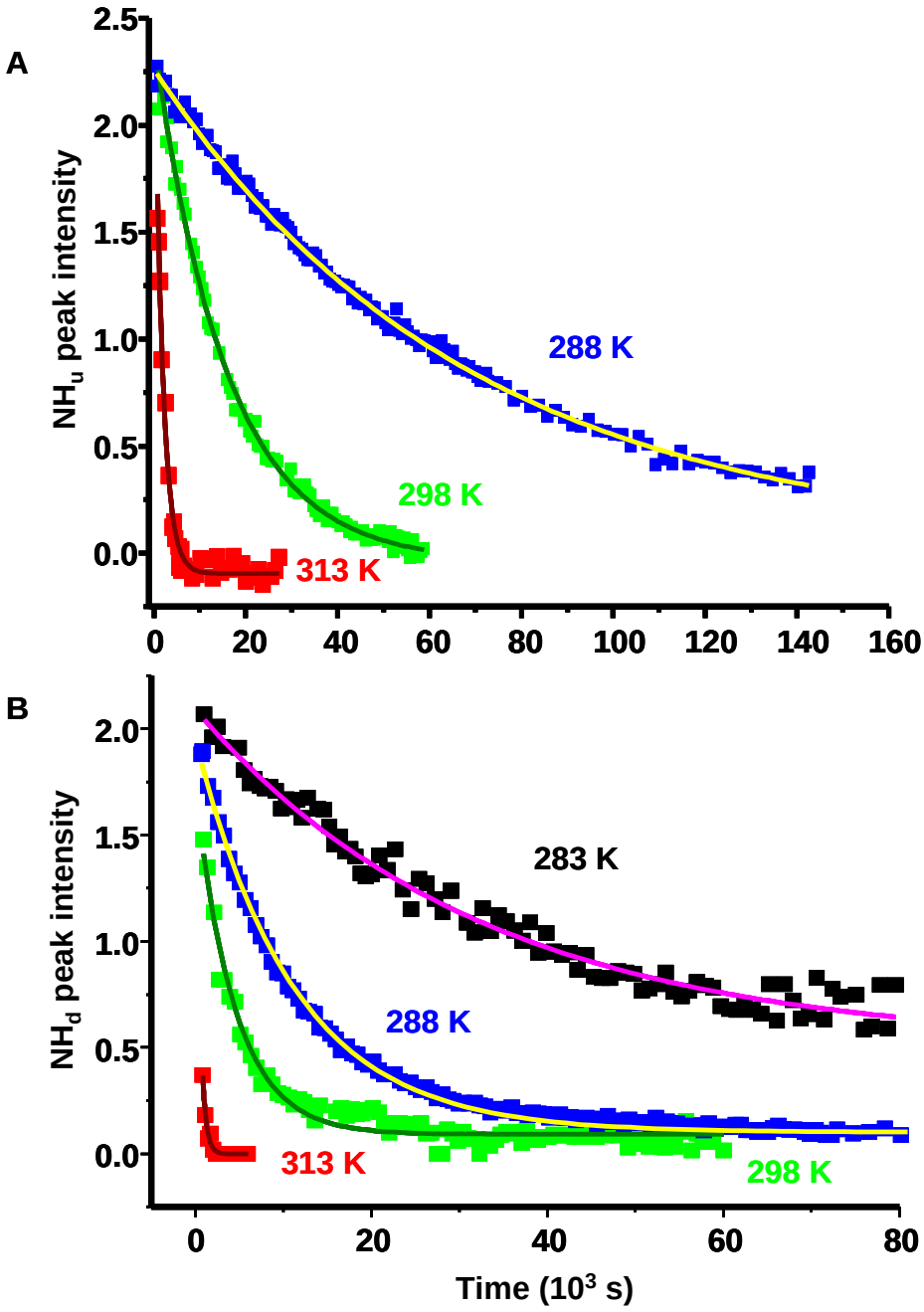

Figure 3.18. Dependence of A) N-H_u and B) NH_d peak intensities on time at various temperatures; 283 K (black), 288 K (blue), 298 K (green) and 313 K (red). The solid lines represent first order best fits to the data.

From Figure 3.19 the rate constants and half life of this exchanges were determined and are tabulated in Table 3.5.

Table 3.5. Rate constants and half life values for the rates of ^{1}H-^{2}H exchange for NH_u and NH_d at various temperatures.

Proton	**NH_u**		**NH_d**	
Temp (K)	Rate Constant (s^{-1})	Half life (min)	Rate Constant (s^{-1})	Half life (min)
283	N/A*	N/A	1.740×10^{-5}	663.9
288	1.44×10^{-5}	802.25	8.491×10^{-5}	136.1
298	6.55×10^{-5}	176.3	2.24×10^{-4}	51.5
313	6.06×10^{-4}	19	2.36×10^{-3}	4.9

* Data at this temperature could not be collected due to the broadening of the HOD signal at high ionic strength.

3.2.7 Determination of Activation Energies

Arrhenius and Erying plots were used to obtain activation parameters for the N-H/D exchange rates (Figure 3.19). The Arrhenius equation provides a linear relationship between the natural log of the rate constant and the inverse of the temperature, with the slope being a function of the activation energy (Equation 3.2). The Eyring equation provides the relationship between ln(k/T) against the inverse of the temperature with the slope being a function of the enthalpy and the intercept related to the entropy (Equation 3.3).

$$ln(k) = \frac{-\Delta E_a^{\ddagger}}{RT} + ln(A) \qquad \textbf{(Equation 3.2)}$$

$$ln(k/T) = \frac{-\Delta H_a^{\ddagger}}{RT} + ln(\frac{k_b}{h}) + \frac{\Delta S_a^{\ddagger}}{R} \qquad \textbf{(Equation 3.3)}$$

Where, k_b is the Boltzmann constant, h is the Planck constant, R is the gas constant, T is the temperature, A is a constant (the intercept of the Arrhenius plot) and $\Delta E_a^{\ddagger}$, $\Delta H_a^{\ddagger}$, and $\Delta S_a^{\ddagger}$, are the activation energy, enthalpy and entropy difference, respectively, between the starting material and the transition state.

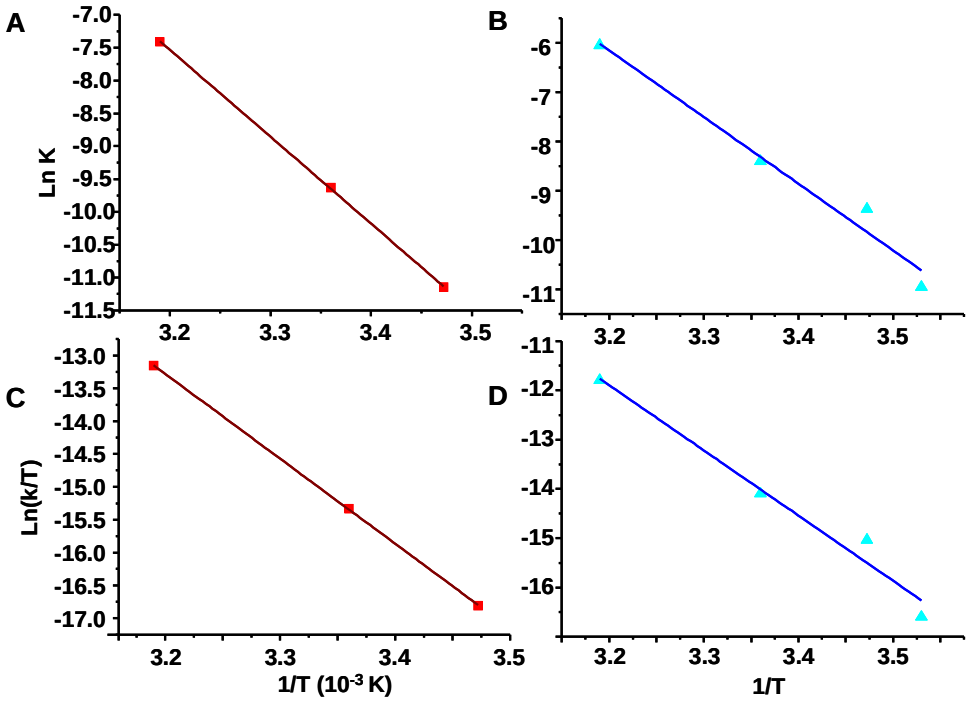

Figure 3.19. A and B: Arrhenius plots for NH_u and NH_d respectively. C and D: Eyring plots for NH_u and NH_d respectively. The solid lines are the best fits to the equation y = mx + c with parameters listed in Table 3.6.

Table 3.6. Activation energy parameters for the intermediate (both NH_u and NH_d values agreed to within 3%)

$\Delta E_a^{\ddagger}$,	111.3 kJ mol^{-1}
$\Delta H_a^{\ddagger}$,	108.84 kJ mol^{-1}
$\Delta S_a^{\ddagger}$,	43.36 J mol^{-1}

Although, these values are subject to large errors due to the fact they are obtained from NMR integrals which are themselves subject to error, it is of note that both NH_d and NH_u provide very similar parameters of activation. The implication here is that both processes involve the same transition state. It is worthy to note that the Arrhenius and Eyring plots both had R^2 values of 0.997 and 0.959 for NH_u and NH_d respectively.

3.2.8 Effects of pH* on rates of exchange

Fresh samples of **1** were prepared in acidic and basic NaCl (154 mM) solutions in D_2O. The pH* was recorded (*c.f.* **§2.2**) before and after NMR spectra were recorded at 298 K. Again a decrease in the integrals of the N-H peaks with time was observed. Table 3.7 lists the exchange rates at various pH* values. The same trends in spectra were noticed in that NH_d NMR peaks disappeared faster than NH_u peaks. The data were collected in the same manner as discussed previously and Table 3.7 provides a full list of the rate constants and half-lives for each experiment.

Table 3.7. Kinetic data for proton/deuterium exchange reactions of the amino protons of **1** at various pH^* values

pH^*	Rate constant k (s^{-1}) NH_u/D_u	Half life (min) NH_u/D_u	Rate constant k (s^{-1}) NH_d/D_d	Half life (min) NH_d/D_d
6.16	1.15×10^{-5}	1001	1.59×10^{-5}	728
6.4	1.94×10^{-5}	595.3	3.15×10^{-5}	366.3
7.125	4.68×10^{-5}	245.1	8.86×10^{-5}	130.4
7.36	6.33×10^{-5}	182.5	2.24×10^{-4}	51.5
8.04	1.51×10^{-4}	76.5	5.94×10^{-4}	19.5
8.47	2.03×10^{-4}	57	6.74×10^{-4}	17.4
9.34	8.19×10^{-4}	15	N/A	N/A

Exchange rates increased with increasing pH^*. This increase is evident for both peaks, but there are still significant differences between the exchange rates of both protons, with exchange of NH_d being 1.4 times faster at 6.16 pH^* than NH_u exchange and 3.2 times faster at 8.47 pH^*.

Figure 3.20 compares the half–life of all these reactions with respect to the pH^* at which the exchange occurred. This provides clear evidence of a base-catalysed reaction.

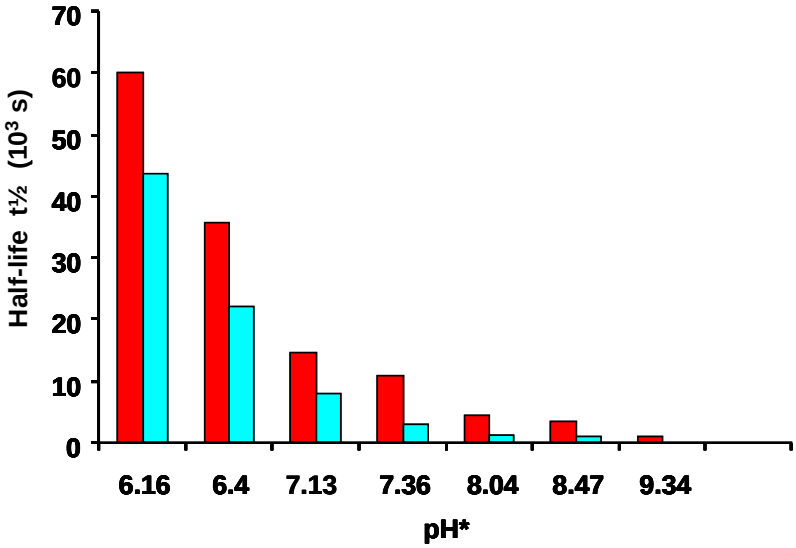

Figure 3.20. Dependence of the half life for $^{1}H/^{2}H$ exchange at various pH^{*} values. ■ NH_u/D_u values and ■ NH_D/D_D values. Exchange of downward protons was too rapid to be observed on the NMR time scale. Above $pH^{*} = 9$ the exchange on NH_d was unobservable.

Lowering of pH^{*} led to a decrease in exchange rate for both NH_u and NH_d. At $pH^{*} < 3$ there was no determinable decrease in either NH peak intensity. This information was useful experimentally and allowed 2D NOESY and COSY experiments in acidic D_2O solutions without loss of intensity of N-H peaks. Acidic conditions allowed for spectra to be obtained without the need of H_2O suppression, leading to sharper and more reliable results. It was this method that allowed observation of the NOESY spectrum of the pyridine adduct (**6**) in D_2O. The use of pH^{*} to control the rate of exchange of the amine protons proved very useful for higher charged species in which inversion could be too rapid at neutral pH to observe on an NMR timescale and could be reduced using acidic solution to

help with observations of the exchange, this will be discussed in more detail in Chapter 4.

Combining the information from Figure 3.20 and comparing to the concentration of free protons in solution ($Log_{10}[k_{obs}]$ log vs. pH^*). a linear relationship is observed; this proved conclusively that the exchange is base-catalysed (Figure 3.21).

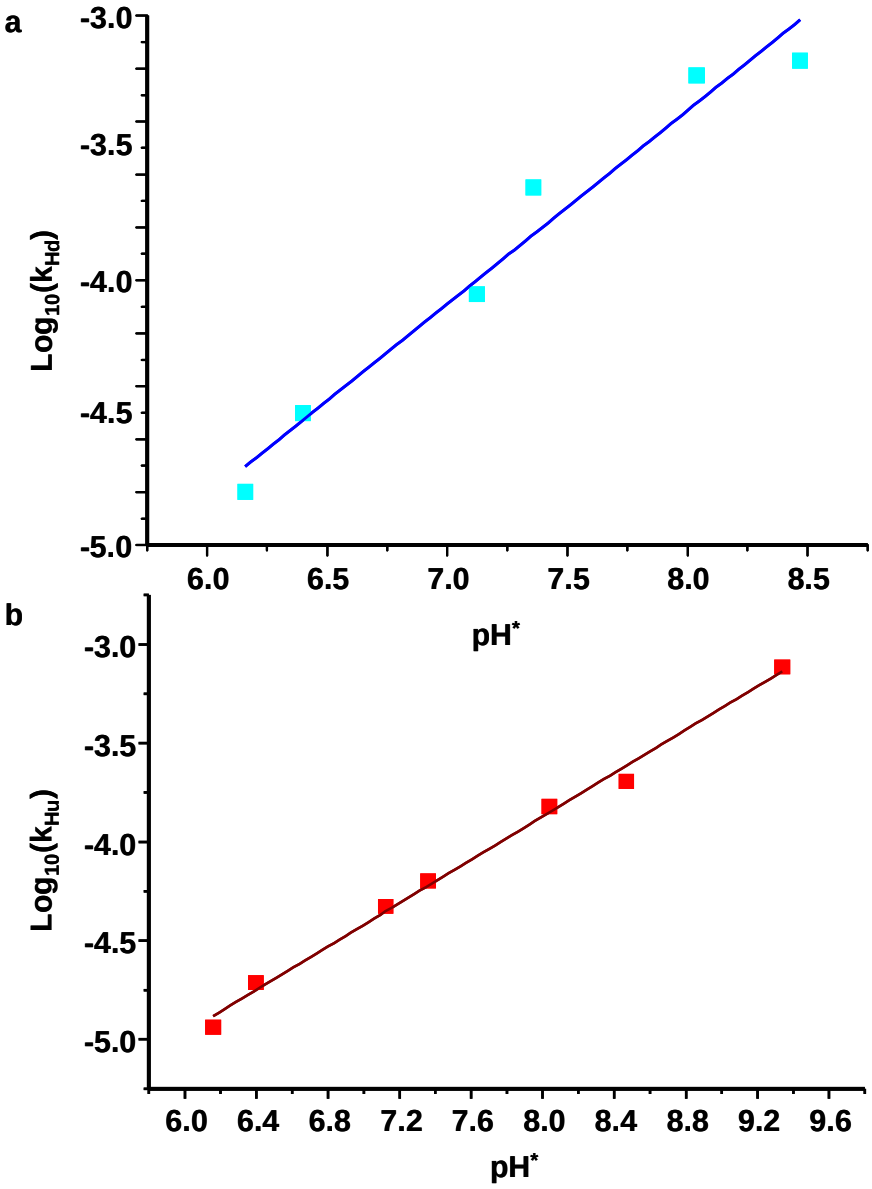

Figure 3.21. Plots of $\log_{10}(k_{Hu})$ and $\log_{10}(k_{Hd})$ vs pH^* showing a linear relationship between pH^* and $\log_{10}(k_{obs})$ for exchange of ^1H for ^2H on the ethylenediamine amino-protons at 298 K in 154 mM NaCl solution in D_2O. a) The linear plot for NH_d exchange, and b) for the NH_u exchange. A clear relationship between the rates of exchange and the basicity of the solution is observed.

Table 3.8. Parameters from the fitting of the linear plots in Figure 3.21.

Exchange	Slope	Intercept	R^2 (G.o.F)
N-H_d	0.73066	-9.20406	0.95576
N-H_u	0.54874	-8.26142	0.99312

These data become useful when comparing solutions of a different ionic strength to those at 154 mM NaCl solutions.

3.2.9 Effects of ionic strength on exchange

Exchange was observed for solutions of different ionic strengths, to study the effects of ionic strength on the exchange rates. Fresh samples of **1** were dissolved in either 300 mM, 500 mM or 1 M NaCl solutions in D_2O and exchange rates were observed and compared to those in 154 mM solutions of NaCl, as derived using the data in Table 3.9. Direct comparisons could not be made with each other as samples were at different pH^* values. Ionic strength was determined using equation 3.4.

$$I = \frac{1}{2}\sum_{i=1}^{n} c_i z_i^2 \qquad \textbf{(Equation 3.4)}$$

Where; I is the ionic strength, c_i is the concentration of ion i, and z_i is the charge on ion i. For NaCl I will equal the concentration in molar units, as both ions have a charge of 1.

$$I = \frac{1}{2}\left(\left[0.154\times 1^2\right] + \left[0.154\times(-1)^2\right]\right) = 0.154$$

Table 3.9. Rate constants for solutions of varying ionic strength, compared to those of the calculated values obtained at I = 0.154 using the data from Table 3.8.

Ionic Strength (pH*)	k_{obs} (NH_d) s^{-1}	k_{calc} (NH_d)‡ s^{-1} (0.154 M NaCl)	k_{obs} (NH_u) s^{-1}	k_{calc} (NH_u)‡ s^{-1} (0.154 M NaCl)
0.3 (8.2)	2.13×10^{-3}	6.13×10^{-4}	2.04×10^{-4}	1.73×10^{-4}
0.5 (7.9)	1.18×10^{-3}	3.7×10^{-4}	9.25×10^{-5}	1.18×10^{-4}
1.0 (6.6)	5.71×10^{-5}	4.15×10^{-5}	1.77×10^{-5}	2.29×10^{-5}

‡ Calculated values for the exchange rates of Ionic strength = 0.154 and at the same pH* as the samples at different ionic strengths so that comparisons can be made.

When the exchange rates at different ionic strengths are compared to that at I = 0.154, a definite effect of ionic strength on the exchange rates is observed. As the ionic strength increases, the exchange rates of the NH_d protons increase substantially, whereas the effects on the NH_u exchange rates are not as pronounced.

3.2.10 $^2H/^1H$ Exchange rates

The reverse reaction (exchange of ^2H for ^1H) was monitored. A lyophilised deuterated sample (**1D**) in NaCl was prepared (*c.f.* **§ 2.15**) and dissolved in 1 mL H_2O and monitored using ^2H NMR. (I = 0.6, pH = 7.27) and (I = 0.3, pH = 7.2) (Figure 3.22). Table 3.10 shows the kinetics data observed. There are many difficulties with ^2H NMR, one of which is the lower signal-to-noise ratio which

made it difficult to monitor the signal for NH_d for I = 0.6, as before monitoring could begin, much of the signal had disappeared.

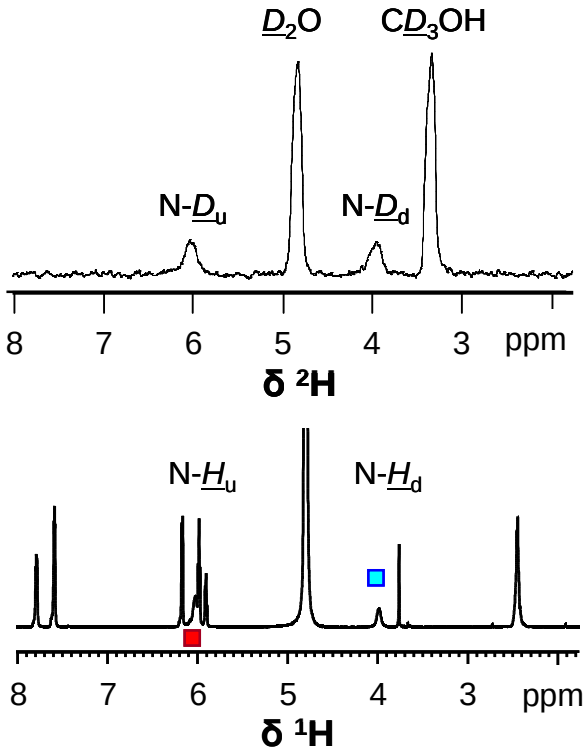

Figure 3.22. A comparison of a ^2H and ^1H NMR spectrum of **1D** and **1** (^2H at I=0.3, pH = 7.27, 76.7 MHz). When the ^2H NMR is calibrated to C$\underline{D}_3$OH the ^2H and ^1H signals for the N-^2H and N-^1H peaks appear in a very similar range, as would be expected.

Table 3.10. Kinetic data observed from ^2H NMR of $^2H/^1H$ exchange on **1D**.

^2H	***I***	**pH**	**k_{obs} s^{-1}**	**$t_{½}$ (min)**
N^2H_u	0.60	7.3	8.308×10^{-5}	139.4
N^2H_u	0.30	7.2	7.17×10^{-5}	161.2
N^2H_d	0.30	7.2	3.59×10^{-4}	32.6

3.2.11 Computational Analysis

Using the x-ray crystal structure of $[(\eta^6\text{-bip})Ru(en)Cl]^+$ (**1**) the molecular orbitals were calculated (*c.f.* **§2.13**) to look in detail at the HOMO (highest occupied molecular orbital) and the LUMO (lowest unoccupied molecular orbital). Analysis of the HOMO showed an overlap between the antibonding orbital of the Ru-Cl bond and what looks very like a p-orbital around the nitrogen of the ethylenediamine ligand. (Figure 3.23)

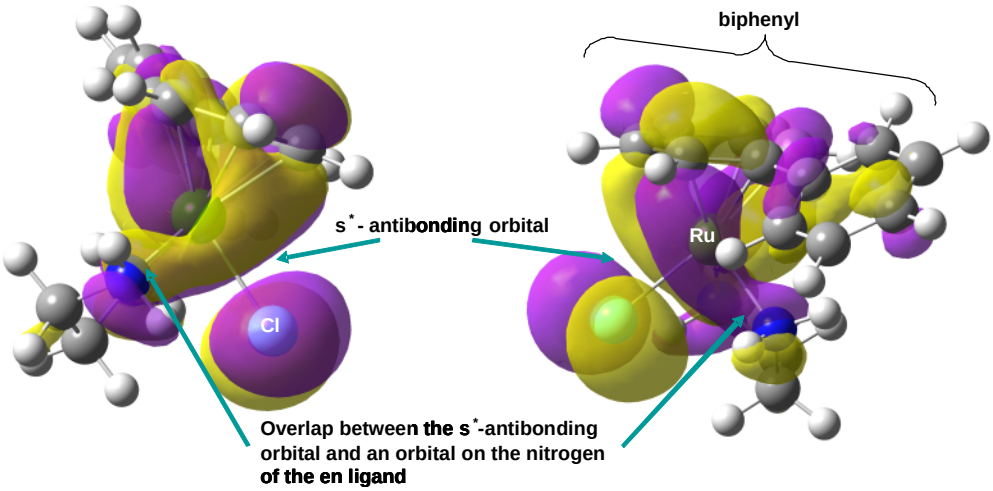

Figure 3.23. A representation of the HOMO of **1** $[(\eta^6\text{-bip})Ru(en)Cl]^+$. There appears to be an overlap between the σ^*-antibonding orbital of Ru-Cl and a potential location of a p-orbital on the nitrogen of the ethylenediamine ligand.

3.3 Discussion

3.3.1 The presence of two N-*H* peaks in the NMR spectra of 1_PF_6 and 6_$2PF_6$

By ^{1}H NMR the presence of 2 non-equivalent NH protons was observed. This is believed to be a result of the ethylenediamine-ruthenium 5-membered ring not being in a symmetrical magnetic field. In a magnetic field a ring current is induced in the overlying biphenyl ring which can influence the magnetic field around the amine and ethyl protons on the ethylenediamine. Protons which occupy the space close to the arene will be affected differently than those further away. This phenomenon has been noted many times before.[28] The observstoion of NOESY peaks for the pyridine adduct (**6**) allowed NOE crosspeaks to be detected between the ortho-proton on the pyridine (o-H_{pyr}) and the downward pointing protons on the amine (N-H_d) to determine the identity of each N-H peak in the NMR spectrum. Assuming **1** would be subject to similar effects from the ring current, conclusive assignments of δ (N-$\underline{H_u}$) = 6.03ppm and δ (N-$\underline{H_d}$) = 3.99ppm for solutions of **1** in 154 mM D_2O were made.

3.3.2 Exchange rates of NH_u and NH_d

Studies were carried out in 154 mM NaCl solutions to monitor exchange rates of ^{1}H for ^{2}H in D_2O as a method of studying the mechanism for inversion of the stereochemistry on $[(\eta^6\text{-bip})Ru(Et\text{-}en)Cl]^+$. There were two reasons for the design of this experiment. Firstly, the NaCl suppresses hydrolysis[38] and ensures that only NH/D exchange of the chlorido species would be investigated, without the added complications of aqua species forming. Secondly, the reason for

studying the non-chiral complex was similar and it was to prevent the kinetics being complicated by the interconversion between diastereoisomers.

These initial studies on the exchange rates of NH_u and NH_d showed two distinct rates of exchange. The reason for this difference in exchange rates became the main area of focus of this work. A similar effect was noted on ethylenediamine Co(III) complexes[33,39] and was believed to be a result of *cis* and *trans* effects. However, in the complex studied here (**1**) both ethylenediamine nitrogens appear to be exposed to the same *cis* and *trans* effects, so there must be other factors leading to the difference in rates.

3.3.3 Exchange rates at various temperatures

Studies at various temperatures have shown a continuous trend with NH_d undergoing exchange substantially faster than the NH_u protons. Using the rate constants for exchange at various temperatures the activation parameters for the exchange process were determined. The activation parameters of both NH_d and NH_u exchange were almost identical to within 3%, with average activation energy of 111.3 kJ mol^{-1}. This clearly implies that both proceed via the same transition state. Of further interest is the entropy of activation of 43.4 J mol^{-1}, the positive value being indicative of a dissociative pathway as entropy increases when an atom dissociates. The activation energy is less than the dissociation energy of free N-H bonds (319 kJ mol^{-1})[40]; this is to be expected as the lone pair of electrons on the nitrogen is coordinated to the metal, weakening the N-H bond on the ethylenediamine (Figure 3.24).

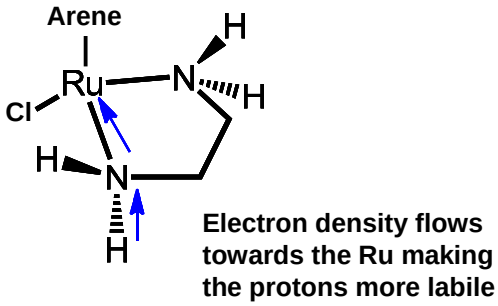

Figure 3.24. A representation of the electron flow from the nitrogen to the ruthenium weakening the N-H bond.

3.3.4 Effects of ionic strength on exchange rates

To confirm the mechanism is indeed dissociative, the effects of ionic strength were investigated. It was found that ionic strength had an effect on the exchange rates of NH_d and NH_u. The rates of exchange for NH_d increased with ionic strength, but decreased for NH_u. The increase in the rate of reaction with increasing ionic strength is indicative of a dissociative mechanism, adding further weight to evidence from **§3.3.3** (above). The reduction in the exchange rates of the NH_u protons may be a result of the increased ionic strength stabilising an intermediate in the exchange mechanism.

3.3.5 Exchange rates of ND_u and ND_d

When the reverse reaction was studied ($^2H/^1H$ exchange), the exchange rates were reduced (when effects of ionic strength were taken into account). As with the exchange of protons for deuterons, there is an observable difference between the exchange rates of the up and downward pointing deuterons. This confirms the hypotheses that the rate limiting step is the abstraction of the proton, given the decrease in reaction rates when a heavier isotope is used.

3.3.6 Effects of pH on exchange rates

The proportionality between the rates of exchange and the pH* (Figure 3.20) of the sample provides insight into the mechanism. The exchange of protons for deuterons on **1** at low pH* is almost negligible, with no exchange is observed at pH* < 3 over 48 h. This observation further supports the conclusion that the initial step in the reaction must be proton abstraction. Unlike exchange of protons for deuterons on proteins which are both acid and base catalsysed[41], the exchange of the ligand amino protons appears to only be base-catalysed, given that at low pH* values, exchange was not observed. This is in agreement with observation of the rates of interconversion of stereoisomers of the ethyl-en complexes **5A** and **5B** which appear to be base catalysed.[8] These results are also in agreement with much of the previous work by Fujita,[31,42] where a dependence of [$^{-}$OH] on the rate of proton exchange was also observed.

3.4 Potential Mechanisms

The amino protons on the ethylenediamine ligand of $[Ru(II)(\eta^6\text{-bip})enCl]^+$ have been found to undergo exchange in aqueous solutions. The rates of exchange are dependent on pH, temperature and ionic strength. However of most interest to this study is the difference in the exchange rates of amino protons dependent on their orientation relative to the biphenyl ring system. Protons which point towards the ring (NH_u) are found to undergo exchange at a slower rate than those protons that point away from the ring (NH_d).

In the course of this work a number of phenomena were noted, all of which contribute towards explaining the mechanism of exchange of protons.

1. Thermodynamic data for the transition state implies that exchange of both NH_u and NH_d occur via the same intermediate species.
2. The proton exchange process is base-catalysed, so the rate limiting step must be abstraction of a proton.
3. Dependence of the rates of exchange on ionic strength further provides proof that the process is a dissociative one, so the abstraction of a proton corresponds to this well.
4. Further evidence of the abstraction of a proton being the rate-determining step was provided by the kinetic isotope effect on the rate constant for the back reaction of deuterons being exchanged for protons.

All these observations lead to the conclusion that the complex must undergo proton abstraction as a rate-limiting step and that it is the breaking of the N-H bond, rather than the Ru-N or Ru-Cl bond, that is crucial to this mechanism. The possibility of the Ru-N or Ru-Cl bonds being broken as part of this mechanism is ruled out by the observation that both the types of protons (NH_u and NH_d) exchange at different rates. If Ru-N or Ru-Cl bond breaking was occurring during this process, as is seen with some catalytic processes where the Ru-H bond breaks[25], in order to change the stereo centres in **1** or in complexes **5A** and **5B**, this bias in exchange of NH_d over NH_u would not occur. (Figure 3.25 and 3.26)

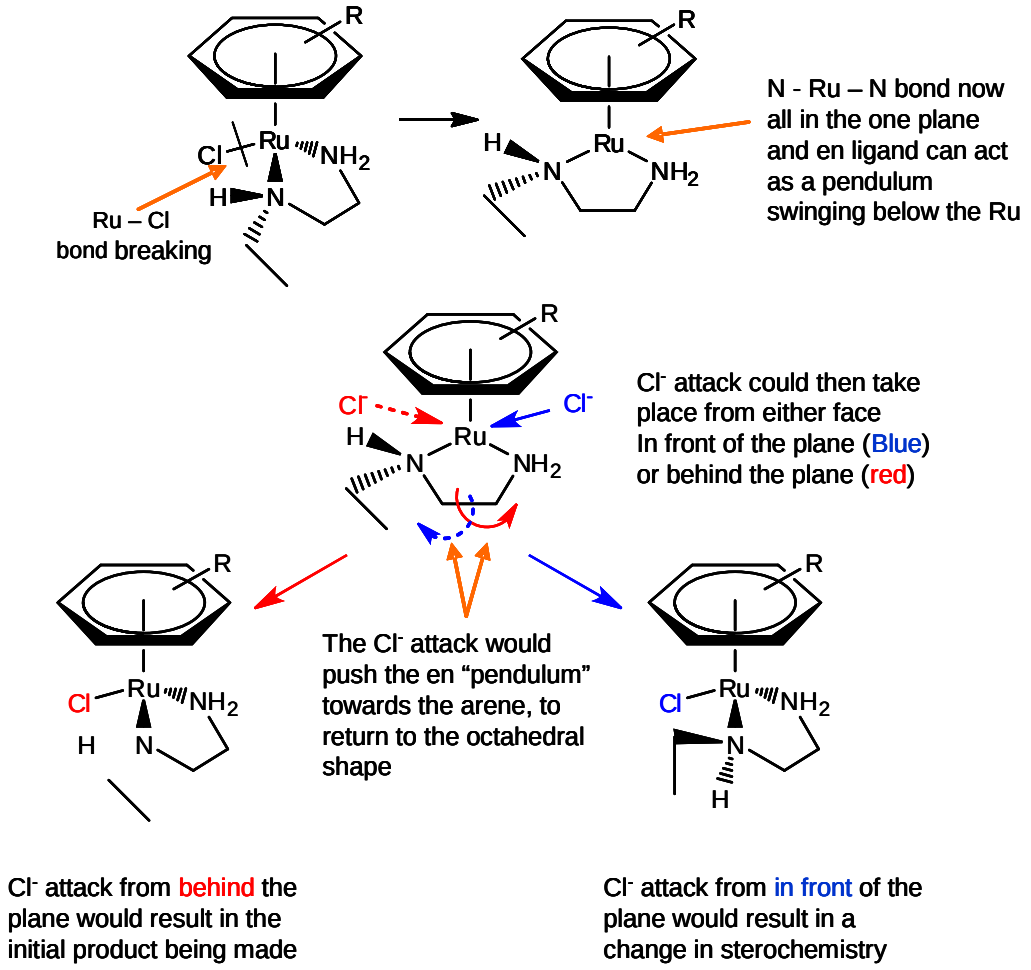

Figure 3.25. Representation of how Ru-Cl bond breaking would cause inversion of stereochemistry of **5A** to form **5B**. *Charges have been excluded from the complex for clarity and the arene ring system is in constant rotation.*

If the mechanism shown in Figure 3.25 is the route to inversion, then the probability of Cl^- attack on either face would be equal and would not lead to the difference in exchange rates of NH_u and NH_d seen for complex **1**, which has been used in this study to explain the inversion on **5A**. If the mechanism involves a 16-electron species, as with the catalytic processes,[17] the probability NH_u and NH_d being replaced would be equal. This is clearly not occurring and so exchange must proceed via another mechanism.

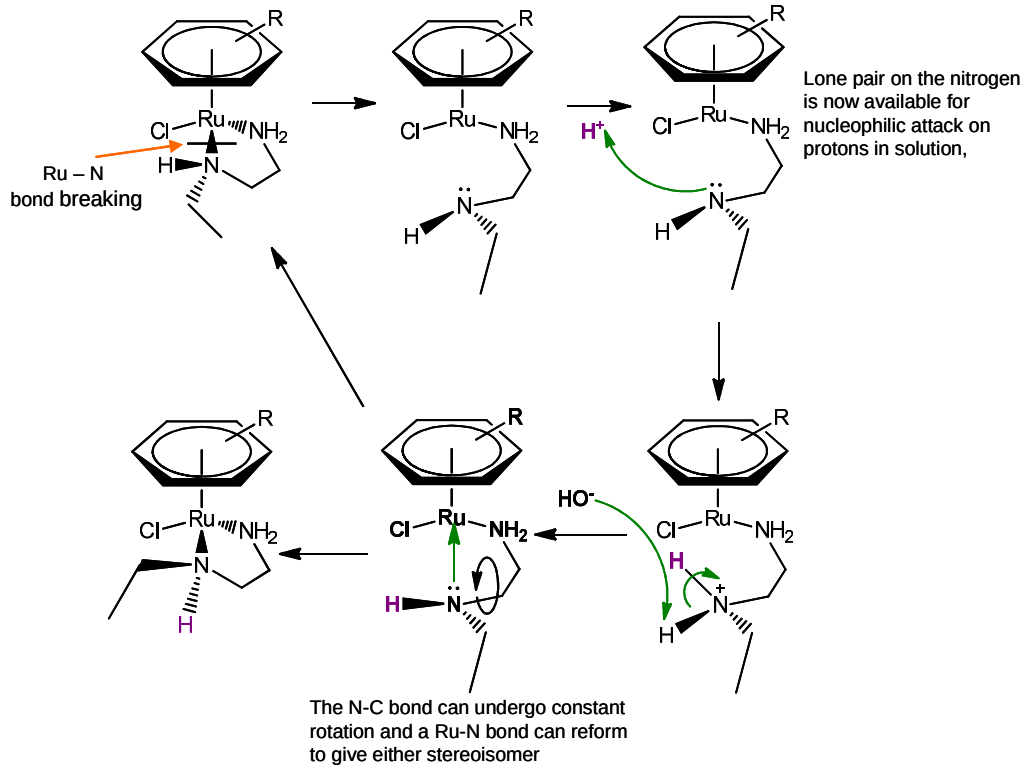

Figure 3.26. Proposed mechanism of stereo inversion involved Ru-N bond breaking. *The overall charges on the complexes have been omitted for clarity.*

While the mechanism shown in Figure 3.26 would explain how an inversion of stereo centres can occur, it would not however, explain the difference in exchange for up and down protons. Once Ru-N or Ru-Cl bond-breaking has been ruled out, the only other alternative is N-H bond breaking. This agrees with the observations confirming that the rate-limiting step of the exchange process is proton abstraction.

Once the rate-determining step was elucidated, the issue of why NH_u exchange is so much slower than NH_d needed to be addressed. Activation parameters for the transition state species showed that the $\Delta E_a^{\ddagger}$,, $\Delta H_a^{\ddagger}$, and $\Delta S_a^{\ddagger}$, for both exchange pathways are almost identical, so both processes are likely to involve the same transition state. This led to the conclusion that the product

determining step (i.e.: the step in the reaction which determines which face of the ethylenediamine is deuterated) must occur after the transition state is formed and be influenced by accessibility of deuterons to the nitrogen lone pair which has been freed by the loss of a proton.

Given the fact that the two protons, NH_u and NH_d, are in different physical environments, as a result of their proximity to the arene ring system, perhaps it is the arene system that influences this difference in exchange rates. The abstraction of a proton and addition of a deuteron might be concerted, and so the limiting step would be access of a deutroxide ion into close enough proximity to the amine groups in order to abstract a proton. The face of the en ligand away from the biphenyl ring will be more accessible than that of the face nearest the biphenyl ring. If the reaction involves a concerted exchange, then as one proton is abstracted to form HOD, at the same time the deuteron can rapidly replace the displaced proton. (Figure 3.27). This would explain the difference in rates of exchange for the up and down protons, but it would not account for changes in stereochemistry that are observed on complexes with chiral ethylenediamine ligands.

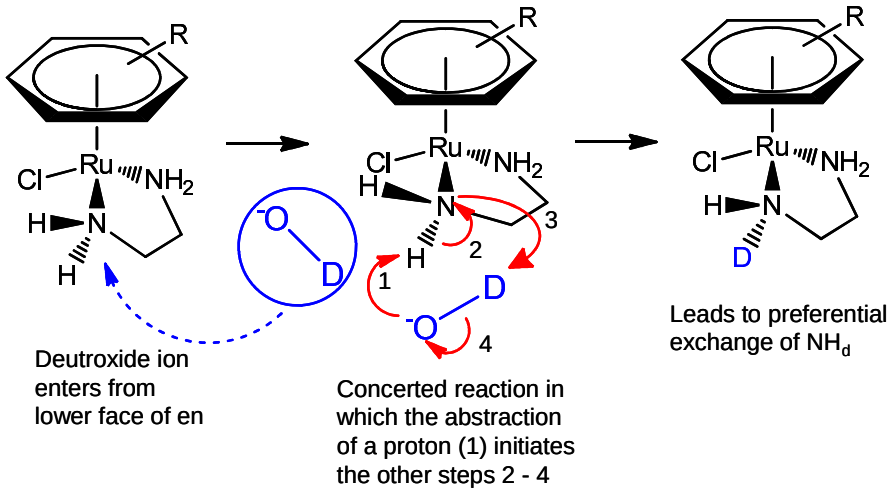

Figure 3.27. Proposed mechanism for a concerted mechanism which would explain a bias for NH_d exchange faster than that of NH_u but would not explain the change in stereoisomerism that is observed on complexes with chiral ethylenediamine ligands

Following elimination of the mechanisms discussed above, there are only two other possible explanations which would fit the experimental data for both the difference in the exchange rates of up and down protons and the inversion of stereochemistry. Figure 3.29 gives an overview of how proton abstraction can lead to stereochemical inversion for complex **5A**. This method confirms that ring opening has no role in the conversion of **5A** to **5B**, but conversion is through the exchange of protons in aqueous solution.

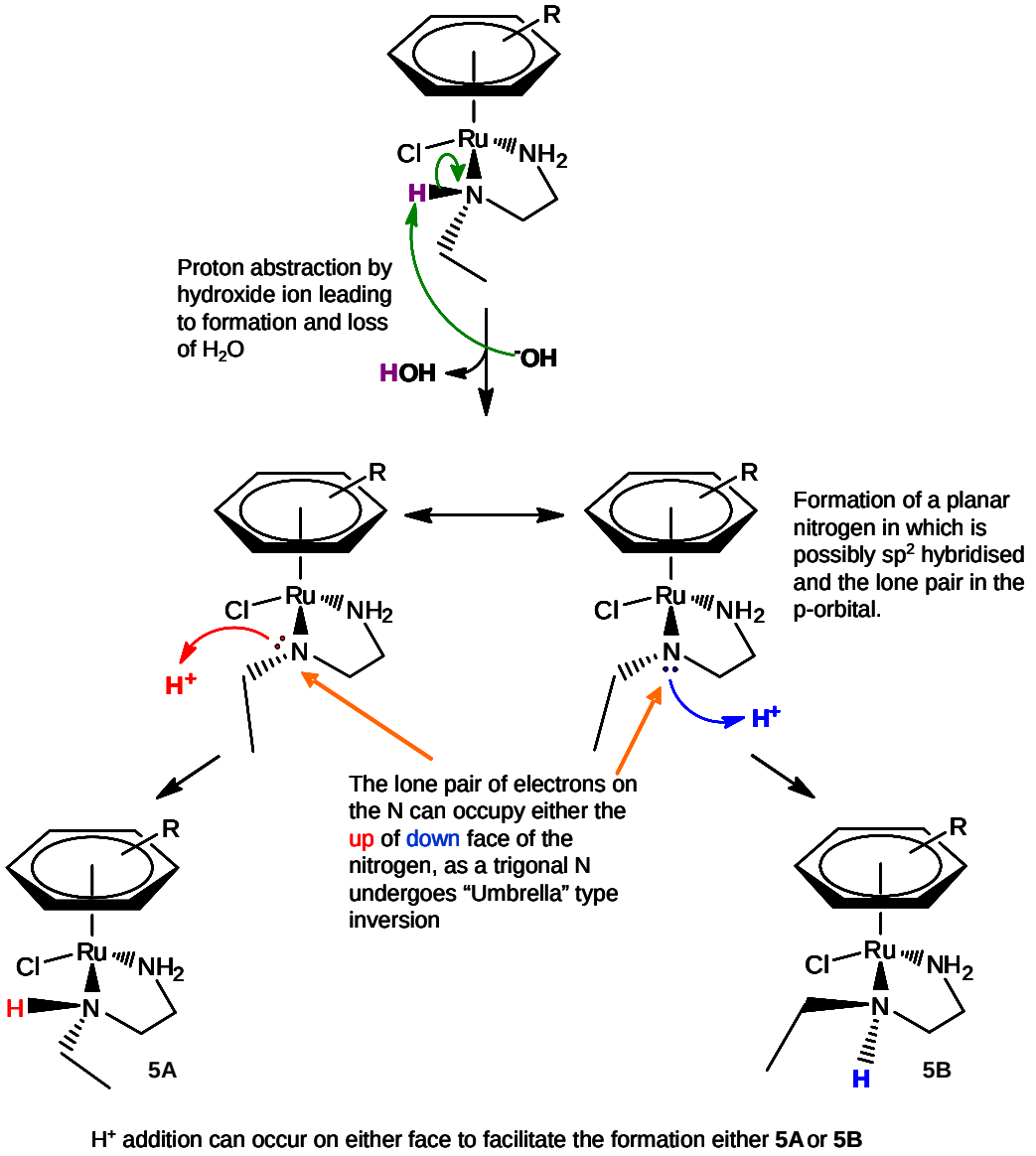

Figure 3.28. Possible mechanism for the inversion of the stereochemistry of **5A** in aqueous solution. Here the direction in favour of one product over another is driven more by steric factors. *Charges on the complexes have been omitted for clarity.*

While the mechanism in Figure 3.28 can explain the interconversion between **5A** and **5B**, it does not explain the bias for NH_d exchange over NH_u exchange. A look at all the data obtained so far, suggests that there are two possible reasons for this bias.

1) Steric hinderance towards deuterated water molecule getting close to the lone pair of electrons on the nitrogen's upper face (nearest the biphenyl ring). The possibility of hydrophobic repulsion by the biphenyl ring, which would overlap the upperface of the 5-membered ring system, should not be discounted as part of this theory either.

2) Molecular orbital effects of the anti-bonding orbital associated with the Ru-Cl bond stabilising the lone pair of electrons on the upper face of the nitrogen, therefore making them less available for protonation. Molecular orbital calculations on an optimised structure of **1** have shown some evidence for an overlap between the σ*-antibonding orbital of the Ru-Cl bond and what could be the upper face of a p-orbital on the nitrogen of the ethylenediamine (Figure 3.29).

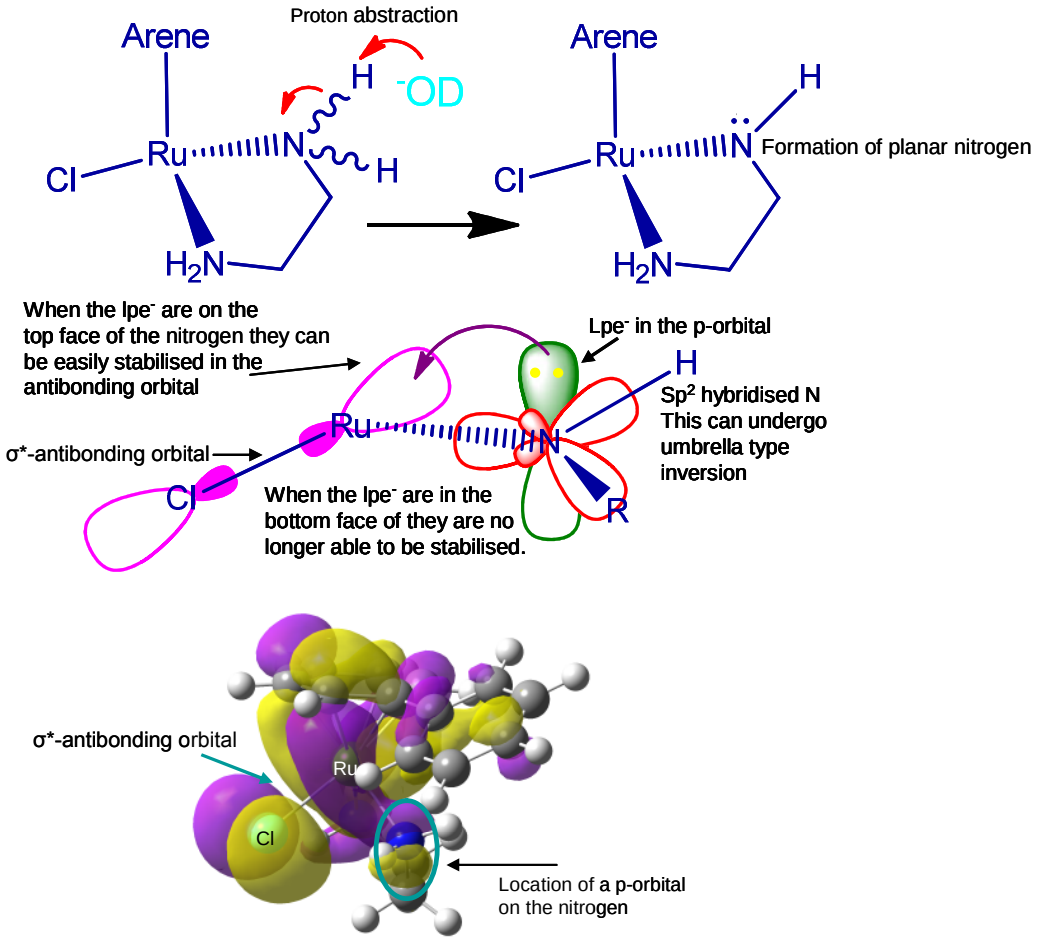

Figure 3.29. A schematic representation of how the σ*-antibonding orbital on the Ru-Cl bonds could interact with the p-orbital housing the lone pair of electrons (lpe^-) on the nitrogen.

The calculations appear to show an overlap between a p-orbital on the nitrogen and the Ru-Cl antibonding orbital. If this interaction is taking place it would be a pseudo-anomeric effect on the metal where antibonding orbitals on one bond are stabilising empty lone pairs of electrons on another. This interaction explains the bias for NH_d over NH_u proton exchange. This, together with the information so far discussed in this Chapter, leads to the conclusion that the mechanism for exchange of amino protons for deuterons (and by implication the stereo centre inversion on the N-ethyl-diethylamine adduct) involves a rate-

limiting step which is proton abstraction. Abstraction is then followed by the formation of a planar nitrogen centre. The deuteration on the nitrogen is then biased in favour of attack on the lower face due to a number of factors including steric hindrance from the biphenyl ring and molecular orbital effects stabilising the lone pair on the upper face of the nitrogen. (Figure 3.30).

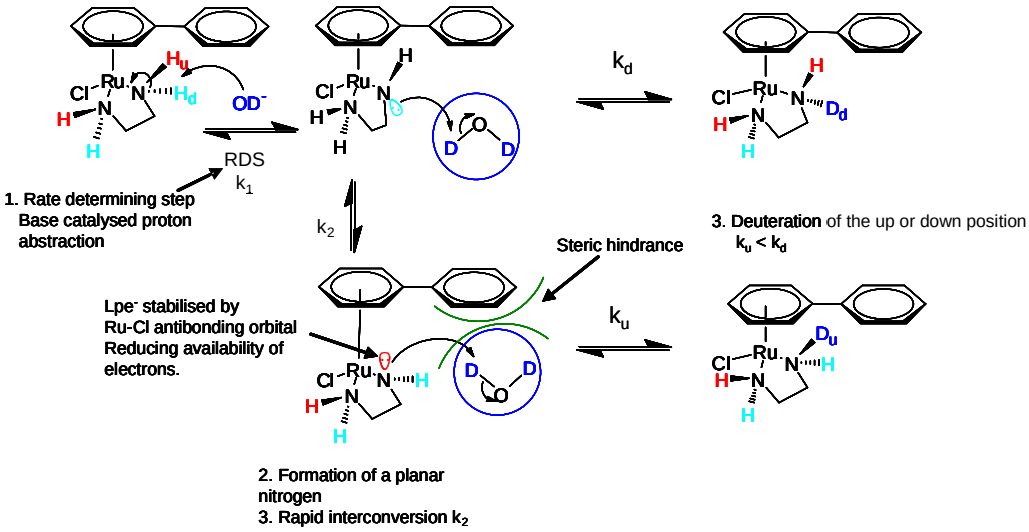

Figure 3.30. A schematic representation of the overall exchange mechanism of the $^{1}H/^{2}H$ exchange on $[Ru(\eta^{6}\text{-bip})en.Cl]^{+}$ in aqueous solution. *Charges on the complexes have been omitted for clarity.*

3.5 Conclusions

From NMR investigations into the mechanism of N-^{1}H/^{2}H exchange on [(η^{6}-bip)Ru(en)Cl]$^{+}$ a number of conclusions can be drawn.

1. Abstraction of a proton from the ethylenediamine is the rate limiting step.
2. There appear to be two possible factors influencing why one proton (NH_d) undergoes exchange more rapidly than the other (NH_u). These appear to be steric effects and effects of the Ru-Cl σ^{*}-antibonding orbital on the lone pair of the nitrogen following proton abstraction.

Putting all this information together, leads to the following mechanism being proposed (also Figure 3.30).

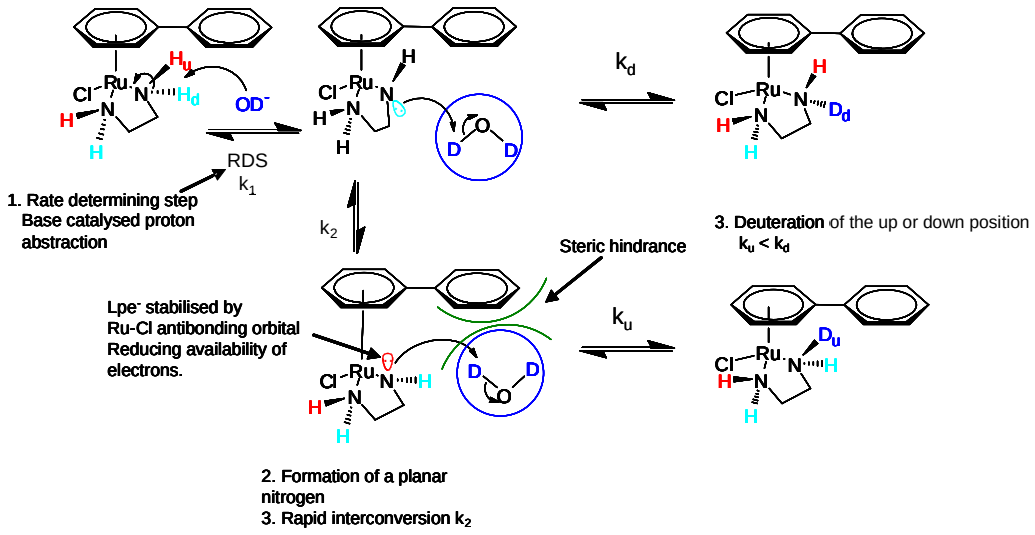

3.6 References

(1) Fernandez, R.; Melchart, M.; Habtemariam, A.; Parsons, S.; Sadler, P. J. *Chem.--A Eur. J.*, **2004**, *10*, 5173.

(2) Morris, R. E.; Aird, R. E.; Murdoch, P. d. S.; Chen, H.; Cummings, J.; Hughes, N. D.; Parsons, S.; Parkin, A.; Boyd, G.; Jodrell, D. I.; Sadler, P. J. *J. Med. Chem.* **2001**, *44*, 3616.

(3) Yan, Y. K.; Melchart, M.; Habtemariam, A.; Sadler, P. J. *Chem. Commun.*, **2005**, 4764.

(4) Liu, H.-K.; Berners-Price, S. J.; Wang, F.; Parkinson, J. A.; Xu, J.; Bella, J.; Sadler, P. J. *Angew. Chem. Int. Ed.*, **2006**, *45*, 8153.

(5) Chen, H.; Parkinson, J. A.; Parsons, S.; Coxall, R. A.; Gould, R. O.; Sadler, P. J. *J. Am. Chem. Soc.* **2002**, *124*, 3064.

(6) Chen, H.; Parkinson, J. A.; Morris, R. E.; Sadler, P. J. *J. Am. Chem. Soc.* **2003**, *125*, 173.

(7) Habtemariam, A.; Melchart, M.; Fernandez, R.; Parsons, S.; Oswald, I. D. H.; Parkin, A.; Fabbiani, F. P. A.; Davidson, J. E.; Dawson, A.; Aird, R. E.; Jodrell, D. I.; Sadler, P. J. *J. Med. Chem.* **2006**, *49*, 6858.

(8) Chen, H.; Parkinson, J. A.; Novakova, O.; Bella, J.; Wang, F.; Dawson, A.; Gould, R.; Parsons, S.; Brabec, V.; Sadler, P. J. *Proc. Natl. Acad. Sci. U. S. A.* **2003**, *100*, 14623.

(9) Zhang, Z.; Post, C. B.; Smith, D. L. *Biochemistry* **1996**, *35*, 779.

(10) Hamuro, Y.; Molnar, K. S.; Coales, S. J.; OuYang, B.; Simorellis, A. K.; Pochapsky, T. C. *J. Inorg. Biochem.* **2008**, *102*, 364.

(11) Dempsey, C. E. *Prog. Nucl. Magn. Reson. Spectrosc.* **2001**, *39*, 135.

(12) Krauss, E. M.; Cowburn, D. *Biochemistry* **1981**, *20*, 671.

(13) Mandal, C.; Englander, S. W.; Kallenbach, N. R. *Biochemistry* **1980**, *19*, 5819.

(14) Englander, S. W.; Kallenbach, N. R. *Q. Rev. Biophys.* **1983**, *16*, 521.

(15) Pluth, M. D.; Bergman, R. G.; Raymond, K. N. *J. Am. Chem. Soc.* **2008**, *130*, 6362.

(16) Wilkins, R. G. *Kinetics and Mechanism of Reactions of Transistion Metal Complexes*; 2nd ed.; VCH Publisher, Inc,: Weinheim, Germany, 1991.

(17) Wu, X.; Liu, J.; Di Tommaso, D.; Iggo, J. A.; Catlow, C. R. A.; Bacsa, J.; Xiao, J. *Chem.--A Eur. J.*, **2008**, *14*, 7699.

(18) Sandoval, C. A.; Bie, F.; Matsuoka, A.; Yamaguchi, Y.; Naka, H.; Li, Y.; Kato, K.; Utsumi, N.; Tsutsumi, K.; Ohkuma, T.; Murata, K.; Noyori, R. *Chem.--An Asian J.* **2010**, *5*, 806.

(19) Ohkuma, T.; Utsumi, N.; Tsutsumi, K.; Murata, K.; Sandoval, C.; Noyori, R. *J. Am. Chem. Soc.* **2006**, *128*, 8724.

(20) Hayes, A. M.; Morris, D. J.; Clarkson, G. J.; Wills, M. *J. Am. Chem. Soc.* **2005**, *127*, 7318.

(21) Hannedouche, J.; Clarkson Guy, J.; Wills, M. *J. Am. Chem. Soc.* **2004**, *126*, 986.

(22) Casey, C. P.; Johnson, J. B. *J. Org. Chem.* **2003**, *68*, 1998.

(23) Haack, K.-J.; Hashiguchi, S.; Fujii, A.; Ikariya, T.; Noyori, R. *Angew. Chem.Int. Ed.* **1997**, *36*, 285.

(24) Fryzuk, M. D.; Petrella, M. J.; Patrick, B. O. *Organometallics* **2005**, *24*, 5440.

(25) Abdur-Rashid, K.; Clapham, S. E.; Hadzovic, A.; Harvey, J. N.; Lough, A. J.; Morris, R. H. *J. Am. Chem. Soc.* **2002**, *124*, 15104.

(26) Davies, M. W.; Shipman, M.; Tucker, J. H. R.; Walsh, T. R. *J. Am. Chem. Soc.* **2006**, *128*, 14260.

(27) Davies, M. W.; Clarke, A. J.; Clarkson, G. J.; Shipman, M.; Tucker, J. H. R. *Chem. Commun., (Cambridge, United Kingdom)* **2007**, 5078.

(28) Nakazawa, H.; Sakaguchi, U.; Yoneda, H.; Morimoto, Y. *Inorg. Chem.* **1981**, *20*, 973.

(29) Yoneda, H.; Nakashima, Y. *Bull. Chem. Soc. Jap.* **1974**, *47*, 669.

(30) Nakashima, Y.; Sakaguchi, U.; Yoneda, H. *Bull. Chem. Soc. Jpn.* **1975**, *48*, 762.

(31) Kojima, M.; Hibino, T.; Ouyang, Y.; Fujita, J. *Inorg. Chim. Acta* **1986**, *117*, 1.

(32) Yoneda, H.; Sakaguchi, U.; Nakashima, Y. *Bull. Chem. Soc. Jpn.* **1975**, *48*, 209.

(33) Taura, T.; Sakaguchi, U.; Yoneda, H. *Bull. Chem. Soc. Jpn.* **1976**, *49*, 1867.

(34) House, D. A. *Coord. Chem. Rev.*,**1992**, *114*, 249.

(35) Sheldrick, G. M., SADABS Version 2006-1,*University of Gottingen, Gottingen, Germany* **2006**.

(36) Mo, Y.-d.; Fu, Z.-q.; Fan, H.-f.; van Smaalen, S.; Lam, E. J. W.; Beurskens, P. T. *Acta Crystallogr., Sect. A Found. Crystallogr.* **1996**, *A52*, 640.

(37) Richardson, D. E.; Walker, D. D.; Sutton, J. E.; Hodgson, K. O.; Taube, H. *Inorg. Chem.* **1979**, *18*, 2216.

(38) Wang, F.; Chen, H.; Parsons, S.; Oswald, I. D. H.; Davidson, J. E.; Sadler, P. J. *Chem.--A Eur. J.* **2003**, *9*, 5810.

(39) Sakaguchi, U.; Maeda, K.; Yoneda, H. *Bull. Chem. Soc. Jpn.* **1976**, *49*, 397.

(40) Housecroft, C. E.; Sharpe, A. G. *Inorganic Chemistry*; Third ed.; Pearson Education Ltd.: Harlow, England, 2008.

(41) Connelly, G. P.; Bai, Y.; Jeng, M. F.; Englander, S. W. *Proteins Struct., Funct., Genet.* **1993**, *17*, 87.

(42) Ma, G.; Hibino, T.; Kojima, M.; Fujita, J. *Bull. Chem. Soc. Jpn.* **1989**, *62*, 1053.

Chapter 4

Influence of Arenes and Pyridine Derivatives on the Kinetics of N-H/D Exchange in $[Ru(\eta^6\text{-arene})(en)(X)]^{n+}$ complexes

Chapter 4

Influence of Arenes and Pyridine Derivatives on the Kinetics of N-H/D Exchange in $[Ru(\eta^6\text{-arene})(en)(X)]^{n+}$ complexes

4.1 Introduction

Ruthenium(II) complexes with pyridine derivatives have many chemical purposes, from solar cell devices[1] to potential anticancer drugs[2]. The pyridine derivative ligands have varying electronic effects on the ruthenium and play an important role in tuning the electrochemistry of the compounds. Studies have shown that changes in pyridines on metals can change many properties including spin crossover energy[3], photochemistry[4] and redox chemistry.[5] These studies were found to yield well-fitting Hammett plots, showing that there is often a relationship between the pK_a of the ligand and the observed activity.

Since ruthenium and nitrogen-containing aromatics are deemed "soft" metals and "soft" donors, respectively,[6] they have a high affinity for each other and form very stable bonds. Indeed, it is this strong affinity of ruthenium for nitrogen which is believed to dominate the mechanism of action of ruthenium(II) η^6-arene anticancer complexes in the body leading to their cytotoxic activity[7]. The chlorido complex $[(\eta^6\text{-biphenyl})Ru(en)Cl]^+$ (**1**) hydrolyses to form the aqua complex[8] (**1a**), via an associative S_N2 type reaction,[9] and can bind preferentially to N7 of guanine residues on DNA[10-13], peptides[14], histidine[15,16], cytochrome c[16,17] and enzymes[13] (Figure 4.1).

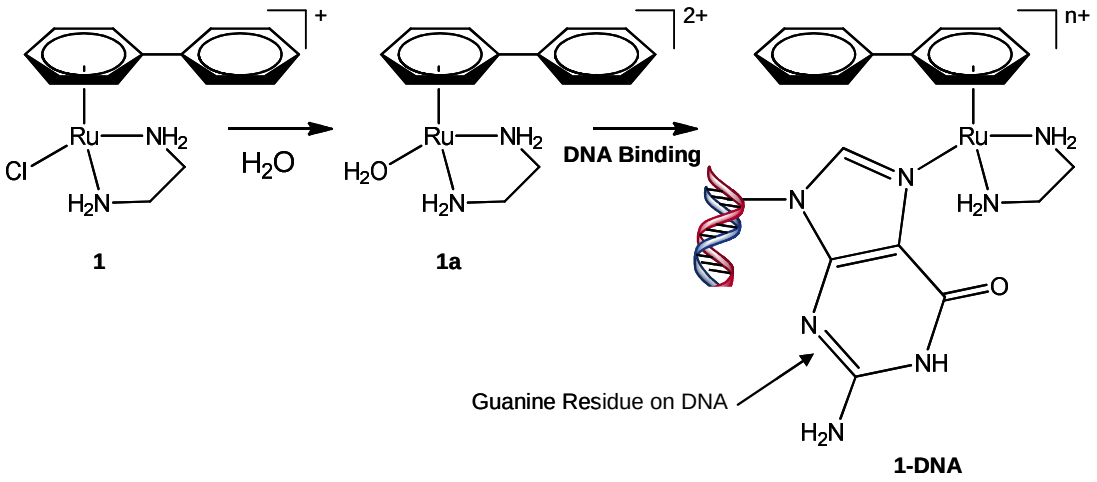

Figure 4.1. The hydrolysis of **1** to **1a** and subsequent binding to DNA via the N7 of guanine residues.

In Chapter 3, the effects of pH*, ionic strength and temperature on the exchange rates of the amino protons for deuterons in the ethylenediamine ligand on $[(\eta^6\text{-biphenyl})Ru(en)Cl]^+$ were investigated. Results showed that the reaction is pseudo first order via a dissociative pathway (ionic strength dependent) and is pH* dependent. The results also implied that the rate-limiting step is abstraction of a proton from the nitrogen of the ethylenediamine ligand (Figure 4.2). More noticeable was the difference in exchange rates for protons which point towards the biphenyl ring system (H_u) and those which point away from the ring system (H_d). It was observed that the upward-pointing protons exchanged much more slowly than those which point away from the ring system. A number of theories for this difference were proposed including; steric effects of the biphenyl ring system, steric hindrance in the abstraction of the protons from the ethylenediamine, and effects of the chloride–ruthenium σ^* anti-bonding orbital on stabilising the negative charge on the nitrogen after abstraction of a proton.

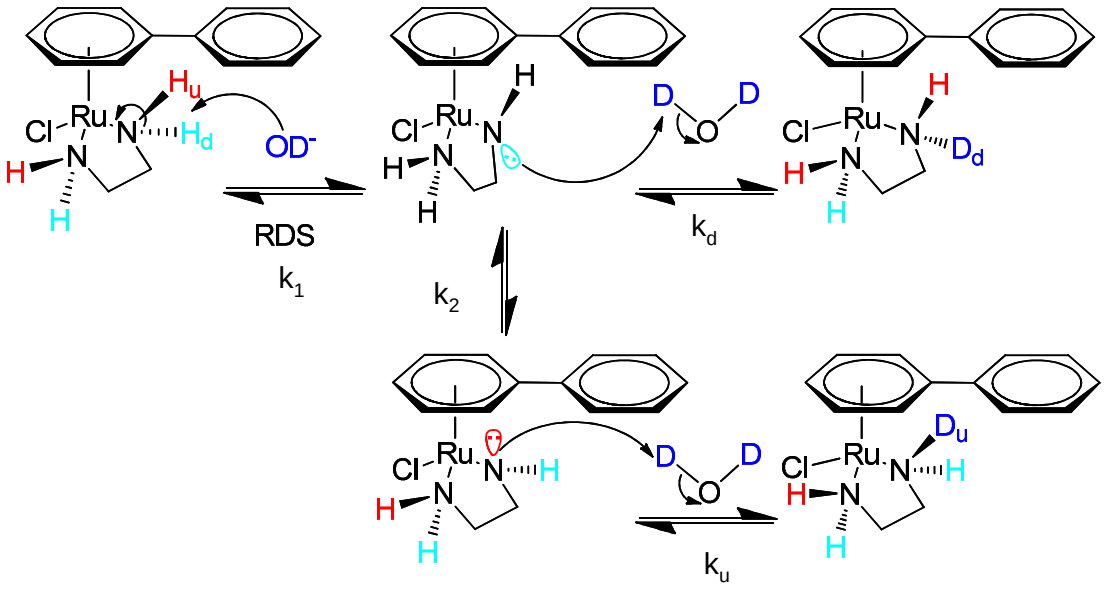
Cl
Ru
N
H
H
H

In this Chapter the effects of changing the arene and the effects of changing the electron-donating ability of pyridine derivatives, in the chlorido position on the rates of NH/D exchange are investigated. In addition to this, the effects of ligand on the ruthenium on the isomeric bias (favourability of NH_d exchange over NH_u exchange) for substitution of the up and down protons for deuterons is investigated. The rationale for use of 4-substituted pyridines was the ease with which the electronic character of the ligand could be changed without steric influences. Pyridine ligands have tuneable pK_a values by changing the 4-substituent and so their effects on the ruthenium and the NH/D exchange rates as a result of electronic effects on the ruthenium can easily be investigated. Another benefit of using pyridine ligands is that these complexes do not readily undergo hydrolysis and so there is no need to suppress hydrolysis, as was the case with the chlorido complexes.

4.2 Results

A series of $[Ru(II)(\eta^6\text{-arene})enX]^{2+}$ complexes was synthesised as detailed in Figure 4.3. Crystal structures were obtained and analysed. The rate of N-H/D exchange on the amine protons was determined for each complex and compared to those determined in Chapter 3. This enabled the effects of different pyridine groups and arenes on the rates of exchange to be investigated. Finally computational analysis revealed molecular orbitals that may affect the rates of exchange.

4.2.1 Synthesis and Characterisation

The novel complexes synthesised in this Chapter are shown in Figure 4.3. All were made via the aqua adduct of the relevant chlorido complex, $[(\eta^6\text{-biphenyl})Ru(en)Cl]^+$ or $[(\eta^6\text{-benzene})Ru(en)Cl]^+$, were converted to the aqua adducts by removal of the chloride ligand by precipitation with silver nitrate in water. The aqua adduct was then reacted with the pyridine derivative. Ligand substitution readily occurred. The synthesised pyridine complexes do not readily hydrolyse and are stabilised by strong Ru-N bonding.

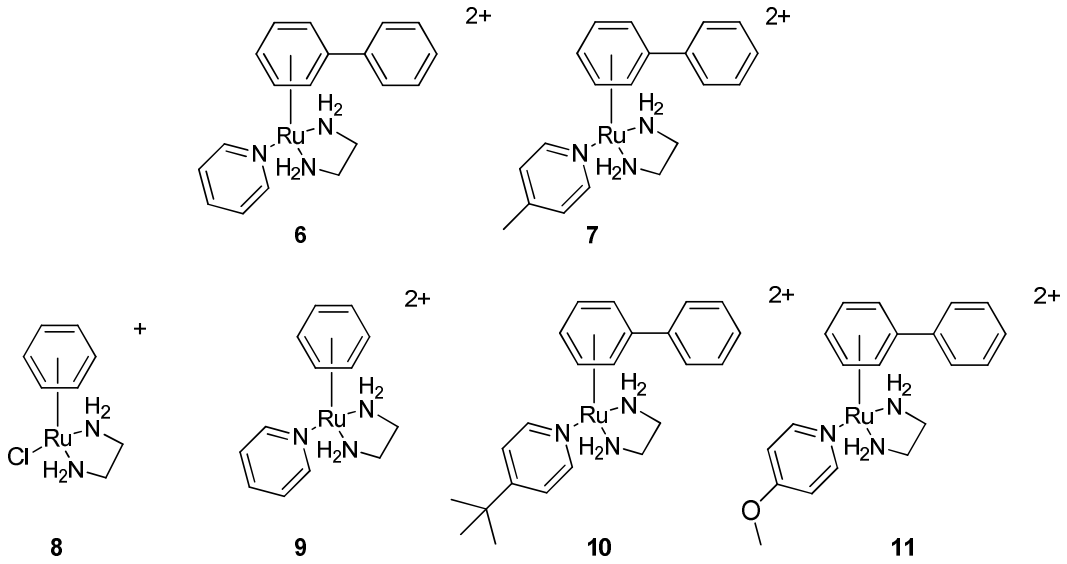

Figure 4.3: The ruthenium complexes synthesised and studied in this chapter. All these complexes (except **6** and **8**) are novel complexes.

4.2.2 X-Ray crystal structures

X-ray diffraction data were collected and the structures solved by Dr Guy Clarkson (University of Warwick). Diffraction data for complexes [(η^6-bip)Ru(en)(*N*-4-Me-pyr)]2PF_6, **7-2PF$_6$** and [(η^6-ben)Ru(en)(*N*-pyr)].2PF_6 **9-2PF$_6$** were collected while the crystal was held at 120 K on an Oxford Cryosystem Cryostream Cooler using a Siemens SMART three circle system with CCD detector. The structures were solved by direct methods using SHELXS[18] and hydrogens added using Fourier methods.

Diffraction data for complexes [(η^6-bip)Ru(en)(*N*-4-t-Bu-pyr)].2PF_6 **10-2PF$_6$** and [(η^6-bip)Ru(en)(*N*-4-Me-O-pyr)].2PF_6 **11-2PF$_6$** were collected at 100 K (**10-2PF$_6$**) or 296 K (**11-2PF$_6$**) on an Oxford diffraction Gemini four-circle system equipped with a Ruby CCD area detector. The crystal of **10-2PF$_6$** was held with the Oxford Cryosystem Cryosteam Cobra in the detector. For **11-2PF$_6$**, the crystal was glued to a glass fibre and placed in the path of the X-rays. Structures were

solved by direct methods using SHELXS (1990)[19] and refinement was carried out with SHELXS (1997)[18]. Mercury 2.3[20,21] and Ortep 3.2[22] were used to view crystal structures, to measure angles and distances and to produce the images shown in this thesis. Only complex **10_2PF$_6$** crystallised with a solvent molecule (H_2O) in the crystal structure. The author believes this is the first time any of these x-ray crystal structures have been reported.

The 3D structures of these complexes and their corresponding atomic numbering schemes are shown below in Figure 4.4 and 4.5. The corresponding crystallographic data are listed in Tables 4.1 and 4.2. Table 4.3 contains a comparison of all the bond lengths across the series.

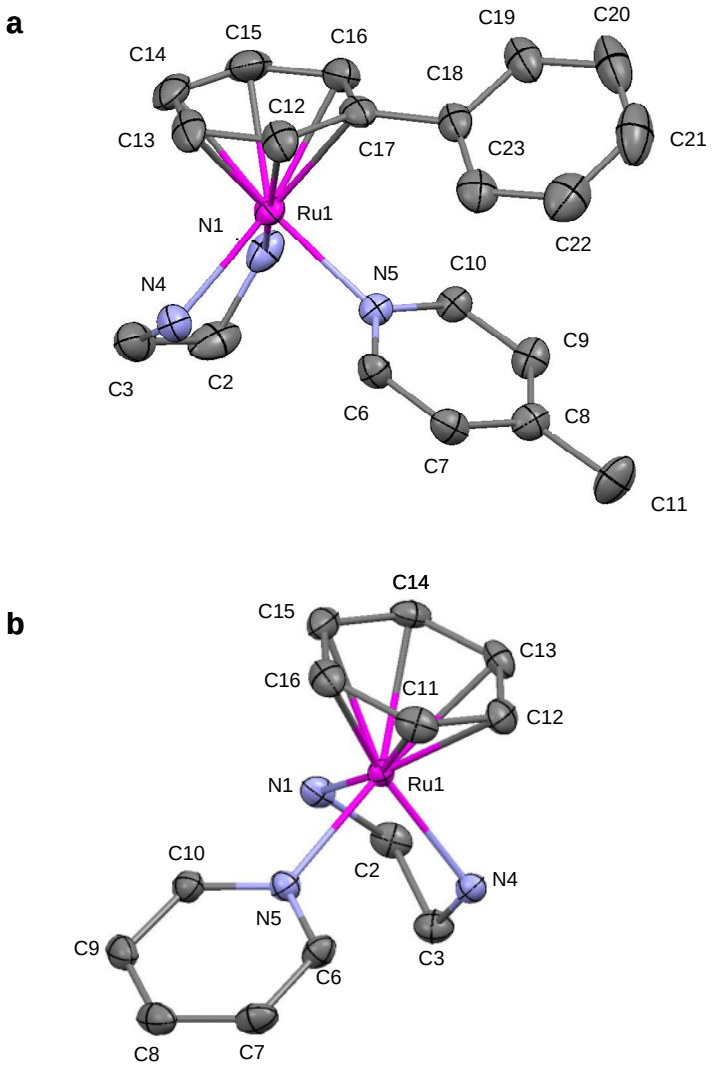

Figure 4.4: X-ray crystal structure and atom numbering scheme for a) [(η^6-bip)Ru(en)(*N*-4-Me-pyr)] (**7**), and b) [(η^6-ben)Ru(en)(*N*-pyr](**9**). The thermal ellipsoids show 50% probability. The PF_6^- counterions and all hydrogen atoms are omitted for clarity

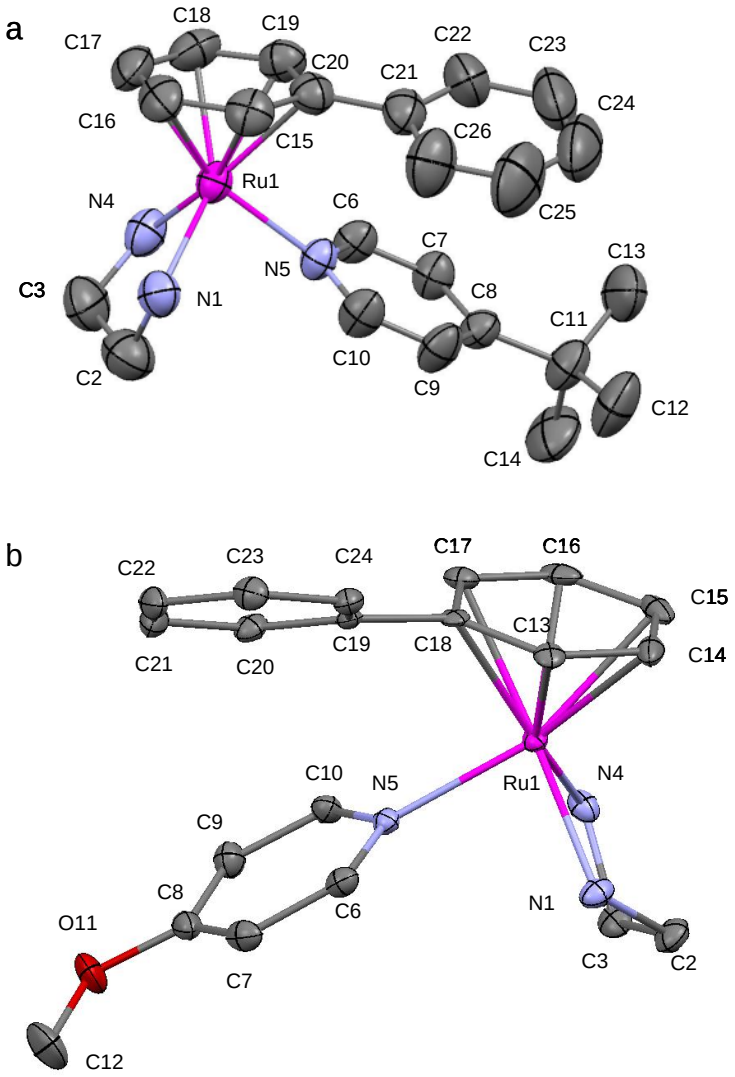

Figure 4.5. X-ray crystal structure and atom numbering scheme for a) [(η^6-bip)Ru(en)(*N*-4-t-Bu-pyr)] (**10**) (the water of crystallisation, all hydrogens, the PF_6^- counterions and the disorder of the t-butyl group are omitted for clarity), and b) [(η^6-bip)Ru(en)(*N*-4-Me-O-pyr)](**11**). Again the PF_6^- counterions and hydrogen atoms are omitted for clarity. The thermal ellipsoids show 50% probability. *Note: the larger ellipsoids for **10** are due to data being acquired at higher temperature (296 K)*

All structures showed the expected "piano-stool" geometry that is typical of this type of complex.[7] The arene is π-bound to the ruthenium atom and forms the "seat" of the piano stool, while the nitrogen bound ligands take the role of the "legs" and "feet" of the stool. All complexes were found to have similar distances between ruthenium and the centroid of the π-bound arene of 1.684 - 1.689 Å. In all the biphenyl complexes the free phenyl ring is in close proximity to the aromatic ring of the pyridine ligand, however not close enough to be classified as π-stacking. Crystallographic data are shown in Table 4.1 – 4.2 and a selection of bond lengths and angles are shown in Table 4.3. Within the long range packing structure of these complexes some CH-π interactions were observed. This were more intermolecular interactions and as a result of packing within the matrix as opposed to intramolecular interactions.

Table 4.1: Crystallographic data for complexes **7_2PF$_6$** and **9_2PF$_6$**

	7_2PF$_6$	**9_2PF$_6$**
	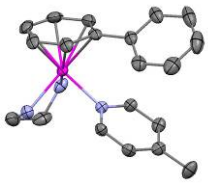	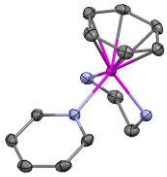
Formula	$C_{20}H_{25}F_{12}N_3P_2Ru$	$C_{13}H_{19}F_{12}N_3P_2Ru$
Molar mass	698.44	608.32
Crystal system	Triclinic	Monoclinic
Crystal size /mm	0.40 x 0.18 x 0.08	0.12 x 0.06 x 0.02
Space group	P-1	P2(1)/n
Crystal	Yellow block	Yellow block
a / Å	11.3660(2)	9.7734(2)
b / Å	13.7029(4)	13.2206(2)
c / Å	17.5135(4)	15.5490(3)
α / deg	91.9920(10)	90
β / deg	91.405(2)	95.8130(10)
γ / deg	108.893(2)	90
T / K	120(2)	120(2)
Z	4	4
R [F > 2σ (F)][a]	0.0445	0.0366
R_w[b]	0.1251	0.0771
GOF[c]	1.027	1.099
Δρ max and min / eÅ^{-3}	1.152, -0.963	0.466, -0.585

[a] $R = \sum||F_o| - |F_c||/\sum|F_o|$. [b] $R_w = [\sum w(F_o^2 - F_c^2)^2/\sum wF_o^2)]^{1/2}$. [c] $GOF = [\sum w(F_o^2 - F_c^2)^2/(n-p)]^{1/2}$, where n = number of reflections and p = number of parameters.

Table 4.2. Crystallographic data for complexes **10_2PF$_6$** and **11_2PF$_6$**

	10_2PF$_6$.H$_2$O	**11_2PF$_6$**
	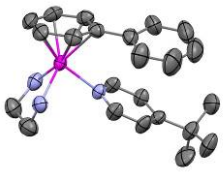	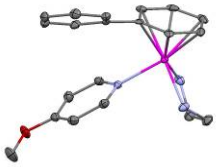
Formula	$C_{22}H_{33}F_{12}N_3OP_2Ru$	$C_{20}H_{25}F_{12}N_3OP_2Ru$
Molar mass	758.53	714.44
Crystal system	Triclinic	Monoclinic
Crystal size /mm	0.80 x 0.14 x 0.04	0.40 x 0.08 x 0.02
Space group	P-1	P2(1)/c
Crystal	Light yellow block	Yellow rod
a / Å	9.6369(3)	9.8194(3)
b / Å	11.2578(3)	27.6354(8)
c / Å	15.9640(3)	9.5380(3)
α / deg	102.5993(19)	90
β / deg	97.737(2)	101.396(3)
γ / deg	112.388(2)	90
T / K	296	100
Z	2	4
R [F > 2σ (F)][a]	0.0388	0.0305
R_w [b]	0.1149	0.0577
GOF[c]	1.097	0.918
Δρ max and min / eÅ^{-3}	0.892, -0.556	0.852, -0.834

[a] $R = \sum||F_o| - |F_c||/\sum|F_o|$. [b] $R_w = [\sum w(F_o^2 - F_c^2)^2/\sum wF_o^2)]^{1/2}$. [c] $GOF = [\sum w(F_o^2 - F_c^2)^2/(n-p)]^{1/2}$, where n = number of reflections and p = number of parameters

Table 4.3. Selected bond lengths (Å) and angles (º) for complexes **7, 9, 10** and **11.**

Bond/Angle	**7-2PF$_6$**	**9-2PF$_6$**	**10-2PF$_6$.H$_2$O**	**11-2PF$_6$**
Ru1-N1	2.128(3)	2.133(3)	2.117(3)	2.127(2)
Ru1-N4	2.127(3)	2.126(3)	2.117(2)	2.1421(19)
Ru1-N5	2.106(3)	2.119(3)	2.130(3)	2.1131(18)
Ru – C (arene)	2.201(4)	2.192(3)	2.193(3)	2.176(2)
	2.177(4)	2.183(3)	2.197(3)	2.190(2)
	2.214(4)	2.207(3)	2.203(4)	2.198(2)
	2.177(4)	2.205(3)	2.176(4)	2.204(2)
	2.201(4)	2.204(3)	2.203(4)	2.212(2)
	2.245(3)	2.198(3)	2.225(3)	2.235(2)
Ru – Centroid of arene	1.688	1.685	1.689	1.685
N1-Ru-N4	79.26(13)	78.54(11)	79.21(13)	78.88(8)
N1-Ru-N5	86.99(11)	88.23(10)	88.45(11)	85.59(8)
N2-Ru-N5	89.70(11)	86.23(10)	85.94(11)	86.98(8)

Other interesting features of these complexes are the "biphenyl orientation" angle relative to the X ligand, and the "biphenyl twist" angle, which is the angle through which the free (pendant) phenyl ring on the biphenyl has twisted from the plane of the bound phenyl ring (i.e.: the seat of the piano stool) (Figure 4.6).

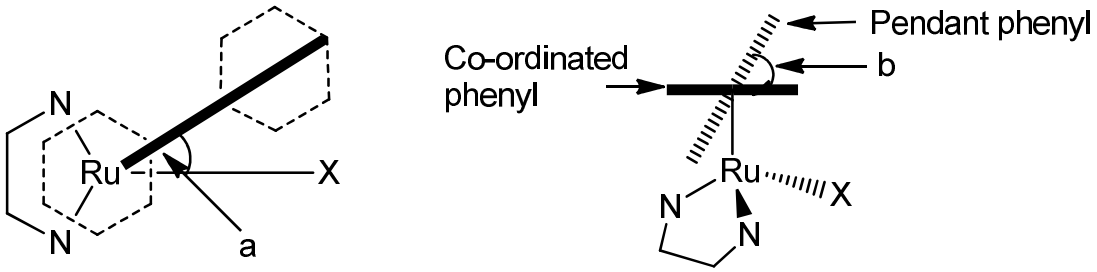

Figure 4.6. Schematic of the biphenyl orientation (a) and biphenyl twist (b) angles

These angles are detailed in Table 4.4, for complexes **4, 6,** and **7**.

Table 4.4. Biphenyl orientation and twist angles (^{o}) for complexes **4, 6** – **7**.

	7-2PF$_6$	**10-2PF$_6$.H$_2$O**	**11-2PF$_6$**
Biphenyl orientation	7.26	14.71	31.51
Twist angle	29.64	19.31	22.38

There appears to be no obvious cause other than a packing effect, for these twists and the biphenyl orientation. It was noted in the packing of the crystal cell, that there is some interaction between hydrogens on one molecule with the centre of the π-cloud on the free phenyl ring of another molecule. This appeared to lead to

efficient packing within the cell. This type of interaction is called CH- π bonding and is widely seen in inorganic complexes packing structures.

4.2.3 N-H/D exchange rates

As was observed in Chapter 3 for $[(\eta^6\text{-biphenyl})Ru(en)Cl]^+$, the up and downward pointing NH protons exchange with deuterium at different rates. Details of the exchange rates and decay curves for each of the complexes studied in this chapter are listed below. These pyridine complexes do not appear to hydrolyse and with that in mind all the samples were prepared as low ionic-strength solutions. Samples were prepared in acidic solution (pH^* detailed in each experiment) in an attempt to make sure $^1H/^2H$ exchange was slow enough to be observable.

4.2.3.1 Determination of rates

Rates were determined in a very similar manner to those of Chapter 3 (*c.f.* **§2.3** for method). Unlike **1**, the NMR signals of complexes with pyridine derivatives do not have an overlap of NH_u and the bound phenyl region. This made integration of peak areas simpler and so the method used is summarised in Figure 4.7.

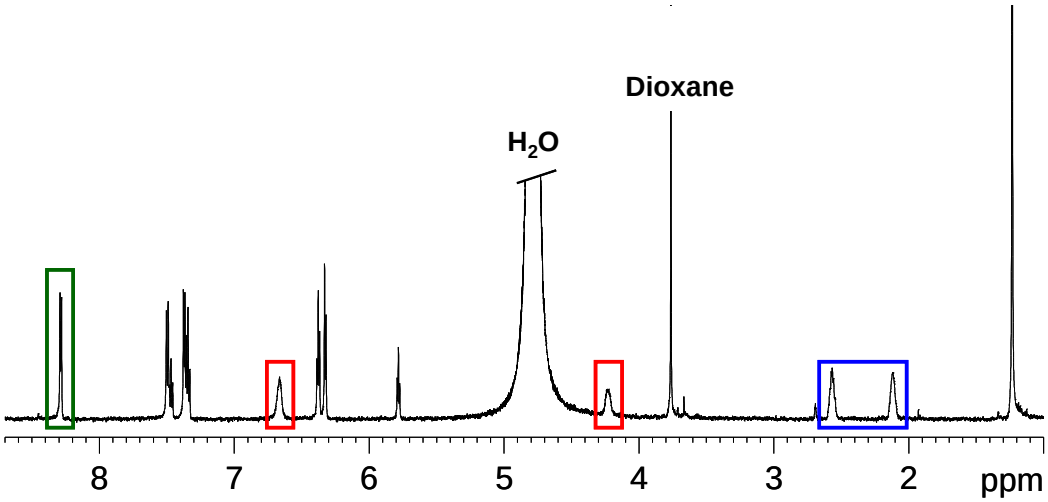

Figure 4.7. ^{1}H NMR spectrum of [(η^6-bip)Ru(en)(*N*-4-Me-O-pyr)].2PF6. **[11-2PF6]** in D_2O, within 20 minutes of mixing. Highlighted in green is the peak for *H*-*ortho*-4-methyoxypyridine. The value of this integral was set at 2 and used to normalise the integrals of the N-H peaks. (red (N*H*$_2$-en) and blue (C*H*$_2$-en)).

4.2.3.2 [(η^6-bip)Ru(en)*N*-pyr]$^{2+}$ [6]

Complex **6** was dissolved in D_2O at 298 K with pH* = 6.3. NMR spectra were recorded over time and are shown in Figure 4.8. It can be seen that the peak for the NH_d protons disappears significantly faster than that for the NH_u protons.

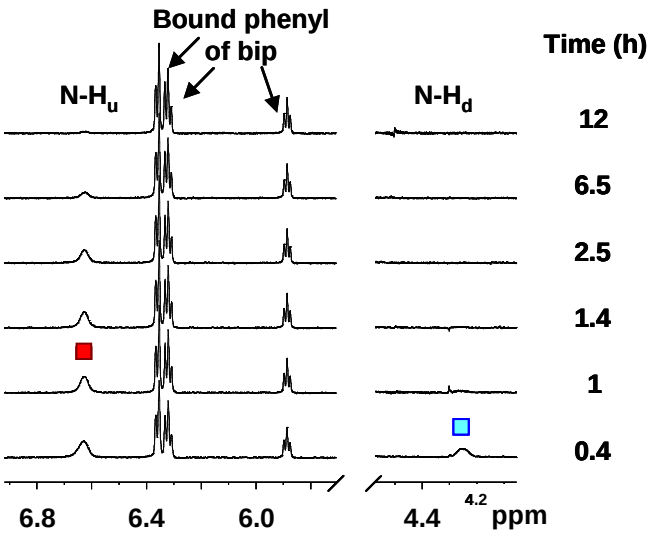

Figure 4.8. N-H segments of the ^{1}H NMR spectra over time of **6** in D_2O at 298 K pH* = 6.3 and the time from mixing to the first NMR acquisition was 20 min 43 s. The upward orientated protons (■) and the downward orientated protons (■) are marked for clarity.

Plotting the intensity of the peaks against time produced two exponential decay curves (Figure 4.9) and yielded the rate constants and the half times for the H – D exchange reactions (Table 4.5).

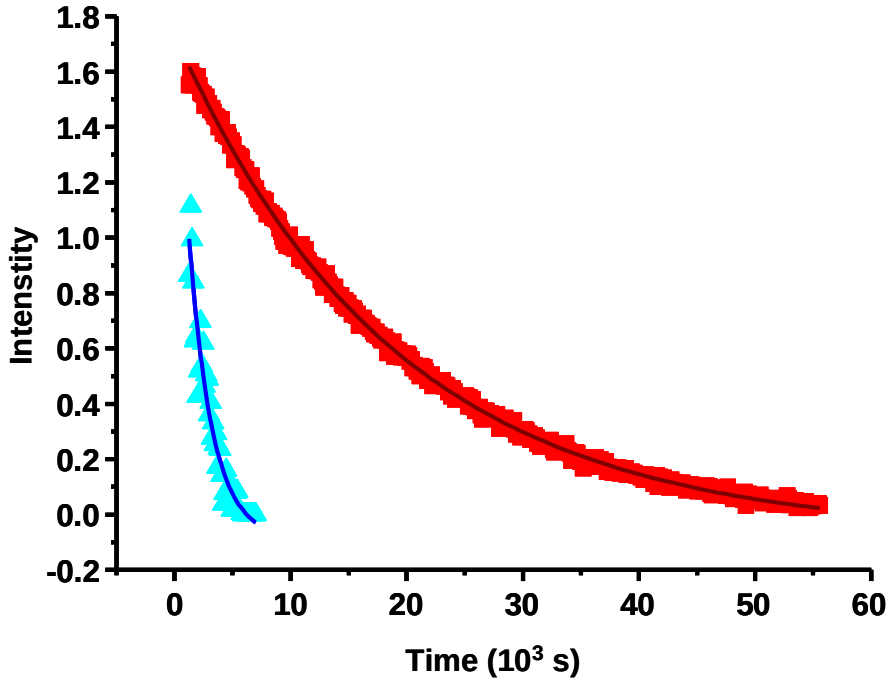

Figure 4.9. Exponential decay curves of the intensity of the up ■ and down ▲ facing protons of **6** at pH^* = 6.3 in D_2O. The lines are best fits for the NH_u (—) and the NH_d (—) protons.

Table 4.5. Kinetic data for the deuterium exchange of N-H_u and N-H_d on **6**.

Proton	Rate Constant (s^{-1})	Half life (s)
N-H_u	5.66 x 10^{-5}	12.5 x 10^3
N-H_d	55.2 x 10^{-5}	1.26 x 10^3

4.2.3.3 $[(\eta^6\text{-ben})Ru(en)Cl]^+$ [8]

A sample of **8** was dissolved in 154 mM NaCl in D_2O and the decay of the intensity of the exchange of N-H/D was observed over time by monitoring the NMR peaks, Figure 4.10.

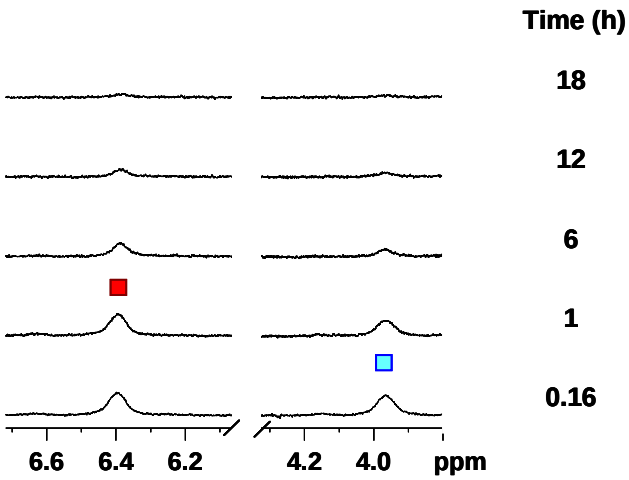

Figure 4.10. Decay of the N-H ^{1}H NMR peaks over time for **8** in 154 mM NaCl in D_2O, pH^* = 7.4 and at 298 K. The time from mixing to the first NMR acquisition was 9 min 50 s. The peaks for the upward orientated NH_u protons (■) and the downward orientated NH_d protons (■) are labelled.

Exponential fits to plots of the intensities of the peaks against time (Figure 4.11) yielded rate constants and half-times for the exchange and shown in Table 4.6. It is noticeable that the differences in exchange rates are not as dramatically different for this complex as seen for others.

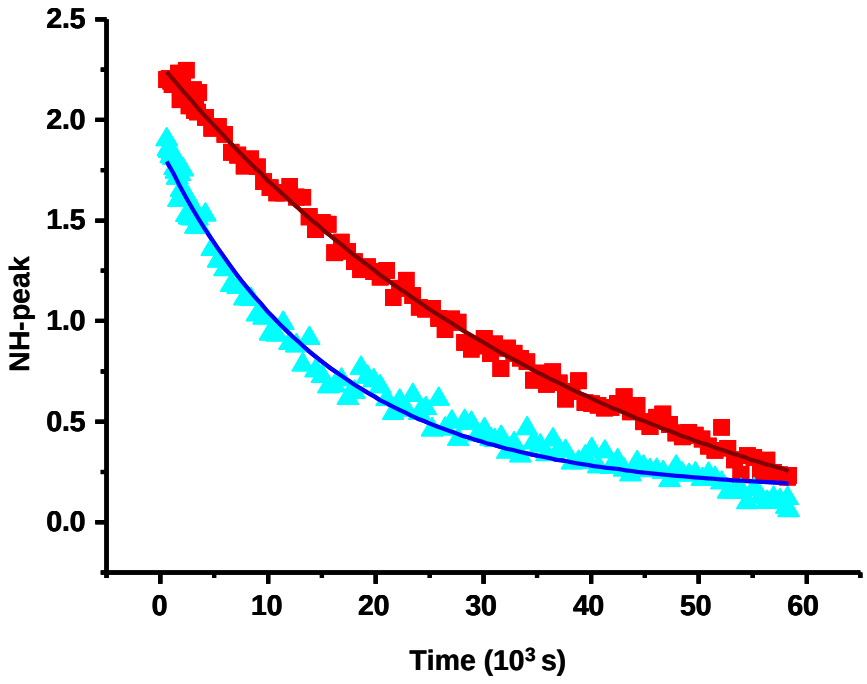

Figure 4.11. Exponential decay curves of the intensity of the up ■ and down ▲ facing protons of **8** at pH* = 7.4 in 154 mM NaCl in D_2O at 298 K. The lines are best fits for the NH_u (—) and the NH_d (—) protons, with the decay constants in Table 4.6.

Table 4.6. Kinetic data for the exchange of N-H_u and N-H_d on **8**.

Proton	Rate Constant (s^{-1})	Half life (s)
N-H_u	2.766 x 10^{-5}	25.4 x 10^{3}
N-H_d	6.379 x 10^{-5}	10.9 x 10^{3}

4.2.3.4 [(η^6-biphenyl)Ru(en)(*N*-4-Me-py)]2PF_6. [7]

When the rates of exchange for the pyridine complex (**6**) are compared to those for the chlorido adduct (**1**), it was noted that the exchange rates increased when the charge on the complex increased. To control this and make rates of N-H/D exchange

observable, the pH^* of the sample was lowered (as Chapter 3 has shown that exchange is base catalysed).

A sample of **7** was dissolved in D_2O and the intensity of the N-H peaks in a ^1H NMR spectrum was recorded at various time intervals. Selected NMR spectra showing the decrease in the N-H peak intensities over time is shown in Figure 4.12.

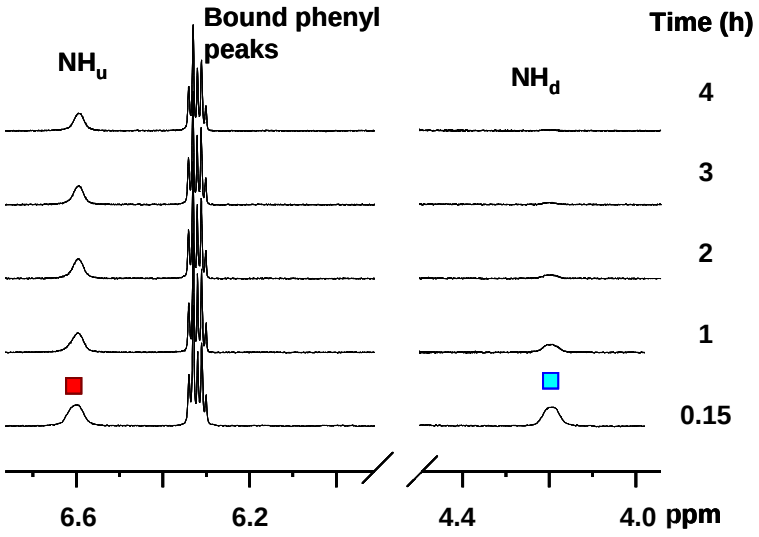

Figure 4.12. N-H segments of the ^1H NMR spectra over time of **7** in D_2O at 298 K pH^* = 5.68 and the time from mixing to the first NMR acquisition was 9 min 10 s. The upward, $N\text{-}H_u$ (■) and the downward $N\text{-}H_d$ (■) orientated protons are marked for clarity.

Plots of the intensity of the peak against time produced two very different exponential decay curves (Figure 4.13). The rate constants and the half times for the exchange reactions are shown in Table 4.8.

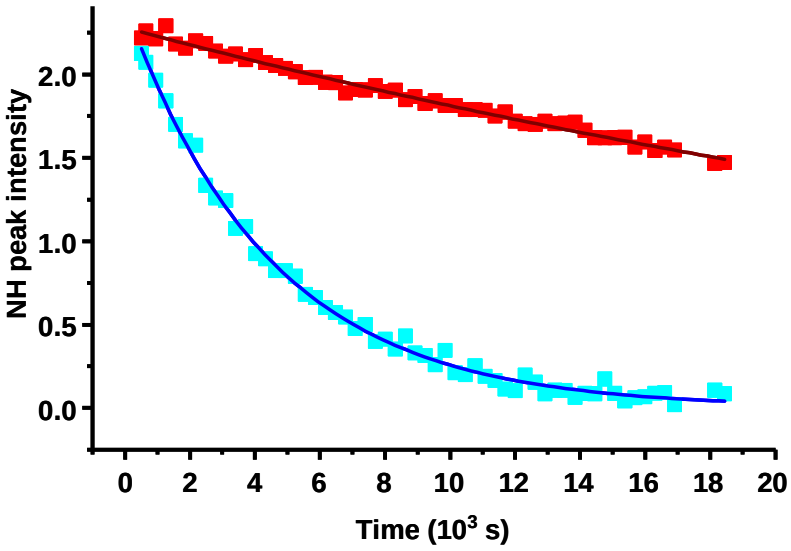

Figure 4.13. Time dependence of the decay of the NH_u (■) and NH_d (■) ^1H NMR peaks for complex **7** in D_2O at pH^* = 5.68 and 298 K. The solid lines are the best fits for first order exponential decays and corresponding to the rate constants in Figure 4.7.

Table 4.7. Kinetic data for the exchange of N-H_u and N-H_d on **7** at pH^* = 5.68.

Proton	Rate Constant (s^{-1})	Half life (s)
N-H_u	2.19 x 10^{-5}	31.7 x 10^3
N-H_d	23.11 x 10^{-5}	3 x 10^3

4.2.3.5 [(η^6-ben)Ru(en)(*N*-pyr)]$^{2+}$ [9]

Since comparisons have been made between different charges on the biphenyl complexes, it is interesting to look at the differences in charges on the benzene complexes. Figure 4.14 shows the time dependence of the ^1H NMR spectrum of **9** in D_2O, pH^* = 5.38 at 298 K.

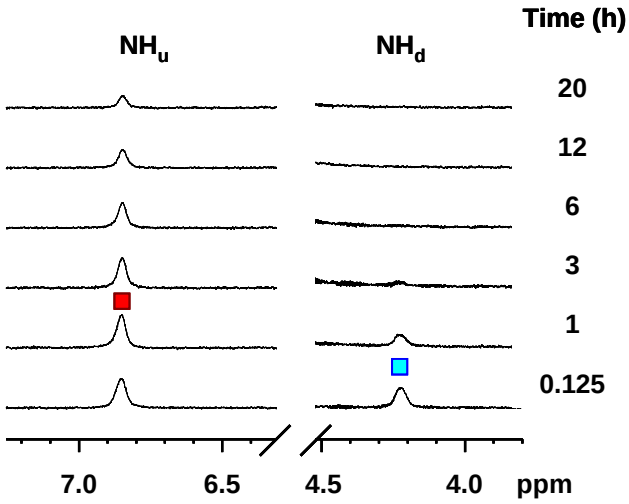

Figure 4.14. Time dependence ^{1}H NMR spectra of **9** in D_2O, pH^* = 5.38 at 298 K showing the decrease in the intensity of the N-H_u (■) and N-H_d (■) peaks over time.

Exponential fits showing the effects of time on the intergrals of the NH peaks were plotted (Figure 4.15). From this the rate constants for the exchange of protons and deuterons were determined and are shown in Table 4.8.

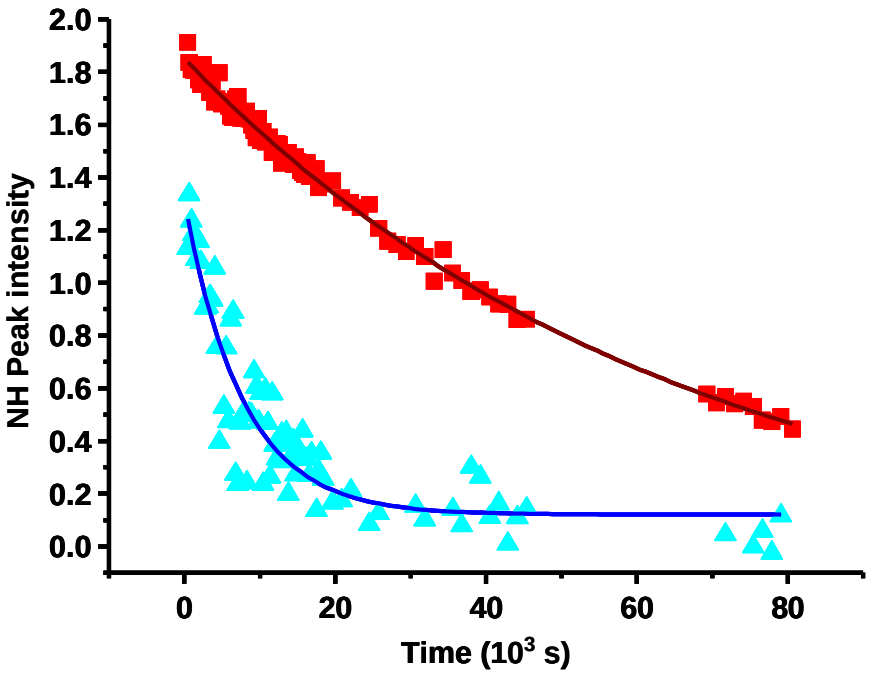

Figure 4.15. Time dependent decay of the integrals of ^{1}H NMR peaks of the NH_u (■) and the NH_d (▲) protons of **9** in D_2O at pH^* = 5.38 at 298 K. The best fit lines are shown in — for up and — for the down protons respectively and yield the rate constants listed in Table 4.8. The large spread of data points in the 0 – 20 x 103 s region is due to the low signal-to-noise ratio since there is peak overlap with the H_2O signal in the NMR spectra.

Table 4.8. Kinetic data for the exchange of N-H_u and N-H_d on **9** at pH^* = 5.68.

Proton	Rate Constant (s^{-1})	Half life (s)
N-H_u	1.7 x 10^{-5}	40.8 x 10^{3}
N-H_d	13.4 x 10^{-5}	5.2 x 10^{3}

4.2.3.6 [(η^6-bip)Ru(en)(*N*-4-t-Bu-pyr)] [10]

As part of the series of pyridine complexes, **10** was synthesised and the exchange of amino protons on the ethylenediamine ligand was observed using ^{1}H NMR of solutions in D_2O. A selection of NMR spectra showing the decrease in the intensity of the N-H peaks with respect to time are shown in Figure 4.16.

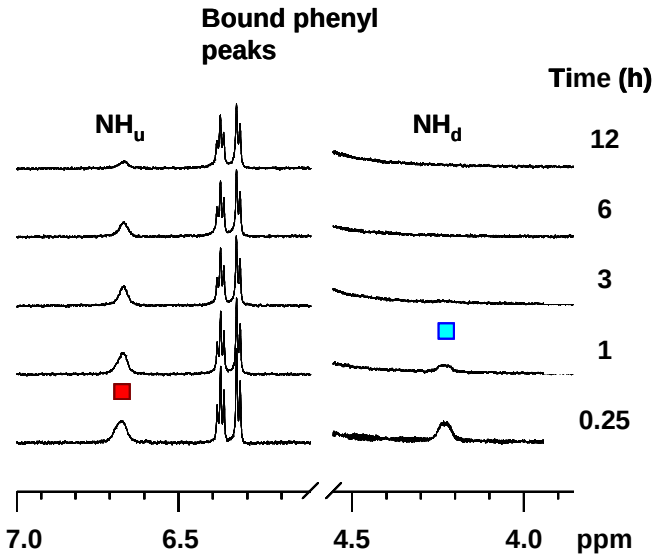

Figure 4.16. Time dependent ^{1}H NMR spectra of **10** in D_2O, pH^* = 5.55, T = 298 K of the N-H_u (■) and N-H_d (■) peaks.

Plotting the intensities of the N-H peaks against time produced two exponential decay curves for both the sets of protons on the nitrogens (Figure 4.17). Upon calculation of the best fit for the decay curves, the kinetic parameters were determined. (Table 4.9)

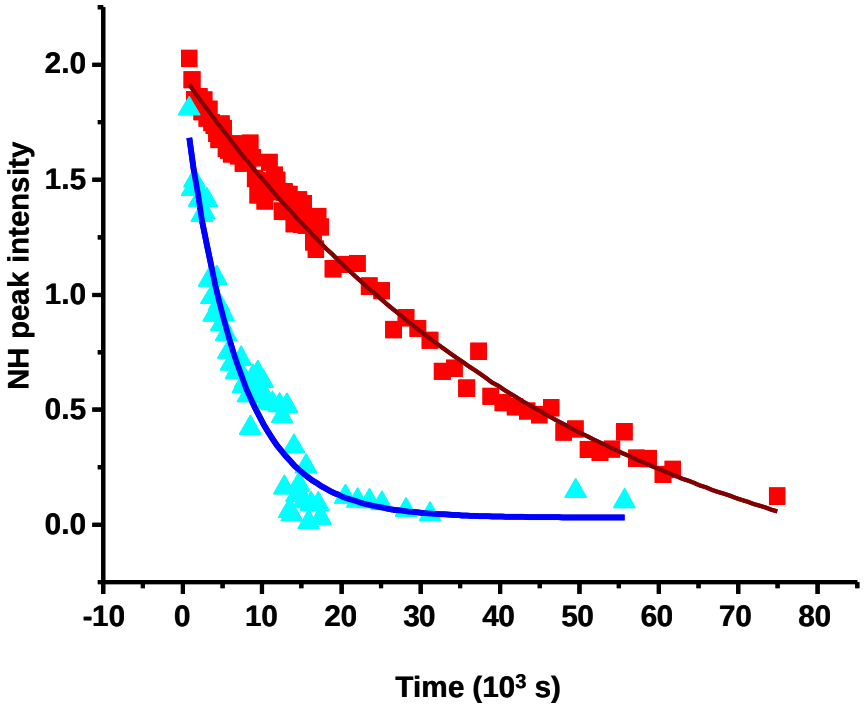

Figure 4.17. Time dependent decay of the NH_u (■) and NH_d (▲) ^1H NMR peaks for complex **10** in D_2O at pH^* = 5.55 and 298 K. The solid lines are the best fit for single exponential decays and giving the rate constants listed in Table 4.9

Table 4.9. Kinetic data for the exchange of protons for deuterons on N-H_u and N-H_d on **10** at pH^* = 5.55.

Proton	Rate Constant (s^{-1})	Half life (s)
N-H_u	2.406 x 10^{-5}	29.3 x 10^3
N-H_d	12.16 x 10^{-5}	6.0 x 10^3

4.2.3.7 [(η^6-bip)Ru(en)(*N*-4-Me-O-pyr)] [11]

The last of the complexes with pyridine derivatives to be synthesised was **11_2PF$_6$**, which contains a 4-methoxypyridine ligand. This was chosen as a ligand due to its high pK_a value (6.62) for the free ligand and also for the strong electron donating abilities of the methoxy group to the pyridine ring. As with previous studies, the exchange rates of the amino protons on the ethylenediamine group were studied using ^{1}H NMR. Figure 4.18 shows how the intensities of the N-H peaks decrease with time.

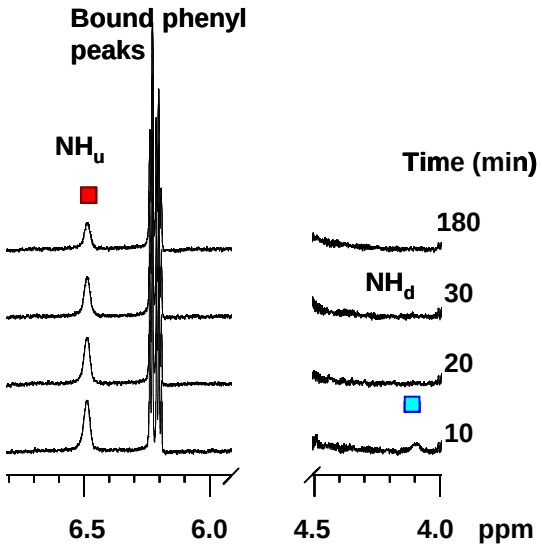

Figure 4.18. Time dependent ^{1}H NMR spectra of **11** in D_2O, pH* = 6.9, T = 298 K. The N-H$_u$ (■) and N-H$_d$ (■) peaks can be seen to decrease in intensity over time. The decrease in the intensity of the downward proton was very rapid and after 40 minutes the peak was negligible.

From the NMR data, time-dependent exponential decay curves were plotted (Fig 4.19) and the kinetic parameters were determined (Table 4.10).

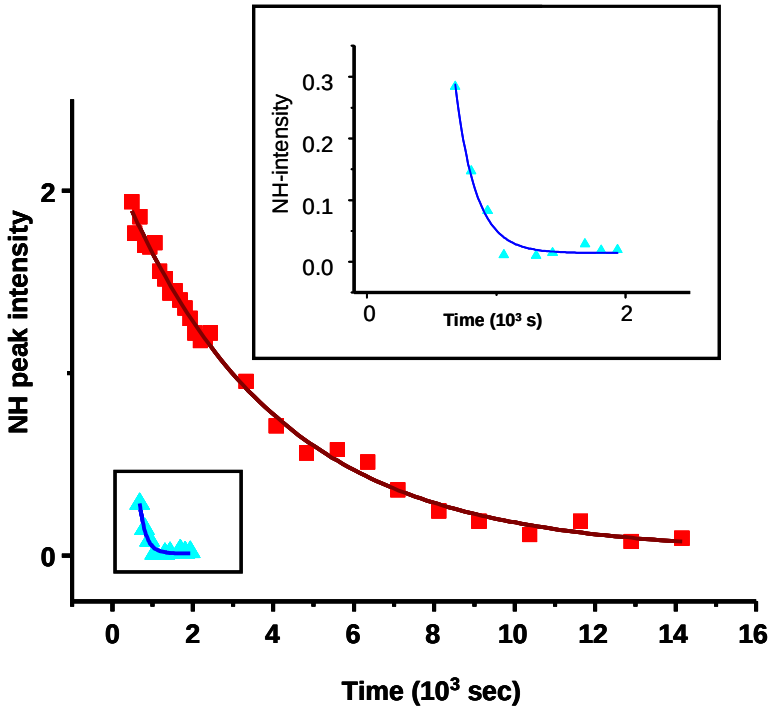

Figure 4.19. Time dependent exponential decay curves of the peaks of the NH_u (■) and NH_d (▲) in ^1H NMR spectra of **11** in D_2O at pH^* = 6.9, T = 298 K. The solid lines are the best fit which corresponds to the data listed in Table 4.10 below.

It is important to comment here that the exchange rates are very rapid for NH_d and so there is a larger error in calculating the best fit and in turn the rate constant. These errors are of the order of 15% compared to 5% for NH_u.

Table 4.10. Kinetic data for the exchange of protons for deuterons on N-H_u and N-H_d on **11** at pH^* = 5.55, T = 298 K.

Proton	Rate Constant (s^{-1})	Half life (s)
N-H_u	2.3 x 10^{-4}	2.75 x 10^3
N-H_d	62.3 x 10^{-4}	111

4.2.4 Computational analysis

Computational studies were carried out as described in Chapter 2 (*c.f.* **§2.13**). The aim of computational analysis was to characterise the HOMO and LUMO molecular orbitals of each complex since these may play a role in the mechanism of NH/D exchange. First the geometry of the biphenyl containing complexes **6**, **9**, **10** and **11** as determined by X-ray crystallography was optimised. Their molecular orbitals calculated *in silico* were compared to those for **1** reported in Chapter 3. As will be discussed later, only subjective conclusions on a qualitative level can be drawn from these results as the energy levels are only comparative within each calculation; they are relative values and not absolute. Also of note is the fact that all calculations were carried out on the stable molecular ion (as found in the crystal structure) and not on the charged transition state. *It is with this caveat and understanding that any conclusions should be drawn from these data.*

4.2.4.1 [η^6-biphenyl)Ru(*en*)*N*-pyridine]$^{2+}$ [6]

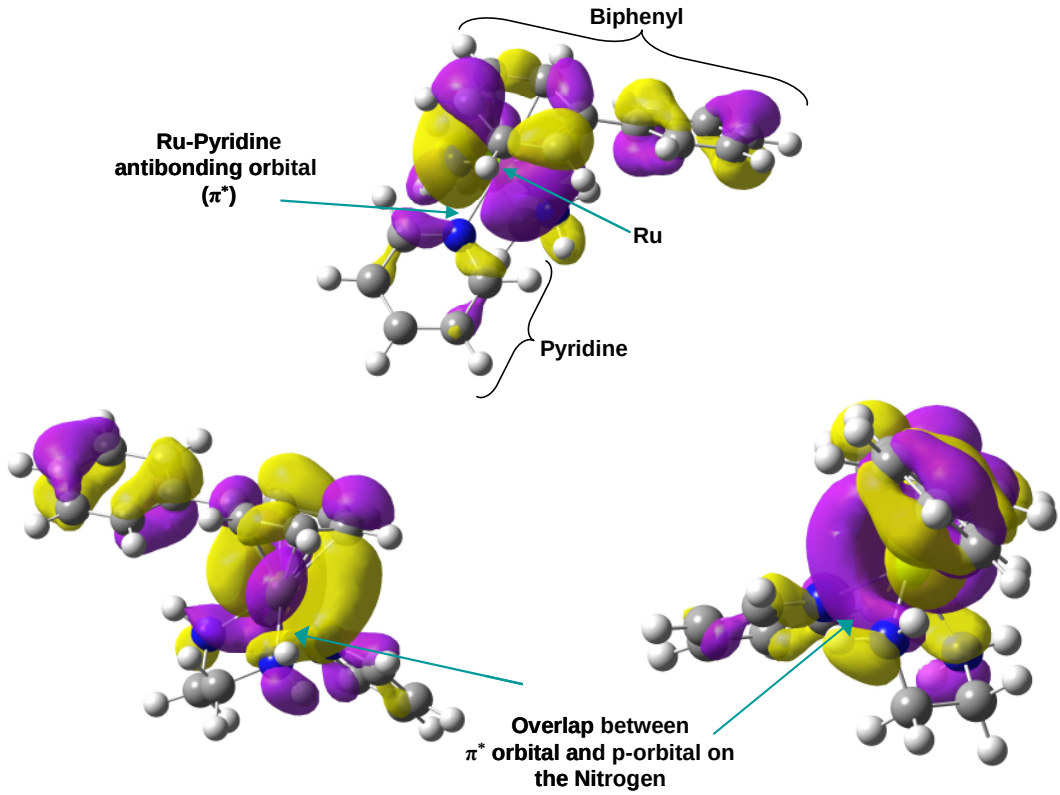

Figure 4.20. A series of representations, from different orientations, of the highest occupied molecular orbital (HOMO) of **6** ([(η^6-bip)Ru(en)*N*-pyr]$^{2+}$). The central ruthenium is obscured by the orbitals (in the upper image), but is green in colour. Yellow lobes represents the positive phase and purple the negative phase of the wavefunction.

The HOMO contains the π^* antibonding orbital of the Ru – N(pyridine) bond. Of interest is the observation that there is a clear overlap between the antibonding orbital and a p-orbital on nitrogen (and with some of the bonding orbitals from the π-bonding to the arene ring). This could potentially play a role in stabilising the lone pair of electrons on the nitrogen (of the ethylenediamine) following abstraction of a proton and explain why the exchange of NH_u and NH_d protons occurs at different rates.

4.3.4.2 [η^6-bip)Ru(*en*)*N*-4-Me-pyr]$^{2+}$ [7]

The analysis of the HOMO of [η^6-bip)Ru(en)*N*-4-Me-pyr]$^{2+}$ **(7)** was not as straight forward (Figure 4.21), as the HOMO appears to contain a bonding orbital between the ruthenium and the 4-methylpyridine. This combined orbital appears to have very little overlap with the p-orbitals on the nitrogen; on one face there does appear to be some overlap, but it is very small.

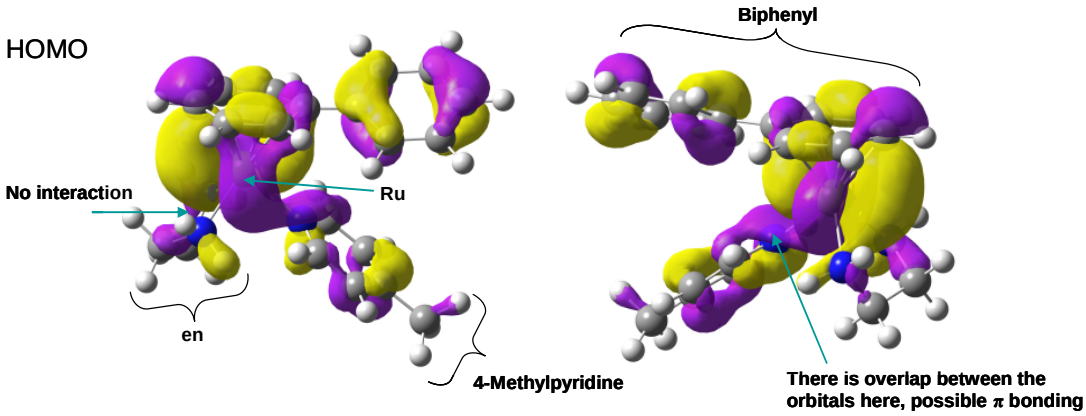

Figure 4.21. Representation of the HOMO of **9** ([(η^6-bip)Ru(en)*N*-Me-pyr]$^{2+}$). The central ruthenium is obscured by the orbitals, but is marked and is green in colour. Yellow lobes represent the positive phase and purple lobes are the negative phase of the wavefunction.

Upon investigation of the lowest unoccupied molecular orbital (LUMO) the presence of what appears to be the σ*-antibonding orbital of the {Ru-N(4-Me-pyr)} fragment was observed and it has a small interaction with the p-orbital on one of the nitrogens (Figure 4.22).

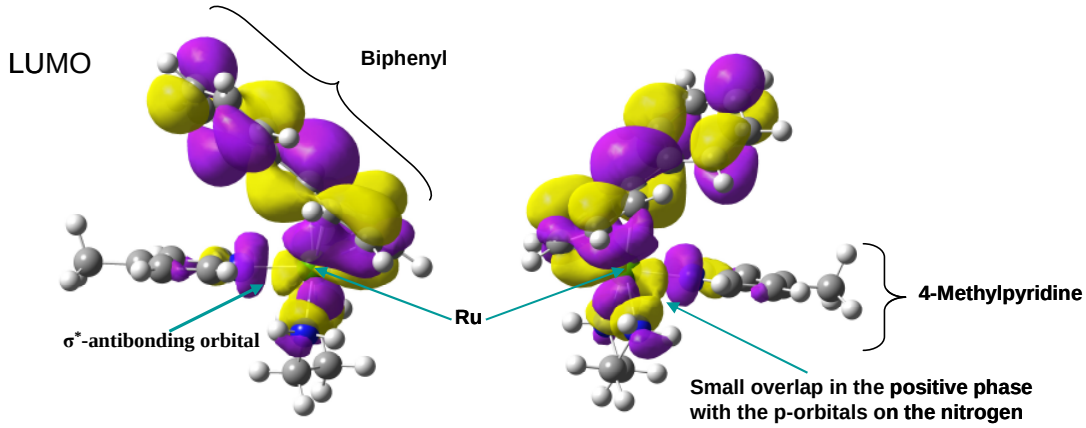

Figure 4.21. A representation of the LUMO of **9**. Labelled is a small overlap between the σ^* of the Ru-N(4-Me-pyr) bond and what appears very similar to a p-orbital on the nitrogen of the en ligand. The central ruthenium is obscured by the orbitals, but is marked and is green in colour. Yellow represents the positive phase and fuchsia is the negative phase of the wavefunction.

4.2.4.3 $[(\eta^6\text{-bip})Ru(en)N\text{-4-t-Bu-pyr}]^{2+}$ [10]

While the HOMO of **7** did not show overlap between the p-orbitals and the π* or σ*-antibonding orbitals, (which as previously stated may have a role in the bias of exchange rates for NH_d over NH_u), the data for **10** are somewhat clearer. Figure 4.22 shows that there is an overlap with a p-orbital on a nitrogen atom of the ethylenediamine ring and the π*-antibonding orbital of the Ru-N(4-t-Bu-pyr) fragment. On the other side of the ethylenediamine, the sign of the phase of the upper part of the p-orbital on the nitrogen is the same as that for the antibonding orbital which is in very close proximity. So, potentially, in the transition state of the exchange reaction there could be some overlap, this will be discussed further later in this chapter.

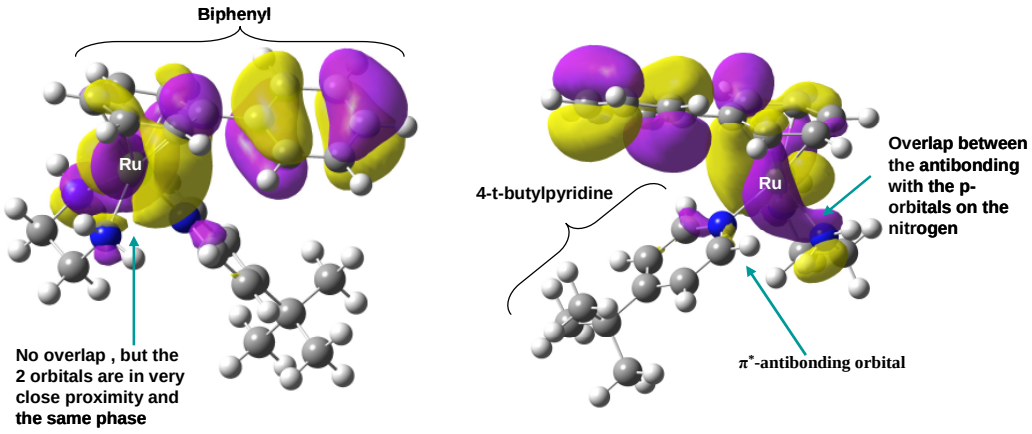

Figure 4.22. A representation of the HOMO of the 4-t-butylpyridine complex [**10**]**.** The π^*-antibonding orbital of the Ru-N can been seen and overlaps with a p-orbital on the nitrogen (image on the left). The central ruthenium is obscured by the orbitals, but is marked green in colour. Yellow represents the positive phase and fuchsia is the negative phase of the wavefunction.

4.2.4.4 [(η^6-bip)Ru(en)*N*-4-Me-O-pyr]$^{2+}$ [11]

As with **9** the HOMO showed some evidence of π-bonding between the N on the pyridine ring and the ruthenium (Fig. 4.23). There was an overlap between the Ru-Arene bonding orbitals and a nitrogen on the ethylenediamine, but this is small compared to those seen for **6** and **10**.

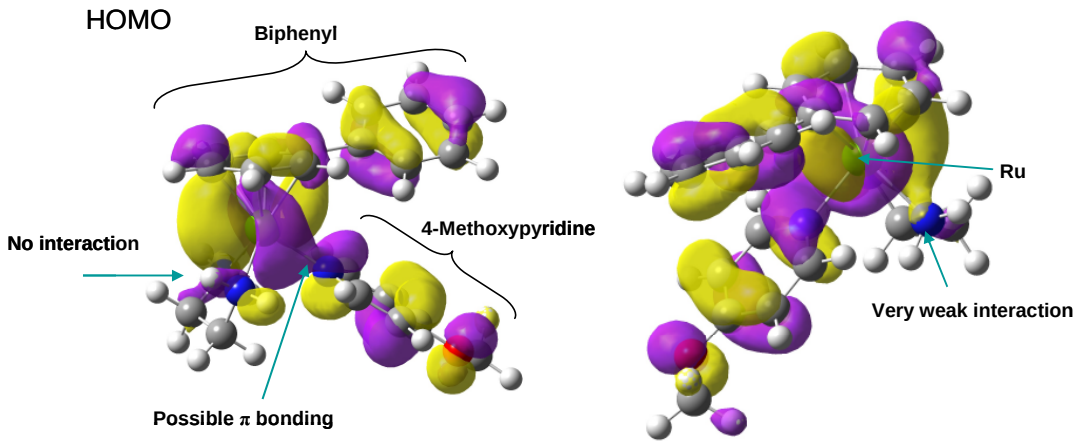

Figure 4.23. A representation of the HOMO of the 4-methoxypyridine complex (**11**). There appears to be a small amount of π-bonding characteristic of the orbitals present. The central ruthenium is obscured by the orbitals, but is marked and is green in colour. Yellow lobes represents the positive phase and purple lobes are the negative phase of the wavefunction.

The energy gap between the LUMO (Fig. 4.24) and the HOMO was calculated as 4.95 eV. There appears to be a σ^*-antibonding orbital present and a (very) small overlap between the antibonding orbital and a p-orbital on one nitrogen of the ethylenediamine ligand.

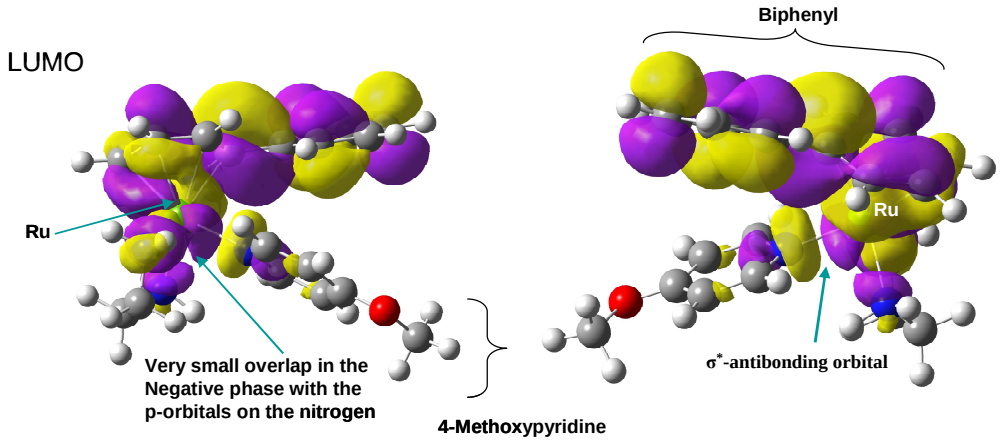

Figure 4.24. A representation of the LUMO of 4-methoxypyridine complex (**11**). The central ruthenium is obscured by the orbitals, but is marked and is green in colour. Yellow represents the positive phase and purple is the negative phase of the wavefunction. Here the σ* antibonding orbital of the Ru-N(pyr) bond can be seen and it has a small amount of overlap with the position of the p-orbitals on the nitrogen of the ethylenediamine ligand.

The σ^*-antibonding orbital on the Ru-N(4-Me-O-pyr) bond can be seen and a very small overlap between this orbital and the p orbital (or possibly sp^3/sp^2 hybrid – as the shape of the orbital around the nitrogen is highly unsymmetrical). These orbitals may play a role in stabilising the transition state, leading to NH_u proton exchange being substantial slower when compared to NH_d exchange.

4.3 Discussion

A series of $[Ru(\eta^6\text{-arene})(en)X]^{2+}$, where X = 4-R-pyridine derivatives, complexes, where R = H, Me, t-Bu and MeO, complexes **4, 7, 10** and **11** (Figure 4.3) was synthesised and the kinetics of proton exchange on the ethylenediamine nitrogens was determined by NMR. These were then compared to the kinetics of exchange for previously-synthesised complexes **1** and **8**.

In Chapter 3 it was observed that NH_u and NH_d protons of complex **1** exchanged at different rates. However, thermodynamic data indicated exchange took place via the same transition state. The bias for exchange of NH_d over NH_u may arise from steric effects of the biphenyl group and the electronic effects of the X ligand (in this case chlorine) on ruthenium and associated orbitals. This was investigated in attempt to elucidate further the mechanism of proton exchange on the amines and mechanism of stereochemical inversion in complexes with chiral ethylenediamine ligands.

The effects of charge, electron density on the Ru atom and the size of the arene group were investigated by comparing and contrasting the kinetic data. Comparisons were also made between the crystal structures and the calculated molecular orbitals of each complex to each other to investigate if these play a role in the exchange mechanism.

4.3.1 Synthesis and Characterisation

The synthesis of complexes **6**, **7**, **9**, **10** and **11** was achieved via the aqua adduct of **1** and **8**, using Ag^+ to abstract of chloride ligands. As was expected, all the pyridine derivatives bound via the pyridine nitrogen to the ruthenium. Pyridine has dual characteristics, it is both a σ-donor and a π-acceptor and to this end all the

bond lengths of the Ru – N(pyridine) are all shorter in length (2.11 – 2.13 Å) compared to those of the Ru(II) – NH_3 bonds of previously reported (2.15 – 2.17 Å) as shown in Table 4.11.

Table 4.11. Comparison of bond lengths.

Complex	Ru – Cl/N(pyr) (Å)	Ru – Centroid[a] of arene ring (Å)
$[(Bip)Ru(en)Cl]^{+}$ (**1**)	2.408(15)	1.662
$[(Bip)Ru(en)(N\text{-pyr})]^{2+}$ (**2**)	2.1315(16)	1.690
$[(Bip)Ru(en)(N\text{-4-Me-pyr})]^{2+}$ (**4**)	2.106(3)	1.688
$[(Bip)Ru(en)(N\text{-t-Bu-pyr})]^{2+}$ (**6**)	2.130(3)	1.689
$[(Bip)Ru(en)(N\text{-Me-O-pyr})]^{2+}$ (**7**)	2.1131(18)	1.685

[a] as calculated using Mercury, based on the position of all 6 carbons in the arene ring

Upon consideration of the error bars for these data (3σ) it is clear that all the pyridine derived complexes have very similar bond lengths. Some variation based on the pK_as of the pyridine complexes was expected, however upon examination of Ru-N(Pyr) bond lengths versus pK_a of the free pyridine derivatives, no relationship was observed, as can be seen in Figure 4.25.

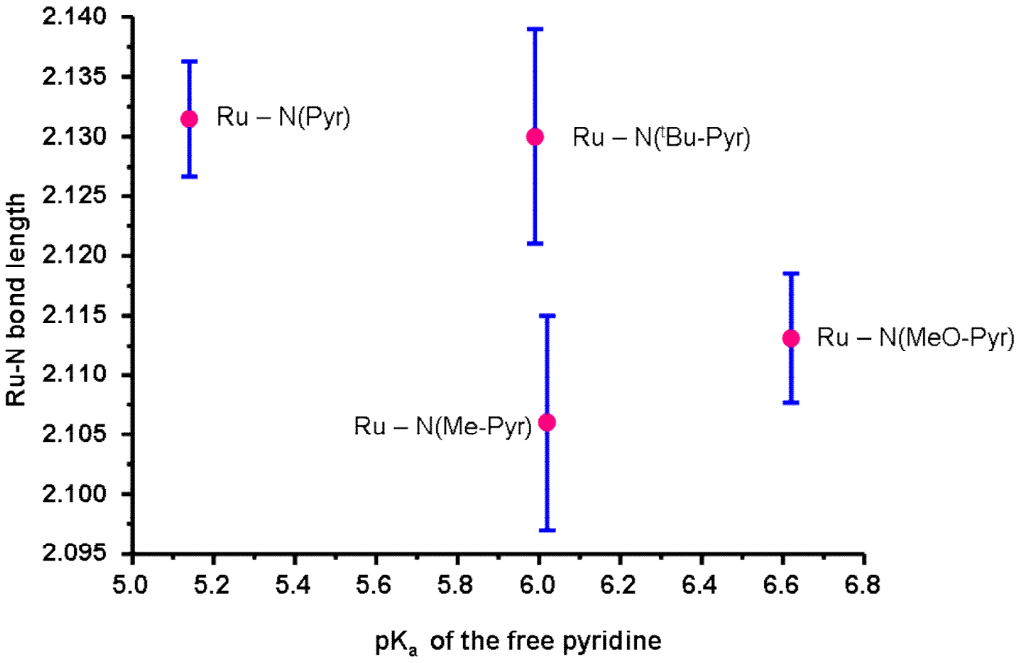

Figure 4.25. Dependence of the Ru – N(Pyr) bond lengths (●) in the crystal structures of **6**, **7**, **10** and **11** (with errors of 3σ in blue) on the pK_a of the free pyridine derivative.

All ruthenium complexes with pyridine derivatives were also found not to hydrolyse in water at various pH* values. This was part of the design process for this experiment, to allow kinetics to be observed at ionic strengths close to zero without have the added complication of the complex undergoing hydrolysis while doing so.

4.3.2 Effects of arene change on exchange rates

Two sets of complexes with different arenes (biphenyl and benzene) as the η^6 ligand were synthesised. The objective was to investigate the effects of the arene size on the exchange rates: i.e.: does steric bulk effects the exchange rates of anisotropic amino protons? It was noted that upon change of the arene from

biphenyl to benzene that the exchange rates of up and down protons became more similar (Table 4.12).

Table 4.12. Comparisons of the half life ($t_{½}$) for N-H/D exchanges on **1** and **8**

Proton	**1** ($t_{½}$) (min) Arene = Bip	**8** ($t_{½}$) (min) Arene = Ben
N-H_u	182.48	422.8
N-H_d	49.3	181.2
$t_{½up}$: $t_{½down}$	3.7:1	7:3

The observation that the exchange rates for both protons on the benzene complex (**8**) are slower than those in the biphenyl complex (**1**) is to be expected, some studies[23] have shown that in a series of $[(\eta^6\text{-arene})Ru(en)Cl]^+$ complexes the hydrolysis rates are proportional to the size of the arene system. While **8** is not mentioned in study[23] which deals with $[(\eta^6\text{-arene})Ru(en)Cl]^+$, where the arene is biphenyl, tetrahydroanthracene and dihyfroanthracene, by extrapolation of the results an assumption can be made that since benzene is the smallest of all arene systems, the hydrolysis rate must be slower than that of the biphenyl analogue. This is possibly a reflection of the overall reactivity of **8** and therefore it could be the arene that is affecting the activity of the amine protons on the ethylenediamine, slowing down the exchange rates.

Of most interest is the similarity in the rates of exchange of the up and down protons. For $[(\eta^6\text{-ben})Ru(en)Cl]^+$, the rates of proton-for-deuteron exchange are much more similar, compared to those of $[(\eta^6\text{-bip})Ru(en)Cl]^+$ (**1**) under the same conditions, 154 mM NaCl, pH^*=7.4, T = 298 K (Table 4.13). When

comparisons are made to the exchange rates of the *N*-pyridine derivatives, it can be seen that the trend holds (Table 4.13).

Table 4.13. Comparisons of the half time ($t_{½}$) for N-H/D exchanges on **7** and **9**

	6 ($t_{½}$) (min)	**9** ($t_{½}$) (min)
Arene	Biphenyl	Benzene
(pH*)	(6.3)	(5.4)
N-H_u	204.8	679.4
N-H_d	21.1	85.5
$t_{½up}$: $t_{½down}$	9.7:1	7.95:1

Although in this case the conditions are not exactly the same (different pH* values), based on the trends observed in Chapter 3, a number of conclusions can be drawn.

1. In the chlorido adduct, as the pH* decreases so does the ratio between the up and down exchange rates, therefore the same would be expected for pyridine adducts.

2. Rates of exchange slow down as pH* is reduced, so the absolute rates cannot be compared.

3. All these pyridine complexes have a 2+ charge and so the rates cannot be compared to those of the chlorido adduct, due to effects of the additional positive charge on the complex, as will be discussed later.

It was observed that the rates of exchange of amino protons on the pyridine adducts (**6** and **9**) are very much increased compared to those of the chlorido

adduct (**1** and **8**) and also that the downward proton exchange is considerably faster than the upward proton exchange in both cases. However, in the case of **6** and **9**, the pH* value is not the same so we can not make comparisons on absolute rates. It seems likely that rates of exchange on the biphenyl complexes are larger than those on the benzene analogue, as was the case for the chlorido adducts.

At this point it is appropriate to mention that attempts were made to study the effects of larger arenes (arene = tetrahydroanthracene) on the exchange rates of the up and down amino protons. Unfortunately solubility problems in NaCl solutions (to suppress hydrolysis of chlorido complexes) led to reduced signal-to-noise ratios in the NMR spectra, and the data therefore proved to be unreliable for determining kinetic parameters.

From comparisons of the exchange rates of NH_u and NH_d protons on **1** to those of **8** it can be clearly seen that when there is a smaller arene on the complex, the up and down protons exchange at a more similar rate. This could be indicative of there being a steric effect from the arene on top of the ruthenium on the exchange rates. The larger arene may block the upper face of the ethylenediamine making entry of the deuterated water into the upperface of the nitrogen more difficult, as shown in Scheme 4.2.

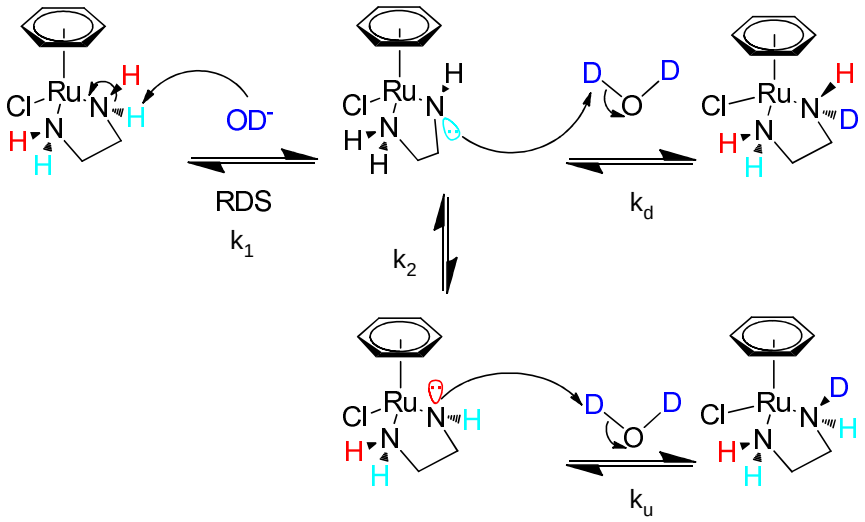

Scheme 4.1. A scheme of how the reduced arene bulk may cause k_u and k_d to become more similar. When there is less bulk, as in the case of benzene as the arene, there is less hindrance to entry of D_2O to the unpaired electrons on the upper-face of the nitrogens.

In Chapter 3, it was proposed that the mechanism involves abstraction of the proton from the nitrogen of the ethylenediamine (k_1). This abstraction is then followed by the formation of an sp^2 hybridised nitrogen with a lone pair in a p-orbital, which undergoes rapid umbrella type inversion (k_2), and finally addition of a deuteron to the lone pair on the nitrogen. The reason that downward protons maybe replaced more rapidly could be due to steric hindrance and also the hydrophobicity of the overlying biphenyl ring system, resulting in $k_d >> k_u$. The observation that the k_d and k_u for the benzene complex are closer together than those of the biphenyl complexes provides evidence that this is a factor in the difference of exchange rates for NH_u and NH_d.

4.3.3 Effects of Ruthenium (II) electronic density on the exchange rate

The purpose of attaching a variety of pyridines to the central ruthenium atom to yield complexes **6**, **7**, **10** and **11** was to look at the effects of different electron densities on the ruthenium on the exchange rates on the amino protons. The ratio of NH_u and NH_d proton exchange relative to the chlorido species (**1**) at the same pH^* was also observed. The aim was to also investigate whether or not the antibonding orbitals of the Ru-N(pyr) bond had a role in the stabilisation of the negative charge on the nitrogen post abstraction of the proton, to make one face of the nitrogen more favourable to exchange over the other.

Table 4.14 and 4.15 lists details of the exchange rates for each complex, the pH^* of the exchange and the ratio between up and down exchange rates. Also listed are the predicted exchange rates for up and down protons for the chlorido adduct as determined by the linear equation in Table 3.8 (Chapter 3) of which an abridged version is reproduced here.

Table 3.8. (Chapter 3) Parameters for the linear equation of the best fit on $Log_{10}k = m.pH^* + c$ for predicting the exchange rates of up and down protons at various pH^* values and $I = 0.154$.

Exchange	Slope (m)	Intercept (c)
$N\text{-}H_d$	0.73066	-9.20406
$N\text{-}H_u$	0.54874	-8.26142

Table 4.14a. Half-times for the H/D exchange of **6**, **7**, **10** and **11**

Complex/pH*	**$t_{½}$ [N-H_u]** (min)	**$t_{½}$ [N-H_d]** (min)	**Ratio**[a] up/down
6 / 6.3	204.8	21.1	9.7
7 / 5.68	527.5	50	10.55
10 / 5.5	488.3	100.5	4.86
11 / 6.97	45.9	1.85	24.8

[a] Ratio of up/down half-lives for exchange [$t_{½}(H_u)/t_{½}(H_d)$]

Table 4.15 Half-time for NH/NDexchange for **1** determined at various pH* values

	[(Bip)Ru(en)Cl]$^+$ (**1**)[b]		
pH*	**$t_{½}$ [N-H_u]** (min)	**$t_{½}$ [N-H_d]** (min)	**Ratio**[a] up/down
6.3	736.3	460.9	1.6
5.68	1611.6	1307.9	1.23
5.5	2023.1	1770.5	1.14
6.97	315.7	149.9	2.1

[b] As calculated from Chapter 3, Table 3.8 and associated information

The first observation is that when the complex has a 2^+ charge, as is the case with the N-pyridine derivatives, the half lives are significantly reduced compared to those of the 1^+ chlorido complex. This was observed early on in this study and so the addition of acid (HCl in D_2O, solutions at 1, 0.1 and 0.01 M) to reduce the pH* was used to reduce the exchange rate and allow for observable exchange rates.

In Chapter 3, it was noted that the rates of exchange of up and down protons exchange rates increase linearly with pH^*. The difference between up and down exchange rates is however not always the same. It was of interest to note that at higher pH^* the exchange of NH_d is almost four times faster than that for NH_u. However, in the examples studied in this Chapter the gap between up and down proton exchange rates is larger than those explored in Chapter 3. These differences do not appear to be a result of pH* changes alone, but as a result of the effects of the pyridine derivative on the ruthenium. The pyridine may be exerting some long range effects on the nitrogen lone pair of electrons, or stabilising the transition state. It was there for prudent to investigate this. Table 4.16 highlights the increase in the bias for NH_d exchange over NH_u with changing pK_a of the pyridine ligand when compared to the chlorido complex.

Table 4.16. Comparisons between the k_d:k_u ratios of **6**, **7**, **10**, and **11** relative to those of **1** are shown.

Complex (ligand)	$(k_d:k_u)_{complex}$: $(k_d:k_u)_{\mathbf{1}}$
6 (pyr)	6.01
7 (4-Me-Pyr)	8.58
10 (4-t-Bu-Pyr)	3.47
11 (4-Me-O-Pyr)	11.81

The pK_a values of the pyridine ligands (Table 4.17), are a measure of the electron donating ability if the ligand. The higher the pK_a the better an electron donor the ligand is. When these are compared as a Hammett plot to the values

from Table 4.17, a clear trend can be seen. (Figure 4.26) For these studies σ is calculated as:

$$(-pK_a(\text{free 4-pyridine derivative}) + pK_a(\text{free pyridine}) = \sigma$$

Table 4.17. pK_a and σ values of the free ligands

Ligand	**pK_a of ligand**[24,25, 26]	**σ**
Pyridine	5.14	0
4-Methylpyridine	6.02	- 0.88
4-*t*-Butylpyridine	5.99	- 0.85
4-Methoxypyridine	6.58	- 1.44

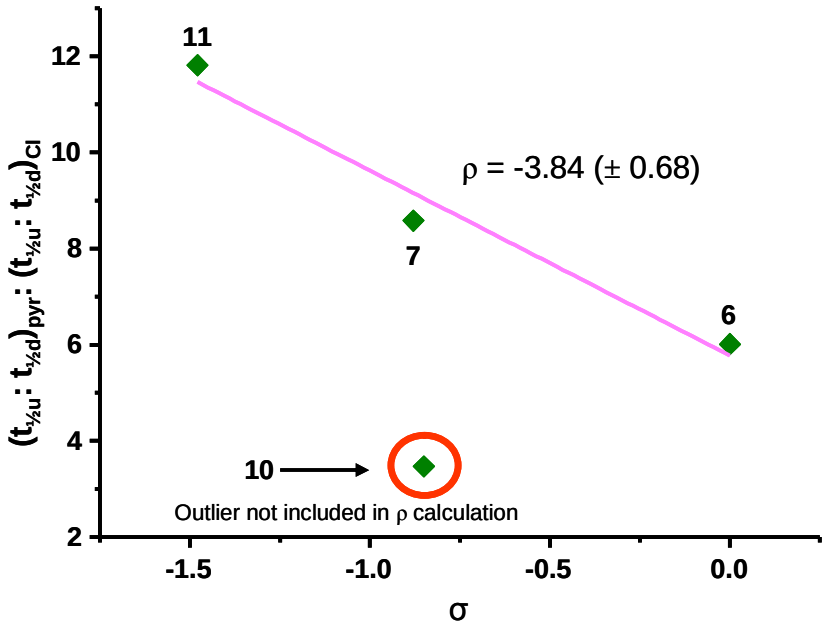

Figure 4.26. A Hammett plot of the difference in the relative up and down proton exchange rates of **6**, **7**, **10**, and **11** compared to **1**. Complex **10** is an outlier and was not used to determine the best fit linear plot.

A clear relationship between σ and the relative exchange rates was observed in these reactions. With the exception of **10**, which has been marked here as an outlier, data from **6**, **7** and **11** clearly have a linear relationship. The best fit line has a slope of -3.92 with a 92% fit on the 3 data points. Hammett plots can provide information on mechanisms and there are two interesting trends that can be observed[27] from Figure 4.26.

Firstly, the sign of the slope, in this case the slope is negative. A negative slope in a Hammett plot implies that the greater the electron donating ability of the ligand, the greater the difference between the NH_u and NH_d exchange rates, in favour of faster down rates. Secondly, in a Hammett plot points which are large outliers are usually indicative of the fact that the comparisons may not be easily made as steric effects (from the outlier) may have a greater influence than electronics on the reaction. This is reasonable given the fact that complex **10** contains the bulkiest ligand of all those investigated. A large t-butyl group may cause some form of steric hindrance as it is in constant motion and effect the accessibility of water molecules to the amino protons to allow exchange.

The link between the electron donating ability of the ligand and the increased preference for exchange on the down face first may be explained by the effects of the electron density on the N-Ru σ-, π-bonding and the π*- and σ*-antibonding orbitals as will now be discussed.

4.3.4 Effects of HOMO and LUMO of the Ru-N(pyr) bond on exchange rates of NH_d and NH_u

As was postulated in Chapter 3, the difference in the up and down proton exchange rates cannot result solely from the steric effects of the biphenyl ring.

Further evidence and confirmation of this theory is provided in the results discussed so far. While a bias in favour of exchange of the downward protons first is still observed for smaller arenes, the bias is smaller. These results imply that there is some influence from the aromatic ring system on exchange rates. However, the biphenyl is in constant motion (as can be seen by the lack of NMR splitting of the signals) so the steric hindrance is clearly not a constant effect. In the pyridine derivatives discussed in this Chapter we see that the bias for downward protons is increased compared to the chlorido adduct. While the same arene is present in all the complexes, this would conflict with the suggestion that the overhanging biphenyl ring is solely responsible for the difference in NH_u and NH_d exchange rates.

To this end, computational analysis of the highest occupied molecular orbitals (HOMOs) and lowest unoccupied molecular orbitals (LUMOs) of each complex was studied. Comparisons were made and interesting overlaps between orbitals were observed which may provide further insight into the effects of the electron donating ability of the ligand on the bias towards faster downward proton exchange.

In Chapter 3, it was observed that there was an overlap between the σ*-antibonding orbital on the Ru-Cl bond with the probable location of the p-orbital. This overlap could potentially have a role that this may have in affecting the bias for NH_d is discussed below. (Figure 4.27)

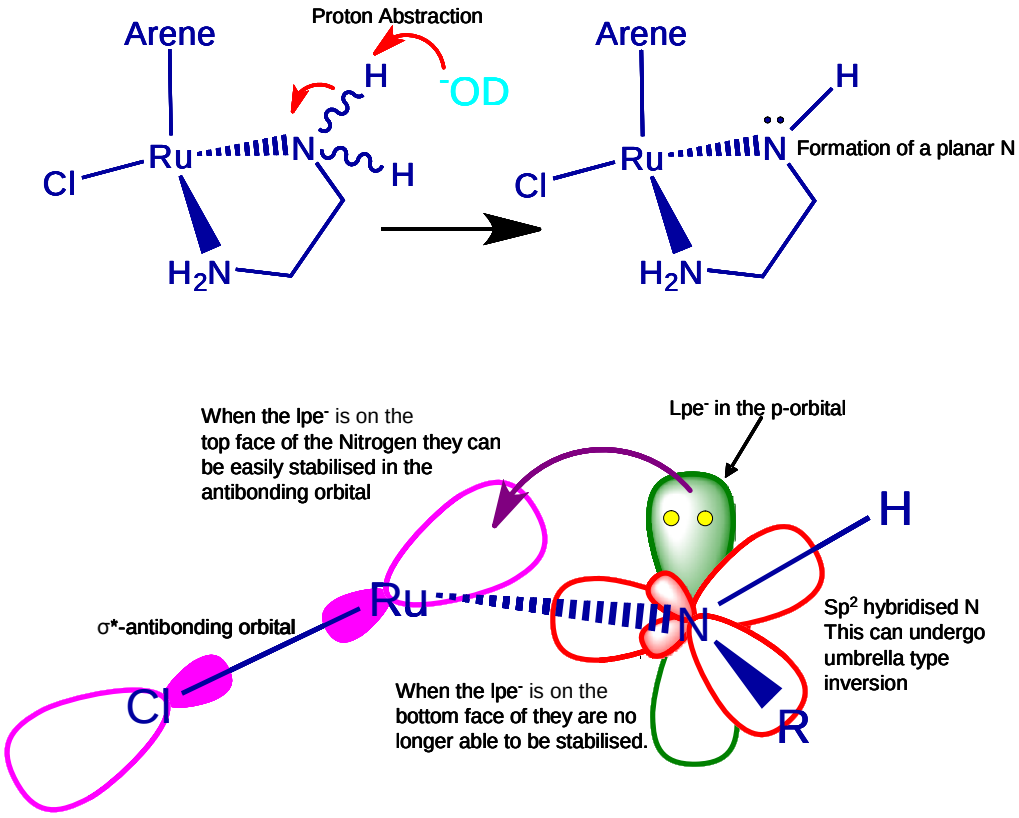

Figure 4.27. A possible transition state for N-H/D exchange. The lower image is a schematic of the some of the important orbitals present in the Cl-Ru-N(en) bond following proton abstraction. (lpe^- = lone pair of electrons)

The hypothesis is as follows; the lone pair electrons (lpe^-) on the upper face of the nitrogen can be more readily stabilised in the empty antibonding orbital of the Ru-Cl bond and therefore is less available for deuteration. When the lpe^- is in the downward face of the nitrogen there is no such orbital available for stability, making these electrons available to nucleophilically attack any deuterons in solution.

Figures 4.20 – 4.24 show images obtained by computational analysis of the HOMO and LUMO of complexes **6**, **7**, **10** and **11**. As previously mentioned, in Chapter 3, there was an overlap between the antibonding orbitals of the Ru-Cl bond and the p-orbitals on the nitrogen observed. In this Chapter, some similarly

interesting trends can be observed. In complex **6** the π*-antibonding orbital overlaps with the p-orbital on the nitrogens as shown in Figure 4.27.

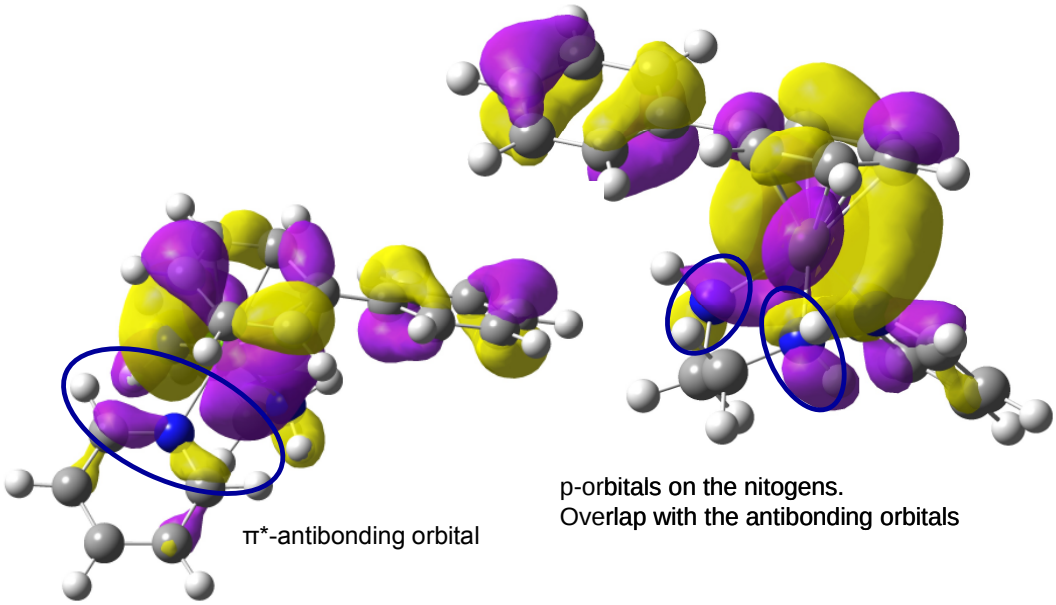

Figure 4.28. A representation of the HOMO of **6** with important characteristic orbitals highlighted.

In Figure 4.28 the overlaps of orbitals can be seen and are highlighted. While these are not seen in all the complexes, this may be as a result of the calculations not being carried out on the intermediate species (i.e.: the deprotonated species). Although all molecular orbitals could not be determined, other interesting effects are observed that would imply that a similar effect is taking place. The potential for antibonding orbitals on the Ru-N(pyr) bond to stabilise p-orbitals containing the lpe^- after proton abstraction appears as a recurring trend.

Further investigation into the HOMO +/- 10 levels of **9** and **11**, did not show any clear π*-antibonding orbitals. However some σ*-antibonding orbitals were seen in the LUMOs of these species, with small overlap to the p-orbitals on the nitrogen of the ethylendiamine.

4.4 Conclusions

A series of investigations into the effects of arene size, charge on the ruthenium and electron donating qualities of the monodentate ligand on the rates of exchange of amino protons on the ethylenediamine was carried out. These results provided much insight into the mechanism of exchange. A number of conclusions can be drawn about the mechanism and what effects both the rates of product formation and why one product is more kinetically favoured than the others.

It can be seen that there appears to be a number of factors that affect the rates of exchange of the amino protons on the ethylenediamine ligands. As discussed in Chapter 3, ionic strength and pH^* both have a proportional effect on the rates of exchange. While these are external conditions that have an effect on the rates of exchange, they have little influence on the difference in bias towards the formation of one isomer (up or down replacement) over another.

In this Chapter the constituents of the complex are shown to have varying effects on not only the exchange rates but also on the bias of exchange rates for one isomer over another. Firstly, decreasing the size of the arene reduces the bias for downward proton exchange over the upward exchange. The implication being that there are some steric effects which control which face of the nitrogen is available for electrophillic attack from deuterons in solution (Scheme 4.3). The

absolute rates were found to slow down with smaller arenes leading to slower overall rates of exchange. This however is expected as previous work has shown that smaller arene ruthenium (II) complexes are less reactive compared to those with larger arene systems.[23]

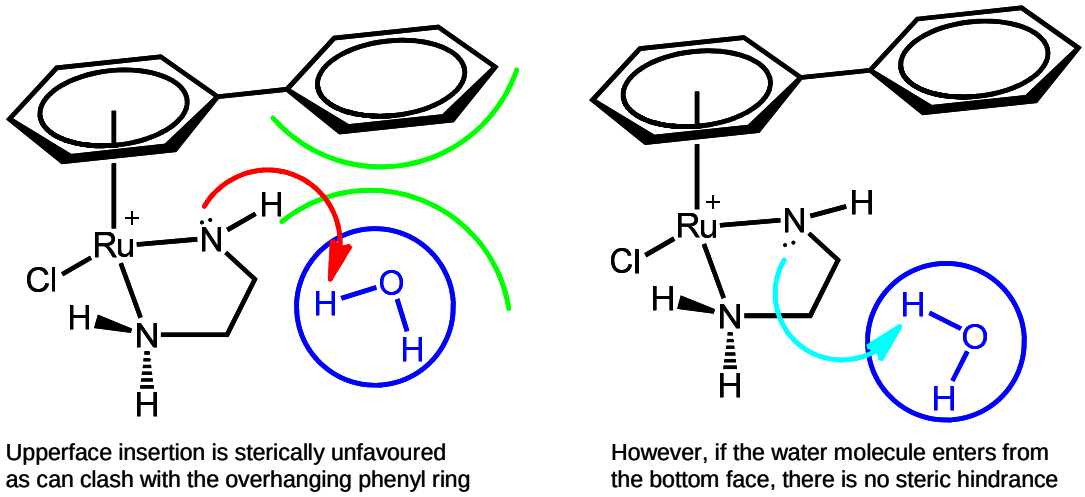

Scheme 4.2. Steric effects of the over hanging phenyl on the insertion of a water molecule into the reaction sphere of the nitrogen lone pair

Secondly, when neutral ligands are used, in this case pyridine derivatives, leading to an overall charge of 2^+ on the complex, there is an increase in the rates of exchange. This is due to movement of electron density from the nitrogen – hydrogen bond to the nitrogen (en) – ruthenium bond making the N-H bond weaker and so more labile. In Chapter 3, it was proposed that the rate limiting step is the abstraction of the proton. The fact that the protons in 2^+ species are more labile than those in 1^+ correlates well with this theory. (Figure 4.29)

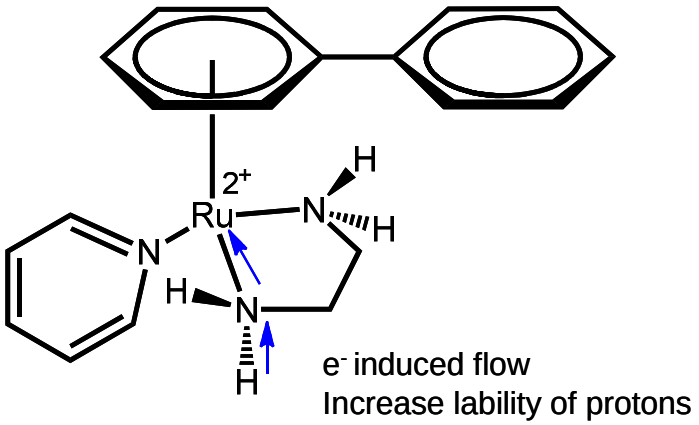

Figure 4.29. The direction of e^- flow to make a more stable central ruthenium atom. This reduced the strength of the N-H bonds, making it easier for protons to be abstracted.

With regard to the bias for downward pointing proton exchange, a more interesting trend is observed other than the impact of the arene size. There is a direct correlation between bias for downward proton replacement and the electron donating ability of the pyridine derived ligand. The electron donation to the ruthenium from the nitrogen shortens the Ru-N bond (N on the pyr ligands), through both σ-donation and π-backbonding. In addition to this the electron donating ability of the pyridine ligands appears to increase the bias for downward proton exchange (up to 11 times as much for the greatest electron donating ligand). This appears to provide evidence for an involvement of molecular orbitals in stabilising the transition state in favour one type of product over another.

One theory for how this occurs is that an anomeric-like effect exists in metals also and not just in cyclic organic systems. (Figure 4.30)

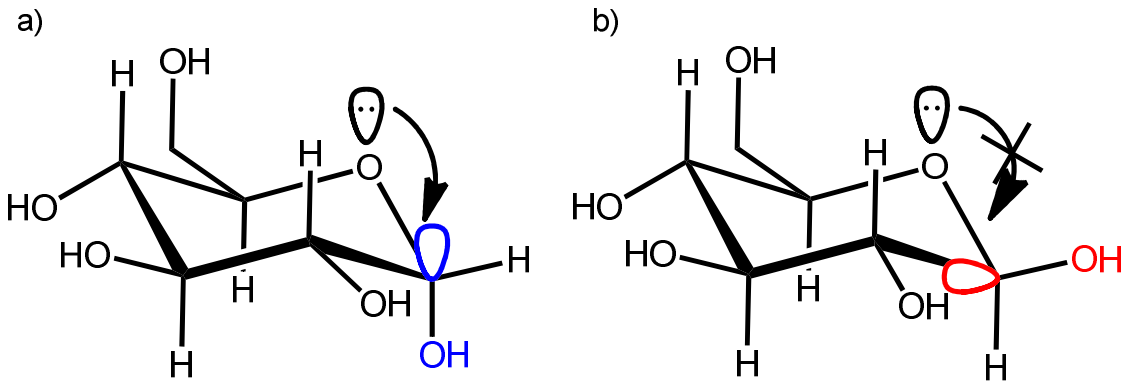

Figure 4.30. The stabilising effect of the C-OH σ*-antibonding orbital interacting with the lone pair on the oxygen – the anomeric effect. While equatorial OH positions are usually preferred for 6-membered rings in boat or chair formation, the anomeric effect allows for formation of (a) is much more preferred than (b).

In the studies discussed here, the less electronegative a ligand (i.e.: the more electron donating it is, across the pyridine complexes) the more there appears to be some stabilising effect on the up facing nitrogen compared to those of the chlorido adduct. So the theory for stabilisation on the chloride adduct, **1**, holds, perhaps also for complexes **6**, **9**, and **11** the stabilisation is not so much on the σ*-orbital but the π*-orbital of the back-bonding (Figure 4.30). Indeed, the computational analysis of some of the complexes in the ground state would imply that there is overlap between the π*-antibonding orbitals and the p-orbitals on the nitrogen of the ethylenediamine. This overlap may play a role in stabilising the lpe^- in the transition state. Ligands which have the best σ-donors (higher pK_a) will partake in more back bonding through the π-orbitals on the pyridine interacting with the d-orbitals on the ruthenium (Figure 4.30a). This is seen from the crystal data showing shorter bond lengths in Ru-N(Pyr) bond with increasing pK_a. As the electrons are pulled away from the ruthenium, the antibonding orbital is more

accessible to the lpe$^-$ in the p-orbital, stabilising the electron charge and making that face of the nitrogen less prone to electrophilic attack from deuterons in solution (Figure 4.31b).

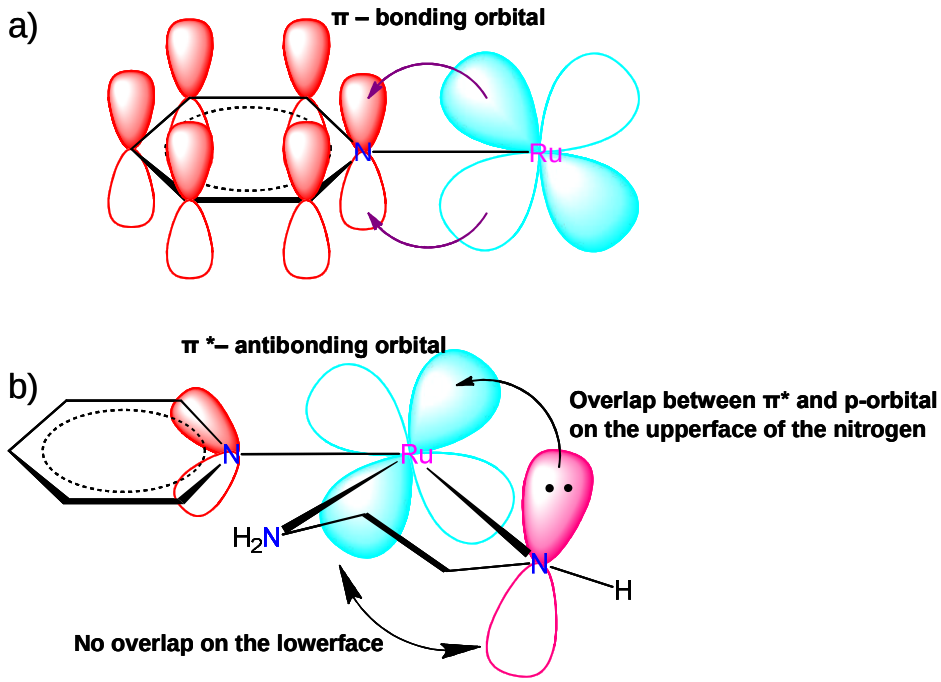

Figure 4.31. a) The orbitals involved in π bonding and **b**) those orbitals involved in antibonding which may interact with the p-orbital on the nitrogen to stabilise the intermediate transition state.

While this is only a theory, it fits well with the experimental data that is presented in this chapter, and would explain the role played by each constituent of the complex plays on the exchange of amino protons on the ethylenediammine ligand.

This ability to tune the exchange rate and the selectivity of replacement of the up and down NH protons may be useful in the synthesis of chiral amine ligands on the ruthenium. By attempting to both slow down exchange and allow a

strong electrophile to bind to the lone pair on the nitrogen in a fixed position stereoselective synthesis can be carried out. This can all be controlled by the electron-donating or -withdrawing character of the monodentate ligand. The author believes this is one of the first studies to show evidence of an anomeric effect existing in metal complexes.

4.5 References

(1) Ryan, M. *Platinum Metals Review* **2009**, *53*, 216.

(2) Dougan, S. J.; Melchart, M.; Habtemariam, A.; Parsons, S.; Sadler, P. J. *Inorg. Chem.* **2006**, *45*, 10882.

(3) Nakano, K.; Suemura, N.; Yoneda, K.; Kawata, S.; Kaizaki, S. *Dalton Trans.* **2005**, 740.

(4) Sizova, O. V.; Ivanova, N.; Sizov, V. V.; Ershov, A. Y.; Baranovski, V. I. *Inorg. Chim. Acta* **2004**, *357*, 354.

(5) Leventis, N.; Rawaswdeh, A.-M. M.; Zhang, G.; Elder, I. A.; Sotiriou-Leventis, C. *J. Org. Chem.* **2002**, *67*, 7501.

(6) Seddon, E. A.; Seddon, K. R. *Topics in Inorganic and General Chemistry, Vol. 19: The Chemistry of Ruthenium*, Elsevier; Amsterdam 1984.

(7) Morris, R. E.; Aird, R. E.; Murdoch, P. d. S.; Chen, H.; Cummings, J.; Hughes, N. D.; Parsons, S.; Parkin, A.; Boyd, G.; Jodrell, D. I.; Sadler, P. J. *J. Med. Chem.* **2001**, *44*, 3616.

(8) F. Wang, H. C., S. Parsons, I. D. H. Oswald, J. E. Davidson and P. J. Sadler *Chem. Eur. J.* **2003**, *9*, 5810

(9) Wang, F.; Habtemariam, A.; van der Geer, E. P. L.; Fernandez, R.; Melchart, M.; Deeth, R. J.; Aird, R.; Guichard, S.; Fabbiani, F. P. A.; Lozano-Casal, P.; Oswald, I. D. H.; Jodrell, D. I.; Parsons, S.; Sadler, P. J. *Proc. Natl. Acad. Sci. U. S. A.* **2005**, *102*, 18269.

(10) Chen, H.; Parkinson, J. A.; Parsons, S.; Coxall, R. A.; Gould, R. O.; Sadler, P. J. *J. Am. Chem. Soc.* **2002**, *124*, 3064.

(11) Chen, H.; Parkinson, J. A.; Morris, R. E.; Sadler, P. J. *J. Am. Chem. Soc.* **2003**, *125*, 173.

(12) Liu, H.-K.; Berners-Price, S. J.; Wang, F.; Parkinson, J. A.; Xu, J.; Bella, J.; Sadler, P. J. *Angew. Chem. Int. Ed.* **2006**, *45*, 8153.

(13) Williams, J. P.; Lough, J. A.; Campuzano, I.; Richardson, K.; Sadler, P. J. *Rapid Commun. Mass Spectrom.* **2009**, *23*, 3563.

(14) Williams, J. P.; Brown, J. M.; Campuzano, I.; Sadler, P. J. *Chem. Commun.* **2010**, *46*, 5458.

(15) Wang, F.; Xu, J.; Habtemariam, A.; Bella, J.; Sadler, P. J. *J. Am. Chem. Soc.* **2005**, *127*, 17734.

(16) Wang, F.; Bella, J.; Parkinson, J. A.; Sadler, P. J. *JBIC, J. Biol. Inorg. Chem.* **2005**, *10*, 147.

(17) McNae, I. W.; Fishburne, K.; Habtemariam, A.; Hunter, T. M.; Melchart, M.; Wang, F.; Walkinshaw, M. D.; Sadler, P. J. *Chem. Commun. (Cambridge,* **2004**, 1786.

(18) Sheldrick, G. M. SHELXS-97, *University of Gottingen, Gottingen, Germany* **1997**.

(19) Sheldrick, W. S.; Heeb, S. *Inorg. Chim. Acta* **1990**, *168*, 93.

(20) Macrae, C. F.; Edgington, P. R.; McCabe, P.; Pidcock, E.; Shields, G. P.; Taylor, R.; Towler, M.; van de Streek, J. *J. Appl. Cryst.* **2006**, *39*, 453.

(21) Macrae, C. F.; Bruno, I. J.; Chisholm, J. A.; Edgington, P. R.; McCabe, P.; Pidcock, E.; Rodriguez-Monge, L.; Taylor, L.; van de Streek, J.; Wood, P. A. *J. Appl. Cryst.* **2008** *41*, 466.

(22) Farrugia, L. J. *J. Appl. Crystallogr.* **1997**, *30*, 565.

(23) Wang, F.; Chen, H.; Parsons, S.; Oswald, I. D. H.; Davidson, J. E.; Sadler, P. J. *Chem.--A Eur. J.* **2003**, *9*, 5810.

(24) Bjerrum, J.; Schwarzenbach, G.; Sillen, L. G.; Berecki-Biedermann, C.; Maltesen, L.; Rasmussen, S. E.; Rossotti, F. J. C. *Chem. Soc. (London), Spec. Publ.* **1958**, *No. 7*.

(25) Fischer, A.; Galloway, W. J.; Vaughan, J. *J. Chem. Soc.* **1964**, 3591.

(26) Grandberg, I. I.; Faizova, G. K.; Kost, A. N. *Khim. Geterotsikl. Soedin.* **1966**, 561.

(27) Johnson, C. D. in *The Hammett Equation*, Cambridge University Press; New York, 1980.

Chapter 5

Investigation of Shape Modifications of Oligoneucliotides Following Binding to Metal-Based Anticancer Agents.

Chapter 5

Investigation of Shape Modifications of Oligoneucliotides Following Binding to Metal-Based Anticancer Agents.

5.1 Introduction

The earliest work on complexes of the type $[(\eta^6\text{-arene})Ru(en)Cl]^+$ has showed strong interaction of the ruthenium molecules with oligonucleotides, this has been observed both experimentally[1,2] and *in silico*[3,4]. This is important, as binding to DNA is believed to be a key part of the mechanism of action of these types of drugs[5].

Cisplatin (cis-diamminedichloroplatinium(II)) is also believed to work in a similar manner. Much more work into DNA binding with cisplatin has been carried out and has shown some very interesting results. The shape changes induced to DNA strands and the subsequent recognition by high mobility group proteins of these kinked strands is believed to play an integral part in the mechanism[6,7] of action in instigating intracellular processes that lead to cell death.

The key differences between $[(\eta^6\text{-arene})Ru(en)Cl]^+$ and cisplatin, is the fact that the Ru has only one active site versus the two active sites on cisplatin. This can lead to a variation in the mechanism of action compared to that of cisplatin.

Unlike cisplatin, there are no x-ray crystal structures of the ruthenium arene adducts DNA. During the course of this work, efforts to crystallise ruthenium-DNA adducts were made and have so far been fruitless. However, it is believed that with some effort these may be successful in the future.

In the absence of a crystal structure, other attempts are being made to investigate the shape changes brought about by metallation of DNA strands. In this Chapter two potential methods for the investigation of shape changes to DNA strands upon binding of ruthenium or cisplatin complexes are examined. These methods are ion-mobility mass spectrometry (IM-MS) (*c.f.* **§2.4**) and Förster Resonance Excitation Transfer (FRET) (*c.f.* §**2.11**). Both methods show potential for investigating shape changes. Below the rationale behind the development of each method, the main hurdles and the potential for use of each method are discussed.

5.2 Method Development – Ion Mobility Mass Spectrometry

5.2.1 Introduction

Previously Ion-Mobility Mass Spectrometry (IM-MS) has been used to investigate the 3D shape of proteins in the gas phase.[8] Recent investigations have shown IM-MS is capable of separating isomers of larger Ru(η^6-arene) complexes.[9] Prior to this work, no studies have reported the use of IM-MS to determine the Collision Cross Section (CCS) of molecules < 100 Å^2.

This work appears to be the first to use IMMS to determine the CCS of small molecules. To develop this, a new method of calibration using glycine oligomers was employed.

Traditionally collision cross-sections (the molecular equivalent of an area of gyration in proteins and other large biomolecules) have been calculated using the open source software MOBCAL[10]. MOBCAL provides outputs which are based on the three different models, Projection Approximation (PA) and Exact Hard Sphere Scattering (EHSS), which both model the ion as a series of

overlapping hard sphere, and the trajectory method, in which all atoms in the ion are modelled, using the ions three-dimensional coordinate file. However, in the work presented here, a new approach is used; this is an algorithm developed by Waters Corp. (Manchester, UK).This new algorithm is included in their Windows® based ion mobility software (Driftscope) and together with Waters a study was carried out to test the efficiency of the new algorithm both compared to MOBCAL results and those obtained through IM-MS.

5.2.2 Experimental Design

The binding of $\{Ru(\eta^6\text{-bip})(en)\}^{2+}$ to DNA through the N7 on guanine residues has been well documented.[5,11-16] Prior to this, IM-MS had not been used to investigate shape changes to DNA strands.[8,17,18] It was hoped that this technique could be used for future studies of the interaction between ruthenium complexes and DNA. If successful, then information on the shape changes to DNA (and other biomolecules) may provide insight into possible cell death pathways initiated by this class of compounds.

In the design of this process, careful consideration was given to the sequence of DNA to be chosen. Since binding to guanine is well known, it was essential to include at least one guanine residue. Previous mass spectrometry studies investigating cisplatin binding to small oligonucleotides used the sequence 5'-CACGTG-3'.[19] It was therefore considered useful to use this sequence. While this strand is self-complementary, it was hoped to prevent the stabile formation of duplexes by maintaining a low salt concentration. For other studies not discussed here the ^{15}N labelled $[Ru(\eta^6\text{-bip})(^{15}\text{N-en})Cl]PF_6$ (**1-^{15}N_PF$_6$**) was synthesised (*c.f.* **§2.15.2.9**) and a fixed concentration solution was prepared and concentration

determined by ICP-MS. Due to the limited supply of DNA used, some of this sample was used in some of the later studies.

5.2.3. Systematic approach and results

5.2.3.1 Preparation of d(CACGTG)-[(η^6-bip)Ru(en)]$_2$

A 25 μL aliquot of the d(ACAGTG) (stock solution 530 μM in H_2O, determined by UV/Vis) was added to 25 μL of **1_PF$_6$** (stock solution 2.017 mM, determined by ICP-MS); this was then incubated at 310 K for 14 h. (total concentrations, DNA: 265 μM, Ru: 1.085 mM, DNA:Ru = 1:4). This was then diluted approximately 100 times with aqueous acetonitrile prior to MS analysis.

5.2.3.2 MS Analysis of d(CACGTG)-[(η^6-bip)Ru(en)]$_2$

After mixing of **1-PF$_6$** with d(CACGTG), MS was obtained showing that two {Ru(η^6-bip)en}$^{2+}$ had bound to the 6-mer (Figure 5.1). Mass spectrometry was carried out as per **§2.4.2** by Dr Jonathon Williams, University of Warwick using the facilities at Waters Corps. Manchester. An insert showing the isotopic distribution pattern for the 2$^-$ species seen in the spectrum is also shown. Negative electospray ionisation mass spectrometry (ESI-MS) is of particular useful in the analysis of oligonucleotides due to the negative phosphate back bone of DNA strands.

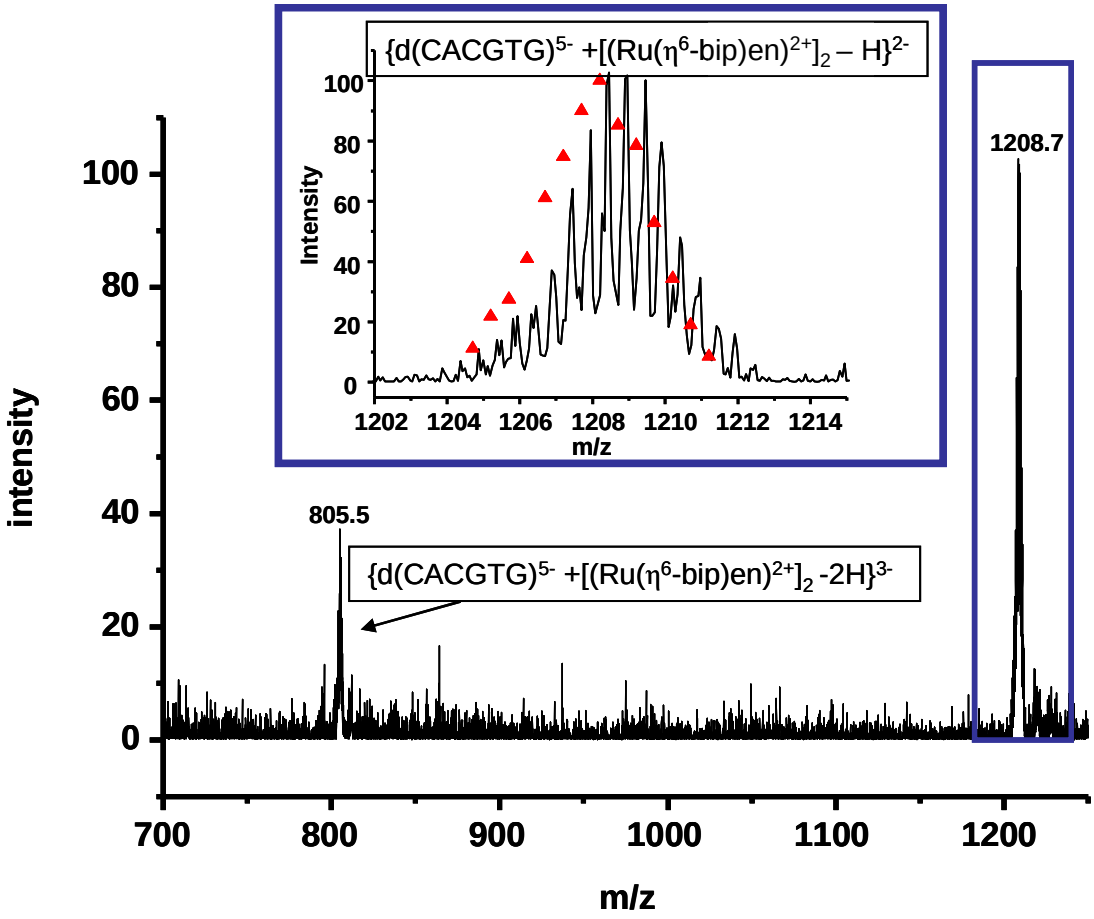

Figure 5.1. Negative ion ESI mass spectrum from a sample of d(CACGTG) mixed with **1-PF$_6$** at 310 K after 14 h. Inset: Expansion of the major ion seen in the spectrum – 1208.7 as a 2^- ion, and the simulated isotope pattern (▲). (Difference between calculated and obtained = 0.5 Da)

To confirm that binding of the ruthenium complex was to the guanine residues, tandem MS/MS was carried out. There was difficulty in fragmenting the negative ions, however the positive ions fragmented easily using low energy CID on the ion of interest, using SF_6 as a collision gas. (Figure 5.2)

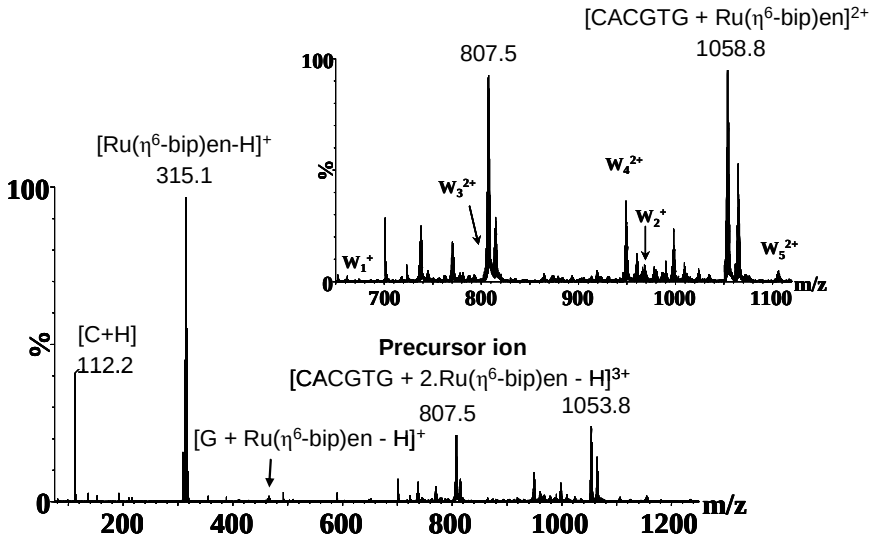

Figure 5.2. The expanded MS/MS spectrum of 3^{+} ion, [CACGTG-2.Ru(η^6-bip)en-H]$^{3+}$ species with *m/z* 807.5. The inset image is the expansion of 650 – 1120 m/z region and highlights the location of the w_n^{z+} ion species observed in the m/z range 650 – 1120.

Collision-induced decay breaks bonds along the phosphate back bone of the DNA.[20] Figure 5.3 defines ions classed as w-ion which are identified and listed in Table 5.1

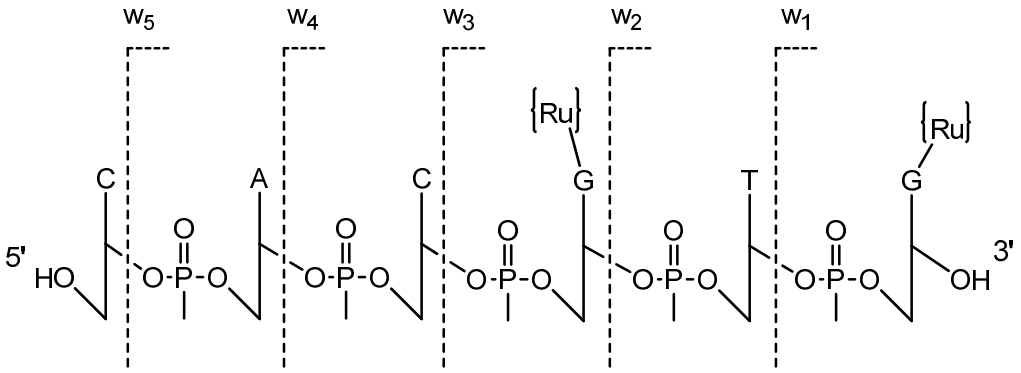

Figure 5.3. A scheme showing the fragmentation pattern of [CACGTG-2.Ru(η^6-bip)en-H]$^{3+}$ forming a variety of w-ions. {Ru} = {Ru(η^6-bip)en}$^{2+}$.

Table 5.1. Identity of each of the w ions observed in Figure 5.2

w_n^{z+} ion	*m/z*	Identity
w_5^+	1106	3'-GpTpGpCpAp + Ru(η^6-bip)en
w_4^{2+}	949	3'-GpTpGpCp + 2.Ru(η^6-bip)en
w_3^{2+}	805	3'-GpTpGp + 2.Ru(η^6-bip)en
w_2^+	966	3'-GpTp + Ru(η^6-bip)en
w_1^+	662	3'-Gp

Of interest is the presence of w_3^{2+} which confirms that two ruthenium complexes are attached to the 5'-GTG-3' portion of the hexamer. However upon further examination, the w_2^+ ion was identified as containing the 5'-pTpG-3' with one ruthenium complex attached. This confirms that one ruthenium complex is bound to the guanine in the 4 position. Further fragmentation produced a 5'-pG-3' ion (w_1^+) without a ruthenium complex attached. Thymine residues have only

shown very weak binding to ruthenium-arene complexes and so the distinct absence of a [3'-Gp-Ru(η^6-bip)en] species was unexpected. A G-{Ru} ion was observed at m/z 466, however this could be from the G_4-{Ru} or the G_6-{Ru} fragment being cleaved from the hexamer during the CID process. Interestingly no [T-Ru(η^6-bip)en]$^+$ ion was observed either. It was postulated that the fragmentation energy of the w_2^+ ion may have been sufficient to fragment the N7-Ru bond on the guanine at the 3' end of the sequence. To investigate if binding of the ruthenium complex is exclusive to the guanine residues, binding to an alternative hexamer, d(CACGTA), was studied.

5.2.3.3 Preparation of d(CACGTA)-[(η^6-bip)Ru(en)]$_2$

A 300 μL aliquot of the d(ACAGTA) (stock solution 11.6 μM in H_2O) was added to 3 μL of **1-^{15}N-PF$_6$** (stock solution 2.0165 mM); this was then incubated at 310 K for 14 h. (total concentrations, DNA: 3 μM, Ru: 32 μM, DNA:Ru = 1:10). This solution was injected directly into the mass spectrometer.

5.2.3.4 Analysis of d(CACGTA)-[(η^6-bip)Ru(en)]$_2$

The ^{15}N-labelled form **(1_^{15}N-PF$_6$)** was bound to d(CACGTA) to confirm that binding indeed is selective for guanine residues. Figure 5.4 shows the mass spectrum obtained on a Bruker MaXis instrument (*c.f.* **§2.3**). The spectrum clearly shows that despite a ten fold molar excess of the ruthenium complex, only one Ru(II) is attached to this strand of oligo hexamer. This provides strong evidence that binding is exclusively to guanine residues.

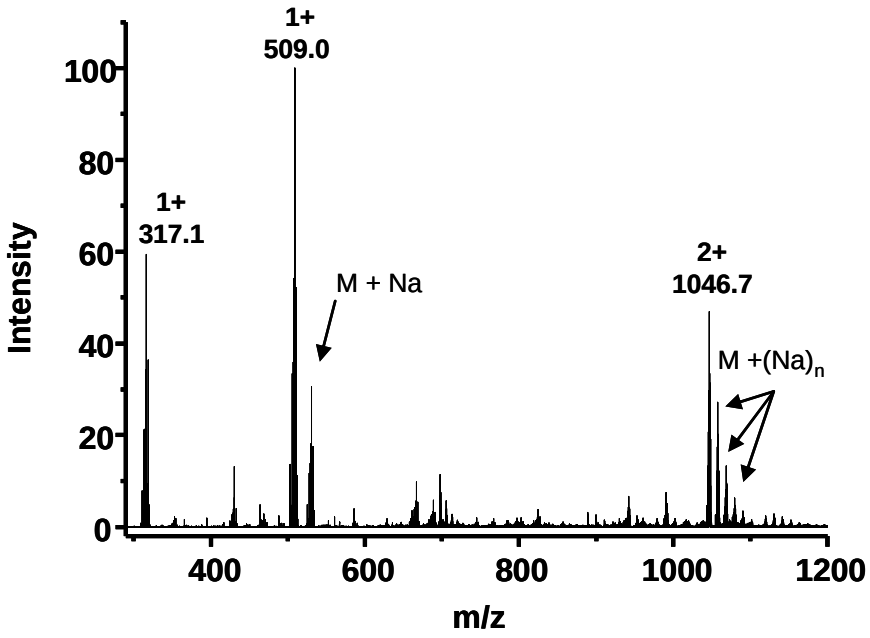

Figure 5.4. A mass spectrum of a mixture of d(CACGTA) and **1**-^{15}**N**-$\mathbf{PF_6}$ after 24 h at 310 K. The main species and charges are highlighted.

There are three main clusters of peaks visible in the spectrum; these have been identified and the isotopic simulation pattern is shown in Figure 5.5a, b and c. The large remaining complex (**1**_^{15}**N**) peak at 317 amu. The peak at 509 amu can be identified as **1**_^{15}**N** flying with as an ethanol molecule and PF_6^- ion. At 1046.7 amu the 2^+ species which corresponds to $[d(CACGTA)\text{-}Ru(\eta^6\text{-}bip)(^{15}N\text{-}en)]^{2+}$ species.

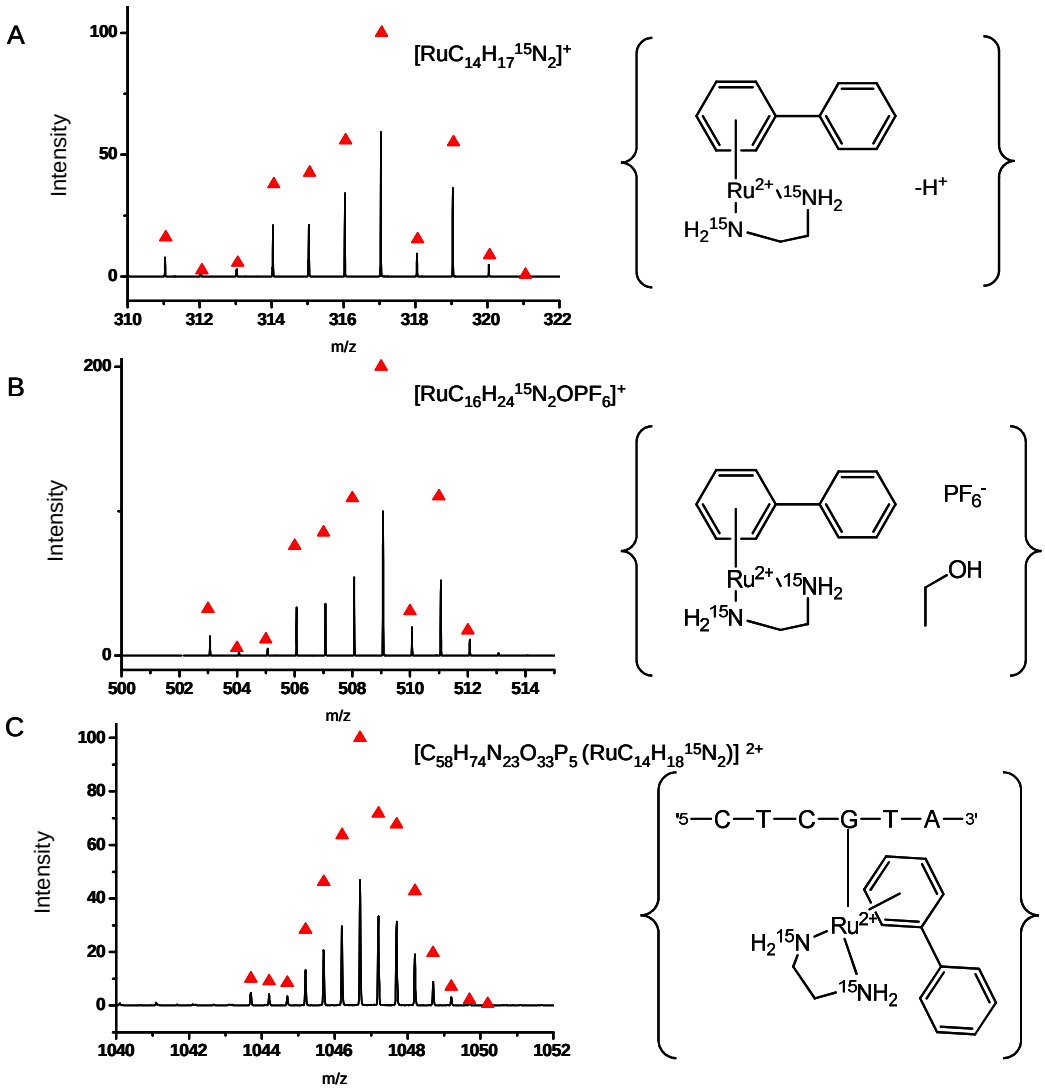

Figure 5.5. Expansion of the main species found in the MS of d(CACGTA)-**1**_^{15}**N** mixture after 24 h at 310K. The spectrum is in black and the simulated isotope pattern, ▲ is also shown for A) *m/z* centred at 317.1, B) *m/z* centred at 509.0 and C) *m/z* centred at 1046.7. (Labels define each peak)

5.2.3.5 Ion-mobility mass spectrometric analysis of [Ru(η^6-bip)enCl]$^+$ (1)

Previously, ion-mobility mass spectrometry studies were carried out using singly-charged peptide ions produced from human haemoglobin (Hb) which had undergone tryptic digestion, to calibrate the T-Wave mobility device[21]. The limiting factor to this approach was that only collision cross sections (CCS) values

of 94 – 279 $Å^2$ can be determined. A new approach using protonated gylcine oligomers $[Gly_{n=2-6} + H]^+$, of which all the CCS values was used for the first time in this work to calibrate the T-Wave mobility device over a range of 62 – 107 Å.[22] Using this technique the CCS values for $[Ru(\eta^6\text{-bip})en\text{-}H]^+$ and $[Ru(\eta^6\text{-bip})enCl]^+$ (**1**) ions in the gas phase were analysed. These results were then compared to CCS values calculated from the crystal structure using a variety of algorithms and also to the radius of the molecule as determined by Diffusion Ordered SpectroscopY (DOSY) NMR of **1-PF$_6$** in solution.[23]

A sample of **1-PF$_6$** was prepared from a 2.17 mM solution in H_2O to ca. 1 ng/mL in methanol and injected at a rate of 4 μL min^{-1} into the mass spectrometer. Two major peaks were observed (Figure 5.6) at m/z 315 and 351; these correspond to $\mathbf{1}^+$ and $[\mathbf{1\text{-}HCl}]^+$ as detailed below.

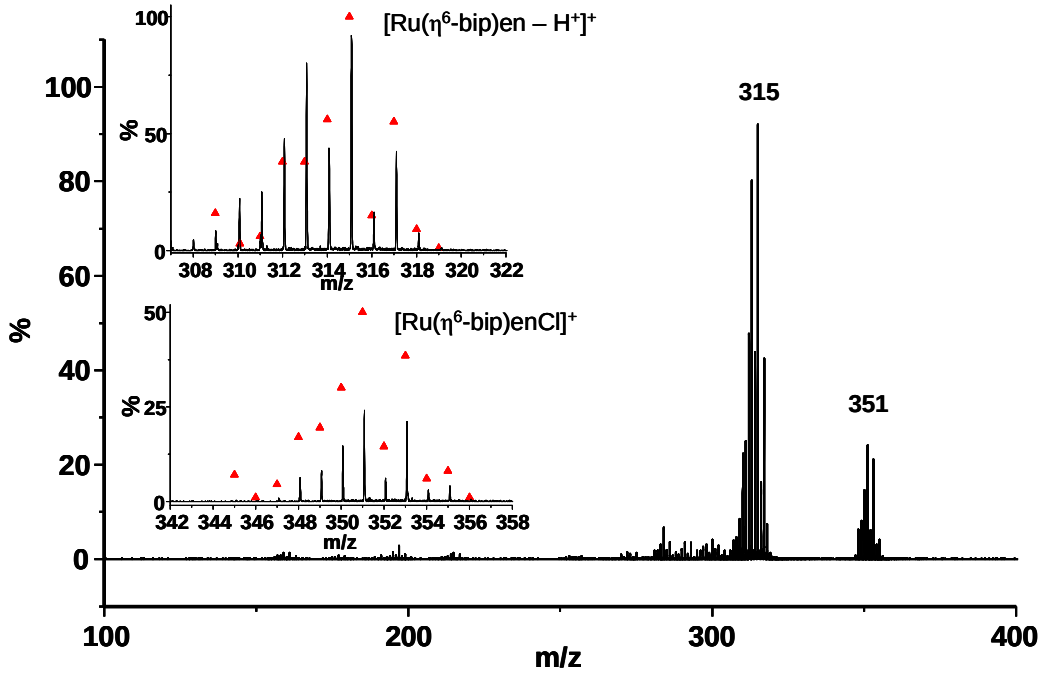

Figure 5.6 Positive ion mass spectrum of **1** in solution (ca 1 ng/mL) in methanol. The expected isotope pattern ▲and an expansion shown in the inset for the 2 species centred at 315 and 351 m/z.

The two major species observed in Figure 5.6 were isolated in the quadrupole and then each one entered the T-Wave chamber separately (*c.f.* **§2.4**). Once the ions had entered the T-Wave chamber the mobility drift times (sometimes referred to as arrival time distribution, ATD) could be recorded. This was then calibrated against the ATD for the protonated glycine oligomers. Figure 5.7 shows the chromatograph of the ion-mobility cell and the corresponding ion and ATD.

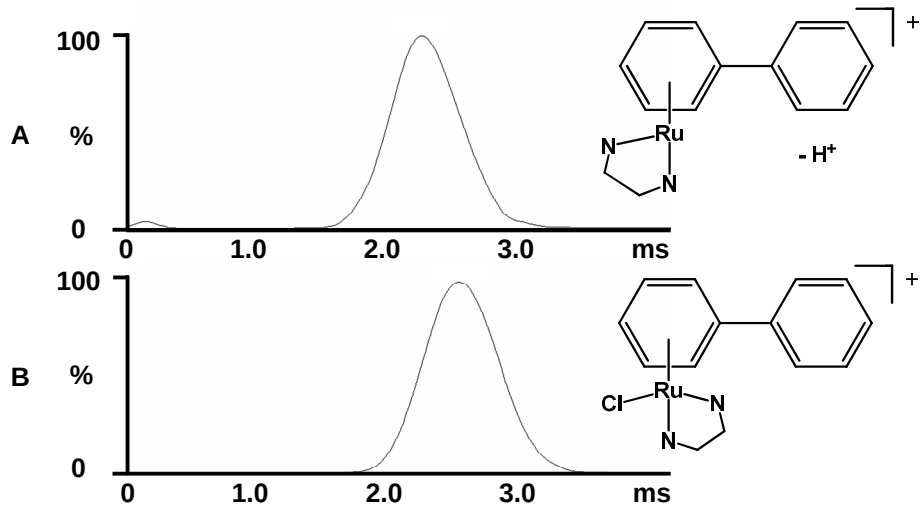

Figure 5.7. Drift times for A) $[Ru(\eta^6\text{-bip})en\text{-}H^+]^+$ and B) $[Ru(\eta^6\text{-bip})enCl]^+$ ions in a T-Wave Ion mobility device.

These data, along with those from MOBCAL calculations and the Waters® algorithm produced CCS values shown in Table 5.2. Complementary to this, Diffusion Ordered Spectroscopy was carried out to determine the radius of the $[Ru(\eta^6\text{-bip})enCl]^+$ species in solution. DOSY NMR is an NMR technique which allows a diffusion constant for a molecule in solution to be determined.[24] DOSY NMR applies a magnetic gradient along the z-axis and the effects of magnetisation as the protons pass through the magnetic gradient provide insight into the diffusion constant of the complex. Together with the Stokes-Einstein equation the hydrodynamic radius can be determined, and from that the CCS. The DOSY NMR spectrum is shown in Figure 5.8 and the data are further added to that of Table 5.2. DOSY NMR applies a magnetic gradient along the z-axis and the effects of magnetisation as the protons pass through the magnetic gradient provide insight into the diffusion constant of the complex

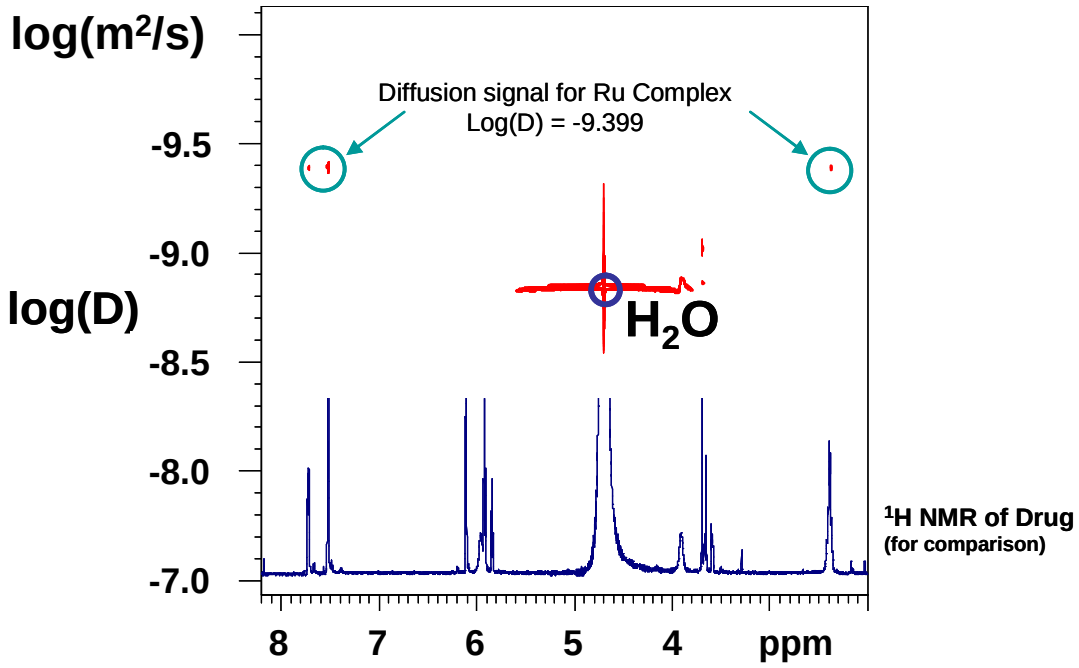

Figure 5.8. ^{1}H diffusion spectrum of [Ru(η^6-bip)enCl]$^{+}$ in 154 mM NaCl in D_2O (to suppress hydrolysis) at 298 K at 600 MHz. From log (D) = -9.399, the diffusion constant of 3.989 x 10^{-10} m^2/s is determined.

Using D = 3.989 x 10^{-10} m^2/s and the viscosity of the solution[25] at 0.9037 x 10^{-3} Pa.s and applying to the Stokes Einstein equation, yields a radius of 6.05 Å and a cross section of 114.99 $Å^2$ .This is comparable to those determined by calculations when considering that this radius also includes water molecules in the solvation sphere, which would increase the radius somewhat.

Table 5.2. CCS ($Å^2$) values as determined by calculation and experiment.

m/z	ion	MOBCAL Projection approx	MOBCAL Exact hard sphere	MOBCAL Trajectory Method	Waters Algorithm	T-Wave (± 1.0)	DOSY NMR
315	[Ru(η^6-bip)enCl]$^{+}$	93.5	99.0	93.9 ± 6.3	95.8	97.5	114.99
351	[Ru(η^6-bip)en-H^{+}]$^{+}$	91.6	96.5	90.9 ± 4.7	89.0	93.0	N/A

5.2.3.6 Ion-mobility mass spectrometric analysis of d(CACGTG)-{(bip)Ru(en)}$_2$

Next of interest was a study through ion-mobility into the shape change of oligonucleotide strands upon addition of this ruthenium complex. Cisplatin has been shown to cause shape changes to DNA strands.[26-28] However, cisplatin has 2 active sites whereas [Ru(η^6-bip)enCl]$^+$ has only one and so will interact with DNA differently.

Firstly, the CCS of the oligonucleotide d(CACGTG) was determined using IM-MS to acquire the arrival time distribution of both the 2^- and 2^+ species (Figure 5.9). These were calibrated against the human haemoglobin and against sperm whale myoglobin, of which there is a variation of <1 %.

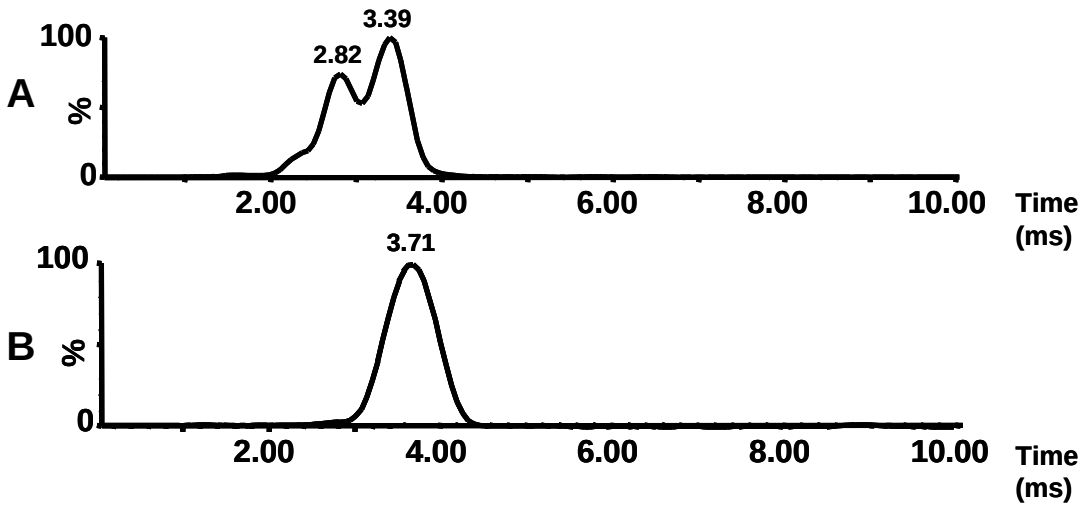

Figure 5.9. Arrival Time distributions (ATD) or drift times for A) [CACGTG - 2H$^+$]$^{2-}$ and B) [CACGTG + 2H$^+$]$^{2+}$ ions.

Figure 5.9 shows two different, possibly three, conformations ATDs (2.82 and 3.39 ms, and shoulder to the left of 2.82 ms peak) for the 2^- species. These conformations are clearly stable in gas phase as interconversion is not seen on the timescale of the experiment. The different conformations are more than likely a

result of different distributions of H^+ ions on the five phosphates on the back bone of the 6-mer. (The phosphates on the back bone of DNA structures tend to be deprotonated). The observation that the ATD for the positive species is larger than the negative ion is not unexpected, positive molecular ions generally, are larger in size than negative molecular ions due to the extra hydrogen atoms.

Once the ATDs of the non-ruthenated DNA have been observed, the ATDs for the 6-mer bound to two ruthenium molecules, $[Ru(\eta^6\text{-bip})en]^{2+}$ were next to be studied. Again, it is noticeable that the ATD of the negative ion is less than that of the positive ion. (Figure 5.10)

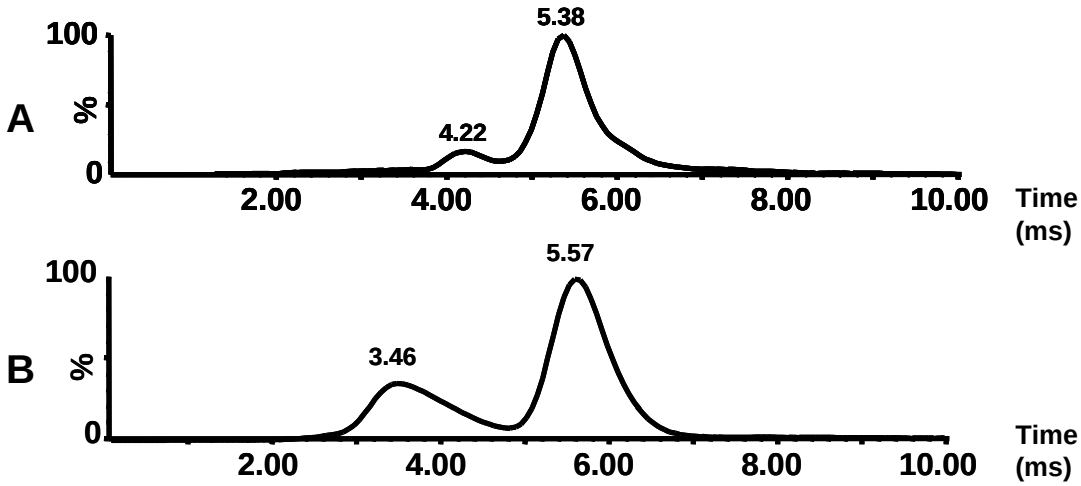

Figure 5.10. ATDs of A) $[CACGTG + 2[Ru(\eta^6\text{-bip})en] - 6H^+]^{2-}$ and B) $[CACGTG + 2[Ru(\eta^6\text{-bip})en] - 2H^+]^{2+}$

It was observed once more, that there appears to be more than one configuration of each species. This is again probably due to distributions of protons on the backbone phosphate backbone on the oligonucleotide, for the negative ion mode (Figure 5.10A). However for the positive ion, the 2 ATDs are significantly separated (by 2.11 ms). Individual mass spectra of each peak

explained this very easily. The peak at 3.46 ms is a 4^+ species of an associative dimer (m/z = $[(CACGTG + 2[Ru(\eta^6\text{-bip})en] - 2H^+)_2]^{4+}$). While a dimer was not expected due to the low ionic strength of the solution, it appears in this case that there has been some associative binding in the gas phase.

Table 5.3 shows a compiled list of all CCS values as determined from the drift times, when calibrated against human haemoglobin and sperm whale myoglobin.

Table 5.3. CCS values for both the 6-mer oligonucleotide and the ruthenated oligonucleotide for both 2^+ and 2^- species.

Ions	Collision Cross Section (CCS) , $Å^2$
$[CACGTG - 2H^+]^{2-}$	289.5, 300.3
$[CACGTG + 2H^+]^{2+}$	312.8
$[CACGTG + 2[Ru(\eta^6\text{-bip})en] - 6H^+]^{2-}$	315.8, 337.4
$[CACGTG + 2[Ru(\eta^6\text{-bip})en] - 2H^+]^{2+}$	350.2

5.2.4 Discussion

It has long been known that $[Ru(\eta^6\text{-bip})en]^{2+}$ residues bind to N7 of guanine bases on DNA strands[5,11,13,14,29-31]. Reactions between **1-PF_6** and d(CACGTG) and d(CACGTA) yielded exclusive binding to the guanine residues. Following confirmation of the binding positions, ion-mobility mass spectrometry was carried out on both d(CACGTG) bound to two ruthenium complexes and of the ruthenium complex on its own.

5.2.4.1 Ion mobility of $[Ru(\eta^6\text{-bip})enCl]^+$ (1) ions.

Ion-mobility studies on **1** and the subsequent determination of the collision cross section (CCS) compared well to the computationally-derived CCS values and the cross section as determined by DOSY NMR. This study is the first reported where a CCS of < 100 $Å^2$ is determined.[23] This was made possible by using new calibration method of using protonated glycine oligomers. Also investigated was the accuracy of the Waters® algorithm in accurately predicting the CCS of complexes from their 3D coordinate file (crystal structure). All calculated CCS values were within 5% of the values determined by IM-MS, indicating that a good correlation between solid state (crystal structure) and gas phase (MS) CCS values exists. Of interest is the DOSY NMR determined CCS value of 114.99 $Å^2$; the difference between this and the IM-MS value, can be explained by the presence of a solvation shell around the complex. With **1** being a charged molecule the probability of a water solvation shell is large.

5.2.4.2 Ion mobility of d(CACGTG) and $[d(CACGTG) + 2.[Ru(\eta^6\text{-bip})en]]^{2+}$ ions.

Ion-mobility mass spectrometry was also used for analysis of shape changes that occur in oligomers when bound to ruthenium complexes. Initial measurements on the 2^- and 2^+ species of d(CACGTG) showed some interesting results. Firstly negative ions were found to have a smaller CCS than positive ions; this is not unexpected and has been observed before.[8] Secondly, more than one conformation was observed in the negative ion studies. This is most likely due to the location of protons on the backbone of the oligonucleotide. DNA strands are very stable as -(n-1) ions, where n is the number of base pairs present when in

solution. The negative charges are on the phosphate backbone, where each diester link has one negative charge. (Figure 5.11)

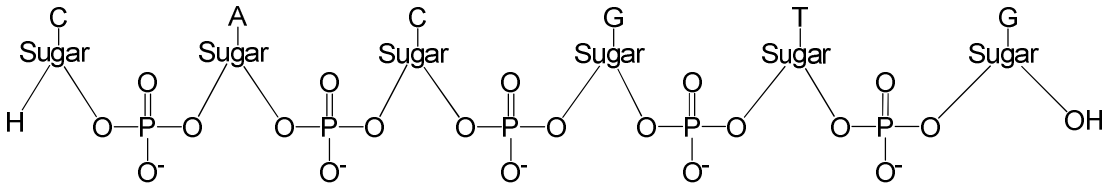

Figure 5.11 A schematic diagram of d(CACGTG) showing the location of the negatively charged sites. In the neutral 6-mer species these are protonated.

This leaves five places for three protons to reside on the back bone and electrostatic repulsive and attractive forces would lead to different folding patterns and therefore different 3D conformations. The effects of the positive charges on the backbone of the oligomer must be considered when comparing with the CCS values of the diruthenated strand. While CCS values were obtained for both the $[d(CACGTG) - 6H^+ + 2.[Ru(\eta^6\text{-bip})en]^{2+}]^{2-}$ species and for $[d(CACGTG) - 2H^+ + 2.[Ru(\eta^6\text{-bip})en]^{2+}]^{2+}$, comparisons can only be made accurately when looking at the two species which have lost two protons from the backbone. This means to compare the shape change upon ruthenation $[d(CACGTG) - 2H^+ + 2.[Ru(\eta^6\text{-bip})en]^{2+}]^{2+}$ must be compared with $[d(CACGTG) - 2H^+]^{2-}$. Changes in the shape of these species are more likely to be a result of ruthenation only. Table 5.4 shows the difference between the two species.

Table 5.4. CCS values for the non-ruthenated and bi-ruthenated strands of $d(CACGTG)^{2-}$

Ion	CCS ($Å^2$)
$[CACGTG - 2H^+]^{2-}$	289.5, 300.3
$[CACGTG + 2[Ru(\eta^6\text{-bip})en]^{2+} - 2H^+]^{2+}$	350.2

The above results show that the addition of two ruthenium complexes of CCS 93 $Å^2$ (loss of chlorido group from the ruthenium when attached to oligonucleotides), to this oligonucleotide results in a change to the size overall of 50–60 $Å^2$. This suggests that binding the ruthenium complex to the oligonucleotide compresses the shape or is bound in such a way as to have little effect on the overall shape of the product. This would agree well with some previous studies of 14-mer oligonucleotides in which the biphenyl ring system on the ruthenium complex has been shown to intercalate between the guanine and thymine base pairs of DNA.[14]

5.3 Method Development – Förster Resonance Energy Transfer

5.3.1 Introduction

Previous work[26,28,32] has shown that when DNA strands are platinated, kinking of the duplex strands occurs and this leads to programmed cell death. Förster Resonance Energy Transfer (FRET) has been used in the past to investigate the shape of DNA duplexes, which have been synthesised to be kinked[33]. Studies of DNA dissociating from nucleosomes[34] and investigations into HIV reverse transcriptase interactions with nucleic acids[35] have also been carried out. A previous study[7], has looked at the effects of cisplatin binding to a

20-mer duplex and observed FRET indicating that the DNA was bent at an angle of 58^{o} when 1,2 GpG intrastrand platinum crosslinks are present. It was with this in mind that attempts were made to study a platinated 30-mer DNA duplex using FRET and to develop the method for use on ruthenated sequences.

5.3.2 Experimental design

A fundamental part of the design of this experiment involved choosing a suitable DNA sequence. When making decision on the sequences to be used, the ability of guanine residues to quench fluorescence must be considered. However, to allow for platination, two adjacent guanine residues must be included in the sequence. In addition to this guanine and cytosine residues must be used as "zipper" points at the end of the DNA strands to stabilise the duplex. To this end, it was decided to have the two guanine residues in the middle of the sequence to allow for platination. The choice of FRET tags must also be considered and has been discussed previously (*c.f.* **§2.11**). To allow for significant FRET between tags, they would initially be placed 12 base pairs apart on complementary strands. The initial 30-mer DNA sequence chosen was the following; d(TATCATAAATAAATGGTATATT(Alexa488)TTATAACT) and the d(ATAGTATTT(Cy5)ATTTACCATATAAAATATTGA) complementary strand. These sequences took into account the need for a GG portion to allow platination, a large amount of A and T, C and G residues to "zip" the duplex and a lack of self complementarily of the sequence so only the donor and acceptor strand will pair with each other. Once the DNA sequence was decided upon, a variety of approaches were then attempted. Scheme 5.1 shows the variety of approaches considered and the subsequent changes to optimise the procedure.

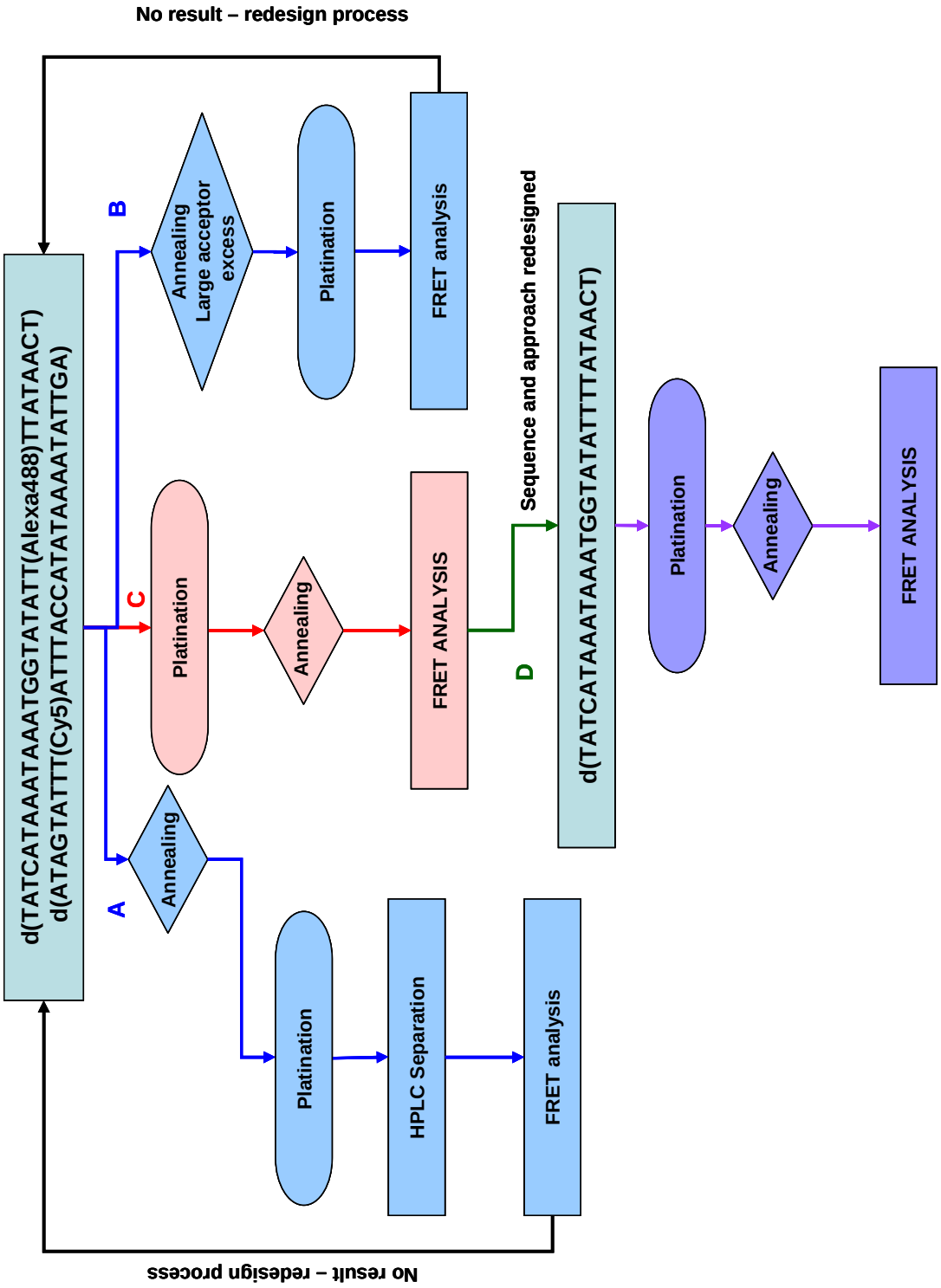

Scheme 5.1. A schematic approach to the variety of processes used in this chapter. A,B, C and D will all be discussed sequentially below.

5.3.3 Preparation and analysis of fluorescent DNA samples.

Parts of this work was carried out in collaboration with Ms Anita Toulmin and Dr Steven Magennis in the Photonics Institute, University of Manchester, UK.

5.3.3.1 (A) Formation of a duplex and subsequent binding of cisplatin

5.3.3.1.1 Sample preparation.

In this initial approach, the two strands of DNA were annealed and then platinated. In addition to this, a duplex with only a donor label was also synthesised to confirm that any FRET signals observed would be from the Donor-Acceptor strands only. Table 5.5 lists the DNA strands and their short code labels as used in this approach. Figure 5.12 shows a photograph of the vials of DNA. It is clearly evident how coloured and fluorescent these DNA samples are.

Table 5.5. DNA sequences, short codes and concentrations.

Sequence	Code	Conc. (µM)
d(TATCATAAATAAATGGTATATT(Alexa488)TTATAACT)	**D**	70
d(ATAGTATTT(Cy5)ATTTACCATATAAAATATTGA)	**A**	80
d(ATAGTATTTATTTACCATATAAAATATTGA)	**U**	77

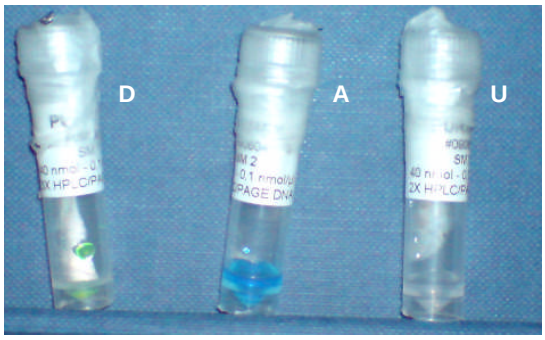

Figure 5.12. Photograph of solutions of each of the strands of 30-mer used; clearly it can be seen that the donor (**D**) strand is yellow/green, the acceptor (**A**) strand blue, and the unlabelled (**U**) strand is colourless.

Solutions of **D** (64 µL), **A** (56 µL) and 45 µL of $NaClO_4$ (2 M solution) were combined and diluted to a total volume of 500 µL in H_2O. This solution was annealed by heating to 363 K, slowly cooled over 4 hours and the left to stand at 277 K overnight (total duplex concentration: 4.48 µM, $NaClO_4$; 90 mM). The product was labelled **SMDA1.** Follow annealation, cisplatin (0.32 µL, 9.857 mM solution in DMF) was added to 350 µL of **SMDA1** and 149.68 µL of deionised H_2O, and incubated at 310 K for 48 h. (Total duplex concentration 3.14 µM; $NaClO_4$ 90 mM, Pt 6.3 µM) . The product was labelled **SMDA1-Pt.**

The unlabelled duplex was synthesised in a similar manner. A solution of **D** (64 µL), **U** (58.1µL) was annealed in the same manner. (Total duplex concentration 4.48 µM, $NaClO_4$ 90 mM) . The product is labelled **SMDU1.** Following annealation, cisplatin (0.32 µL, 9.857 mM solution in DMF) was added and the duplex was platinated as described above. (Total duplex concentration 3.14 µM, $NaClO_4$ 90 mM, Pt 6.3 µM) . The product is labelled **SMDU1-Pt.**

5.3.3.1.2 CD, HPLC and FRET analysis of samples.

After annealing a sample of each duplex (**SMDA1** and **SMDU1**) CD analysis was used to ensure annealing had occurred. The CD spectrum (Figure 5.13) showed that bands characteristic of B-DNA had formed; a negative signal in the region of 240 – 250 nm and a positive signal close to 275 nm. Once platination had occurred, another sample was extracted for CD analysis. Again, the CD spectrum was characteristic of B-DNA, but despite both platinated and non-platinated) samples being at the same concentration, there was a decrease in the intensity of the CD signal.

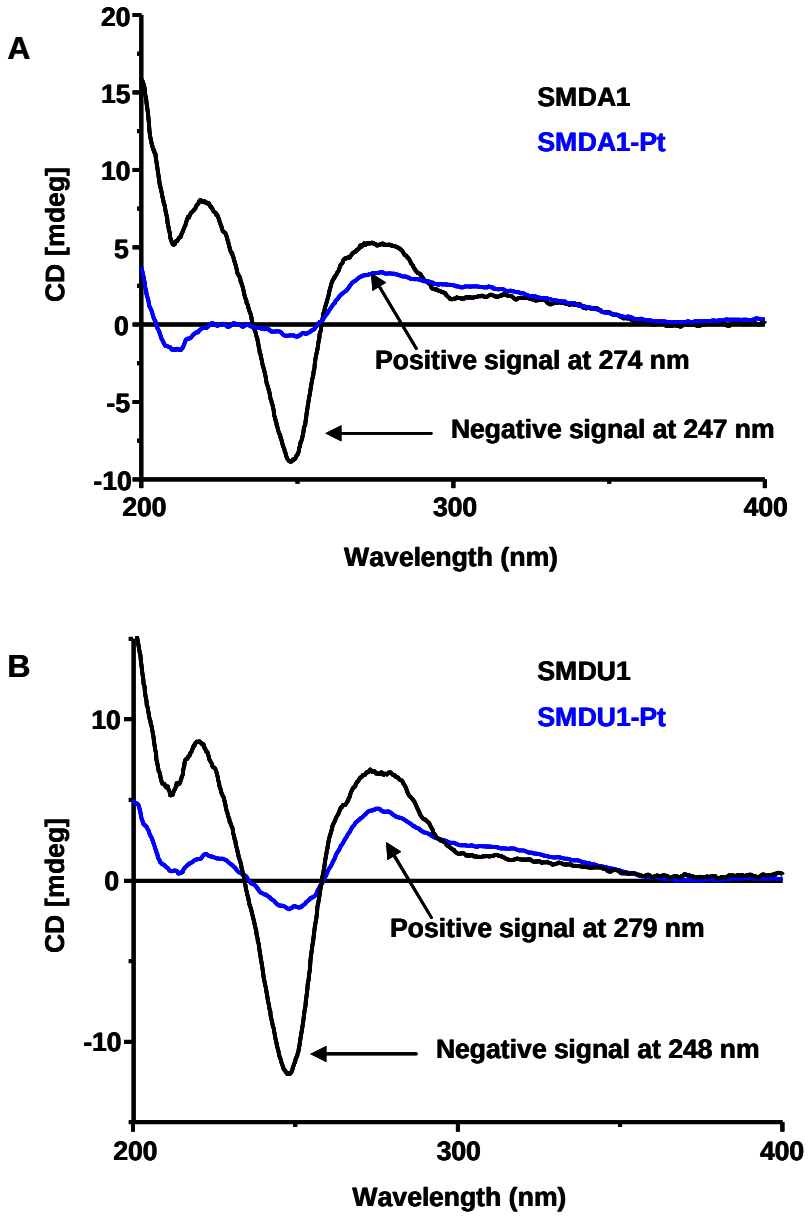

Figure 5.13. CD spectra of A) the duplex with a donor and acceptor tag (SMDA1) and the platinated duplex in blue. B) A duplex formed with only a donor tag (SMDU1) and the platinated duplex.

The difference in the magnitude of absorbance in the CD spectra for platinated and non platinated duplex suggests some loss of chirality. This can occur due to distortions of the double helix and similar effects on the CD of DNA strand upon binding of cisplatin have been observed previously.[36]

Once binding to cisplatin had been confirmed, reverse phase HPLC was carried out in an attempt to separate the complexes to allow for FRET analysis to be carried out on purified species. Figure 5.14 shows the HPLC chromatogram acquired. Identification of the peaks was by elimination of the peaks of the starting materials (i.e.: chromatographs of the starting material were recorded). While cisplatin peaks are generally observed at 305 nm,[37] UV data has shown that the intensity of UV signals at 254 nm is approximately a half that intensity at 305 nm. As a result all HPLC chromatograms were recorded at 254 nm, which is best for DNA samples where λ_{max} is 260 nm. Separation was carried out using a C18-PLRPS column. The benefit of C18 columns for DNA separation in this case is the hydrophobic DNA and the fluorescent tags will interact with the column and so elute later than the hydrophilic platinum salts. A major draw back with using a C18 column is that the complex may be binding to the stationary phase as recovery rates were very low.

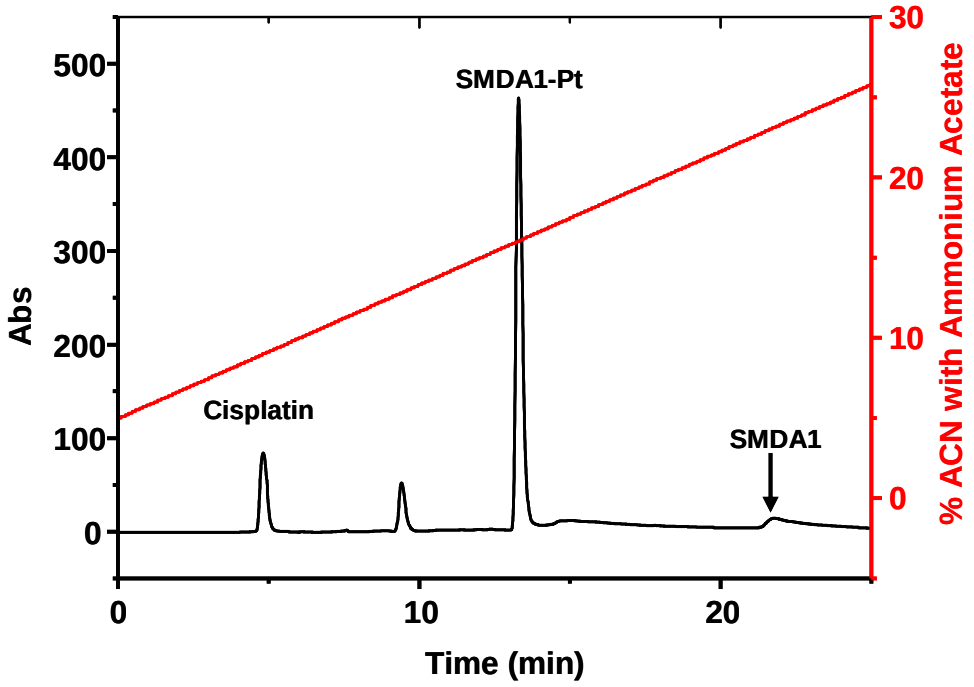

Figure 5.14. HPLC chromatogram of the purification of **SMDA1-Pt** with the important peaks identified. HPLC was carried out using a C18-PLRPS analytical column. A linear gradient from buffer A (H_2O, 10 mM NH_4OAc) to buffer B (60 % ACN in H_2O. 10 mM NH_4OAc) with a flow rate of 1 mL min^{-1}. The best separation was found to occur with a gradient of B from 5 – 30 % over 30 minutes at a 1 mL min^{-1} shown in red. HPLC gradient was developed based on a method previously used for DNA-cisplatin complexes[19]. Absorbance was recorded at 254 nm.

The HPLC fractions were collected and purified a second HPLC cycle with 5% HPLC grade methanol at a rate of 1 ml min^{-1} for 15 minutes followed by 95% methanol for 15 minutes, with a desalted fraction eluting at 16 minutes. Once confirmation of the formation of **SMDA1-Pt** was confirmed, FRET experiments were attempted on the products purified from HPLC . However no FRET was observed. This may have been due to photobleaching of the fluorescent tags from

the UV in the HPLC machine or from daylight. While it had been shown that annealing and binding of cisplatin to the duplex had occurred the lack of FRET indicated not everything had worked as planned. This led to the development of **method B** (*c.f.* Scheme 5.1) in a further attempt to get samples for FRET analysis.

5.3.3.2 (B) Formation of a duplex using a different approach and subsequent binding of cisplatin

Following difficulty in obtaining FRET results from **SMDA1-Pt**, a new method was developed. Fresh batches of the two labelled oligos were purchased to ensure that if there had been no photobleaching of the previous samples, this would not carry over. Table 5.6 lists the concentration and short codes for the new batches of DNA. This time it was decided to use an excess of the acceptor strand to ensure as much duplex formation as possible occurred. Following annealing cisplatin was added and the sample incubated to aid binding. Aside from this, an attempt to bind cisplatin to the FRET donor strand and following binding anneal the donor and acceptor strand together.

Table 5.6. Concentrations and short codes of the second batch of FRET donor and acceptor DNA strands.

Sequence	Code	Conc. (μM)
d(TATCATAAATAAATGGTATATT(Alexa488)TTATAACT)	**D2**	99.6
d(ATAGTATTT(Cy5)ATTTACCATATAAAATATTGA)	**A2**	81.1

5.3.3.2.1 (B) Sample preparation

Solution of **D2** (50.2 μL, 5 nmol), **A2** (123.2 μL, 10 nmol) and $NaClO_4$ (1 μL, 2 μmol) were mixed to give a total volume of 500 μL, and annealed as before (**SMDA2**). (This was confirmed by UV/Vis melting curves; concentration of duplex 0.5 μM). Once annealed, 50 μL was abstracted for analysis and to the remaining solution cisplatin (1 μL, 9.857 mM solution in DMF) was added and incubated at 310 K for 48 h (**SMDA-Pt**). This sample was sent without further purification to Manchester for FRET analysis. The decision not to use HPLC for purification at this point was to ensure no losses as such small amounts of material were in use and also there were concerns that the UV lamp in HPLC and the exposure of fragments to light may have detrimental effects on the photoactivity of the Alexa488 or Cys5 tags. In a similar manner **D2** was reacted with **U** to produce **SMDU2** which was also sent for FRET analysis. The colour of the duplexes is one identifying feature and is shown below in Figure 5.15.

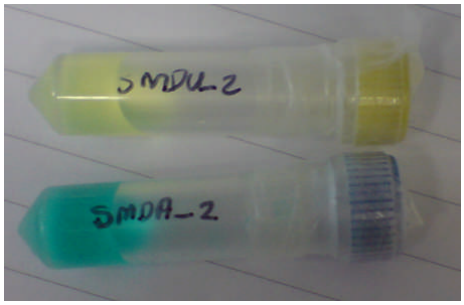

Figure 5.15. Solutions of dimer of the **D2** and **U** strands (**SMDU2**) and the dimer of the **D2** and **A2** strands (**SMDA2**).

5.3.3.2.2 FRET analysis of SMDU2, SMDA2 and SMDA2-Pt

Single molecule FRET studies were carried out at the Photonics Institute in the University of Manchester. Some of these complexes yielded results as shown in Table 5.7 below. These plots of F_g/F_r vs τ provide the most accurate results and rule out any artefact signals. In these studies an ensemble of *ca.* 5 – 10,000 molecules are having their FRET observed. Molecules that undergo fluorescence decay through the same pathway, either FRET or through photon release, will have the same decay time, so by plotting F_g/F_r vs τ any artefacts are eliminated.

When looking at Table 5.7 the following must be pointed out; the first image shows a large F_g/F_r value which is indicative of no FRET occurring and only green light fluorescing. This is a result of the presence of only the donor strand on the DNA duplex. In the absence of the acceptor tag, no FRET can occur. In the second image, which is the FRET of a non-platinated donor and acceptor duplex, FRET is observed between the donor and acceptor tag. The presence of some unannealed donor strand is identified by the large F_g/F_r value. Finally the last image shows the presence of some unannealed donor strands, some donor acceptor strands, but no FRET is observed from a platinated strand.

Table 5.7. Details of the observed single molecule FRET experiments

	Comments
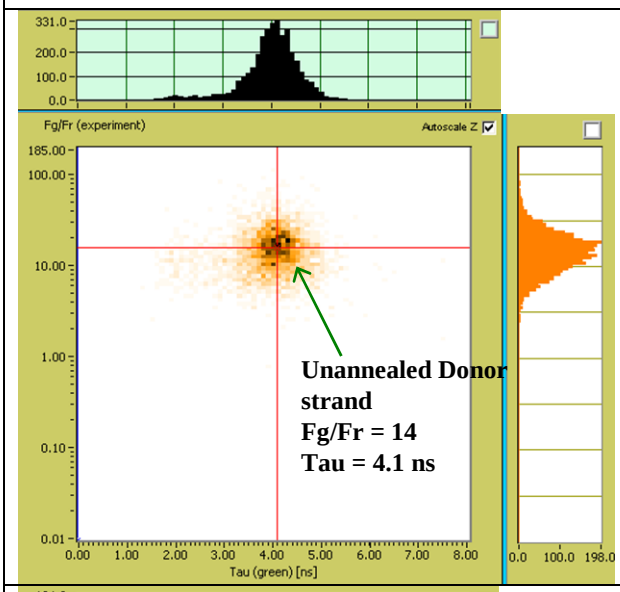	Sample: **SMDU2** This contained no acceptor strand and so no FRET signal is seen here. F_g/F_r is the intensity of green fluorescence to red fluorescence.
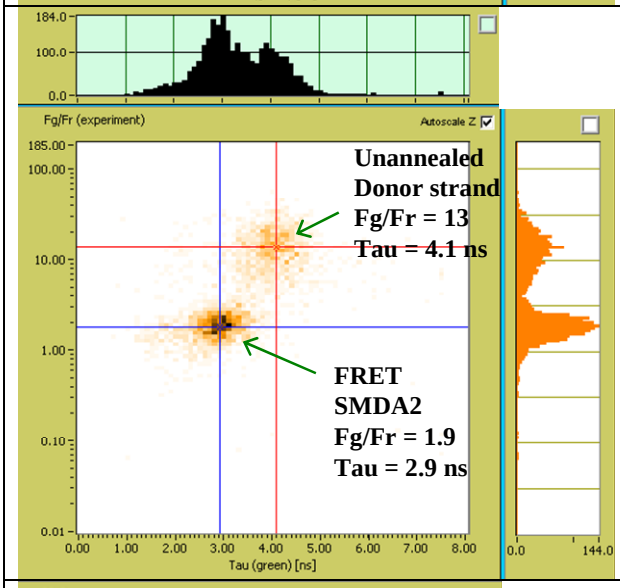	Sample: **SMDA2** The presence of FRET shows that the two strands have annealed and the donor and acceptor tags on the 30-mer are in close proximity Tau, is the lifetime of fluorescence.
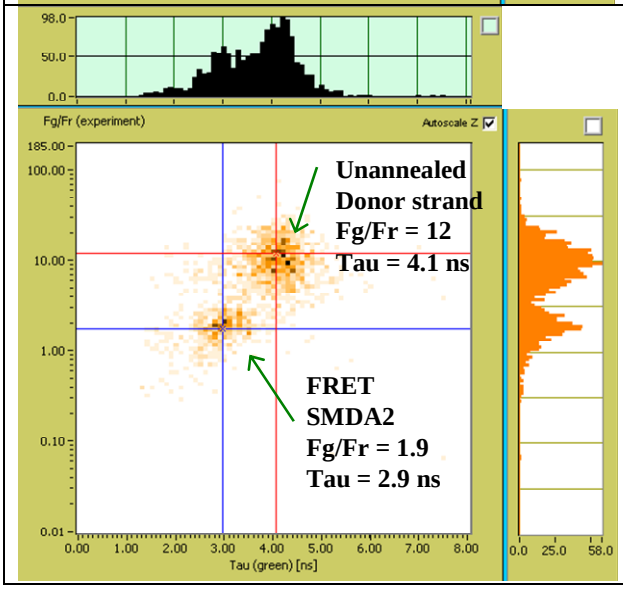	Sample: **SMDA2-Pt** Here there appears to be fluorescence from the donor strand only and some FRET from **SMDA2** but no observed FRET from **SMDA2-Pt**

5.3.3.3 (C) Binding of Donor strand to cisplatin, followed by annealing of acceptor to platinated donor strand.

Given that the results of **§5.3.3.2** contained no evidence for FRET for the platinated duplex **SMDA2-Pt**, concern was raised over the possibility of the heating process (310 K) required for platination damaging the fluorescent tags. As a result the donor tagged DNA strand was platinated prior to annealing with the acceptor strand and then analysed for any FRET activity.

5.3.3.3.1 Sample Preparation

To a solution of **D2** (25 μL, 2.5nmol), cisplatin (0.25 μL, 9.857 mM solution in DMF, 2.5 nmols) was added and the solution volume increased to 100 μL and left to stand for 72 h at 310 K. Following incubation, **A2** (30.8 μL, 2.5 nmol) was added and the solution volume increased to 300 μL with a final $NaClO_4$ concentration of 200 mM. (**SMDA3-Pt)** Due to low concentrations of solution (7.5 μM) and difficulties in purifying, no further analysis was carried out before being sent for annealing and FRET analysis.

5.3.3.3.2 FRET analysis SMDA3-Pt

Results similar to those shown for **SMDA2-Pt** in Figure 5.7 were obtained. As a result of this it was decided to change the sequence and approach the whole problem differently.

5.3.3.4 (D) Change of sequence and use of a doubly labelled strand.

Following difficulties in observing efficient FRET signals from the previous studies, a new method was employed. In this new approach an unlabelled

30-mer would be platinated and then annealed to a 30-mer DNA strand which has a donor and an acceptor FRET tag attached. Table 5.8. details the new sequence used along with their concentrations and short codes.

Table 5.8. Non-labelled sequences used.

Sequence	Conc. (μM)	Code
TAT CAT AAA TAA ATG GTA TAT TTT ATA ACT	**265.07**	**U_GG**
AGT TAT AAA ATA TAC CAT TTA TTT ATG ATA	**332.36**	**U_CC**

The changes in these compared to **D** and **A** used previously are the moving of one guanine base closer to the end of the sequence to increase the stability to the duplex. The presence of G-C base pairings in a duplex prevents "unzipping" of AT bonds at the ends which can unravel more easily. Annealing of the unlabelled duplex occurred and the melting temperature was found to be 325.8 K.

5.3.3.4.1 Preparation of samples

Following determination that duplexes could stably form of this duplex, the single strand of **U_GG** was platinated by preparing an aqueous solution containing 100 μM of **U_GG** (188.6 μL) and 200 μM of cisplatin (12 μL of 8.25 mM solution in DMF) and leaving the solution to stand at 310 K for 72 h.

5.3.3.4.2 MS and FRET analysis of samples

Following binding to the 30-mer over one week, MS was obtained and showed that binding of one cisplatin residue to the 30-mer strand. Figure 5.16

shows the expanded MS spectrum. A large number of negatively-charged ions was observed; this is very common for DNA strands.

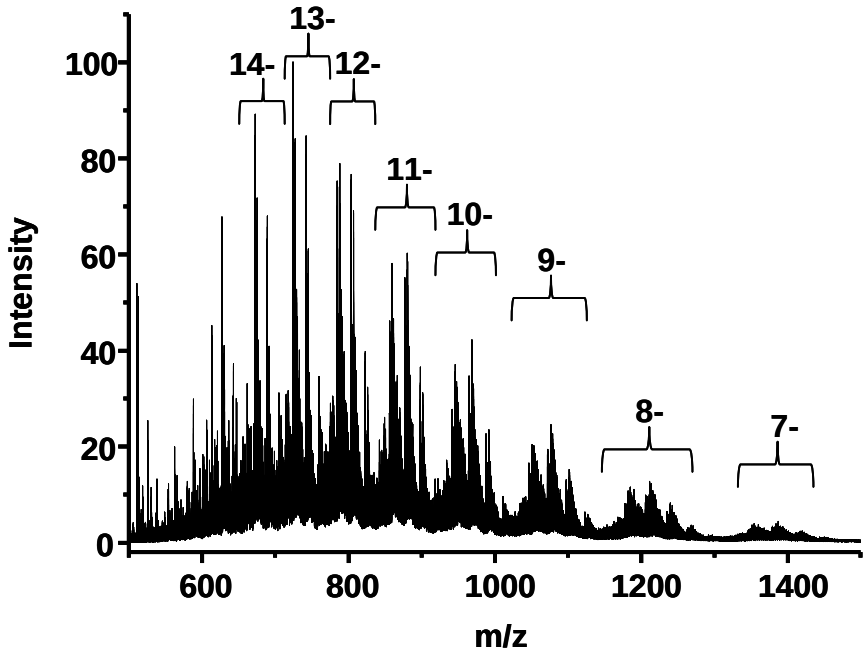

Figure 5.16. Mass spectrum of 30-mer (**U**) after reaction with cisplatin for 7 days. Each charge envelope is highlighted and labelled. Acquired using a Bruker MaXis instrument.

On expansion of the 13^- charge envelope the major species present can be identified. Figures 5.17 a, b, and c compare the charges observed to those predicted in the isotope models.

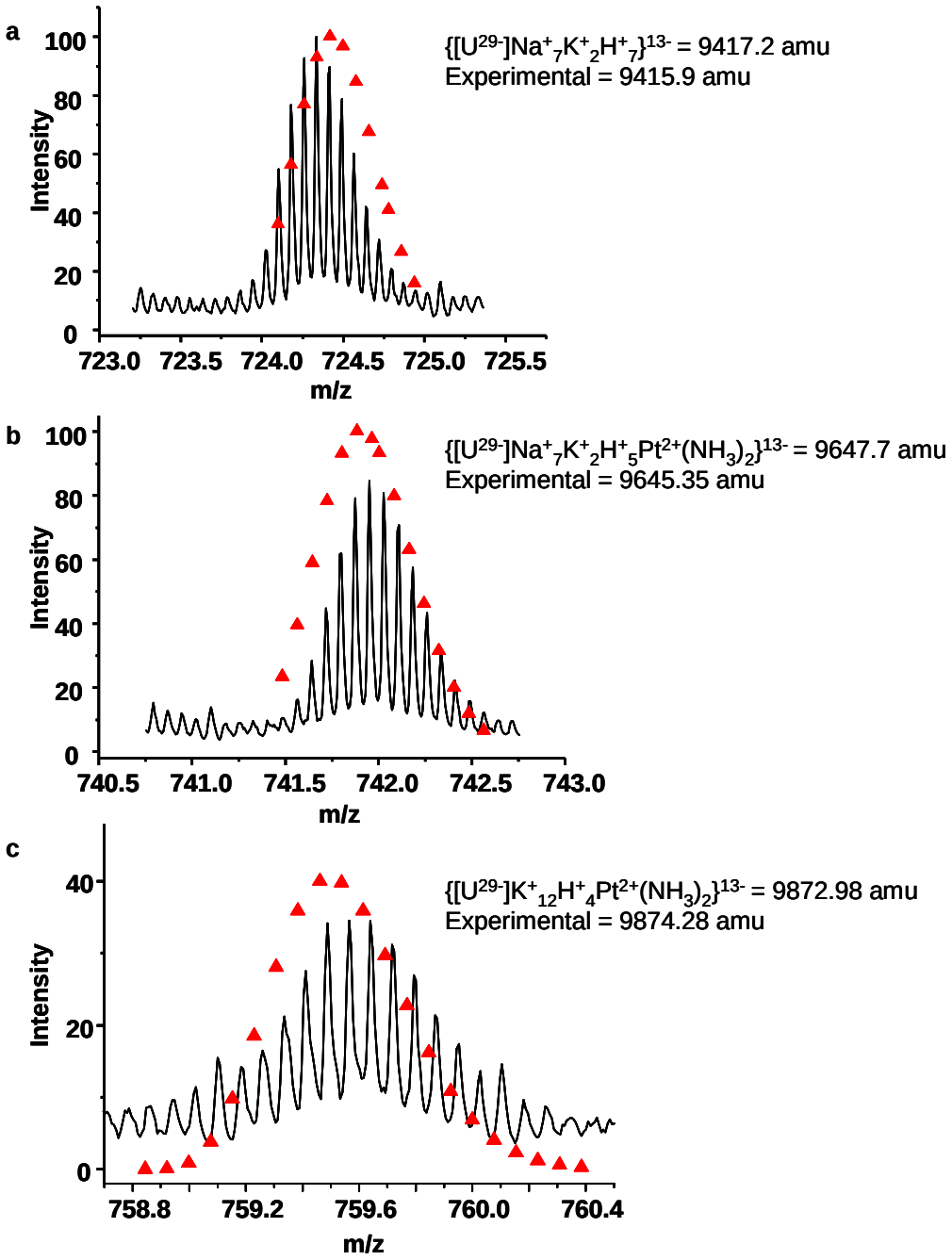

Figure 5.17. Expanded spectra and the simulated isotope pattern for the species centred at a) 724.335 amu b) 741.950 and c) 759.564 m/z. U = unlabelled 30-mer.

Given the fact that only one cisplatin has bound to the 30-mer, the assumption can be made that this binding is to the GpG section in the middle of the sequence. This is based on the favourability for 1,2-GG intrastrand cross links

being formed[6,38]. These samples were sent directly to the Photon Institute in Manchester where there were annealed with the complimentary strand (AGT TAT(Cy5) AAA ATA TAC CAT TTA TTT ATG ATA-Alexa488) for FRET analysis. However, no FRET efficiency for the platinated duplex was observed.

In a final attempt to investigate why no FRET was observed a large excess (10:1) of platinated DNA was annealed with the double tagged strand. The large excess was to ensure that all fluorescent tagged DNA annealed. Upon fluorescence, no FRET whatsoever was observed, either from the fluorescent DNA single strand or from the platinated duplex. This would imply that the platinum may be quenching all fluorescence in the molecule. This was an unexpected result as previous studies of FRET on platinated species have been observed before.[32,33]

The initial aim of this work had been to try the procedure on long strands of DNA bound to cisplatin using FRET to calculate the kinking angle as a proof of concept, if that worked then studies into the effects of ruthenium binding would have been made in a similar way.

5.3.3.4.3 Discussion

The initial aim of this work had been to develop a procedure to determine the kinking angle for long strands of DNA bound to cisplatin using FRET. It was hoped to further utilise the technique to monitor the effects of binding $\{Ru(\eta^6\text{-arene})en\}^+$ fragments to DNA. Currently the only mention in the literature of ruthenium FRET studies, is in the use of fluorescent tags[39].

From the experiments carried out to date, the principle of using FRET to study to monitor formation of long chained DNA duplexes is feasible. However,

platinum adducts on the DNA appear to cause some form of quenching of fluorescence, making FRET analysis impossible. This result was unexpected as previous studies have shown FRET can be observed for platinated biomolecules.[32,33]

5.4 Conclusions

A number of different types of experiments have been listed in this chapter and a variety of conclusions that can be drawn.

5.4.1 Ion Mobility Mass Spectrometry

The IM-MS study discussed in this chapter is an exciting piece of work using this technique and was the first to be published[23] which uses the technique to determine the collision cross section (CCS) of molecules < 100 $Å^2$. The study showed that the CCS values can be accurately determined from IM-MS, comparable to both the X-ray crystal form and, within a reasonably acceptable range to the radius of gyration of the sample of **1** in solution. This ability to determine CCS for small molecules can play a major role in drug discovery. Where compounds are required to be within a certain size, i.e. to enter an enzyme cleft (active site) or to fit into transporter or transmembrane proteins, whole libraries of complexes can be studied to ensure their CCS is within the range.

Further work on the binding of ruthenium complexes to short stranded oligos showed exclusive binding to the guanine residues. IMMS studies also showed that the shape of the oligo changed when bound to the ruthenium complex, but not in an additive way. This indicates that intercalation and conformational folding effects may be exhibited by the ruthenium complex causing the DNA to

fold differently from when it is non-ruthenated. If the shape change of DNA strands upon ruthenation plays a crucial role in the mechanism of action leading to cell death, IMMS may provide a key to studying this. The DNA shape changes observed with cisplatin are believed to play an important part in the mechanism of action of cisplatin in inducing programmed cell death in cancer cells as the shape change caused HMG-Protein recognition[40]. There is a great potential for using IM-MS to look at shape changes of oligonucleotides and biomolecules upon binding to metal drugs[9,41]. This technique could easily be used to scan a library of complexes to understand the shape changes they cause to DNA strands.

5.4.2 FRET studies on 30-Mer oligonucleotides

While several methods were employed analysis platinated DNA using FRET, to date no positive results have been obtained. It appears that one inhibiting factor is potential quenching of FRET by the platinum, as has been suggested by some of the work. Other problems included attempts to purify such small amounts with HPLC leading to heavy losses. However, a similar technique has worked in the past[32] and there is much potential for its use in the future. With more tuning, this technique for examining shape changes of DNA after binding of metal anticancer drugs could be coupled with IM-MS for comparison purposes. Alternatively, as with Lippard's work,[32] potential binding targets can be FRET labelled to confirm binding, or at least that the drug (also FRET labelled). These experiments are in their infancy and it is hoped that the work described here will stimulate further studies.

5.5 References

(1) Liu, H.-K.; Parkinson, J. A.; Bella, J.; Wang, F.; Sadler, P. J. *Chemical Science* **2010**, *1*, 258.

(2) Pizarro, A. M.; Sadler, P. J. *Biochimie* **2009**, *91*, 1198.

(3) Deubel, D. V.; Lau, J. K.-C. *Chem. Commun.* **2006**, 2451.

(4) Liu, L. H.-K.; Wang, F.; Parkinson, J. A.; Bella, J.; Sadler, P. J. *Chem.--A Eur. J.* **2006**, *12*, 6151.

(5) Chen, H.; Parkinson, J. A.; Morris, R. E.; Sadler, P. J. *J. Am. Chem. Soc.* **2003**, *125*, 173.

(6) Cohen, S. M.; Mikata, Y.; He, Q.; Lippard, S. J. *Biochemistry* **2000**, *39*, 11771.

(7) Murata, S.; Mizumura, Y.; Hino, K.; Ueno, Y.; Ichikawa, S.; Matsuda, A. *J. Am. Chem. Soc.* **2007**, *129*, 10300.

(8) Gidden, J.; Bowers, M. T. *J. Phys. Chem. B* **2003**, *107*, 12829.

(9) Williams, J. P.; Bugarcic, T.; Habtemariam, A.; Giles, K.; Campuzano, I.; Rodger, P. M.; Sadler, P. J. *J. Am. Soc. Mass Spectrom.* **2009**, *20*, 1119.

(10) Mesleh, M. F.; Hunter, J. M.; Shvartsburg, A. A.; Schatz, G. C.; Jarrold, M. F. *J. Phys. Chem.* **1996**, *100*, 16082.

(11) Chen, H.; Parkinson, J. A.; Novakova, O.; Bella, J.; Wang, F.; Dawson, A.; Gould, R.; Parsons, S.; Brabec, V.; Sadler, P. J. *Proc. Natl. Acad. Sci. U. S. A.* **2003**, *100*, 14623.

(12) Fernandez, R.; Melchart, M.; Habtemariam, A.; Parsons, S.; Sadler, P. J. *Chem.--A Eur. J.* **2004**, *10*, 5173.

(13) Habtemariam, A.; Melchart, M.; Fernandez, R.; Parsons, S.; Oswald, I. D. H.; Parkin, A.; Fabbiani, F. P. A.; Davidson, J. E.; Dawson, A.; Aird, R. E.; Jodrell, D. I.; Sadler, P. J. *J. Med. Chem.* **2006**, *49*, 6858

(14) Liu, H.-K.; Berners-Price, S. J.; Wang, F.; Parkinson, J. A.; Xu, J.; Bella, J.; Sadler, P. J. *Angew. Chem. Int. Ed.* **2006**, *45*, 8153.

(15) Wang, F.; Bella, J.; Parkinson, J. A.; Sadler, P. J. *JBIC, J. Biol. Inorg. Chem.* **2005**, *10*, 147.

(16) Wang, F.; Xu, J.; Habtemariam, A.; Bella, J.; Sadler, P. J. *J. Am. Chem. Soc.* **2005**, *127*, 17734.

(17) Pringle, S. D.; Giles, K.; Wildgoose, J. L.; Williams, J. P.; Slade, S. E.; Thalassinos, K.; Bateman, R. H.; Bowers, M. T.; Scrivens, J. H. *Int. J. Mass Spectrom.* **2007**, *261*, 1.

(18) Kanu, A. B.; Dwivedi, P.; Tam, M.; Matz, L.; Hill, H. H., Jr. *J. Mass Spectrom.* **2008**, *43*, 1.

(19) Iannitti-Tito, P.; Weimann, A.; Wickham, G.; Sheil, M. M. *Analyst* **2000**, *125*, 627.

(20) McLuckey, S. A.; Van Berkel, G. J.; Glish, G. L. *J. Am. Soc. Mass Spectrom.* **1992**, *3*, 60.

(21) Valentine, S. J.; Counterman, A. E.; Clemmer, D. E. *J. Am. Soc. Mass Spectrom.* **1999**, *10*, 1188.

(22) Wyttenbach, T.; Bushnell, J. E.; Bowers, M. T. *J. Am. Chem. Soc.* **1998**, *120*, 5098.

(23) Williams, J. P.; Lough, J. A.; Campuzano, I.; Richardson, K.; Sadler, P. J. *Rapid Commun. Mass Spectrom.* **2009**, *23*, 3563.

(24) Morris, K. F.; Johnson, C. S., Jr. *J. Am. Chem. Soc.* **1992**, *114*, 3139.

(25) Lang, Z. H.; Jun, H. S. *J. Chem. Eng. Data* **1996**, *41*, 516.

(26) Takahara, P. M.; Rosenzweig, A. C.; Frederick, C. A.; Lippard, S. J. *Nature* **1995**, *377*, 649.

(27) Spingler, B.; Whittington, D. A.; Lippard, S. J. *Inorg. Chem.* **2001**, *40*, 5596.

(28) Todd, R. C.; Lippard, S. J. *J. Inorg. Biochem.* **2010**, *104*, 902.

(29) Chen, H.; Parkinson, J. A.; Parsons, S.; Coxall, R. A.; Gould, R. O.; Sadler, P. J. *J. Am. Chem. Soc.* **2002**, *124*, 3064.

(30) Wang, F.; Habtemariam, A.; van der Geer, E. P. L.; Fernandez, R.; Melchart, M.; Deeth, R. J.; Aird, R.; Guichard, S.; Fabbiani, F. P. A.; Lozano-Casal, P.; Oswald, I. D. H.; Jodrell, D. I.; Parsons, S.; Sadler, P. J. *Proc. Natl. Acad. Sci. U. S. A.* **2005**, *102*, 18269.

(31) Yan, Y. K.; Melchart, M.; Habtemariam, A.; Sadler, P. J. *Chem. Commun.* **2005**, 4764.

(32) Jamieson, E. R.; Jacobson, M. P.; Barnes, C. M.; Chow, C. S.; Lippard, S. J. *J. Biol. Chem.* **1999**, *274*, 12346.

(33) Wozniak, A. K.; Schroder, G. F.; Grubmueller, H.; Seidel, C. A. M.; Oesterhelt, F. *Proc. Natl. Acad. Sci. U. S. A.* **2008**, *105*, 18337.

(34) Wozniak Anna, K.; Schroder Gunnar, F.; Grubmuller, H.; Seidel Claus, A. M.; Oesterhelt, F. *Proc. Natl. Acad. Sci. U. S. A.* **2008**, *105*, 18337.

(35) Rothwell, P. J.; Berger, S.; Kensch, O.; Felekyan, S.; Antonik, M.; Wohrl, B. M.; Restle, T.; Goody, R. S.; Seidel, C. A. M. *Proc. Natl. Acad. Sci. U. S. A.* **2003**, *100*, 1655.

(36) Kostrhunova, H.; Brabec, V. *Biochemistry* **2000**, *39*, 12639.

(37) El-Khateeb, M.; Appleton, T. G.; Gahan, L. R.; Charles, B. G.; Berners-Price, S. J.; Bolton, A.-M. *J. Inorg. Biochem.* **1999**, *77*, 13.

(38) Wu, Y.; Bhattacharyya, D.; King, C. L.; Baskerville-Abraham, I.; Huh, S.-H.; Boysen, G.; Swenberg, J. A.; Temple, B.; Campbell, S. L.; Chaney, S. G. *Biochemistry* **2007**, *46*, 6477.

(39) Yun, B. H.; Kim, J.-O.; Lee, B. W.; Lincoln, P.; Norden, B.; Kim, J.-M.; Kim, S. K. *J. Phys. Chem. B* **2003**, *107*, 9858.

(40) Bruhn, S. L.; Pil, P. M.; Essigmann, J. M.; Housman, D. E.; Lippard, S. J. *Proc. Natl. Acad. Sci. U. S. A.* **1992**, *89*, 2307.

(41) Williams, J. P.; Phillips, H. I. A.; Campuzano, I.; Sadler, P. J. *J. Am. Soc. Mass Spectrom.* **2010**, *21*, 1097.

Chapter 6

Conclusions and Future Works

Chapter 6

Closing Comments and Future work

This Chapter is designed to summarise the work presented in this thesis and to place it into the context of previous work in the field. Also in this Chapter future work which may be carried out in this field will be proposed. As with any piece of scientific work, there is always scope for improvement and development, always more questions to be answered and this chapter will deal with some of the challenges that remain.

6.1 Kinetics and mechanism of N-H/D exchange on $[(\eta^6\text{-arene})Ru(en)X]^{n+}$ complexes

In Chapters 3 and 4 of this thesis the kinetics of N-H/D exchange on a variety of complexes were observed (Figure 6.1).

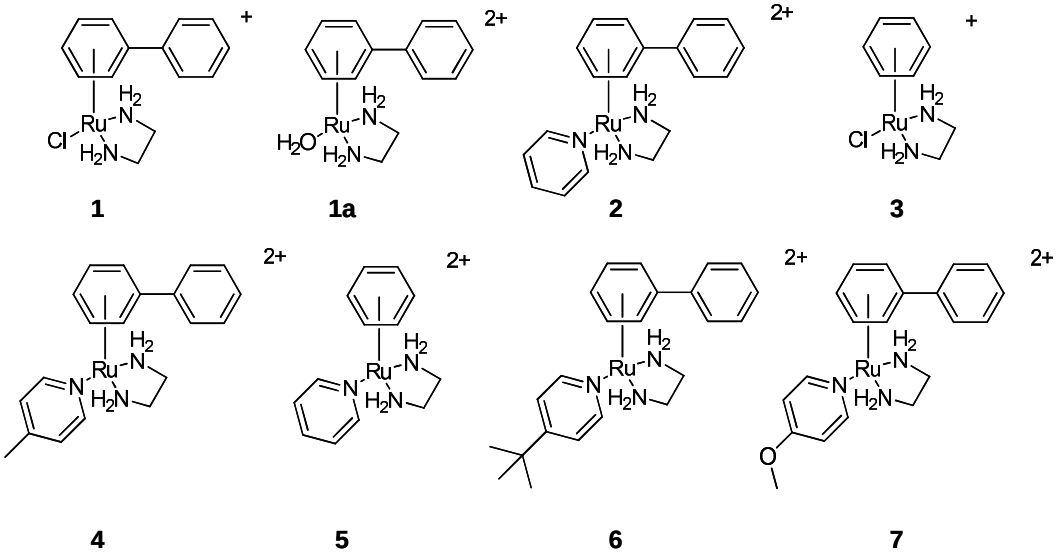

Figure 6.1. The complexes investigated in this thesis.

The aim of this was to proposed a mechanism of stereochemical inversion which had been found to occur on $[(\eta^6\text{-bip})Ru(N\text{-Et-en})Cl]^+$ (**5A** and **5B**).[1] During the course of these studies a number of observations were made. Of interest was the observation that protons nearer the η^6-bound biphenyl ring (NH_{up}) exchanged much more slowly than those which were further away from the arene (NH_{down}). (Figure 6.2)

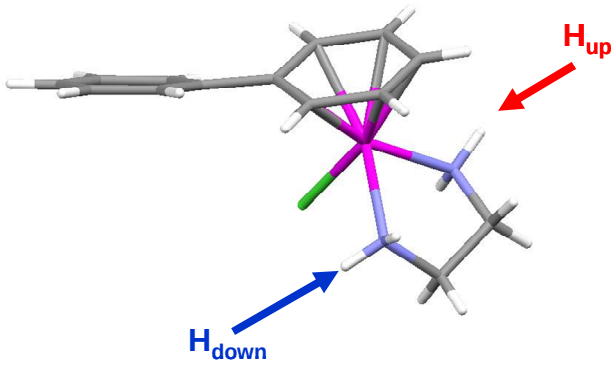

Figure 6.2. Identification of the up and down protons on the ethylenediamine chelating ligand, H_{down} and H_{up} are marked.

It was initially hypothesised that the difference in the exchange rates may simply be a related to the steric hindrance due the biphenyl ring being in close proximity to NH_u. Further analysis in Chapter 4, where the effects of electron donation from the Z ligand (Figure 6.3) were analysed, showed that the monodendate ligand in the Z-position appears to play a role in controlling the rates of N-H/D exchange and the favourability of NH_d exchange over NH_u.

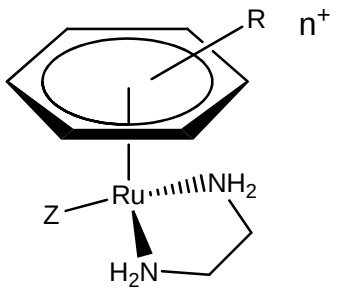

Figure 6.3. The structure of the $[(\eta^6\text{-arene})Ru(en)X]^{n+}$ complexes investigated in this work.

Also of interest in Chapter 4 was the correlation between increasing electron donation of the *p*-pyridine derivatives and the favourability for NH_d to undergo rapid exchange. Further analysis and computational studies suggested there is a stabilisation affect from the π^*-antibonding orbitals of the Ru-Z bonds on the p-orbital on the nitrogen atom after deprotonation. There is no presedence in the literature which proposes this type long range, almost anomeric-like effect on metals ligands, whereby the antibonding orbitials of one metal-ligand bond will affect the stability of another ligand in the *cis* position. Unlike the *trans*-effect of a number of different ligands on metal complexes which is well documented,[2] as far as the author is aware there are no reports about effects on *cis*-ligands, let alone the effects on the liability of protons on the ligands themselves.

Previous work on cobalt(III)(am(m)ine) complexes observed similar effects in that anisotropic N-H protons exchanged at different rates, but no detailed explanation for this effect had been postulated.[3-10] These studies[3-10] have suggested that exchanges of stereochemistry may be as a result of proton abstraction followed by rotation of the nitrogen stereocentre. Also of note in these cobalt studies was the observation that the rates of exchange were base catalysed, similar results were observed in the work presented in this thesis. Other work on

ruthenium catalysts provided evidence for the potential of stereoinversion to occur via a 16 electron species.[11-16]

When all the observations in Chapter 3 and 4 were combined the following mechanism for exchange was proposed. (Figure 6.4)

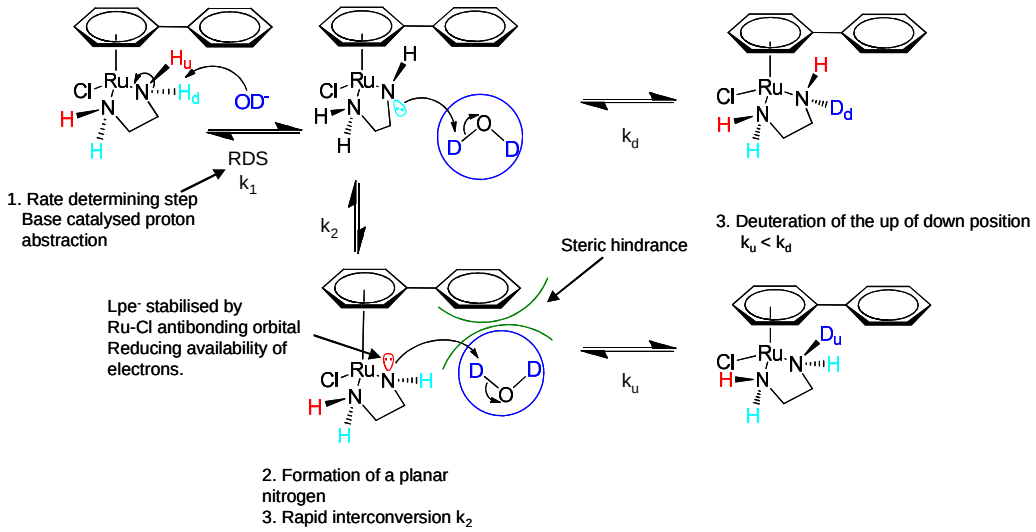

Figure 6.4. The proposed mechanism for NH exchange. The Ru-Cl antibonding orbital can stabilise the upper face of the p-orbital making it less susceptible to protonation.

When the mechanism is applied to the original problem of stereochemical inversion between **5A** and **5B** the following mechanism is postulated (Figure 6.5);

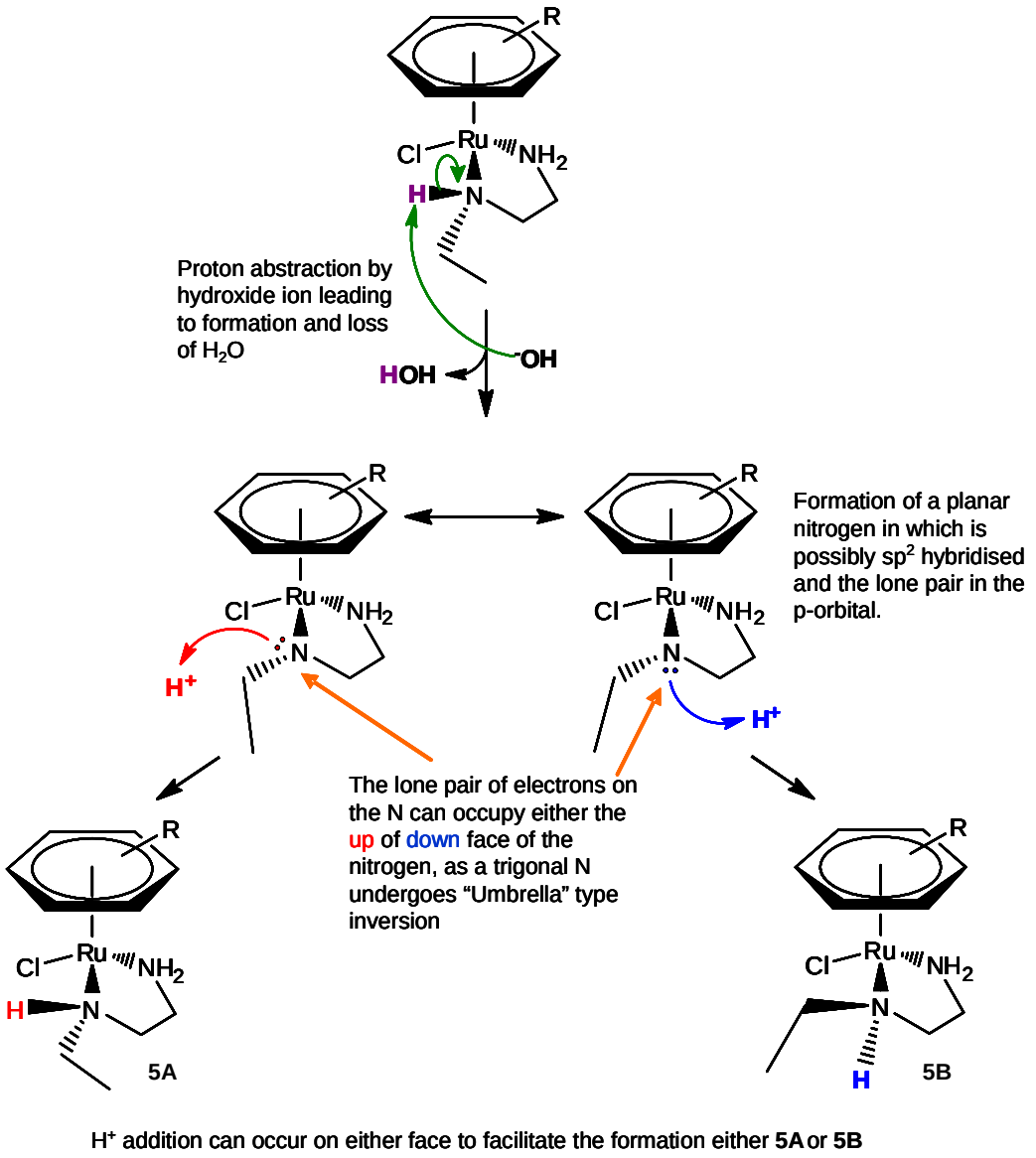

Figure 6.5. The proposed mechanism for the interconversion of **5A** to **5B** in aqueous solutions.

6.1.1 Future work in this field

Further work in this field is the potential to study a variety of electron donating ligands in the Z position. Attempts were made to use 4-Cl-pyridine, 4-Br-pyridine and 4-CF_3-pyridine ligands, however difficulties arose during

synthesis, this may require further tuning. If the electron withdrawing groups allow for stabilisation of the lone pair electron on upper face of the nitrogen after deprotonation, electron donating groups should have the reverse effect.

Comparisons with a series of σ-donor ligands may also prove useful in investigating the long range of effects on the antibonding orbitals of the Ru-Z bond and their stabilising effect on the deprotonated nitrogen of ethylenediamine. Solid state ^{99}Ru NMR may also prove useful in understanding the effects of electron donating and withdrawing groups on the electron density of the ruthenium ion.

6.2 Ion-Mobility Mass Spectometry

In Chapter 5, a series of Ion-mobility Mass Spectrometry (IM-MS) experiments were carried out to analyse the 3D shape of small molecules and ruthenated oligomer strands. These results were the first reported studies of this type[17] and produced many interesting results. Firstly, the use of glycine polymers had been shown as an excellent calibrant to determine the collision cross section (CCS) of less than 100 Å^2. Secondly, the use of IM-MS to study the effects of ruthenating small strands of DNA has also been validated. The results showed that the ruthenation of DNA does not cause and additive effect on the shape of the oligomer. This could be indicative of the type of binding by the ruthenium, i.e.: intercalating or kinking of the DNA strand.

6.2.1 Future work in this field

Future work in this area would be to use IM-MS to analyse the shape changes upon binding to larger oligonucleotides (>30 mer). By using larger

strands, if any kinking occurred, a larger change in collisional cross section would be observed. In a similar manner, duplexes could potentially be investigated to observe any changes in shape upon binding to ruthenium complexes.

Also of interest would be to study the effects of a series of ruthenium-arene complexes on DNA strands. If the ligand is intercalating then the changes to the CCS should be roughly the same irrespective of the size of the arene. For these studies a series of potential intercalators (extended arene systems) and non-intercalators could be bound to DNA oligomers. It would be of interest to observe if there is a difference in the CCS when DNA strands are ruthenated by non-intercalators compared to intercalators. Once these details are established, the potential to investigate shape changes as a function of the location of guanine residues on the DNA sequences can also be investigated.

Since this field is very new and very few ion-mobility studies on short strands of DNA have been studied, much work still needs to be done to understand how to fully interpret the data. As previously mentioned, difficulty arose in making comparisons between the ruthenated and non-ruthenated DNA and that the effects of charge on the phosphate backbone of the DNA must be considered. In this study, comparisons were made between the duplex with three protons on the phosphate backbone. Questions need to be asked, is this approach accurate? Traditionally when comparisons are made between mobility data, ions are usually in the same charge state. However, in theses studies the addition of a charged complex to the molecule changes the charge and charge distribution on the oligomer. What is the best way to handle this? Is the approach of comparing molecular ions of different charges, but would have the same charges when the metal is removed accurate? Also, what, if any, are the effects from the T-wave on

unravelling the small DNA strands which are not stabilised by duplex binding? Work by Bowers *et. al.*[18] has shown some results showing conformations of longer DNA strands changing at various charge states, therefore these are problems that must be considered when investigating longer strands of DNA.

Would computational modelling of the strands of DNA with charges in different positions on the phosphate backbone provide similar results for CCS values? Modelling of DNA strands with the negative charges in a variety of positions on the phosphate back bone may provide some insight into the accurate understanding of the results of ion-mobility mass spectrometry for DNA complexes.

6.3 FRET analysis of platinated oligonucleotides

Results in Chapter 5 showed difficulty in obtaining FRET on platinated 30-mers of oligonucleotides. A number of approaches were attempted and all to no avail. This result was most unusual as previous studies have shown that using FRET to study DNA kinking of metallated duplexes is possible.[19,20]

6.3.1 Future work in this field

The initial plan for this experiment was to investigate the potential of FRET in investigating shape changes on DNA following ruthenium-arene complex binding. While the cisplatin binding studies have proved difficult, potential for this difficulty may be quenching of fluorescence by platinum. Further work is required to investigate this. Separation of the platinated unlabelled oligonucleotide prior to binding with the FRET tagged strand will be essential in this. If upon formation of the duplex no FRET is still observed then the

probability that the problem is with either quenching or other photophysics based issues will be greatly increased. This in itself will provide an interesting problem to be solved, and a potential solution may be to change the FRET donor and acceptor tags.

An example of other tags with potential use are; coumarin 120 and coumarin 151 (Figure 6.6) which have previously been bound directly to platinum without quenching.[21]

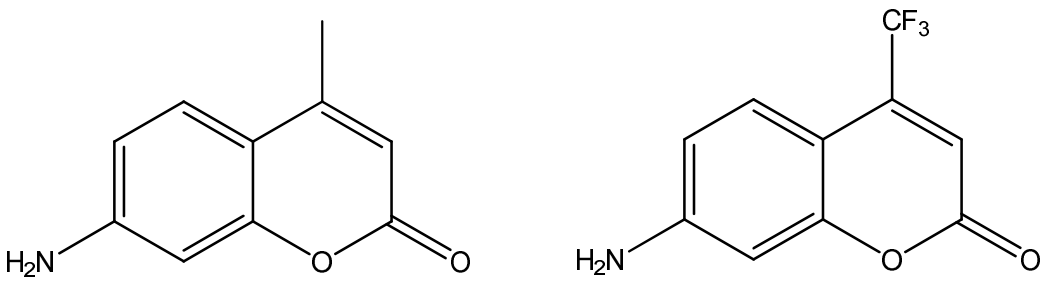

coumarin 120 coumarin 151

Figure 6.6. The chemical structure of the potential FRET tags coumarin 120 and coumarin 151.

Work with ruthenium complexes would hopefully be more successful given that ruthenium complexes are commonly used in FRET studies successfully (implying no quenching).[22,23] In some cases the ruthenium complexes themselves are the FRET acceptors.[24] Calf-thymus-DNA and NMR studies of binding of $\{(\eta^6\text{-bip})Ru(en)\}^{2+}$ to DNA [25,26] have shown a unwinding of supercoiled DNA and no evidence of kinking. This is unlike those results observed with cisplatin which have shown kinking of the DNA strands. It would be of interest to understand if changes to long strands of DNA are bending in someway or if unwinding of the DNA leads to a lengthening of the strand.

6.4 References

(1) Chen, H.; Parkinson, J. A.; Novakova, O.; Bella, J.; Wang, F.; Dawson, A.; Gould, R.; Parsons, S.; Brabec, V.; Sadler, P. J. *Proc. Natl. Acad. Sci. U. S. A.* **2003**, *100*, 14623.

(2) Chernyaev, I. I. *Izvest. Sektora Platiny i Drugikh Blagorodnykh Metal., Inst. Obshchei i Neorg. Khim., Akad. Nauk S.S.S.R.* **1948**, *No. 21*, 27.

(3) Buncel, E.; Clement, O.; Onyido, I. *Acc. Chem. Res.* **2000**, *33*, 672.

(4) Lichtig, J.; Sosa, M. E.; Tobe, M. L. *J. Chem. Soc., Dalton Trans.* **1984**, 581.

(5) Nakazawa, H.; Sakaguchi, U.; Yoneda, H.; Morimoto, Y. *Inorg. Chem.* **1981**, *20*, 973.

(6) Sakaguchi, U.; Maeda, K.; Yoneda, H. *Bull. Chem. Soc. Jpn.* **1976**, *49*, 397.

(7) Taura, T.; Sakaguchi, U.; Yoneda, H. *Bull. Chem. Soc. Jpn.* **1976**, *49*, 1867.

(8) Terrill, J. B.; Reilley, C. N. *Anal. Chem.* **1966**, *38*, 1876.

(9) Yoneda, H.; Nakashima, Y. *Bull. Chem. Soc. Jap.* **1974**, *47*, 669.

(10) Yoneda, H.; Sakaguchi, U.; Nakashima, Y. *Bull. Chem. Soc. Jpn.* **1975**, *48*, 209.

(11) Haack, K.-J.; Hashiguchi, S.; Fujii, A.; Ikariya, T.; Noyori, R. *Angew. Chem., Int. Ed.* **1997**, *36*, 285.

(12) Hashiguchi, S.; Fujii, A.; Haack, K.-J.; Matsumura, K.; Ikariya, T.; Noyori, R. *Angew. Chem., Int. Ed.* **1997**, *36*, 288.

(13) Matsumura, K.; Hashiguchi, S.; Ikariya, T.; Noyori, R. *J. Am. Chem. Soc.* **1997**, *119*, 8738.

(14) Hayes, A. M.; Morris, D. J.; Clarkson, G. J.; Wills, M. *J. Am. Chem. Soc.* **2005**, *127*, 7318.

(15) Ohkuma, T.; Utsumi, N.; Tsutsumi, K.; Murata, K.; Sandoval, C.; Noyori, R. *J. Am. Chem. Soc.* **2006**, *128*, 8724.

(16) Sandoval, C. A.; Bie, F.; Matsuoka, A.; Yamaguchi, Y.; Naka, H.; Li, Y.; Kato, K.; Utsumi, N.; Tsutsumi, K.; Ohkuma, T.; Murata, K.; Noyori, R. *Chem.--An Asian J.* **2010**, *5*, 806.

(17) Williams, J. P.; Lough, J. A.; Campuzano, I.; Richardson, K.; Sadler, P. J. *Rapid Commun. Mass Spectrom.* **2009**, *23*, 3563.

(18) Baker, E. S.; Dupuis, N. F.; Bowers, M. T. *The Journal of Physical Chemistry B* **2009**, *113*, 1722.

(19) Jamieson, E. R.; Jacobson, M. P.; Barnes, C. M.; Chow, C. S.; Lippard, S. J. *J. Biol. Chem.* **1999**, *274*, 12346.

(20) Wozniak, A. K.; Schroder, G. F.; Grubmueller, H.; Seidel, C. A. M.; Oesterhelt, F. *Proc. Natl. Acad. Sci. U. S. A.* **2008**, *105*, 18337.

(21) New, E. J.; Duan, R.; Zhang, J. Z.; Hambley, T. W. *Dalton Trans.* **2009**, 3092.

(22) Klajner, M.; Hebraud, P.; Sirlin, C.; Gaiddon, C.; Harlepp, S. *The Journal of Physical Chemistry B* **2010**, *114*, 14041.

(23) Kramer, R. A.; Flehr, R.; Lay, M.; Kumke, M. U.; Bannwarth, W. *Helv. Chim. Acta* **2009**, *92*, 1933.

(24) Clima, L.; Bannwarth, W. *Helv. Chim. Acta* **2008**, *91*, 165.

(25) Novakova, O.; Chen, H.; Vrana, O.; Rodger, A.; Sadler, P. J.; Brabec, V. *Biochemistry* **2003**, *42*, 11544.

(26) Liu, H.-K.; Berners-Price, S. J.; Wang, F.; Parkinson, J. A.; Xu, J.; Bella, J.; Sadler, P. J. *Angew. Chem., Int. Ed.* **2006**, *45*, 8153.